SHOCK-INDUCED GEOCHEMICAL VARIATIONS IN THE KEPLERITE-BEARING ASSEMBLAGES OF TISSINT AND INTERGROWN APATITE-MERRILLITE ASSEMBLAGES OF ALH 84001,146

by

Ane Slabić, B.S.

THESIS

Presented to the Faculty of

The University of Houston-Clear Lake

In Partial Fulfillment

Of the Requirements

For the Degree

MASTER OF SCIENCE

in Environmental Science

THE UNIVERSITY OF HOUSTON-CLEAR LAKE

DECEMBER, 2022

SHOCK-INDUCED GEOCHEMICAL VARIATIONS IN THE KEPLERITE-BEARING ASSEMBLAGES OF TISSINT AND INTERGROWN APATITE-MERRILLITE ASSEMBLAGES OF ALH 84001,146

by

Ane Slabić

APPROVED BY

Daniel B. Imrecke, Ph.D., Chair

Dongmin Sun, Ph.D., Committee Member

Allan H. Treiman, Ph.D., Committee Member

Justin R. Filiberto, Ph.D., Committee Member

RECEIVED/APPROVED BY THE COLLEGE OF SCIENCE AND ENGINEERING:

David Garrison, Ph.D., Associate Dean

Miguel A. Gonzalez, Ph.D., Dean

Dedication

To Baba, Dide, Mama, and Tata.

Acknowledgements

Thank you to my incredible committee members, Drs. Daniel Imrecke, Allen Treiman, Justin Filiberto, and Dongmin Sun, for supporting this work, providing helpful discussions, and for getting the project off its feet. I appreciate you all so very much, thank you from the bottom of my heart. Thank you, Valerie Tu, Kayla Iacovino, Loan Le, Timmons Erickson, Ryan Jakubek, Roger Harrington, Kathie Thomas-Keprta, Alia Jasim, and the ARES Division of NASA-JSC for helpful discussions and contributions. Funding for this research is generously provided by Barrios Technology and the Geological Society of America (GSA). The use of the EMPA facility at the Department of Earth, Environmental and Planetary Sciences, Rice University, Houston, TX, is kindly acknowledged.

The greatest thanks go out to my loving family and to my caring fiancé, Steven. I couldn't have done this without all of you. Thank you all for being there by my side, every step of the way.

ABSTRACT

SHOCK-INDUCED GEOCHEMICAL VARIATIONS IN THE KEPLERITE-BEARING ASSEMBLAGES OF TISSINT AND INTERGROWN APATITE-MERRILLITE ASSEMBLAGES OF ALH 84001,146

Ane Slabić
University of Houston-Clear Lake, 2022

Master's Project Chair: Daniel B. Imrecke, Ph.D.

Shock metamorphism describes changes (physical, chemical) that occur to materials (structures, rocks, minerals) as a result of shock wave deformation. All Martian meteorites have been subjected to shock, though the degree of shock, and subsequent changes to the physical and chemical characteristics of these rocks, is highly variable. Extensive chemical and structural heterogeneities may occur as a result of shock metamorphism; however, the way in which phosphate minerals respond to shock-metamorphism is not well constrained. Here we present new evidence of shock-induced chemical variations in the keplerite-bearing assemblages of Tissint and the apatite-merrillite assemblages of ALH 84001. Geochemical and structural studies of phosphate phases were investigated using Electron Probe MicroAnalyzer (EMPA), Raman

Spectroscopy, Scanning Electron Microscopy (SEM), and Electron Backscatter Diffraction (EBSD) analytical techniques. Phosphates identified included *Low-Na* (Na# = 2.3) keplerite in Tissint and intergrown Cl-rich-apatite with *High-Na* merrillite (Na# = 8.3) in ALH 84001. Na-number is the calculated atomic ratio of sodium to the sum of sodium and calcium ($[Na_{atomic}/(Na_{atomic}+Ca_{atmoic})]*100$). Presence of keplerite (a newly defined, high-temperature, Na-deficient, phosphate) in Tissint suggests it may be common and occur in a broader range of environments (i.e., meteorite groups) than initially established. ALH 84001 apatite was found to be heterogeneously enriched in halogens with Cl between 3.85 and 5.05 wt% and F between 0.30 and 0.92 wt%. Assuming F + Cl + OH = 1.0 structural formula unit (sfu); average atoms per formula unit (apfu) of F = 0.16, while apfu of Cl = 0.63. Therefore, water content of apatite in ALH 84001 is estimated at 0.21 sfu or, ~21% hydroxyl apatite component. Thus, indicating that parental magmas were Cl-rich and OH-poor. Intergrown apatite-merrillite phases were observed as well, with textures suggesting the replacement of magmatic apatite by merrillite in the solid-state following a shock-metamorphic event.

TABLE OF CONTENTS

CHAPTER 1: INTRODUCTION 1

1.1 Meteorite Classification 1
1.2 Classification of Undifferentiated Meteorites: Chondrites 2
1.3 Classification of Differentiated Meteorites: Achondrites 2
1.4 Martian Meteorite Classification 4
1.5 Phosphate Phases in Extraterrestrial Systems 9
1.5.1 Apatite-group Minerals 9
1.5.2 Whitlockite-group Minerals 14
1.6 Shock Metamorphic Effects in Rocks and Minerals 33
1.7 Objective 36

CHAPTER 2: MATERIALS 37

2.1 Tissint 37
2.2 ALH 84001 40

CHAPTER 3: METHODS 44

3.1 JEOL JXA-8530F Hyperprobe: Tissint and ALH 84001 44
3.1.1 Energy Dispersive Spectrometry (EDS) 44
3.1.2 Electron MicroProbe Analysis (EMPA) 44
3.1.3 Phosphate Analysis 44
3.1.4 WDS quantitative maps 45
3.2 JEOL JXA-8530F Field Emission Electron Probe: Tissint 46
3.2.1 Energy Dispersive Spectrometry (EDS) 46
3.2.2 Electron MicroProbe Analysis (EMPA) 46
3.3 WITec alpha300R Raman Microscope: Tissint 46
3.4 JEOL 7900F Field Emission Gun SEM: Tissint 47

CHAPTER 4: TISSINT 48

4.1 Results 48
4.1.1 Phosphate Discrimination 48
4.1.2 Keplerite Chemical Composition 48
4.1.3 Raman Spectroscopy 57
4.1.4 Electron Backscattered Diffraction (EBSD) 60
4.2 Discussion 63
4.3 Implications 68

4.4 Conclusions ... 69

CHAPTER 5: ALH 84001 ... 70

5.1 Results ... 70
Apatite and Merrillite Chemical Composition ... 70
5.2 Discussion ... 92
5.3 Implications ... 95
5.4 Conclusions ... 95

REFERENCES ... 96

APPENDIX A: INSTRUMENT CONDITIONS ... 101

APPENDIX B: QUANTITATIVE POINT ANALYSES ... 105

APPENDIX C: WAVELENGTH DISPERSIVE SPECTROMETRY (WDS) ... 116

Tissint ... 116
ALH 84001 ... 148
NWA 998 ... 169

APPENDIX D: RAMAN SPECTROSCOPY ... 207

APPENDIX E: ELECTRON BACKSCATTERED DIFFRACTION (EBSD) ... 218

LIST OF TABLES

Table 1. Whitlockite-group minerals that have been approved by The Commission on New Minerals, Nomenclature and Classification (CNMNC) of the International Mineralogical Association (IMA). 15

Table 2. Summarized meteoritic keplerite chemical compositions. 28

Table 3. Measured frequencies of (PO_4) vibration modes (cm^{-1}) for Raman spectra in Figure 23 and Figure 24. 32

Table 4. Average composition of keplerite in Tissint. 53

Table 5. Average chemical composition of apatite in ALH 84001. 72

LIST OF FIGURES

Figure 1. Classification of Chondrites. 2

Figure 2. Classification of Differentiated Meteorites. 3

Figure 3. Representation of all Martian Meteorite types. 6

Figure 4. Plot of isotopic source rations ($^{176}Lu/^{177}Hf$ and $^{147}Sm/^{144}Nd$) of enriched, intermediate, and depleted shergottites, and ALH 84001 against an assumed end-member mixing array (shown by underlying grid) that was generated using end-member compositions (indicated by green circles). 7

Figure 5. Information to be gained by studying Martian Meteorites. 8

Figure 6. Apatite backscattered electron (BSE) images and photographs as sourced from various environments (i.e., asteroidal and planetary bodies)...................... 11

Figure 7. Schematic diagram of the periodic table illustrating elements which occur in apatite super-group minerals (shaded in red). 12

Figure 8. Ternary plots of apatite F-Cl-OH chemistries as they are related to asteroidal parent bodies, lunar samples, and Martian meteorite sources. 12

Figure 9. Ternary plot of apatite F-Cl-OH chemistries as they are related to Terrestrial (basaltic rocks of Earth) and Martian sources. 13

Figure 10. B-site environments of keplerite and whitlockite. 16

Figure 11. Backscattered electron (BSE) images and X-ray element maps of phosphate grains from the Elephant Moraine (EETA) 79001 shergottite. 18

Figure 12.Compositional variations in Martian merrillite. 19

Figure 13. Plot of Na (a.f.u.) versus Mg# in Martian merrillite. 20

Figure 14. Plot of Mn (a.f.u.) versus Mg# in Martian merrillite. 21

Figure 15. Ternary plot of Martian and Lunar merrillite. 22

Figure 16. Cations commonly found in merrillite. 23

Figure 17. Representative section of merrillite crystal structure, looking down the c-axis. 24

Figure 18. Backscattered electron (BSE) images and X-ray maps of merrillite-bearing and apatite-bearing assemblages in Martian meteorites. 25

Figure 19. Backscattered electron (BSE) image and X-ray maps of intergrown apatite-merrillite texture of NWA 7034 (regolith breccia). 26

Figure 20. Backscattered electron (BSE) image and X-ray maps of the apatite and merrillite phases of Northwest Africa 7755 (enriched lherzolitic shergottite). 26

Figure 21. Backscattered electron (BSE) image and X-ray maps of the intergrown apatite-merrillite assemblages of Northwest Africa 7755 (enriched lherzolitic shergottite). ... 27

Figure 22. Representative section of keplerite crystal structure, looking down the c-axis. ... 29

Figure 23. Raman spectra of keplerite, merrillite, and ferromerrillite over the 0 to 1200 cm^{-1} range. ... 30

Figure 24. Raman spectra of keplerite, merrillite, and ferromerrillite over the 900 to 1000 cm^{-1} range. ... 31

Figure 25. Pressure-temperature (P-T) diagram of metamorphic conditions. ... 34

Figure 26. Photograph of a typical fragment of Tissint (Natural History Museum, London: BM.2012,M1). ... 38

Figure 27. Backscattered electron (BSE) image of Tissint thin section investigated in this study. ... 39

Figure 28. Representative photograph of ALH 84001(NASA # S94-32547). ... 41

Figure 29. Photograph and schematic drawing of ALH 84001 after it was sawn in 1994 ... 42

Figure 30. Backscattered electron (BSE) image of ALH 84001,146 thin section investigated in this study. ... 43

Figure 31. Backscattered electron (BSE) images of keplerite grains #1-2 in Tissint. ... 51

Figure 32. Backscattered electron (BSE) images of keplerite grains #3-16 in Tissint. ... 52

Figure 33. Periodic table of elements with Ca-Site (green), Mg-site (blue), and P-site (red) assignments filled in for keplerite. ... 54

Figure 34. Quantitative WDS (Wavelength Dispersive Spectrometry) element map distribution and BSE (BackScattered Electron) image of phosphate keplerite grain #1 in Tissint. ... 55

Figure 35. Quantitative WDS (Wavelength Dispersive Spectrometry) element map distribution and BSE (BackScattered Electron) image of phosphate keplerite grain #2 in Tissint. ... 56

Figure 36. Representative analysis of measured Raman spectra for keplerite (grain #2) in Tissint over the 700 to 1700 cm^{-1} range. Spectrum 214. ... 58

Figure 37. Representative analysis of measured Raman spectra for keplerite (grain #2) in Tissint over the 870 to 1080 cm^{-1} range. Spectrum 214. ... 58

Figure 38. Averaged analysis of measured Raman spectra for keplerite grains #1 and #2 in Tissint over the 600 to 1200 cm-1 range. 59

Figure 39. Averaged analysis of measured Raman spectra for keplerite grains #1 and #2 in Tissint over the 900 to 1000 cm-1 range. 59

Figure 40. Backscattered electron (BSE) image and inverse pole figure (IPF) z-scheme (i.e., IPF map relative to the z direction of the image) of keplerite grain #1 in Tissint. 61

Figure 41. Backscattered electron (BSE) image and inverse pole figure (IPF) z-scheme (i.e., IPF map relative to the z direction of the image) of keplerite grain #2 in Tissint. 62

Figure 42. Backscattered electron (BSE) image and electron backscatter patterns (EBSPs) of keplerite grain #2 in Tissint. 63

Figure 43. Backscattered electron (BSE) images of apatite grains #1-2 and merrillite grains #1-9 in ALH 84001. 71

Figure 44. Periodic table of elements with Ca-Site (green) and P-site (red) assignments filled in for apatite. 73

Figure 45. Periodic table of elements with Ca-Site (green), Na-site (yellow), Mg-site (blue), and P-site (red) assignments filled in for merrillite. 75

Figure 46. Quantitative WDS (Wavelength Dispersive Spectrometry) element map distribution and BSE (BackScattered Electron) image of apatite-merrillite intergrown grains #1-3 in ALH 84001. 77

Figure 47. Quantitative WDS (Wavelength Dispersive Spectrometry) element map distribution and BSE (BackScattered Electron) image of apatite-merrillite intergrown grains #4-6 in ALH 84001. 78

Figure 48. Quantitative WDS (Wavelength Dispersive Spectrometry) element map distribution and BSE (BackScattered Electron) image of isolated merrillite grain #8 in ALH 84001. 79

Figure 49. Detailed view of BSE (BackScattered Electron) image of apatite-merrillite intergrown grains #1-3 in ALH 84001. 80

Figure 50. Quantitative WDS (Wavelength Dispersive Spectrometry) elemental map distribution of sodium (Na) in apatite-merrillite intergrown grains #1-3 in ALH 84001. 81

Figure 51. Quantitative WDS (Wavelength Dispersive Spectrometry) elemental map distribution of chlorine (Cl) in apatite-merrillite intergrown grains #1-3 in ALH 84001. 82

Figure 52. Quantitative WDS (Wavelength Dispersive Spectrometry) elemental map distribution of fluorine (F) in apatite-merrillite intergrown grains #1-3 in ALH 84001. 83

Figure 53. Detailed view of BSE (BackScattered Electron) image of apatite-merrillite intergrown grains #4-6 in ALH 84001 84

Figure 54. Quantitative WDS (Wavelength Dispersive Spectrometry) elemental map distribution of sodium (Na) in apatite-merrillite intergrown grains #4-6 in ALH 84001. 85

Figure 55. Quantitative WDS (Wavelength Dispersive Spectrometry) elemental map distribution of chlorine (Cl) in apatite-merrillite intergrown grains #4-6 in ALH 84001. 86

Figure 56. Quantitative WDS (Wavelength Dispersive Spectrometry) elemental map distribution of fluorine (F) in apatite-merrillite intergrown grains #4-6 in ALH 84001. 87

Figure 57. Detailed view of BSE (BackScattered Electron) image of merrillite grain #8 in ALH 84001. 88

Figure 58. Quantitative WDS (Wavelength Dispersive Spectrometry) elemental map distribution of sodium (Na) in merrillite grain #8 in ALH 84001. 89

Figure 59. Quantitative WDS (Wavelength Dispersive Spectrometry) elemental map distribution of chlorine (Cl) in merrillite grain #8 in ALH 84001 90

Figure 60. Quantitative WDS (Wavelength Dispersive Spectrometry) elemental map distribution of fluorine (F) in merrillite grain #8 in ALH 84001 91

CHAPTER 1:
INTRODUCTION

At current, the only source for Martian material exists in the form of Martian meteorites. Fundamental insight regarding the source, evolution, and concentration of Martian volatile species (Darling et al., 2021; Filiberto et al., 2016), the petrogenesis of Martian magma systems (Howarth et al., 2015), and the dynamics of ejection events on Mars (Min et al., 2017) can be gained by studying minerals, such as phosphate phases, contained within these meteoritic rocks. However, due to a long geologic history of collisions with other solar system bodies (Treiman, 1995, 1998, 2021; Udry et al., 2020), all Martian meteorites have experienced shock metamorphism and therefore have undergone some degree of physical and/or chemical change. Despite this fact, the effect of shock on the chemistry of phosphate minerals is not well constrained (Darling et al., 2021).

1.1 Meteorite Classification

Meteorites are rocky and, sometimes, metallic objects which, after being ejected from their parent bodies, travel through space and eventually collide with the surfaces of Earth, the Moon, and other solar system bodies. If a meteorite is successfully recovered after an individual witnesses it traveling through the earth's atmosphere, then the recovered meteorite is considered to be a *fall*; if a meteorite is recovered but cannot be linked to an observed fall, then it is considered to be a *find*.

Meteorite nomenclature is based on the geographic location where a meteorite was recovered and can include a numbering system as well (with 3-6 digits, depending on the information that is recorded), if the location in question has a high meteorite recovery rate (e.g., MIL 03346 was the 346th sample to be classified from Antarctica's Miller Range during the 2003 – 2004 field season). The Meteoritical Bulletin Database maintains a comprehensive list of all formally recognized and officially classified meteorites; as of 22

October 2022, a total of 70,386 valid meteorite names were recognized. Once a meteorite is recovered and named, it can then be broadly classified as either an undifferentiated chondritic meteorite or differentiated achondritic meteorite, as based on the texture and bulk composition of the sample in question.

1.2 Classification of Undifferentiated Meteorites: Chondrites

Undifferentiated chondritic meteorites are derived from unaltered, primitive, solar system materials, whose components were formed in the solar nebula by high-temperature processes, such as condensation and evaporation (Krot et al., 2014). There are four major components contained within chondritic meteorites which include: chondrules, refractory inclusions (Ca-Al-rich inclusions, CAIs) and amoeboid olivine aggregates (AOAs), FeNi-metal, and fine-grained matrix material (Krot et al., 2014). The classification of chondritic meteorites is based on bulk chemistry, bulk oxygen isotopic compositions, mineralogy, petrology, and the overall proportion of components (Krot et al., 2014). Figure 1 summarizes the major classes, groups, petrological types, and subgroups of chondrites.

	Undifferentiated Meteorites: Chondrites														
Class →	Carbonaceous								Ordinary			Enstatite		Additional	
Group →	**CI**	**CM**	**CO**	**CR**	**CB**	**CH**	**CV**	**CK**	**H**	**L**	**LL**	**EH**	**EL**	**R**	**K**
Petr. Type →	1	1-2	3-4	1-2	3	3	3-4	3-6		3-6		3-5	3-6	3-6	3
Subgroup →					Cb_a		CV_{OxA}								
					CB_b		CV_{OxB}								
							CV_R								

Figure 1. Classification of Chondrites. Modified after Krot et al. (2014). Petr. Type = Petrological Type. Chondrites can be classified as being: carbonaceous, ordinary, enstatite, or an additional type (R and K).

1.3 Classification of Differentiated Meteorites: Achondrites

Differentiated non-chondritic meteorites lack the major components found in chondrites (therefore, non-chondritic meteorites are referred to as achondrites), are derived from differentiated planetary bodies (i.e., the Moon, Mars, asteroids), and were affected by partial or complete melting, either as melt products or as residues after melt removal (Krot et al., 2014). Nonchondritic meteorites are commonly classified on the basis of their FeNi-metal abundances as either achondrites (metal poor), stony irons, or iron meteorites (Krot et al., 2014). These types of nonchondritic meteorites and their associated groups are summarized in Figure 2. Achondrites can then be further divided into two separate categories, primitive and differentiated, as based on the degree of igneous processing that took place (Krot et al., 2014).

Differentiated Meteorites: Achondrites & Other Igneous Meteorites			
Primitive achondrites	**Differentiated achondrites**	**Irons and stony irons**	**Planetary**
Winonaites	Angrites	Mesosiderites	Martian
Acapodranites	Aubrites	Pallasites	Shergottites
Acapulcoites	Ureilites	Main group	Nakhlites
Lodranites	HED	Eagle Station	Chassignites
Brachinites	Howardites	IAB irons	Orthopyroxenite
	Eucrites	IC irons	Lunar
	Diogenites	IIAB irons	
		IIC irons	
		IID irons	
		IIE irons	
		IIG irons	
		IIIAB irons	
		IIICD irons	
		IIIE irons	
		IIIF irons	
		IVA irons	
		IVB irons	

Figure 2. Classification of Differentiated Meteorites. Modified after Krot et al. (2014). Achondrites can be classified as being: primitive achondrites, differentiated achondrites, irons, stony irons, or planetary.

Primitive achondrites are considered to be either (1) the products of ultrametamorphosed chondrites or (2) the residual products created as a result of extremely low degrees of partial melting (Krot et al., 2014). Generally speaking, primitive achondrites exhibit igneous and/or metamorphic textures, with compositions that are moderately fractionated from the range of chondritic materials (i.e., their bulk compositions are 'near-chondritic') (Krot et al., 2014; Mittlefehldt, 2014; Morlok et al., 2012).

Differentiated achondrites are the products of high degrees of partial, or complete, melting and recrystallization; they exhibit igneous textures with compositions that are highly fractionated from the range of chondritic materials (i.e., their bulk compositions are much different than chondrites) (Mittlefehldt, 2014). Within the achondritic group of meteorites, exists a subgroup which is linked to larger planetary bodies; these *Planetary Meteorites*, as they are called, include materials derived from the Moon (Lunar Meteorites) and Mars (Martian Meteorites).

1.4 Martian Meteorite Classification

All of the Martian meteorites (excluding one polymict breccia), which have been studied thus far show evidence of magmatic origins (Udry et al., 2020). As with terrestrial igneous rocks, these igneous Martian rocks have a range in textures (aphanitic, porphyritic, diabasic, oikocrystic) and compositions (mafic to ultramafic) (Udry et al., 2020). Martian meteorites are divided into four groups based on their: elemental geochemistry and radiogenic isotopic compositions; emplacement histories; and crystallization and ejection ages. These groups are the: Shergottites, Nakhlites, and Chassignites (SNCs); Orthopyroxenites; and Regolith breccias (Udry et al., 2020).

The most abundant Martian meteorite group by mass (82%) and total collection by number (89%) are the shergottite type meteorites (Udry et al., 2020) (Figure 3, Figure 4). The geochemical classification of shergottites is based on incompatible trace element (ITE) enrichments or depletions, as ITE compositions reflect unique source (i.e., parent melt) compositions (Udry et al., 2020). Large variations in ITE compositions (and radiogenic isotopic compositions: Lu-Hf, Sm-Nd, and Rb-Sr) are exhibited in shergottites and are believed to have formed during silicate planetary differentiation and crystallization following an early magma ocean phase (Suarez et al., 2022; Udry et al., 2020). Therefore, shergottites derived from compositionally-variable, partially-melted, mantle sources, will inherit unique isotopic compositions which are reflections of original mantle source compositions (Suarez et al., 2022; Udry et al., 2020) (Figure 4).

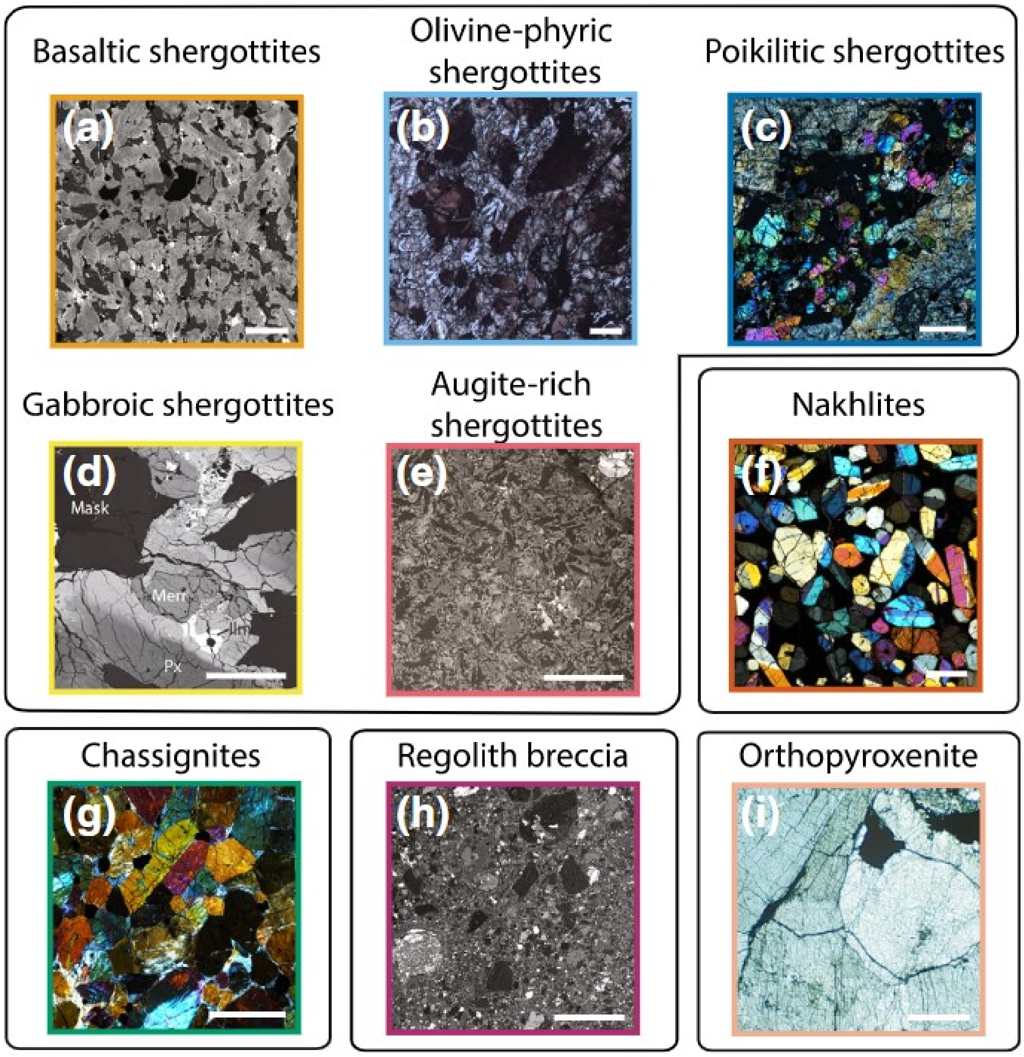

Figure 3. Representation of all Martian Meteorite types. Taken after Udry et al. (2020). Greyscale photos are backscattered electron (BSE) images, while colored photos are photomicrographs, under crossed polarized light (XPL). (a) Basaltic shergottite NWA 8657; sample contains pyroxene and maskelynite and is absent of olivine phenocrysts and megacrysts. (b) Olivine-phyric shergottite LAR 06319; sample contains olivine phenocrysts along with olivine, pyroxene, and maskelynite which crystalized later on. (c) Poikilitic shergottite NWA 4468; sample contains olivine chadacrysts that are enclosed by larger pyroxene oikocrysts along with olivine, pyroxene, and maskelynite which crystalized later on. (d) Gabbroic shergottite NWA 6369; sample contains cumulate pyroxene or plagioclase. (e) Augite-rich shergottite NWA 8159; sample contains intergranular plagioclase, augite, olivine; sample lacks pigeonite. (f) Nakhlite MIL 090030; sample is clinopyroxene-rich and contains cumulus pyroxene and olivine. (g) Chassignite NWA 2737; sample contains olivine cumulates with inclusions of chromite; and interstitial plagioclase, orthopyroxene, and phosphates. (h) Orthopyroxenite ALH 84001; sample contains mosaic-grained orthopyroxene; minor amounts of chromite, augite, glass, olivine, apatite; and secondary phases (e.g., Fe-Mn-Mg carbonate). (i) Regolith breccia NWA 7034; sample contains igneous clasts (basalt, mugearite, trachyandesite, norite, gabbro, monzonite). Scale bars = 500 μm length.

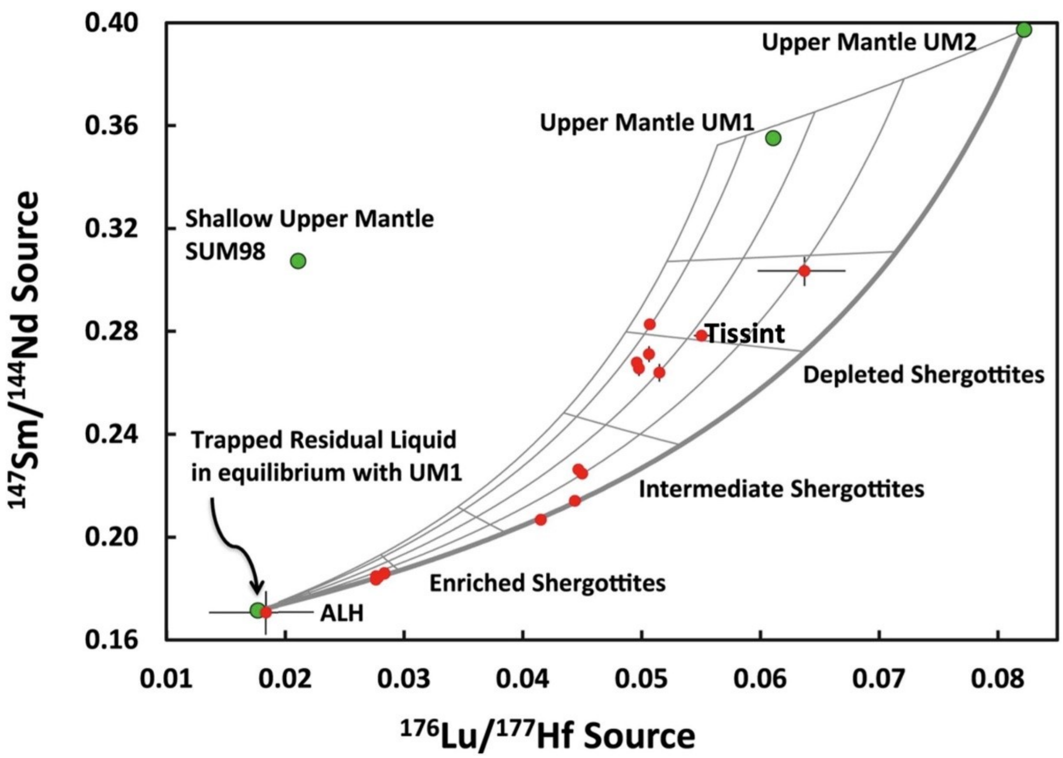

Figure 4. Plot of isotopic source rations ($^{176}Lu/^{177}Hf$ and $^{147}Sm/^{144}Nd$) of enriched, intermediate, and depleted shergottites, and ALH 84001 against an assumed end-member mixing array (shown by underlying grid) that was generated using end-member compositions (indicated by green circles). Taken after Suarez et al. (2022).

Along with geochemical variations, variations in texture (i.e., grain size, shape, modal abundance of minerals) exist as well, which aid in shergottite classification (Udry et al., 2020) (Figure 3). Texturally, shergottites can be divided into five groups: (1) basaltic (2) olivine-phyric (3) poikilitic (4) gabbroic and (5) augite-rich shergottites. Through textural and geochemical investigations of Martian meteorites, numerous fundamental planetary processes can be uncovered, including: the timing of magmatic rock formation and emplacement (along with what conditions were present at the time of these events); planetary accretion and differentiation; timing of secondary processes, such as alteration and weathering; and impact events in the Martian past (Udry et al., 2020) (Figure 5).

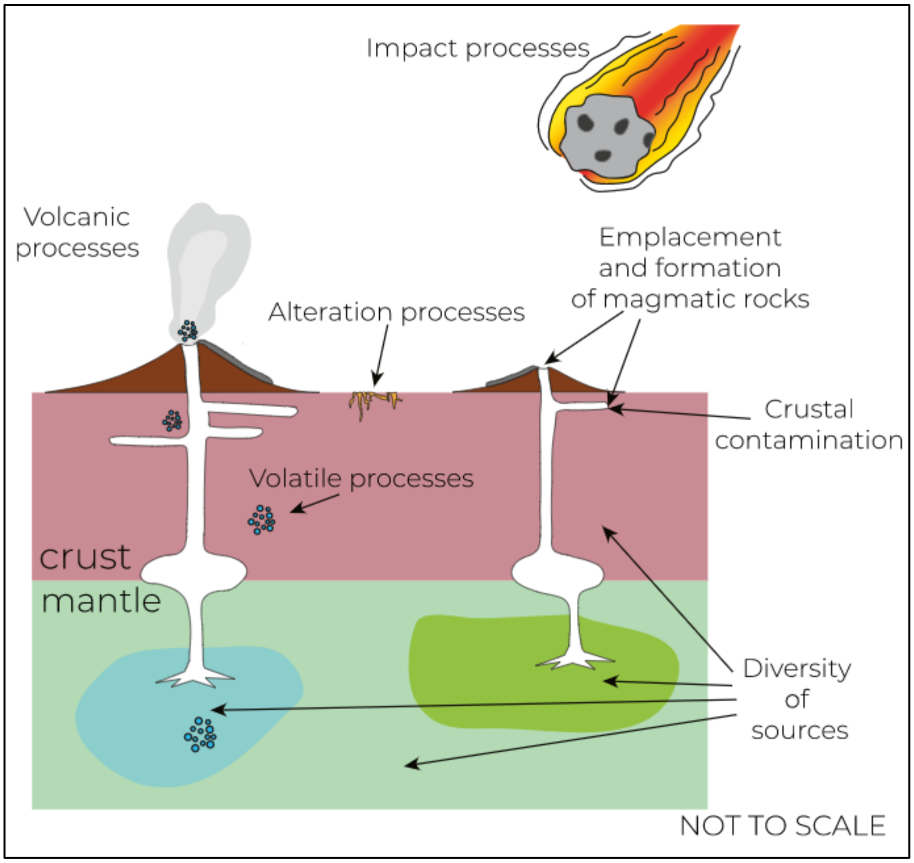

Figure 5. Information to be gained by studying Martian Meteorites. Taken after Udry et al. (2020). Highly volatile compounds (i.e., OH, H_2O, CO_2, Cl, S) are represented by blue bubbles.

The Martian meteorites Nakhlites and Chassignites are geochemically and texturally distinct from shergottites and constitute ~17% of all Martian meteorites by mass and ~10% by total collection number (Udry et al., 2020). Nakhlite and Chassignite meteorites share many similarities (e.g., ~1.3 Ga crystallization age; ~11 Ma ejection age; depleted radiogenic isotope compositions) and are thought to be derived from the same location and volcanic system on Mars (Udry et al., 2020). Nakhlites are igneous rocks that contain: abundant clinopyroxene; cumulus pyroxene and olivine; minor glass, plagioclase, phosphates, iron-rich olivine in mesostasis, titanomagnetite, and sulfides (Udry et al., 2020) (Figure 3f). Lastly, chassignites are dunitic igneous rocks that contain: cumulus olivine; chromite inclusions; interstitial plagioclase; orthopyroxene; and phosphates (Figure 3g).

1.5 Phosphate Phases in Extraterrestrial Systems

Calcium (Ca-) phosphates, notably apatite group minerals $Ca_5[PO_4]_3[F,Cl,OH]$ and merrillite $Ca_9Na(Fe,Mg)(PO_4)_7$, are among the most important minerals investigated in Martian meteorites (Darling et al., 2021; Kenny et al., 2019; Udry et al., 2020). Their significance lies in the fact that phosphate minerals are enriched in volatiles (i.e., apatite group minerals incorporate volatile species such as chlorine, fluorine, and lead) and trace elements (i.e., Ca-phosphates are the primary carriers of REEs in Martian meteorites) (Cox et al., 2020; Darling et al., 2021; Kenny et al., 2019; Walton et al., 2012). Given these elemental enrichments, apatite and merrillite are often targeted for geochemical analyses.

The applicability of phosphate geochemistry is far reaching; phosphates are readily used for (1) evaluating the origin, abundance, and evolution of volatile species contained in Martian systems (2) providing constraints on endogenic and exogenic thermochronological processes (3) geochronological purposes and (4) providing information on the genesis and evolution of magmas through application of trace element and isotopic studies (Cox et al., 2020; Darling et al., 2021; Kenny et al., 2019; Udry et al., 2020). Though phosphate minerals are often targeted for geochemical work, the effect of shock metamorphism on the chemical and isotopic records of these minerals is not well understood (Cox et al., 2020; Darling et al., 2021; Kenny et al., 2019).

1.5.1 Apatite-group Minerals

Apatite is the most abundant, volatile-bearing, phosphate found on Earth and in Martian meteorites (Darling et al., 2021). Apatite occurs in both biological (i.e., as the main inorganic component of bones and teeth) and geological systems (i.e., as an accessory mineral in all geologic environments) and thus is of interest to many scientific fields (Hughes and Rakovan, 2002; Liu et al., 2013; McCubbin and Jones, 2015) (Figure 6). Thus, the variable chemistry and robust structure of apatite allow it to accommodate a wide scope of trace metals, radionuclide species, and volatiles (Hughes and Rakovan, 2002). Therefore, the presence of apatite in the geologic environment strongly influences the evolution and signature of trace elements and volatile contents in any given system which supports apatite formation (Hughes and Rakovan, 2002).

Apatite formation, particularly in the geologic environment, may occur from crystallizing melt, concentrated hydrothermal brines, aqueous solutions at low temperatures, or vapor phases (Rakovan, 2002). The general apatite formula is as follows: $A_5(XO_4)_3Z$, where A is a generally a large divalent cation (e.g., Ca^{2+}), X is a pentavalent cation (P^{5+}), and Z is an anion (F^-, Cl^-, OH^-, O^{2-}) or rarely a vacancy. The atomic arrangement of apatite-group minerals allows for structural variants which accommodate numerous cation substitutions for Ca at the A-site (i.e., Na^+, Sr^{2+}, Pb^{2+}, Ba^{2+}, REE^{3+}, Y^{3+}, Th^{4+}, U^{4+}, U^{6+}, ☐, etc.), alongside replacement of the PO_4^{3-} group for various anionic complexes at the X-site (i.e., AsO_4^{3-}, VO_4^{3-}, SO_4^{2-}, SiO_4^{4-}, CO_3^{2-}, etc.) (Pan and Fleet, 2002); note Figure 7. Crystal lattice vacancies are represented by an open square (i.e., ☐). Ternary plots may be constructed to aid in illustrating the relative abundances of halogens, which are strongly influenced by original source compositions; note Figure 8 and Figure 9 (Filiberto and Treiman, 2009; McCubbin and Jones, 2015).

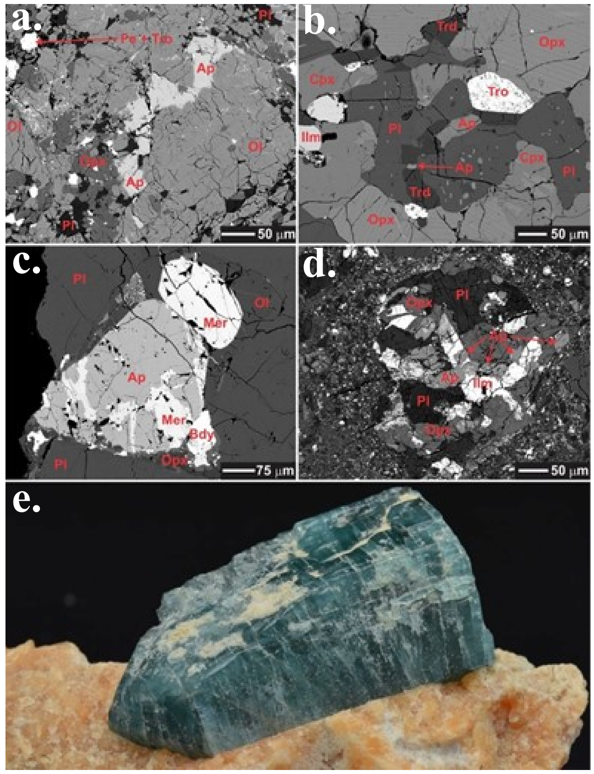

Figure 6. Apatite backscattered electron (BSE) images and photographs as sourced from various environments (i.e., asteroidal and planetary bodies). Taken after McCubbin and Jones (2015). (a) BSE image of apatite in the LL Chondrite (low-iron, low metal ordinary chondrite) Chelyabinsk. Note that apatite exhibits a vein-like texture; this texture is indicative of fluid-deposited apatites. (b) BSE image of apatite in the Eucrite (achondritic stony meteorite) Bates Nunataks 00300. Note apatite occurrence with late-stage crystallization products (tridymite, troilite). (c) BSE image of apatite in the Lunar sample 76535 (lunar highlands magnesian-suite troctolite). Note the intergrown texture of apatite and merrillite. (d) BSE image of apatite in the Martian breccia NWA 7034. Apatite-bearing basaltic clasts are rich in chlorine (not shown) and show evidence of secondary alteration due to fluids. (e) Photograph of terrestrial apatite (blue) occurring with calcite (orange) from Lake Baikal, Russia. Secondary ion mass spectrometry standards are routinely created using apatite derived from Baikal, Russia in order to study extraterrestrial apatite. Ap = apatite; Bdy = baddeleyite; Cpx = clinopyroxene; Fe = Fe-rich metal; Ilm = ilmenite; Mer = merrillite; Opx = orthopyroxene; Pl = plagioclase; Trd = tridymite; Tro = troilite.

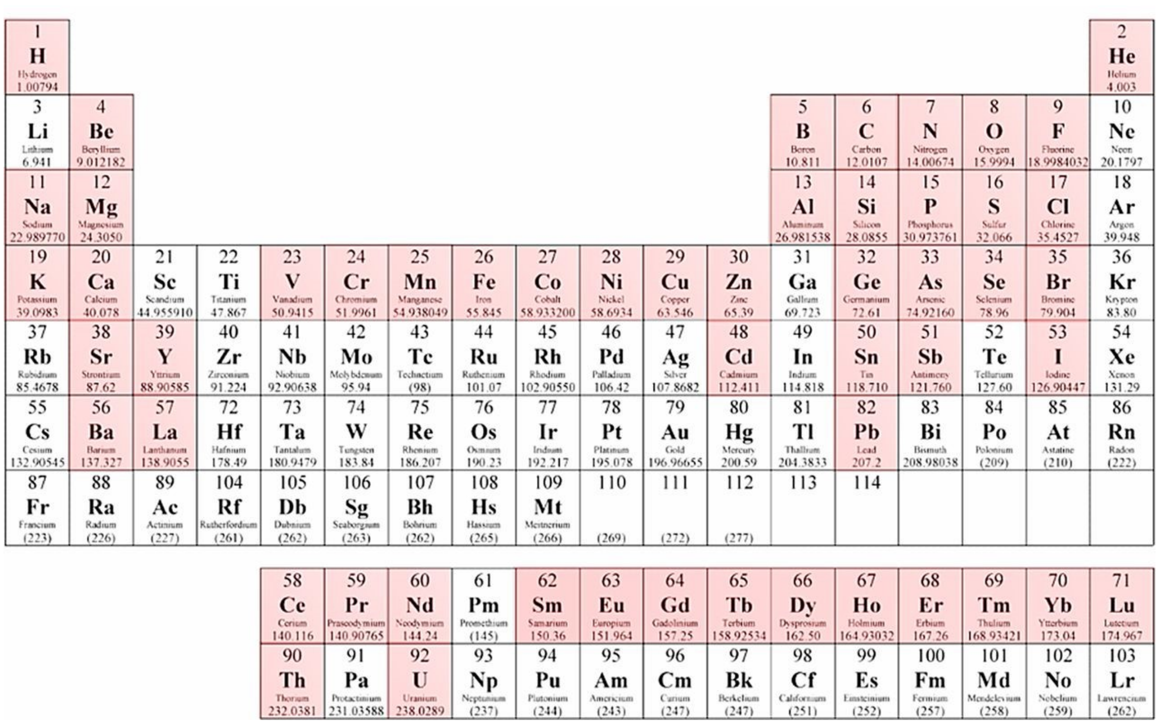

Figure 7. Schematic diagram of the periodic table illustrating elements which occur in apatite super-group minerals (shaded in red). Taken after Hughes and Rakovan (2015). The concentration of these elements in apatite ranges from parts per million (ppm), to tens of weight percent.

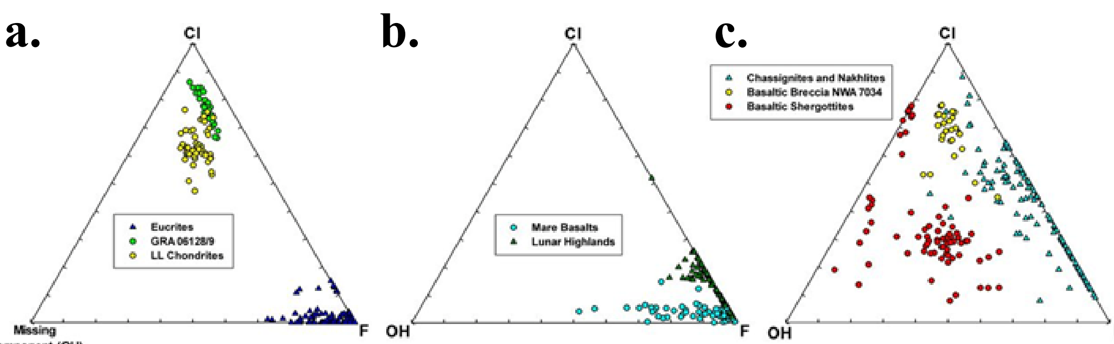

Figure 8. Ternary plots of apatite F-Cl-OH chemistries as they are related to asteroidal parent bodies, lunar samples, and Martian meteorite sources. Taken after McCubbin and Jones (2015). (a) Apatite volatile chemistry as related to differentiated and undifferentiated asteroidal parent bodies. Differentiated parent bodies are represented by eucrites (achondritic stony meteorites) and the anomalous achondrite GRA06128/9 (ancient cumulate lithology which underwent metasomatism). Undifferentiated bodies are represented by LL chondrites (low-iron, low metal ordinary chondrites). (b) Apatite volatile chemistry as related to lunar samples. Mare basalts represent unaltered Lunar basalts, while lunar highlands represent altered crustal materials. (**c**) Apatite volatile chemistry as related to Martian meteorite sources. Basaltic shergottites represent unaltered Martian basalts. Basaltic breccia NWA 7034, chassignites, and nakhlites represent altered crustal materials.

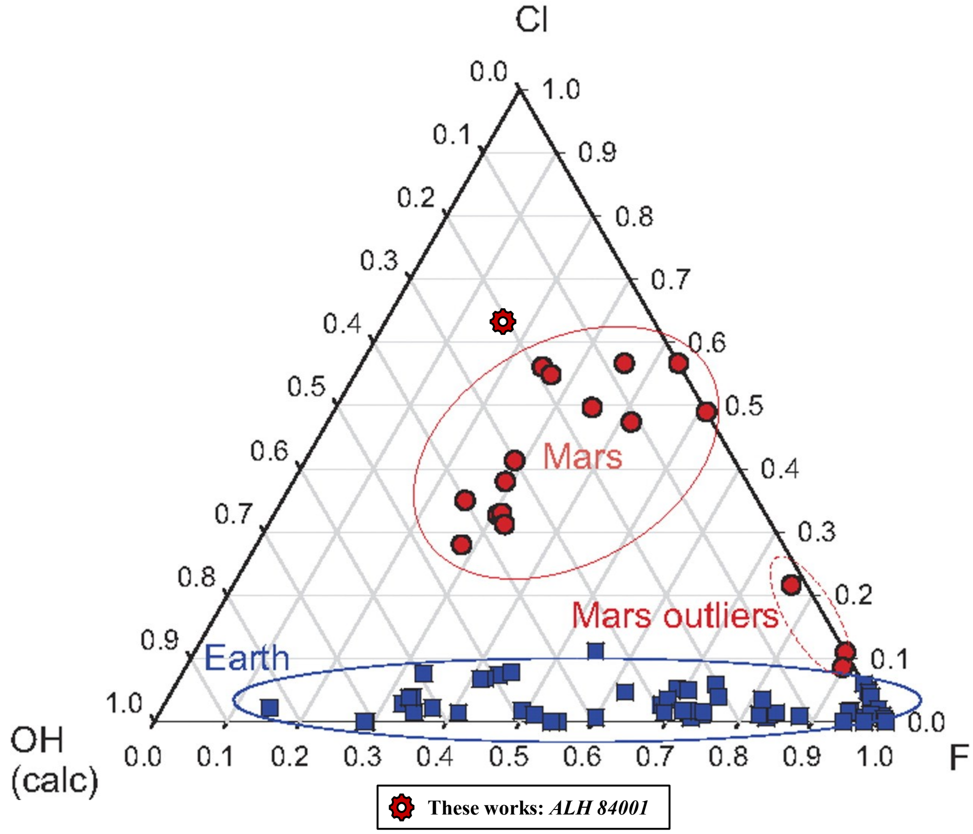

Figure 9. Ternary plot of apatite F-Cl-OH chemistries as they are related to Terrestrial (basaltic rocks of Earth) and Martian sources. Taken after Filiberto and Treiman (2009). Data collected in this study for ALH 84001 apatite are superimposed on the plot. ALH 84001 apatite data plotted are the average of 13 analyses. Assuming that F (fluorine) + Cl (chlorine) + OH (hydroxyl) = 1.0 structural formula unit (sfu), an indirect calculation can be made which estimates the water content of apatite. Average atoms per formula unit (apfu) F = 0.164; average apfu Cl = 0.630 ∴ average estimated water content in ALH 84001 apatite = 0.206 sfu or ~20% hydroxyl apatite component. Blue squares illustrate terrestrial samples while red circles illustrate Martian samples. Martian rocks analyzed included: shergottites, nakhlites, chassignites, and orthopyroxenites (ALH 84001). Mars outliers are highlighted by a dashed red circle and include apatite compositions which contain significant proportions of F. Terrestrial sample analyses shown are of unaltered rocks which did not undergo metasomatism. Note that Martian samples are enriched in Cl and contain low abundances of water (OH) while terrestrial basalts are Cl-poor and contain variable OH:F ratios. Data presented in this study are in general agreement with Martian apatite data; however, apatite analyzed in ALH 84001 are slightly more enriched in Cl relative to other meteorites.

The ability for apatite to readily incorporate halogens from magmatic systems allow the mineral to be used as a tool to constrain preeruptive volatile contents of parent magmas (Filiberto and Treiman, 2009). Therefore, the abundance of volatiles in magmas derived from different planetary bodies can be compared (Filiberto and Treiman, 2009). McCubbin and Jones (2015) found that, while apatite derived from undifferentiated, chondritic, meteorite bodies were Cl-rich (Figure 8A), those apatites derived from differentiated bodies had highly variable volatile chemistries (Figure 8C). Although some variability was reported in the Martian meteorites of Filiberto and Treiman (2009) as well, their results found apatite to be Cl-rich and OH-poor thus indicating that Martian parental magmas were likely dominated by chlorine and contained little water (Figure 9).

1.5.2 Whitlockite-group Minerals

As with apatite-group minerals, the whitlockite-group of minerals comprises both biologically and geologically significant phosphate phases (Britvin et al., 2021; Capitelli et al., 2021). The Commission on New Minerals, Nomenclature and Classification (CNMNC) of the International Mineralogical Association (IMA) currently recognizes eight phosphate phases as members of the whitlockite-group of minerals. Table 1 summarizes ideal formulas and species-defining constituents of these members. Whitlockite-group minerals follow the general chemical formula of $A_9BM(PO_3X)_4(PO_4)_3$, where: A-site = Ca or Sr; B-site = Na, Ca, or ☐ (vacancy; a point defect in crystal lattice); M-site = Mg, Fe^{2+}, or Mn^{2+}; X-site = O^{2-} or OH (Britvin et al., 2021). As such, whitlockite-group minerals can be further divided into two groups: *anhydrous* (e.g., merrillite, keplerite) and *hydrous* (e.g., whitlockite) members.

Table 1. Whitlockite-group minerals that have been approved by The Commission on New Minerals, Nomenclature and Classification (CNMNC) of the International Mineralogical Association (IMA). Adapted after Britvin et al. (2021) and Capitelli et al. (2021). Note that members of the Merrillite subgroup contain only anhydrous minerals while the Whitlockite subgroup contains only hydrous minerals. *Hedegaardite has not been characterized in full and so information regarding its crystal structure are not yet available.

Mineral Phase	**Ideal Formula**	**Species-defining Constituents**			
		A	B	M	X
	Merrillite subgroup (Anhydrous members)				
Merrillite	$Ca_9NaMg(PO_4)_7$	Ca	Na	Mg	O
Keplerite	$Ca_9(Ca_{0.5}\square_{0.5})Mg(PO_4)_7$	Ca	$Ca_{0.5}\square_{0.5}$	Mg	O
Ferromerrillite	$Ca_9NaFe^{2+}(PO_4)_7$	Ca	Na	Fe^{2+}	O
Matyhite	$Ca_9(Ca_{0.5}\square_{0.5})Fe^{2+}(PO_4)_7$	Ca	$Ca_{0.5}\square_{0.5}$	Fe^{2+}	O
	Whitlockite subgroup (Hydrogen-bearing members)				
Whitlockite	$Ca_9Mg(PO_3OH)(PO_4)_6$	Ca	$\square$	Mg	OH
Strontiowhitlockite	$Sr_9Mg(PO_3OH)(PO_4)_6$	Sr	$\square$	Mg	OH
Wopmayite	$Ca_6Na_3\square Mn^{2+}(PO_4)_3(PO_3OH)_4$	Ca	$\square$	Mn^{2+}	OH
*Hedegaardite	$(Ca,Na)_9(Ca,Na)Mg(PO_3OH)(PO_4)_6$				

Structural distinctions between hydrous and anhydrous members of the whitlockite-group of minerals can be made based on the location of [P(1)O4] tetrahedra relative to the truncated apex of the B-site of the crystal (Figure 10) (Britvin et al., 2021). Careful distinction between *hydrous* and *anhydrous* members of the whitlockite-group of minerals is warranted, as nomenclature confusion exists in the literature; this is due partially to early works who equated merrillite to whitlockite (Jolliff et al., 1996). This early confusion may be excused though, as analyses conducted by electron microprobe methods are not able to detect hydrogen. Although merrillite and keplerite are anhydrous mineral phases, their occurrence in a rock does not signify a low-volatile content for its associated parental magma (Shearer et al., 2015). Rather, low-volatile content (i.e., −OH) in these phases may then indicate that their associated rock has not been subjected to hydrothermal fluids or aqueous alteration (Shearer et al., 2015).

Merrillite and keplerite are related by the coupled charge-balanced substitution $Na^{+} \Leftrightarrow \frac{1}{2} Ca^{2+} + \frac{1}{2} \square$ at the B-site of the crystal structure (Britvin et al., 2021) (Table 1). There is a complete solid-solution series between the two compositions (Britvin et al., 2021). Keplerite (*as an end-member*) is defined as the sodium-free, Ca-analogue to merrillite (Britvin et al., 2021). Similarly, end-member merrillite is defined as the Na-analogue to keplerite. A characteristic structural feature of keplerite is a half-vacant occupancy of the sixfold-coordinated B-site (Figure 10), which has been referred to as Ca(IIA) in previous works (Britvin et al., 2021; Dowty, 1977). Though similarities exist between these two minerals, they are chemically distinct; further descriptions of merrillite and keplerite are noted in the sections which follow.

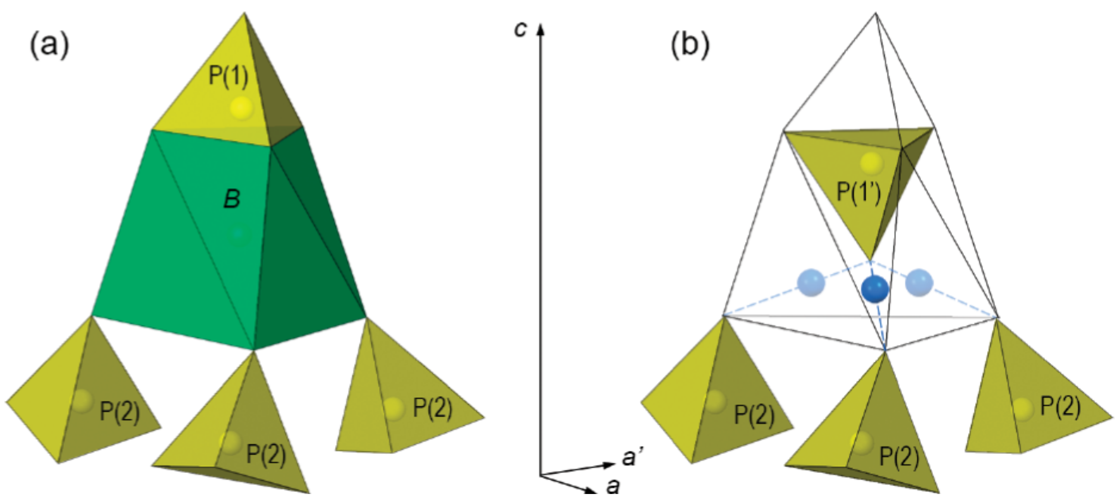

Figure 10. B-site environments of keplerite and whitlockite. Taken after Britvin et al. (2021). (a) B-site of keplerite: $Ca_9(Ca_{0.5}\square_{0.5})Mg(PO_4)_7$. Note that the B-site is half-occupied with Ca^{2+}. Also note that the apex-truncated trigonal pyramid [BO6] is related to the hydrogen-free [P(1)O4] tetrahedra by a common face. (b) B-site of whitlockite-type mineral: $Ca_9FeD(PO_4)_7$. Note that the B-site contains a P-O paired inverted [P(1′)O4] tetrahedron (i.e., the B-site in hydrogen-bearing whitlockite is not vacant) and is free of cations. Also note the presence of a triply split proton (deuteron, shown as blue spheres) which connects the apexes of all four [PO4] tetrahedra through hydrogen bonding (shown as blue dashes).

1.5.2.1 Merrillite in the Literature

Shearer et al. (2015) provide a robust and comprehensive review of the chemical and structural characteristics of end-member merrillite. As discussed, phosphate minerals such as merrillite, keplerite, and apatite are ubiquitous accessory phases in extraterrestrial magmatic systems. These phases are typically amongst the last minerals to crystalize from a magma and thus, commonly occur with other late-stage phases such as silica, sulfides, and oxides (McCubbin et al., 2014; Shearer et al., 2015). Large variations in the chemical composition of Martian merrillite has been well documented in the literature; these variations exist not only within individual samples (e.g., note chemical zonation of sodium in merrillite; Figure 11), but between them as well (e.g., note Martian merrillite compositions vary widely between groups; Figure 12 through Figure 15) (Liu et al., 2018; Shearer et al., 2015; Shearer et al., 2011). This large range in compositions likely reflects intermediate merrillite-keplerite chemistries.

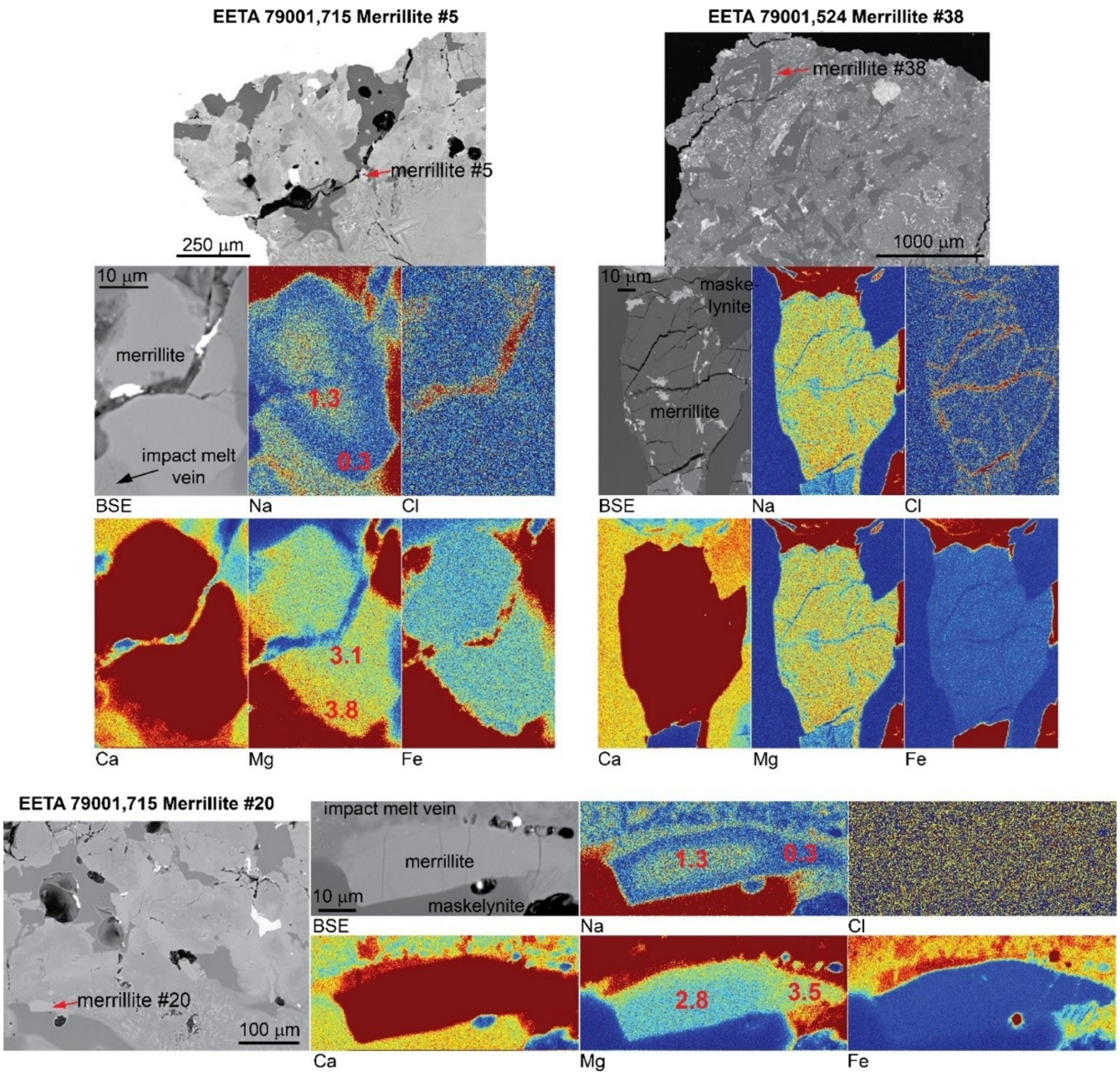

Figure 11. Backscattered electron (BSE) images and X-ray element maps of phosphate grains from the Elephant Moraine (EETA) 79001 shergottite. Taken after Liu et al. (2018). Note that phosphate grains #20 and #5 are in direct contact with impact melt while grain #38 is not. Also note circumferential chemical zonation of Na and moderate zonation of Mg in phosphate grains that directly contact impact melt. Numbers given in red on X-ray maps are Na_2O and MgO contents, given as weight percent (wt%).

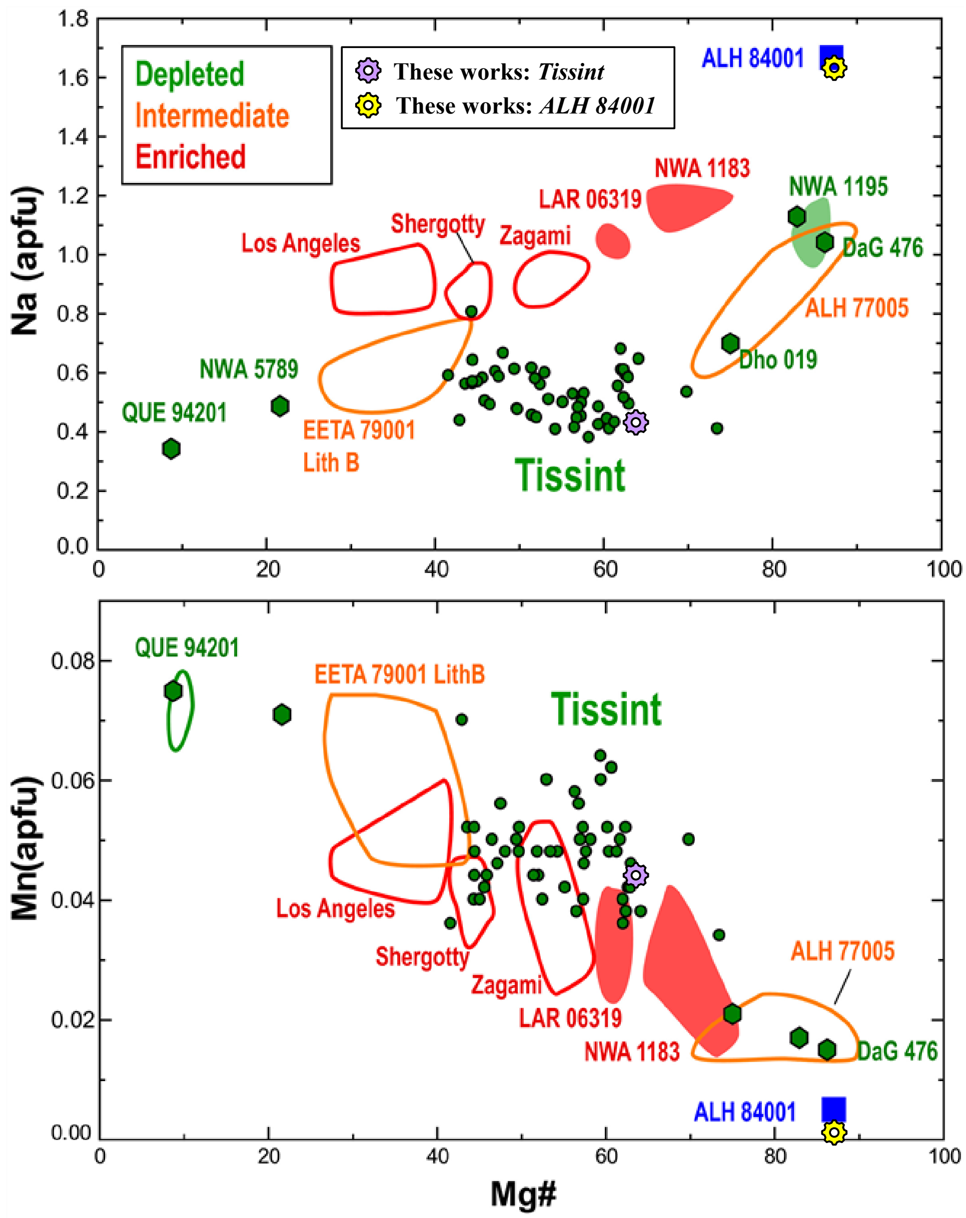

Figure 12.Compositional variations in Martian merrillite. Taken after Liu et al. (2016). Data collected in this study for Tissint keplerite and ALH 84001 merrillite are superimposed on the plot. Na and Mn are given as atoms per formula unit (apfu); formula amounts normalized to 56 oxygen atoms. Mg-numbers are the calculated atomic ratio of magnesium to the sum of magnesium and iron ([Mg_{atomic}/(Mg_{atomic}+Fe_{atmoic})]*100). Tissint keplerite data plotted are the average of 35 analyses. Representative average formula amounts (per 56 O) for keplerite analyzed in this study is 0.43 Na and 0.04 Mn apfu with Mg# 63.2. ALH 84001 merrillite data plotted are the average of 95 analyses. Representative average formula amounts (per 56 O) for merrillite analyzed in this study is 1.63 Na and 0.01 Mn apfu with Mg# 87.6. Meteorites include shergottites (olivine-phyric, basaltic, lherzolitic), and an orthopyroxenite (ALH 84001), and a regolith breccia (NWA 7034). Color classification used to distinguish between depleted, intermediate, and enriched chemical groups.

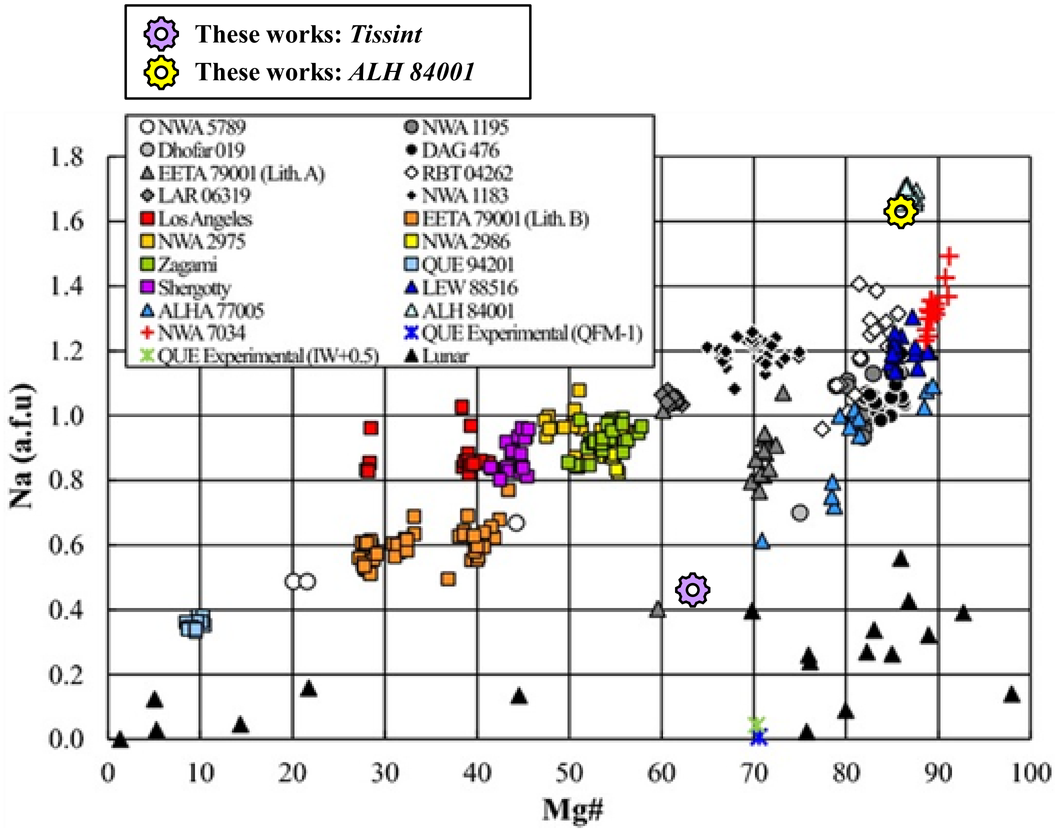

Figure 13. Plot of Na (a.f.u.) versus Mg# in Martian merrillite. Taken after Shearer et al. (2015). Na given as atoms per formula unit (a.f.u); formula amounts normalized to 56 oxygen atoms. Mg-numbers are the calculated atomic ratio of magnesium to the sum of magnesium and iron ($[Mg_{atomic}/(Mg_{atomic}+Fe_{atmoic})]*100$). Tissint keplerite data plotted are the average of 35 analyses. Representative average formula amounts (per 56 O) for keplerite analyzed in this study is 0.43 Na and 0.04 Mn apfu with Mg# 63.2. ALH 84001 merrillite data plotted are the average of 95 analyses. Representative average formula amounts (per 56 O) for merrillite analyzed in this study is 1.63 Na and 0.01 Mn apfu with Mg# 87.6.

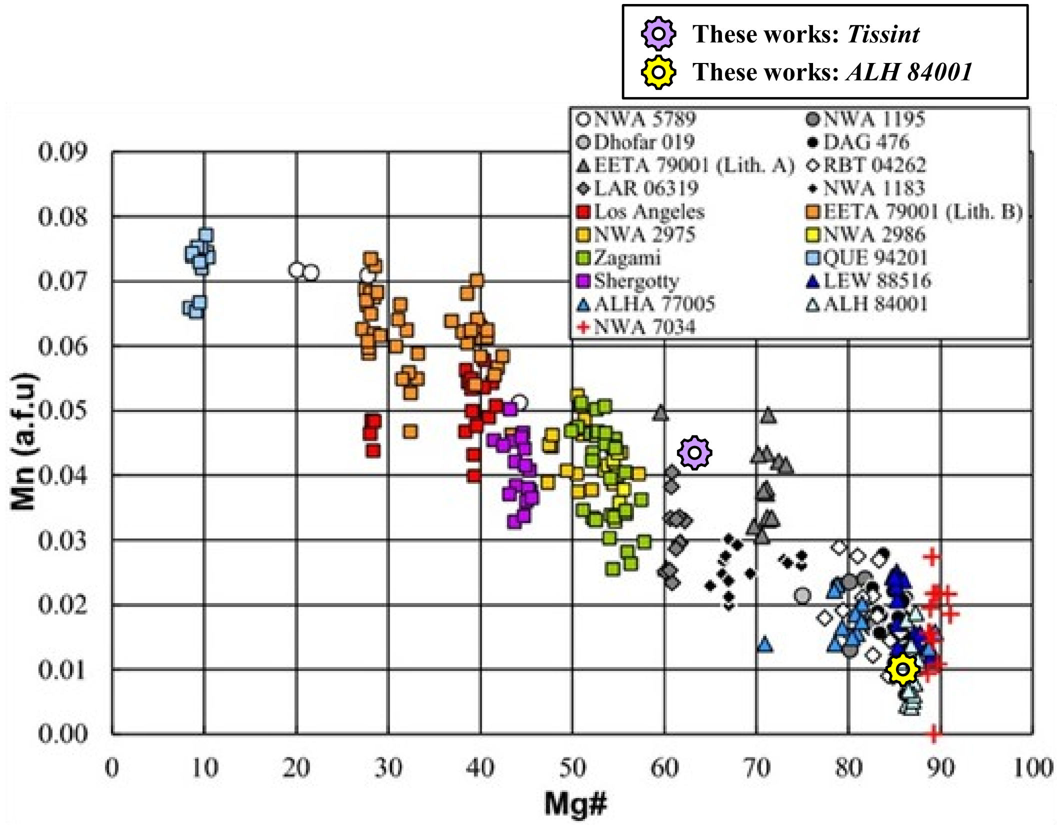

Figure 14. Plot of Mn (a.f.u.) versus Mg# in Martian merrillite. Taken after Shearer et al. (2015). Mn given as atoms per formula unit (a.f.u); formula amounts normalized to 56 oxygen atoms. Mg-numbers are the calculated atomic ratio of magnesium to the sum of magnesium and iron ($[Mg_{atomic}/(Mg_{atomic}+Fe_{atmoic})]*100$). Tissint keplerite data plotted are the average of 35 analyses. Representative average formula amounts (per 56 O) for keplerite analyzed in this study is 0.43 Na and 0.04 Mn apfu with Mg# 63.2. ALH 84001 merrillite data plotted are the average of 95 analyses. Representative average formula amounts (per 56 O) for merrillite analyzed in this study is 1.63 Na and 0.01 Mn apfu with Mg# 87.6. Note that the 1σ precision for Mn at plotted concentrations is ≤ 0.01 wt%. Therefore, significance of Mn variation must be handled with care.

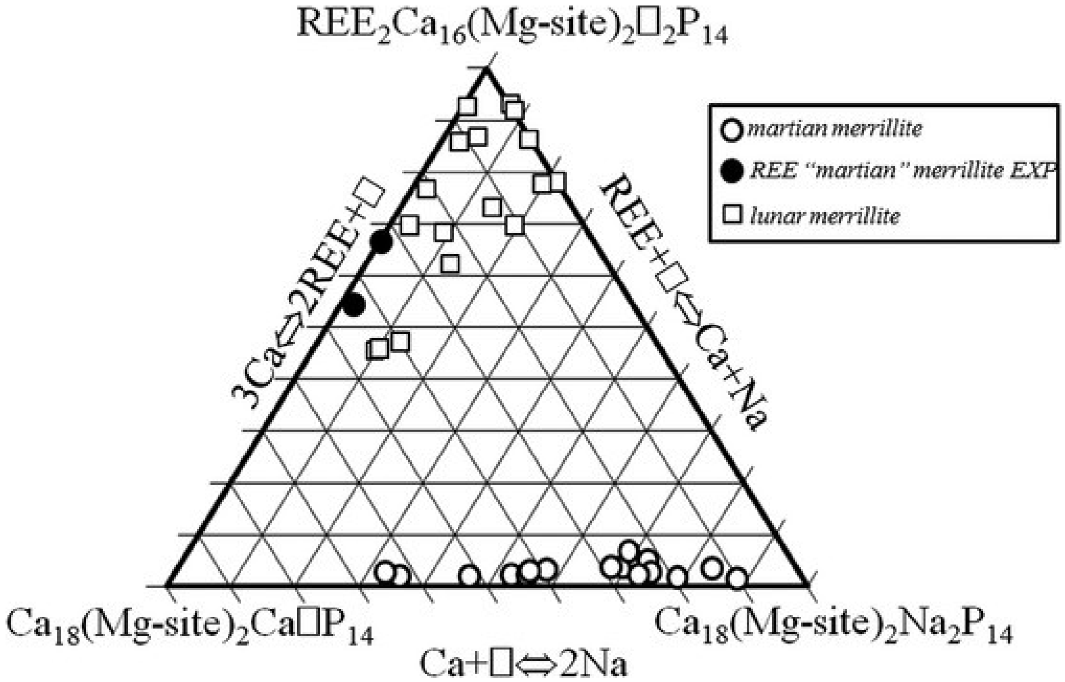

Figure 15. Ternary plot of Martian and Lunar merrillite. Taken after Shearer et al. (2015). Each vertex of the triangle corresponds to one of the three Ca- and Na-site substitutions attributed to merrillite-type minerals. These substitutions include: (1) Ca+□⇔2Na, (2) 3Ca⇔2REE+□, and (3) Ca+Na⇔REE+□. Note that P-site and Ca-site substitutions (e.g., P + Ca⇔Si + REE) are not plotted here. The most significant substitution observed in Martian merrillite phases can be described by variance in vacancies, Ca, and Na within the Na-site of the crystal (i.e., Ca+□⇔2Na). The most significant substitution observed in Lunar merrillite phases is the coupled substitution of (a) REE^{3+} for Ca in the Ca-site with (b) a vacancy in the Na-site (Shearer et al., 2015).

The most common cations found in each of the four structural sites (i.e., P-, Na-, Mg-, and Ca(1,2,3)-sites) of merrillite are shown in Figure 16. Merrillite is trigonal, R3c space group, and has unit cell parameters a = 10.362 Å, c = 37.106 Å (Shearer et al., 2015; Xie et al., 2015) (Figure 17). Texture, as with chemical composition, has been documented to vary considerably in merrillite as well (Howarth et al., 2015; Shearer et al., 2015; Shearer et al., 2011) (Figure 18 through Figure 21). Merrillite grains can range in size from a few microns in diameter to 100s of microns in length (Shearer et al., 2015). Crystal faces can range from anhedral to euhedral and can be deformed, resorbed, and/or rimmed by, or intergrown with, apatite (Bellucci et al., 2017; Greenwood et al., 2008; Howarth et al., 2015; Shearer et al., 2015; Shearer et al., 2011; Walton et al., 2014).

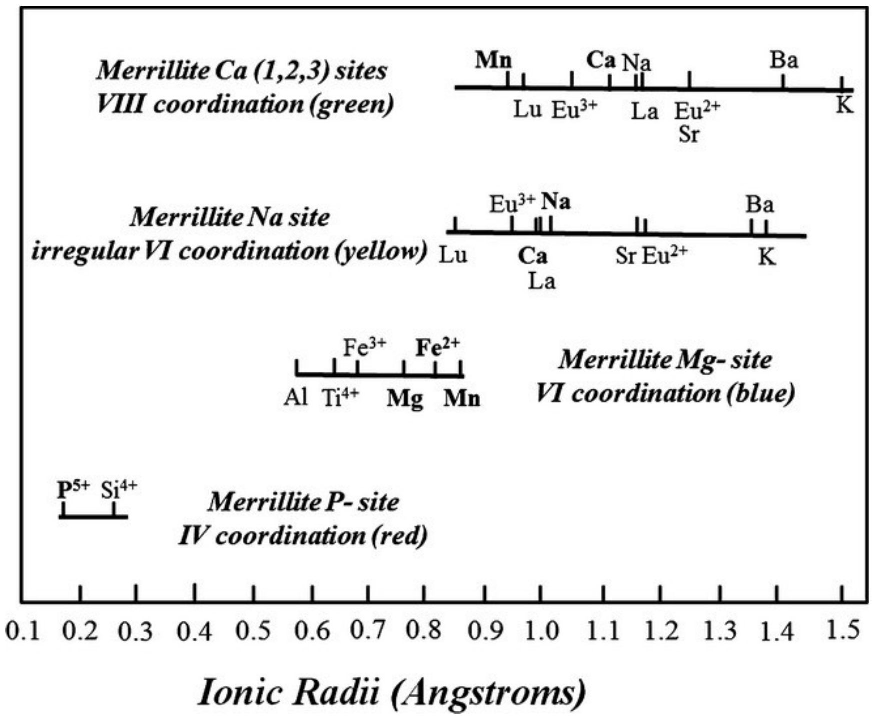

Figure 16. Cations commonly found in merrillite. Taken after Shearer et al. (2015). Figure colors corresponded to Figure 17; P-sites (tetrahedral sites) are shown in red; Mg-sites (octahedral sites) are shown in blue; Na-sites are shown in yellow; and Ca(1,2,3)-sites are shown in green. VIII, VI, and IV correspond to 8-, 6-, and 4-fold coordinated sites.

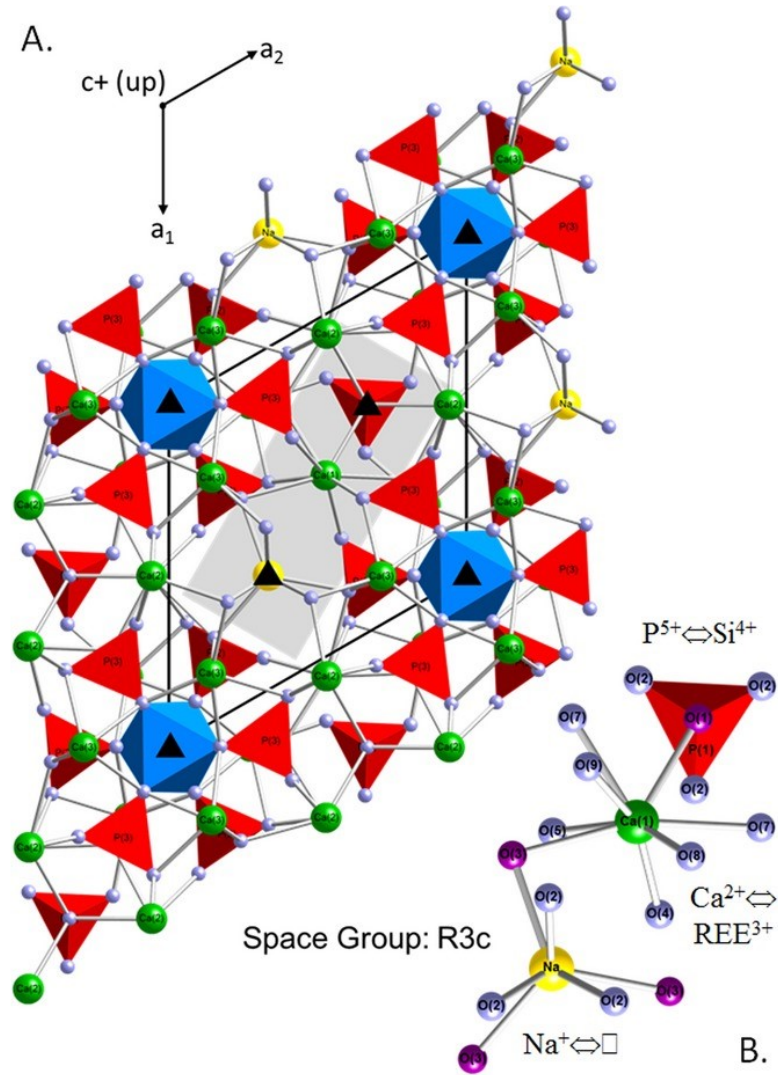

Figure 17. Representative section of merrillite crystal structure, looking down the c-axis. Taken after Shearer et al. (2015). (A) Section of merrillite crystal structure, looking down the c-axis. (B) Magnified knockout of (A). The ball and stick diagram of (B) demonstrates the relationship between Na 6-fold polyhedra, Ca(1) 8-fold polyhedra, and P-tetrahedra. The tetrahedral sites (P-sites) are shown in red while the octahedral sites (Mg-sites) are shown in blue. Na atoms (Na-site) are shown in yellow; Ca atoms (Ca(1,2,3)-sites) are shown in green; and O atoms are shown in purple. A triangular symbol is used to denote the location of the 3-fold axes. Numbers represent symmetrically unique sites.

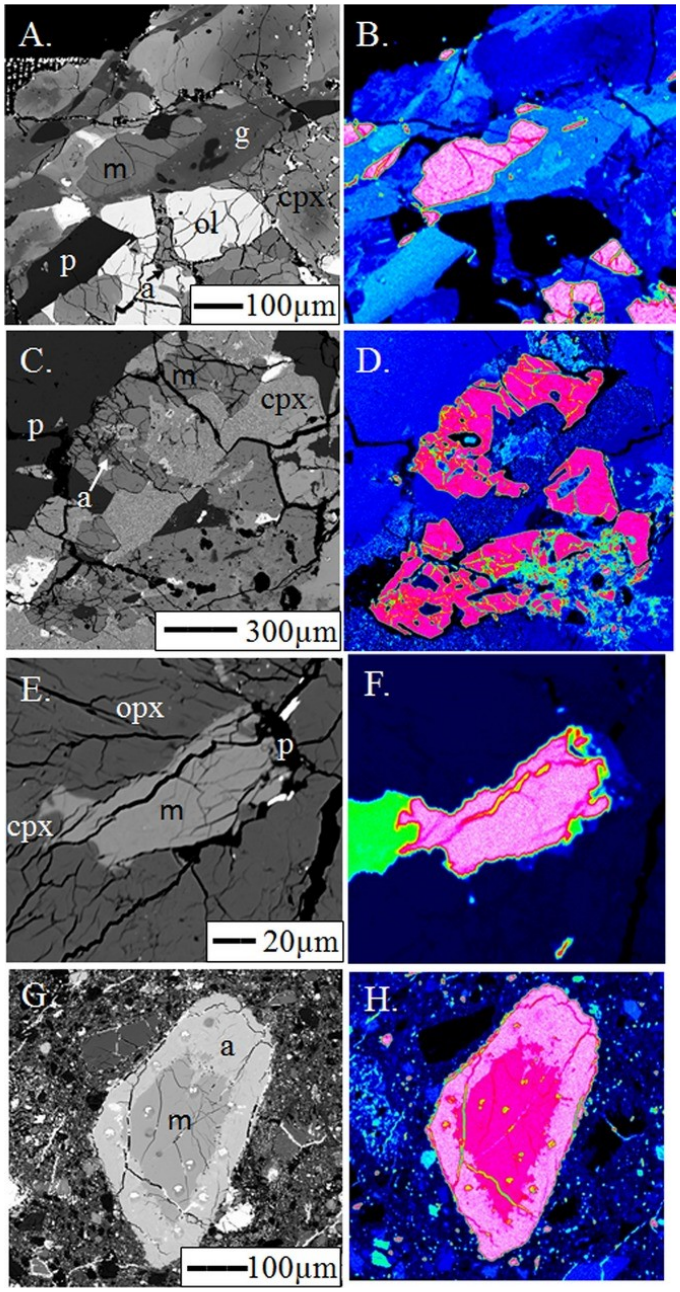

Figure 18. Backscattered electron (BSE) images and X-ray maps of merrillite-bearing and apatite-bearing assemblages in Martian meteorites. Taken after Shearer et al. (2015). (A) BSE image of merrillite in EETA79001 lithology A (olivine-phyric shergottite). (B) Ca X-ray map of the BSE image A. (C) BSE image of merrillite in Los Angeles (basaltic shergottite). (D) Ca X-ray map of the BSE image C. (E) BSE image of merrillite in ALH 84001 (orthopyroxenite). (F) Ca X-ray map of BSE image E. (G) BSE image of merrillite in NWA 7034 (regolith breccia). (H) Ca X-ray map of BSE image G. Mineral abbreviations: m = merrillite; p = plagioclase; cpx = clinopyroxene; opx = orthopyroxene; ol = olivine; a = apatite; g = glass. X-ray maps expressed qualitatively; high Ca counts are indicated by warm colors while low Ca counts are indicated by cool colors.

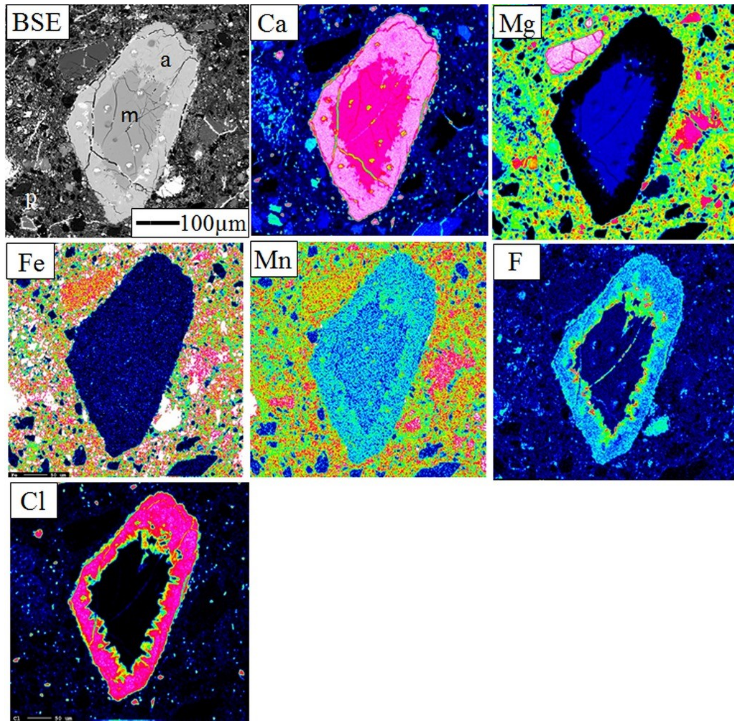

Figure 19. Backscattered electron (BSE) image and X-ray maps of intergrown apatite-merrillite texture of NWA 7034 (regolith breccia). Taken after Shearer et al. (2015). Mineral abbreviations: m = merrillite; p = plagioclase; a = apatite. X-ray maps expressed qualitatively; high Ca counts are indicated by warm colors while low Ca counts are indicated by cool colors.

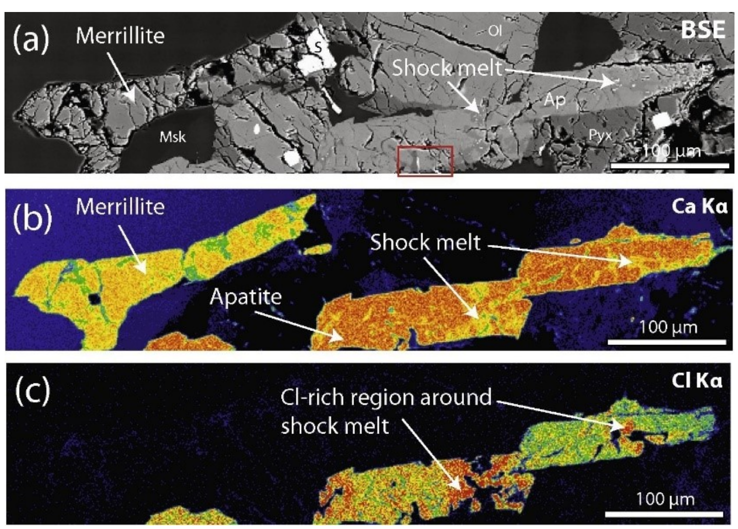

Figure 20. Backscattered electron (BSE) image and X-ray maps of the apatite and merrillite phases of Northwest Africa 7755 (enriched lherzolitic shergottite). Taken after Howarth et al. (2015). Mineral abbreviations: Msk = maskelynite; Ap = apatite; Pyx = pyroxene; Ol = olivine; S = sulfide. X-ray maps expressed qualitatively; high Ca and Cl counts are indicated by warm colors while low Ca and Cl counts are indicated by cool colors. Note the presence of shock melt in apatite and its associated chemical signatures (i.e., Cl-enrichment in presence of shock melt).

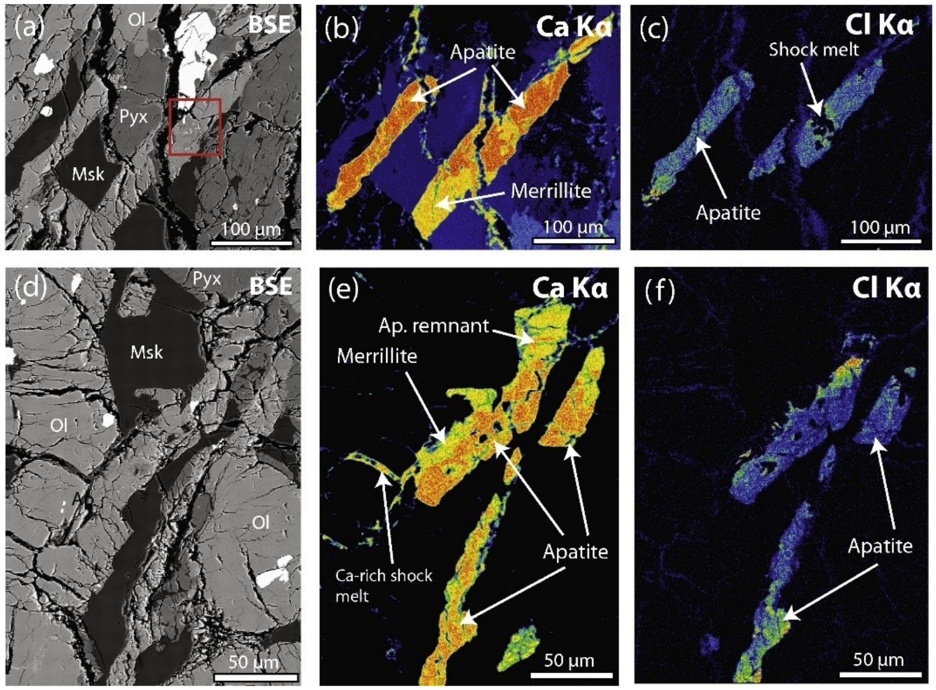

Figure 21. Backscattered electron (BSE) image and X-ray maps of the intergrown apatite-merrillite assemblages of Northwest Africa 7755 (enriched lherzolitic shergottite). Taken after Howarth et al. (2015). Mineral abbreviations: Msk = maskelynite; Ap = apatite; Pyx = pyroxene; Ol = olivine. X-ray maps expressed qualitatively; high Ca and Cl counts are indicated by warm colors while low Ca and Cl counts are indicated by cool colors. Note the presence of shock melt in apatite and its associated chemical signatures (i.e., Cl-enrichment in presence of shock melt). Also note occurrence of merrillite along margin of apatite grains.

1.5.2.2 Keplerite in the Literature

Keplerite, $Ca_9(Ca_{0.5}\square_{0.5})Mg(PO_4)_7$, is a newly defined phosphate mineral (Britvin et al., 2021). Therefore, research discussing keplerite (particularly, end-member keplerite) are currently limited. Britvin et al. (2021) found meteoritic keplerite to occur in the main-group pallasites and angrites (i.e., extremely Na-deficient rocks) (Table 2). Terrestrial keplerite, on the other hand, was found to occur in pyrometamorphic rocks of the Hatrurim Basin, Israel (Britvin et al., 2021). Keplerite is described by Britvin et al. (2021) as an indicator of high-temperature environments that are depleted in sodium and water; presence of sodium in the mineral system promotes intermediate merrillite-keplerite phases to crystallize, while the presence of water promotes whitlockite crystallization.

Structurally, keplerite is trigonal, R3c space group, and has unit cell parameters *a* = 10.3330 Å, *c* = 37.0668 Å (Britvin et al., 2021).

Table 2. Summarized meteoritic keplerite chemical compositions. Taken and adapted after Britvin et al. (2021). References: [1] (Britvin et al., 2021); [2] (Buseck and Holdsworth, 1977); [3] (Keil et al., 1976); [4] (Crozaz and McKay, 1990). Dashed fields indicate below detection limit.

Meteorite:	Marjalahti	Marjalahti	Ahumada	Lew 86010	Imilac	Angra dos Reis	Somervell County
Group:	Pallasite	Pallasite	Pallasite	Angrite	Pallasite	Angrite	Pallasite
Reference:	[1]	[2]	[2]	[4]	[2]	[3]	[2]
wt%							
Na2O	–	–	0.1	0.4	0.52	0.67	0.68
CaO	48.87	48.8	49.1	50.7	50.2	49.4	48.7
MgO	3.9	4.52	3.32	2.68	3.62	2.82	3.76
FeO	1.33	0.88	1.85	1.62	0.36	1.29	0.5
P2O5	46.24	45.2	45.6	44.6	45.9	45.1	46.8
SiO2	–	–	0.32	0.68	–	0.67	0.08
Total	*100.34*	*99.4*	*100.29*	*100.7*	*100.6*	*99.95*	*100.52*
Formula amounts (O = 28 atoms per formula unit; apfu)							
Na	–	–	0.03	0.14	0.18	0.24	0.23
Ca	9.33	9.42	9.42	9.76	9.58	9.52	9.24
Σ(Ca,Na)	*9.33*	*9.42*	*9.45*	*9.9*	*9.76*	*9.76*	*9.48*
Mg	1.04	1.21	0.89	0.72	0.96	0.76	0.99
Fe2+	0.2	0.13	0.28	0.24	0.05	0.19	0.07
Σ(Mg,Fe)	*1.24*	*1.34*	*1.17*	*0.96*	*1.01*	*0.95*	*1.06*
P	6.97	6.89	6.91	6.79	6.92	6.87	7.02
Si	–	–	0.06	0.12	–	0.12	0.01
Σ(P,Si)	*6.97*	*6.89*	*6.97*	*6.91*	*6.92*	*6.99*	*7.03*
Mg-number	84	90	76	75	94	80	93
Na-number	0	0	0.4	1.4	1.8	2.4	2.5

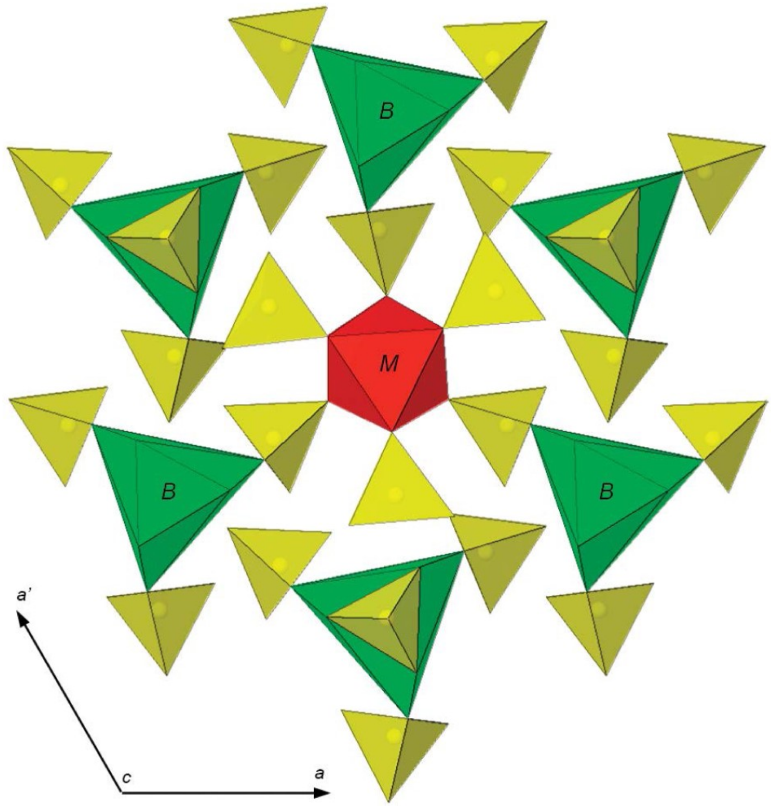

Figure 22. Representative section of keplerite crystal structure, looking down the c-axis. Taken after (Britvin et al., 2021). Species-defining constituents include : [MO_6] octahedra (shown in red); [BO_6] polyhedra (shown in green); and [PO_4] tetrahedra (shown in yellow). Note that [AO_8] polyhedra not shown. Orientation of figure is shown as a parallel slice along the (0001) plane.

Raman spectra of keplerite and merrillite (*along with ferromerrillite*) are given in Figure 23, Figure 24, and Table 3. Raman spectra are emphasized here as they can provide diagnostic information regarding structural and chemical characteristics of phases investigated. Three key features from these figures are noted: 1) as is anticipated for minerals of the merrillite subgroup, doublets (or, "duplets") located in the ~960 cm^{-1} region are observed for both keplerite and merrillite (Britvin et al., 2021; Jolliff et al., 2006; Xie et al., 2015). 2) Though both minerals demonstrate similar spectral characteristics between 400 and 1080 cm^{-1}, keplerite exhibits additional bands ("shoulder") in the ~960 cm^{-1} region while merrillite does not (Britvin et al., 2021) (Figure 24). The reason for this spectral feature in keplerite may be related to bonding-environment distortions caused by the bonding of the half-vacant B-site with adjacent [PO_4] tetrahedra (Britvin et al., 2021) (Figure 10, Figure 22). 3) Neither keplerite nor merrillite exhibit bands at 923 cm^{-1}; this is consistent for HPO_4^{2-} groups which lack essential hydrogen in their crystal structure (as compared to H-bearing phosphates, such as whitlockite, which exhibit a peak at 923 cm^{-1}) (Britvin et al., 2021; Jolliff et al., 1996)

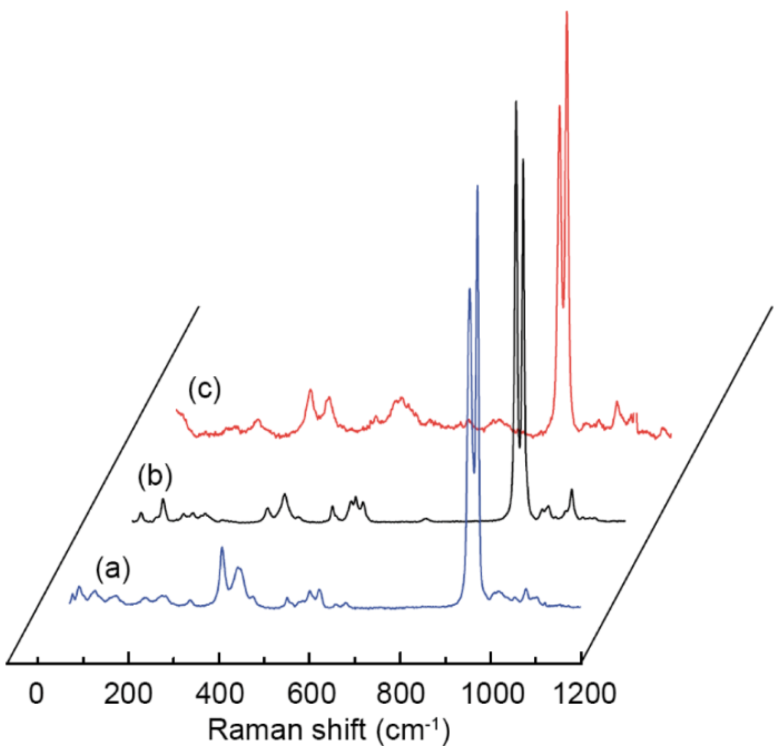

Figure 23. Raman spectra of keplerite, merrillite, and ferromerrillite over the 0 to 1200 cm^{-1} range. Taken after Britvin et al. (2021). Keplerite spectra derived from the Marjalahti pallasite are shown in blue (a); merrillite spectra derived from the Brahin pallasite are shown in black (b); and ferromerrillite spectra derived from the Los Angeles shergottite are shown in red (c). Note that spectra (b) and (c) are offset by 100 cm^{-1} along the x-axis.

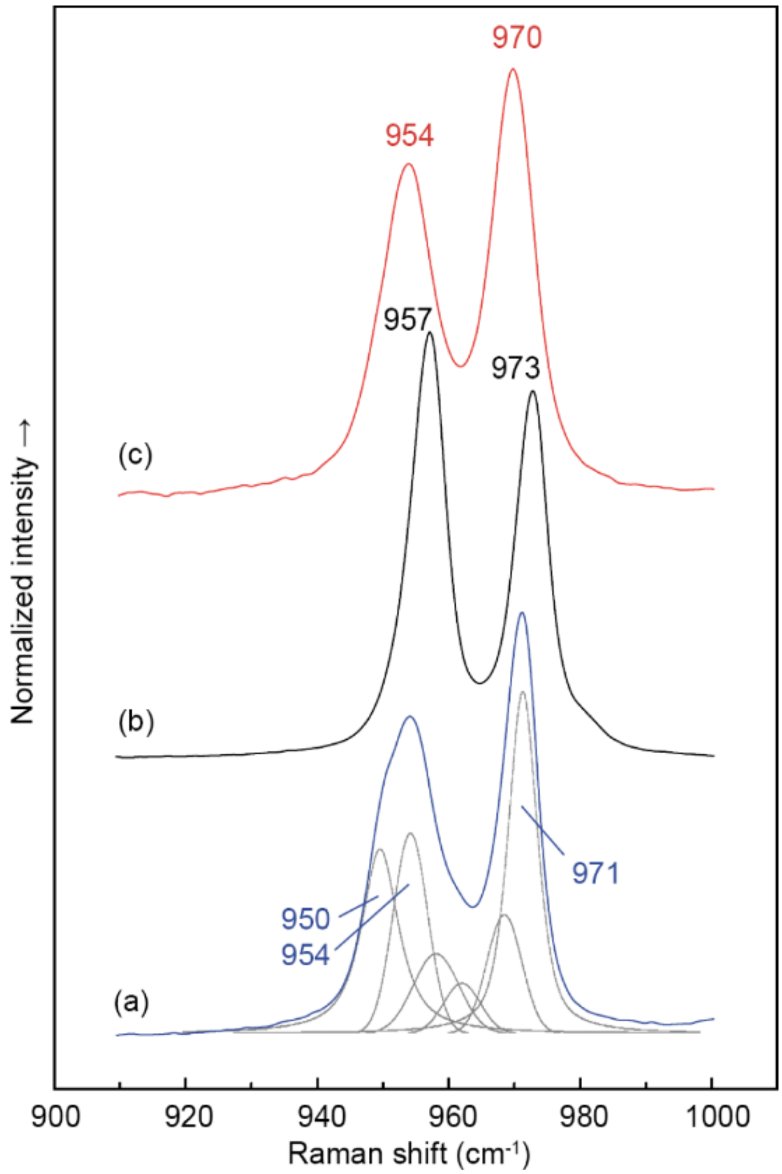

Figure 24. Raman spectra of keplerite, merrillite, and ferromerrillite over the 900 to 1000 cm^{-1} range. Taken after Britvin et al. (2021). Keplerite spectra derived from the Marjalahti pallasite are shown in blue (a); merrillite spectra derived from the Brahin pallasite are shown in black (b); and ferromerrillite spectra derived from the Los Angeles shergottite are shown in red (c). Note that keplerite displays visually resolved shoulders located at 950 and 958 cm^{-1} which cause peak broadening.

Table 3. Measured frequencies of (PO_4) vibration modes (cm^{-1}) for Raman spectra in Figure 23 and Figure 24. Taken and adapted after Britvin et al. (2021). Note that visually resolved shoulders are highlighted in yellow.

Mineral:	Keplerite	Merrillite	Ferromerrillite
Meteorite:	Marjalahti	Brahin	Los Angeles
Band Assignmnet:			
ν_2 (δ_s)	407	409	403
	442	446	445
ν_4 (δ_{as})	551	551	548
		593	591
	601	603	606
	622	618	620
		756	752
ν_1 (ν_s)	**950*		
	954	957	954
	**958*		
	971	973	970
ν_3 (ν_{as})	1016	1015	1012
	1078	1080	1080

It is important to emphasize that although keplerite is a newly *defined* mineral, it is not a newly *discovered* mineral. As is discussed in Britvin et al. (2021), the first documented occurrence of a Ca-enriched, Na-deficient, “whitlockite” phase was by Dowty (1977) in the Angra dos Reis meteorite (angrite group). Similar findings were documented by Buseck and Holdsworth (1977) who conducted a comprehensive study of phosphate phases in pallasite meteorites. Buseck and Holdsworth (1977) demonstrated a wide range of Ca-phosphate compositions, with notable Na-deficiencies, in the Ahumada, Mt. Vernon, and Antofagasta meteorites. Likewise, analyses of ‘merrillite’ in the Marjalahti pallasite show a total absence of Na (Buseck and Holdsworth, 1977), see Table 2 (Buseck and Holdsworth, 1977). Further, distinctions between merrillite subgroup members (e.g., Na-merrillite, Ca-merrillite, REE-merrillite) has been well documented in the literature (Adcock et al., 2014; Jolliff et al., 2006; Liu et al., 2016; Shearer et al., 2015; Xie et al., 2015).

1.6 Shock Metamorphic Effects in Rocks and Minerals

Shock metamorphism, often used interchangeably with *impact* metamorphism, describes the physical and chemical changes that occur to structures, rocks, and minerals that have been subjected to hyper-velocity impact events (DeCarli, 2005; Ferrière and Osinski, 2013). Although impact events can involve the ejecta of material into space, various degrees of shock deformation can occur to a planet as a result of impact metamorphism. For example, shock-related deformation may occur to a planet without any material leaving said planet's surface. Further, impact events may cause materials to temporarily leave their planetary surface, only to fall back to a new location on their parent body later on (e.g., NWA 7034: Udry et al. (2020)). Finally, multiple impact deformation events may occur to a target planet before any material is ejected from its surface (e.g., ALH 84001: Treiman (1995, 1998, 2021). In any case, although impact events are punctuated in nature, they are characterized by extreme temperature (i.e., 100s to 1,000s ˚C) and pressure (i.e., 10s to 100s GPa) spikes, along with extreme rates of quenching and strain, which can produce shock features (Dasgupta and Bhowmik, 2021; Langenhorst and Deutsch, 2012) (Figure 25).

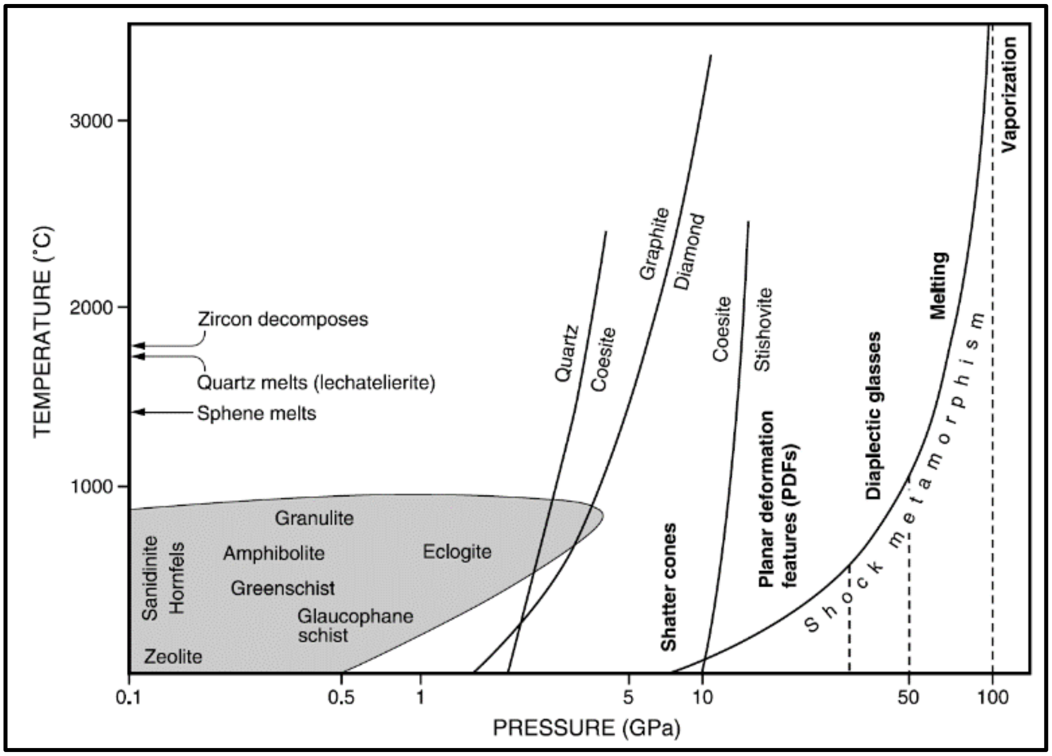

Figure 25. Pressure-temperature (P-T) diagram of metamorphic conditions. Taken after French (1998). The plot above shows the differences in pressure and temperature regimes for terrestrial metamorphic conditions (shaded region, to the bottom left) and shock metamorphic conditions ("shock metamorphism" curve, to the right). Shock pressures exceeding 50 GPa can produce extreme heat and thus can cause melting and vaporization to occur. Shock metamorphic features (i.e., planar deformation features, diaplectic glasses, melting, etc.) are noted along the shock metamorphism curve with approximate P-T regimes (dashed vertical lines). Mineral decomposition reactions for sphene, quartz, and zircon are noted along the temperature axis to the left; note that extreme temperatures are also associated with extreme pressures of shock metamorphism. At center are stability curves for coesite, diamond, and stishovite – at equilibrium conditions for each respective mineral.

The effects of shock on Martian meteorites are highly variable (both between different meteorite types and within individual specimens as well) (Fritz et al., 2005; Udry et al., 2020). Fritz et al. (2005) determined that the minimum shock pressures required for Martian material to be ejected from the surface of Mars and into space to be at least ~5 GPa. Thus, all Martian meteorites have been subjected to shock; though the degree of shock, and subsequent changes to the physical and chemical characteristics of these rocks, is highly variable. As an example: shergottites, the most abundant of all Martian meteorite types by both mass (82%) and total number of collected meteorites (89%), generally show shock pressures of >19 GPa (Fritz et al., 2005; Udry et al., 2020) with the rare occurrence of highly shocked samples exhibiting shock levels of 75-90 GPa (the highest shock level possible before complete melting occurs) (Kizovski et al., 2019).

Evidence of shock-metamorphism in rocks and minerals include 1) deformation features: planar fractures (PFs), planar deformation features (PDFs), dislocations, mechanical twins, kink bands, and mosaicism, 2) phase transformations: such as the formation of amorphous glasses (i.e., diaplectic glass formed from the transformation of plagioclase into maskelynite) and mineral phase transformations (i.e., the formation of high-pressure polymorphs such as coesite and stishovite), and 3) partial-to-complete: melting, decomposition, and vaporization (i.e., formation of impact melt) (DeCarli, 2005; Ferrière and Osinski, 2013; French, 1998; Langenhorst and Deutsch, 2012). Note, those minerals which show evidence of being subjected to shock metamorphism are then termed "shocked" (e.g., shocked quartz, shocked apatite, etc.).

A wide range of shock-metamorphic effects are observed in rocks and minerals due to impact events. Transient shock compressions (i.e., sudden *pressure* spikes) are often the driving force which cause deformation and phase transformation features in minerals (Langenhorst and Deutsch, 2012). Melting, decomposition, and vaporization are shock-metamorphic effects which are often driven by temperature (Langenhorst and Deutsch, 2012). Figure 25 summarizes the pressure and temperature regimes required for the aforementioned shock-induced features to form. Shock-metamorphic features exhibited in quartz, feldspar, olivine and pyroxene have been extensively studied and described, while the general understanding of how nesosilicates, double-chain inosilicates, phyllosilicates, carbonate, sulfate, and phosphate minerals are affected by (and respond to) shock is not as well constrained (Cox et al., 2020; Darling et al., 2021; Ferrière and Osinski, 2013; Kenny et al., 2019).

1.7 Objective

The focus of this study is to investigate shock-induced geochemical variations in Martian phosphate phases. The keplerite-bearing assemblages of Tissint and intergrown apatite-merrillite assemblages of ALH 84001,146 were targeted for further investigation. The two meteorites chosen for this study are both highly-shocked in state and contain chemically distinct phosphate phases. Phosphates were distinguished geochemically; by Electron Probe MicroAnalyzer (EMPA) techniques, Raman Spectroscopy, and Scanning Electron Microscopy (SEM) and structurally; by Electron Backscatter Diffraction (EBSD) analytical techniques.

CHAPTER 2:

MATERIALS

2.1 Tissint

The Tissint meteorite (Figure 26) was observed to fall as a meteor shower over the Moroccan desert on July 18, 2011 (Aoudjehane et al., 2012; Irving et al., 2012). Tissint is now the fifth observed fall which has origins connected to Mars. Estimates for the total sample mass recovered from the Tissint fall range from ~12 kg (Udry et al., 2020) to ~17 kg (Schulz et al., 2020). Subtle heterogeneities between subsamples and fragments of Tissint may therefore be anticipated, due to the large mass of material recovered (Schulz et al., 2020). The first samples of Tissint were collected at the end of October 2011; three months after its fall (Balta et al., 2015). As such, the residence time of Tissint on the surface of earth was limited, as was the exposure of Tissint to terrestrial weathering processes and terrestrial contamination (Balta et al., 2015; Schulz et al., 2020). However, as demonstrated by Barrat et al. (2014), terrestrial contamination cannot be ruled out entirely simply due to Tissint's short residency time on Earth, as was previously proposed by Aoudjehane et al. (2012). Barrat et al. (2014) assert that the interaction between Tissint meteorite fragments with surrounding desert soils on earth may account for the Ce anomaly and enrichments of Ba, Sr, Th, U, and light rare earth elements (LREE) which were observed in impact-melts by Aoudjehane et al. (2012). Therefore, careful consideration must be made when analyzing Martian meteorites: it is suggested that small fragments of the Tissint meteorite be either avoided entirely or analyzed with caution (Barrat et al., 2014).

Figure 26. Photograph of a typical fragment of Tissint (Natural History Museum, London: BM.2012,M1). Taken after Aoudjehane et al. (2012). The exterior of the meteorite is covered in a black fusion crust with a predominately pale grey interior which is composed of light-green olivine macrocrysts and black shock melted regions (veins, pockets). The rock fragment shown is 1.1 kg in mass. The scale bar at the bottom is given in centimeters.

Tissint is an olivine-phyric shergottite with abundant subhedral to euhedral olivine grains of variable size (up to 3.0 mm) which are set in a finer-grained groundmass (Baziotis et al., 2013; Irving et al., 2012; Schulz et al., 2020) (Figure 27). Olivine grains in Tissint are often compositionally zoned, with Mg-rich cores and Fe-rich rims, and commonly contain numerous mineral and melt inclusions (Baziotis et al., 2013; Schulz et al., 2020). The groundmass of Tissint is predominately composed of pyroxene and maskelynite (diaplectic plagioclase glass) with minor olivine, pyroxene-composition glass, Ti-chromite to ulvöspinel, ilmenite, pyrrhotite, merrillite, and shock-induced melt pockets and veins (Balta et al., 2015; Baziotis et al., 2013; Irving et al., 2012). A multitude of high-pressure (HP) minerals and phases have been identified as well (e.g., ringwoodite, akimotoite, majorite, lingunite, hollandite, tuite, stishovite, perovskite, tissintite), which reflect the complex shock history of Tissint (Baziotis et al., 2013; Ma et al., 2015; Walton et al., 2014).

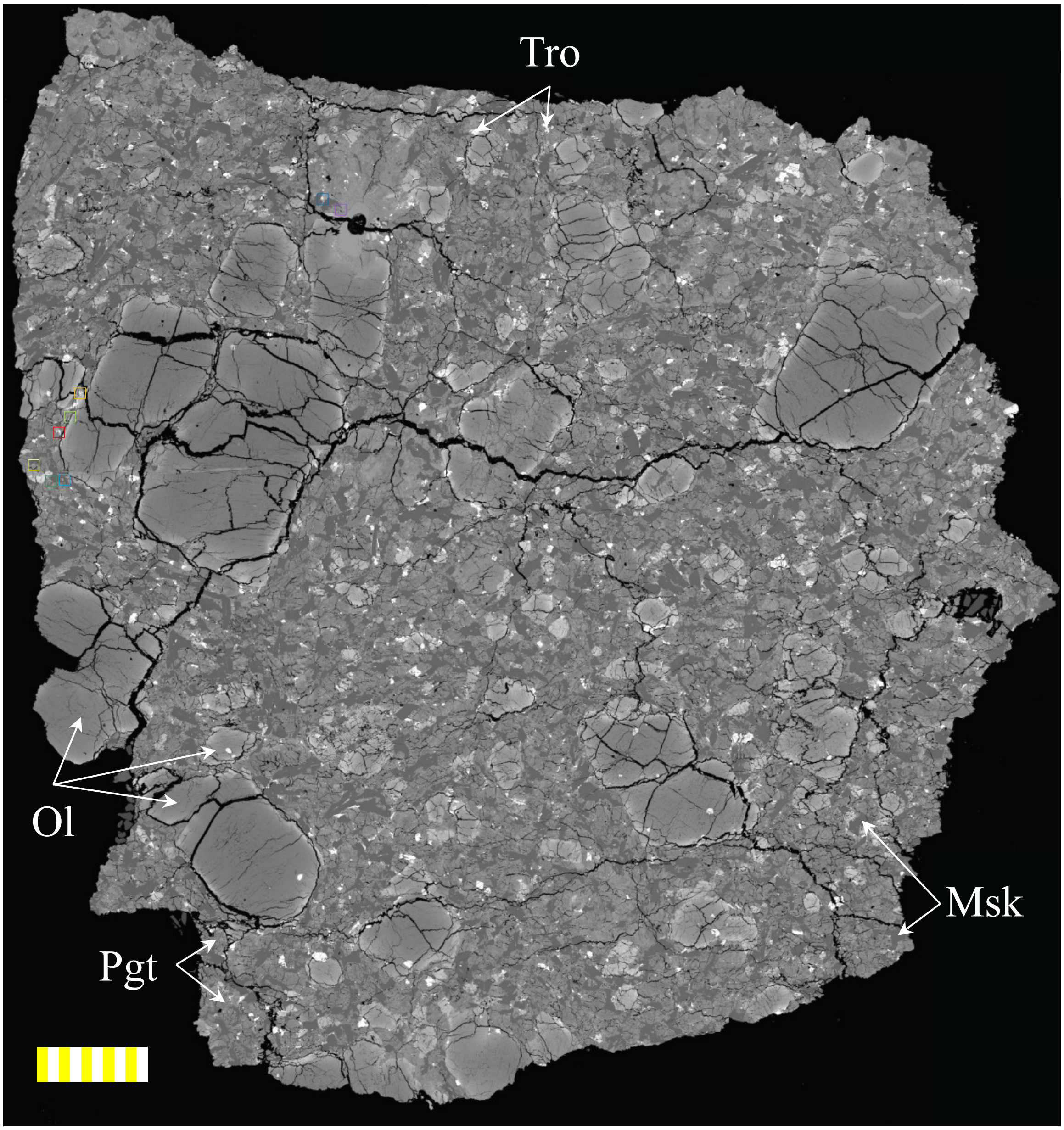

Figure 27. Backscattered electron (BSE) image of Tissint thin section investigated in this study. Tissint is composed of olivine macrocrysts (≤2.0 mm) & microphenocrysts (≤0.4 mm); olivine grains are set in a finer-grained groundmass of pyroxene, maskelynite, ilmenite, troilite, chromite, and phosphates (i.e., keplerite). Sample is approximately 1" in diameter. Scale bar is 1 mm in total length; each individual box is 100 µm in length. Colored boxes represent the location of identified grains; red = grain 1; orange = grain 2; yellow = grain 3; light green = grain 4; dark green = grain 5; dark blue = grains 7-12; purple; grains 13-16. Mineral abbreviations of select phases: Pgt = pigeonite; Tro = troilite; Ol = olivine; Msk = maskelynite.

2.2 ALH 84001

The ALH 84001 meteorite was collected in the Far Western Icefield of Allan Hills (ALH), Antarctica, during the 1984-85 Antarctic Search for Meteorites (ANSMET) Field Season; it was the first rock to be processed and classified from that field season (hence "*84001*") (Meyer, 2012). The sample was quickly identified as being unique given its size, composition (achondrite), and perceived green color (e.g., Figure 28, Figure 29). Figure 29 shows how the meteorite was cut and sectioned; the thin section studied here is ALH 84001,146. The meteorite caught international headlines in 1996 when (McKay et al.) proposed that ALH 84001 recorded evidence of past Martian life. Although habitable environments may have existed in its past, the scientific community still has not found any evidence directly linking the ALH 84001 meteorite to life on Mars (Treiman, 2021; Udry et al., 2020).

Aside from its potential link to biological processes, ALH 84001 is unique in the sense that it is the oldest known igneous rock from Mars, having crystallized from magma at 4.091 ± 0.030 billion years (Lapen et al., 2010). Further, the rock underwent a complex postcrystallization history of aqueous-carbonate alteration and multiple shock-induced metamorphic events (Lapen et al., 2010; Treiman, 1998). ALH 84001 is an igneous cumulate rock, an orthopyroxenite, composed of mosaic-grained orthopyroxene (4-5 mm diameter) which enclose subhedral to euhedral grains of chromite (occurring within recrystallized granular bands) (Lapen et al., 2010; Treiman, 1998). Other igneous minerals include chromite, maskelynite (after plagioclase), apatite, merrillite, augite, olivine, and amorphous SiO_2. Aqueous alteration materials (affected or not by shock) include Mg-Fe-Ca carbonates, magnetite, Fe-sulfide(s), and rare phyllosilicates (Jolliff et al., 2006; Lapen et al., 2010; Treiman, 1995, 1998, 2021). Figure 30 is a backscattered electron (BSE) image of the ALH 84001 thin section used in this study.

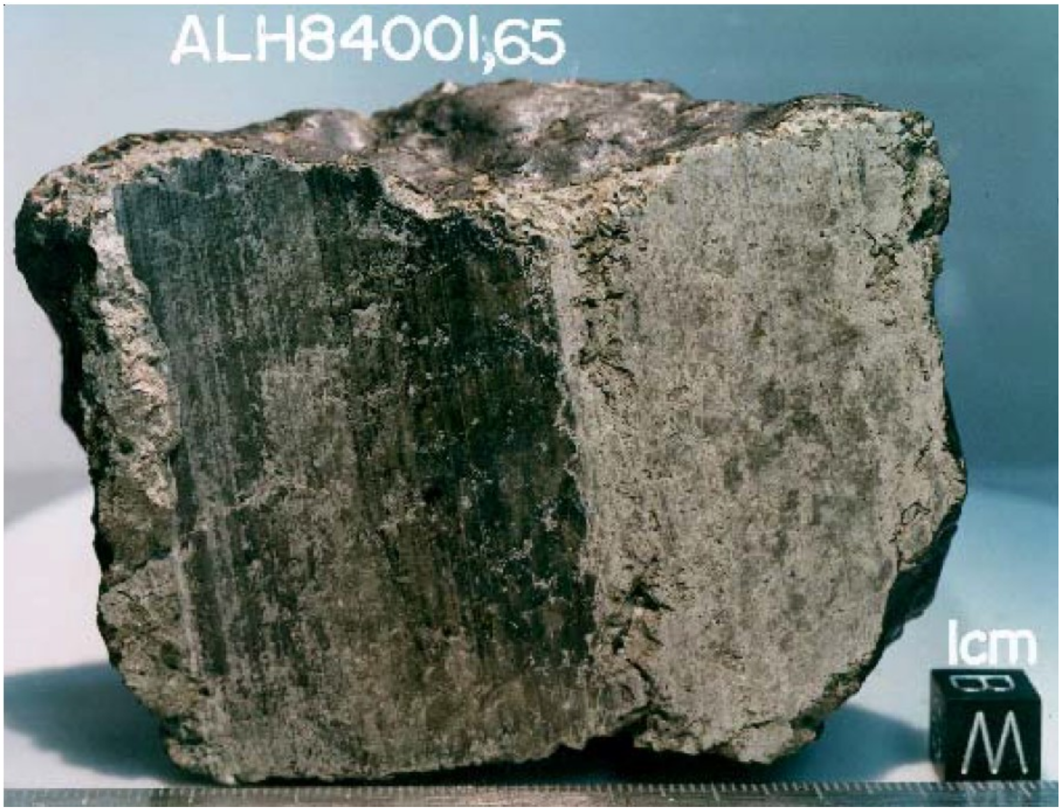

Figure 28. Representative photograph of ALH 84001(NASA # S94-32547). Taken after McKay et al. (1996). The photograph exemplifies the porosity of the interior of ALH 84001. Note that the exterior of the meteorite is covered in a dark black, fusion crust. Scale bar given on the bottom right.

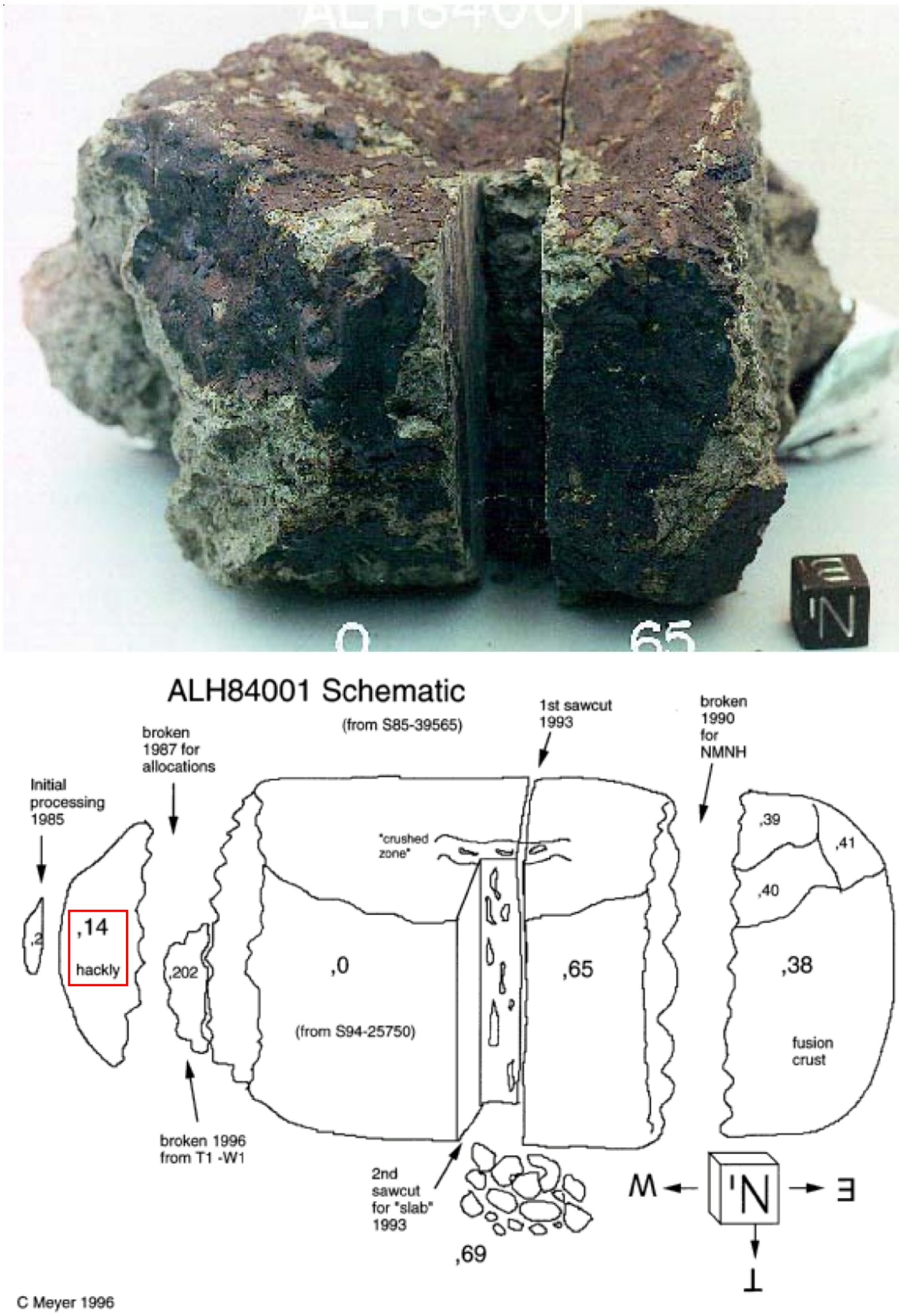

Figure 29. Photograph and schematic drawing of ALH 84001 after it was sawn in 1994. Taken after McKay et al. (1996). Note that sample investigated in this study is ALH 84001,146. Scale bar given on the bottom right.

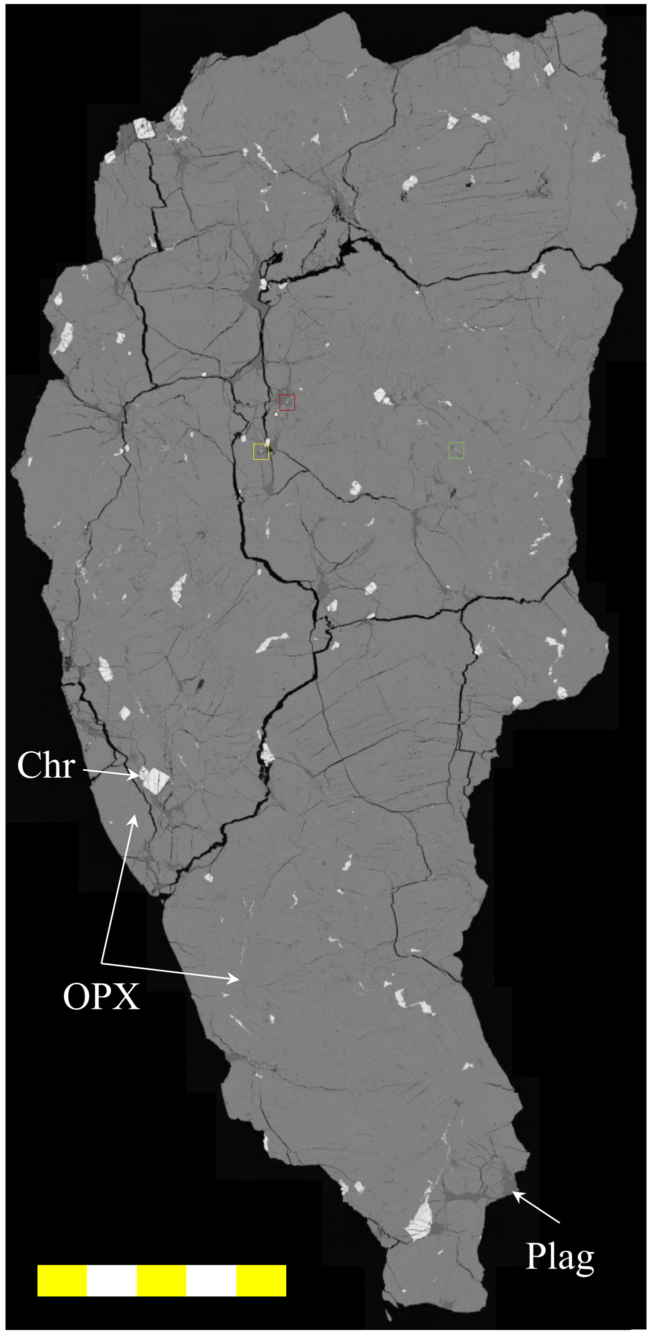

Figure 30. Backscattered electron (BSE) image of ALH 84001,146 thin section investigated in this study. ALH 84001 is composed of mosaic-grained orthopyroxene crystals (0.5 to 1.5 mm diameter), chromite, interstitial plagioclase, apatite, merrillite, clinopyroxene, and SiO_2 phases. Sample is approximately 1" x 2". Scale bar is 0.5 mm in total length; each individual box is 100 µm in length. Location of apatite-merrillite intergrown grains #1-3 noted by red box; apatite-merrillite intergrown grains #4-6 noted by yellow box; individual merrillite grain #8 noted by green box. Mineral abbreviations of select phases: OPX = orthopyroxene; Chr = chromite; Plag = plagioclase.

CHAPTER 3:

METHODS

3.1 JEOL JXA-8530F Hyperprobe: Tissint and ALH 84001

3.1.1 Energy Dispersive Spectrometry (EDS)

The fast identification of minerals by EDS analysis was performed at Rice University EMPA Laboratory (Department of Earth, Environmental and Planetary Sciences) using a JEOL Silicon Drift (SD) X-ray Detector with 10mm² active area and 133eV resolution. The detector is attached to a JEOL JXA 8530F Hyperprobe. The analytical conditions used for EDS analysis were: 15 kV accelerating voltage, 20 nA beam current, and a live time of 20 seconds. DeadTime (DT) during the analysis was 35-40%. The beam diameter size used was “spot” (~300 nm). The EDS spectra were compared to spectra of known minerals, whereas the semi-quantitative EDS analyses were normalized to appropriate numbers of oxygen atoms to easily recognize minerals by stoichiometry.

3.1.2 Electron MicroProbe Analysis (EMPA)

Electron Probe Micro-Analysis (EMPA) of Tissint and ALH 84001 employed BackScattered Electron (BSE) imaging, quantitative point analysis, and Wavelength Dispersive Spectrometry (WDS) quantitative mapping. Data were acquired at the EMPA Laboratory at Rice University, using a JEOL JXA 8530F Hyperprobe equipped with a field emission (Schottky) emitter and five WDS spectrometers.

3.1.3 Phosphate Analysis

The analytical conditions used were 15 kV accelerating voltage, 20 nA beam current, 3-micron beam diameter. The analyzed x-ray lines, diffracting crystal, peak position (L-value in mm), and lower and upper background offsets (BG_L and BK-U) are shown in Supplementary Table 1. The counting times and detector settings are given in

Supplementary Table 2. The PhiRoZ (JEOL) matrix correction was employed for quantification.

Because phosphate minerals can contain significant proportions of rare earth elements (REE), there are potential interferences between K X-ray lines of transition elements and L X-ray lines of the REE, and among L lines of different REE. The interferences between the interfered and interfering elements (La Lα and Nd Lα; F kα and Ce Lα; Nd Lα and Ce Lα, respectively) were corrected by applying an empirically determined correction coefficient k, as follows: (Net intensity of corrected interfering element) = (Net intensity of measured interfered element) – k*(Net intensity of measured interfering element), where the measurements were done on pure REE phosphate standards. The coefficient k is the ratio between the net counts of an interfered element divided by the net counts of the measured interfering element. For example, for the correction for F which is drastically interfered with by Ce, F was analyzed on $CePO_4$ standard (free of F). The fake fluorine counts (interfered element) obtained on $CePO_4$ standard (net intensity of interfered element) divided by the net counts of Ce (interfering element) was used as k correction coefficient for F. The interference corrections applied are presented below (where “cps” stands for “counts per second”):

$(\text{La cps})_{corrected} = (\text{La Net})_{measured} - 0.030739 \text{ x } - (\text{Nd Net})_{measured}$

$(\text{F cps})_{corrected} = (\text{F Net})_{measured} - 0.14098 \text{ x } (\text{Ce Net})_{measured}$

$(\text{Nd cps})_{corrected} = -0.7\ (\text{Nd Net})_{measured} - 0.00223 \text{ x } (\text{Ce Net})_{measured}$

3.1.4 WDS quantitative maps

To evaluate chemical compositions and potential chemical zonation of materials, Wavelength Dispersive Spectrometry (WDS) element mapping were acquired using 15 kV accelerating voltage, 50 nA beam current, using stage mode scanning and 30 ms dwell time for larger maps (< x 3000 magnification) and beam mode and 50 ms dwell time for small maps (> x 3000 magnification). Deadtime correction was applied for every mapped element. Each element map was subsequently quantified employing the same standards used in the phosphate analysis and corrected for dead time.

3.2 JEOL JXA-8530F Field Emission Electron Probe: Tissint

All procedures followed for JEOL JXA-8530F Hyperprobe data collection (i.e., Analytical Conditions for EDS and EMPA) were applied to JEOL JXA-8530F Field Emission Electron Probe analyses. The analysis of phosphate phases contained within Tissint was performed in the Astromaterials Research and Exploration Science (ARES) Electron Beam (EB) Laboratory at Johnson Space Center (JSC).

3.2.1 Energy Dispersive Spectrometry (EDS)

The fast identification of minerals by EDS analysis was performed using a Thermo Scientific UltraDry silicon drift X-Ray Detector with $10 mm^2$ active area and 133eV resolution. The detector is attached to a JEOL JXA-8530F Electron Microprobe. The analytical conditions used for EDS analysis were: 15 kV accelerating voltage, 20 nA beam current, and a live time of 10 to 30 seconds. The beam diameter size used was “circle” (3.0 μm).

3.2.2 Electron MicroProbe Analysis (EMPA)

To evaluate chemical composition of materials, Electron Probe Micro-Analysis (EMPA) of Tissint employed BackScattered Electron (BSE) imaging and quantitative point analysis. Data were acquired using a JEOL JXA-8530F Microprobe equipped with a field emission (Schottky) emitter and five WDS spectrometers. The ZAF correction was employed for quantification.

3.3 WITec alpha300R Raman Microscope: Tissint

To evaluate chemical composition of materials, Raman spectra of keplerite in Tissint were acquired on a WITec alpha300R Raman Microscope with a WITec Diode laser and a 50x / 0.75 Zeiss EC Epiplan objective. Integration times of 30 s with an accumulation of 10–20 scans were selected at a spectral resolution of approximately 2.8 cm^{-1}/pixel. Two Raman spectra were collected for two keplerite grains: #1 and #2. Raman spectra were fitted to a Lorentz function fitting profile. Additional figures and tables pertaining to individual analyses and analytical conditions can be found in the Appendix (e.g., Supplementary Table 13 and Supplementary Table 14).

3.4 JEOL 7900F Field Emission Gun SEM: Tissint

Crystallographic orientations of select keplerite grains in Tissint were studied by Electron backscattered diffraction (EBSD). Data were acquired on a JEOL 7900F Field Emission Gun Scanning Electron Microscope (SEM) coupled to an Oxford Instruments Symmetry detector. A voltage of 20 kV, beam current of 9 nA, and tilt of 70˚ were used for all analyzed grains. Data collected included Inverse Pole Figures (IPFs), band contrast (BC), grain boundaries (GB), and phase (Ph) maps of analyzed keplerite grains. Electron backscatter patterns (EBSP) (i.e., Kikuchi bands; crystal lattice projections) were collected for both keplerite gains and the phases which surrounded them (i.e., clinopyroxene, ilmenite, maskelynite, troilite, olivine, Cr-spinel) to aid in phase identification.

CHAPTER 4:

TISSINT

4.1 Results

A total of 16 phosphate grains were identified in Tissint (Figure 31 and Figure 32). Identified phosphates typically occur with maskelynite, troilite, ilmenite, pigeonite, and olivine. They had either an elongated or "finger-like" texture (e.g., Figure 31a), or occurred as inclusions (e.g., Figure 32d) with subhedral to anhedral crystal faces. Sizes of grains ranged from a few microns in length (or diameter) to 10s of microns in maximum length. Grains which were only a few microns in total length (or in maximum diameter) were not targeted for geochemical or structural work.

4.1.1 Phosphate Discrimination

Discriminating among possible phosphate minerals relies on the three key differences between apatite, merrillite and keplerite. First, Apatite contains Cl and F while merrillite and keplerite are devoid of all halogens (Table 5). Second, both merrillite and keplerite contain higher P_2O_5, Na_2O, and MgO contents along with lower CaO contents, when compared to apatite (Table 4 and

Table **6**). Third, merrillite ($Ca_9NaMg(PO_4)_7$) contains appreciable Na_2O contents when compared to keplerite ($Ca_9(Ca_{0.5}\square_{0.5})Mg(PO_4)_7$). All phosphate grains identified in Tissint are Na-deficient with respect to ideal merrillite compositions. Although apatite was not identified in Tissint, it has been reported in other works (Aoudjehane et al., 2012; Mari et al., 2019).

4.1.2 Keplerite Chemical Composition

A total of 7 keplerite grains were targeted for quantitative analysis and 35 individual points were collected. A comprehensive summary of keplerite chemical composition data is given in Table 4. Normalized formula amounts were calculated from measured oxide weight percentages. Datapoints which measured abnormal oxide concentrations (e.g., low phosphorus content, like 30 wt% P_2O_5) or total percentages (e.g., total wt% ≤98.5%) were excluded from calculations.

Variations in chemical compositions were noted for analyzed keplerite grains (Supplementary Table 4). Na_2O contents ranged from 0.29 to 0.98 wt% with an average of 0.61 wt% (1σ = 0.20). CaO contents ranged from 44.53 to 47.58 wt% with an average of 46.73 wt% (1σ = 0.68). MgO contents ranged from 2.57 to 3.32 wt% with an average of 2.88 wt% (1σ = 0.27). P_2O_5 contents ranged from 43.39 to 46.77 wt% with an average of 45.53 wt% (1σ = 0.80).

Calculated formula amounts (normalized to 28 oxygens), likewise, varied as well. The lowest calculated formula amount for Na was found to be 0.10 atoms per formula unit (i.e., the calculation was based on datapoint with lowest measured Na_2O contents) (Supplementary Table 9). The highest calculated formula amount for Na was found to be 0.34 atoms per formula unit (i.e., the calculation was based on datapoint with highest measured Na_2O contents) (Supplementary Table 10).

The magnesium# ($[Mg_{atomic}/(Mg_{atomic}+Fe_{atmoic})]*100$) of the analyzed phosphate minerals is 63.2. The sodium# ($[Na_{atomic}/(Na_{atomic}+Ca_{atmoic})]*100$) is 2.3. Cation-site occupancies are: Ca-site = 9.26; Mg-site = 1.22; P-site = 7.05 (Figure 33). To the Ca site, we assigned Ca, Na, K., Mn, and the rare earth elements (La, Ce, Nd); to the Mg site, we assigned Mg and Fe; and to the P sites we assigned P, Si, and S. To satisfy ideal keplerite compositions, site occupancies would be assigned as follows: Ca-site = 9.50; Mg-site = 1.00; P-site = 7.00. Note that the Ca-site in analyzed keplerite grains is too low while the Mg-site is too high. This may indicate that the Ca-site in keplerite contains some Fe+Mg+Mn (Table 4).

Maps of element distributions (Na, Ca, Cl, F, S, Si, K, Fe, Mg, and P) in two keplerite-bearing assemblages were obtained by Wavelength Dispersive Spectrometry (WDS) on the EPMAs, see Figure 34 and Figure 35. Shock-melt veins were not observed or identified during analyses and therefore no phosphates were found to occur in shock-melted zones. None of the grains analyzed here showed any chemical zoning in any orientation (Figure 34 and Figure 35).

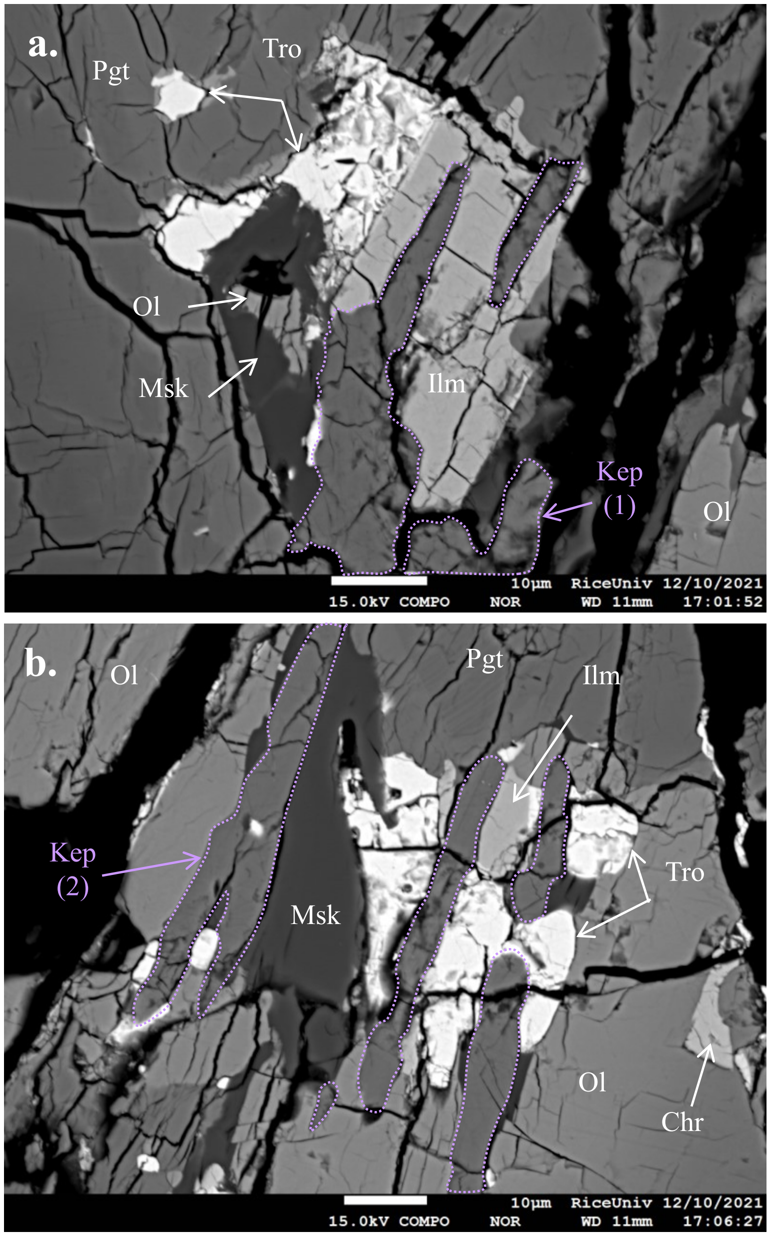

Figure 31. Backscattered electron (BSE) images of keplerite grains #1-2 in Tissint. (a) Keplerite grain #1 in Tissint and (b) Keplerite grain #2 in Tissint. Mineral abbreviations: Pgt = pigeonite; Tro = troilite; Ol = olivine; Msk = maskelynite; Ilm = ilmenite; Kep = keplerite; Chr = chromite. Scale bar is 10 μm in length. Note Figure 27 for location of analyzed points.

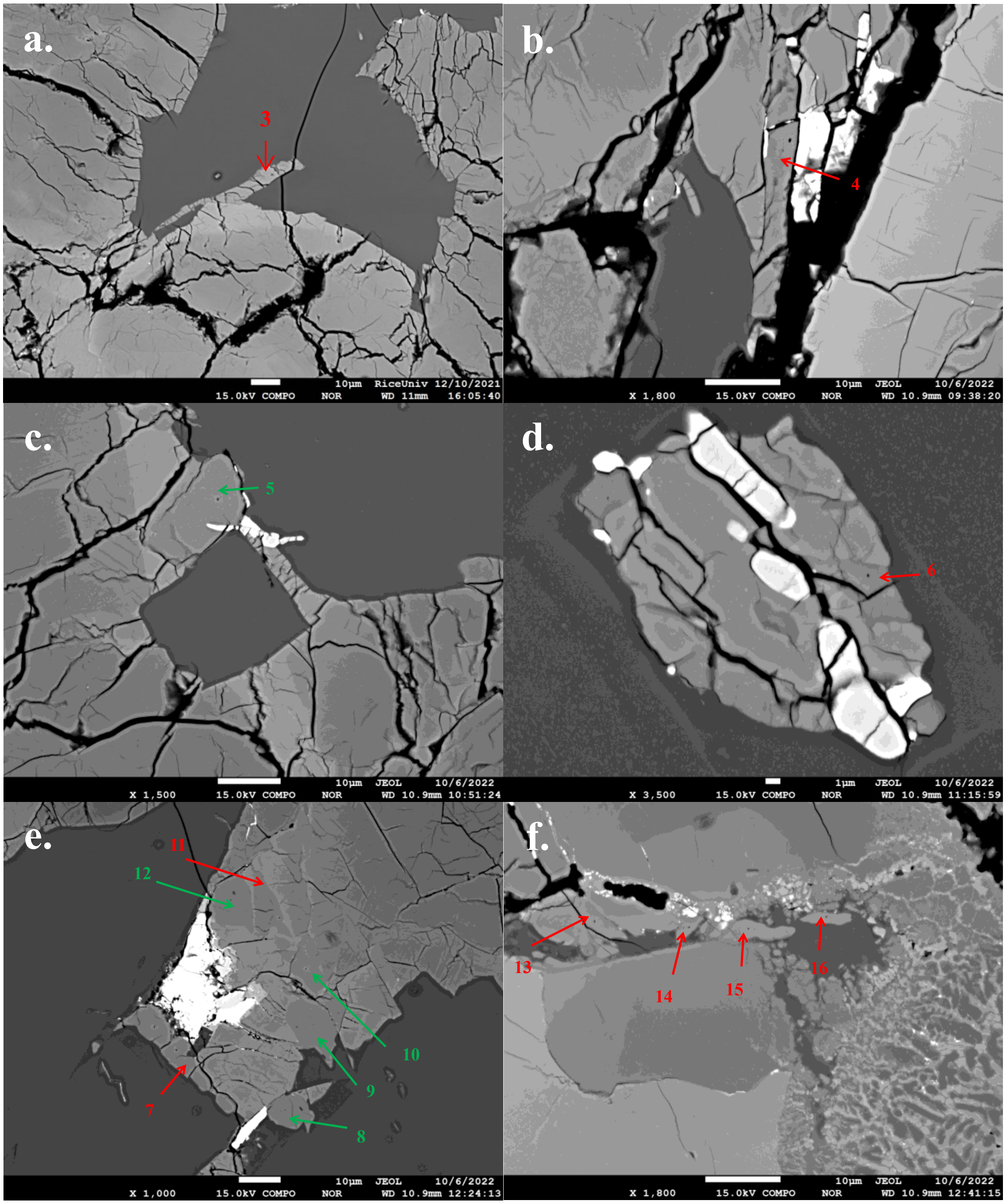

Figure 32. Backscattered electron (BSE) images of keplerite grains #3-16 in Tissint. Grains denoted in green (1, 2, 5, 8, 9, 10, 12) were used in quantitative point analysis calculations. Note occurrence of keplerite grains with symplectite in figure (f). Scale bar is 1 to 10 μm in length.

Table 4. Average composition of keplerite in Tissint.

Chemical composition of Keplerite in Tissint				
	wt%[a]	1σ[a]	To 28 oxygens	
Al_2O_3	0.140	0.17	Al	0.003
Ce_2O_3	0.034	0.03	Ce	0.002
La_2O_3	0.036	0.10	La	0.002
Nd_2O_3	0.035	0.07	Nd	0.002
FeO	2.980	0.54	Fe	0.449
MnO	0.142	0.03	Mn	0.022
MgO	2.876	0.27	Mg	0.771
CaO	46.726	0.68	Ca	9.010
Na_2O	0.614	0.20	Na	0.214
K_2O	0.048	0.02	K	0.011
P_2O_5	45.528	0.80	P	6.937
SiO_2	0.544	0.60	Si	0.098
SO_3	0.090	0.13	S	0.012
*TiO_2	*0.023*	*0.02*	**Ti*	*0.003*
F	0.000	0.00	F	0.000
Cl	0.009	0.01	Cl	0.003
O=F,Cl	-0.002			
Total	**99.823**			

[a] Oxide concentrations; EPMA analyses by mass. Average of 35 analyses. *TiO_2 was not analyzed via JEOL JXA-8530F Hyperprobe at Rice University. Therefore, weight percent and normalized formula amounts are the average of 35 analyses collected via JEOL JXA-8530F Microprobe at NASA-JSC-ARES.

Ca-site	9.264	Includes: Na, La, K, Ca, Mn, Ce, Nd
Mg-site	1.220	Includes: Fe, Mg
P-site	7.046	Includes: Si, P, S

Mg#	63.24	Mg ratio = 100 x Mg / (Mg + Fe)
Na#	2.32	Na ratio = 100 x Na / (Na + Ca)

Keplerite Formula	$Ca_9(Ca_{0.5}\square_{0.5})Mg(PO_4)_7$

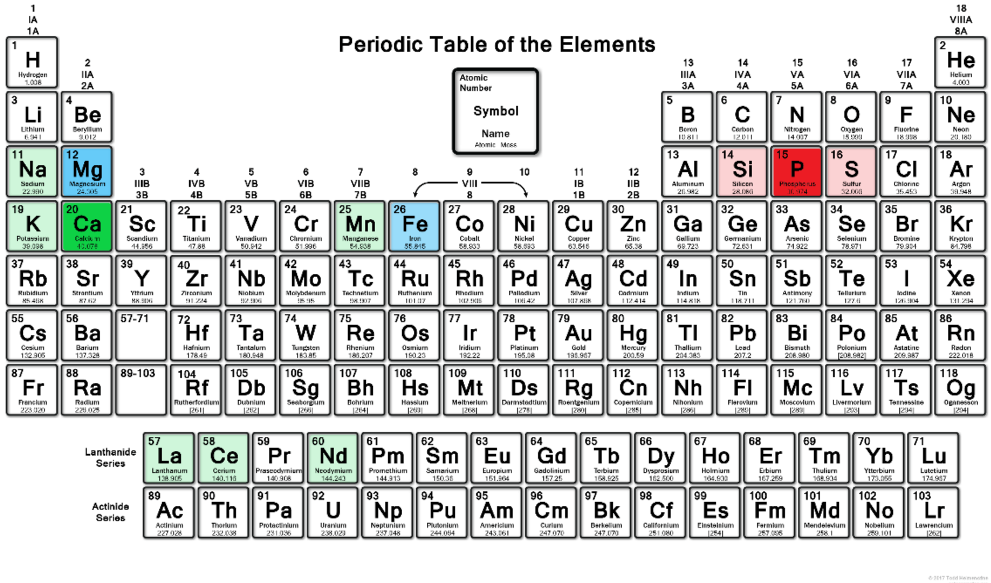

Figure 33. Periodic table of elements with Ca-Site (green), Mg-site (blue), and P-site (red) assignments filled in for keplerite. Source of periodic table: https://sciencenotes.org/. Data corresponds to Table 4. Opacity of colors varies with respect to relative abundances (i.e., 0.001 to 0.250 cations = 20% opacity; 0.251 to 0.500 cations = 40% opacity; 0.501 to 0.750 cations = 60% opacity; 0.751 to 1.000 cations = 80% opacity; >1.001 cations = 100% opacity).

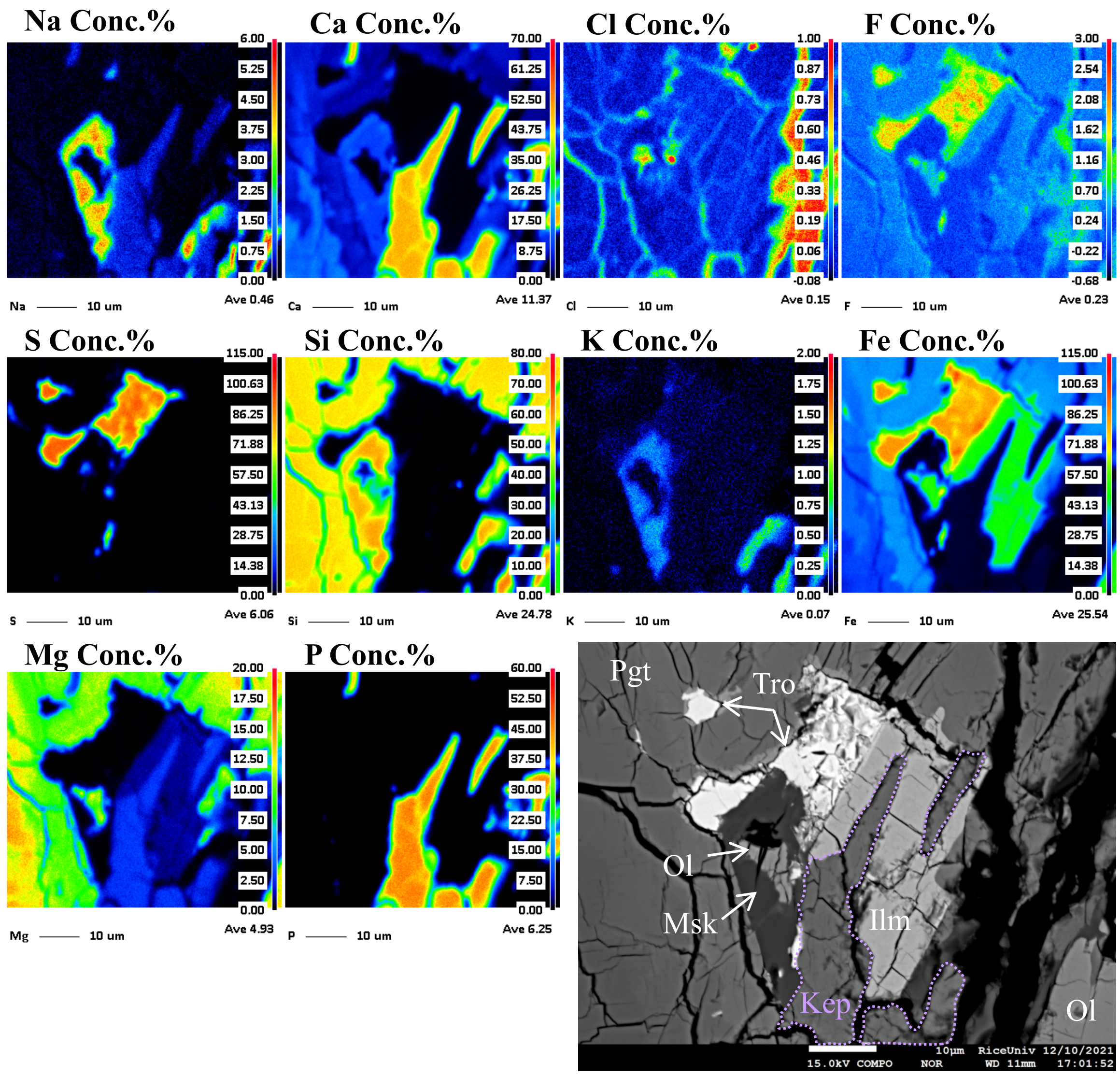

Figure 34. Quantitative WDS (Wavelength Dispersive Spectrometry) element map distribution and BSE (BackScattered Electron) image of phosphate keplerite grain #1 in Tissint. WDS element maps illustrate elemental distributions in phosphates and surrounding phases; maps are given in weight percent (wt%). WDS element maps correspond to BSE image in the bottom right-hand corner. Mineral abbreviations: Pgt = pigeonite; Tro = troilite; Ol = olivine; Msk = maskelynite; Ilm = ilmenite; Kep = keplerite. Scale bar is 10 μm in length.

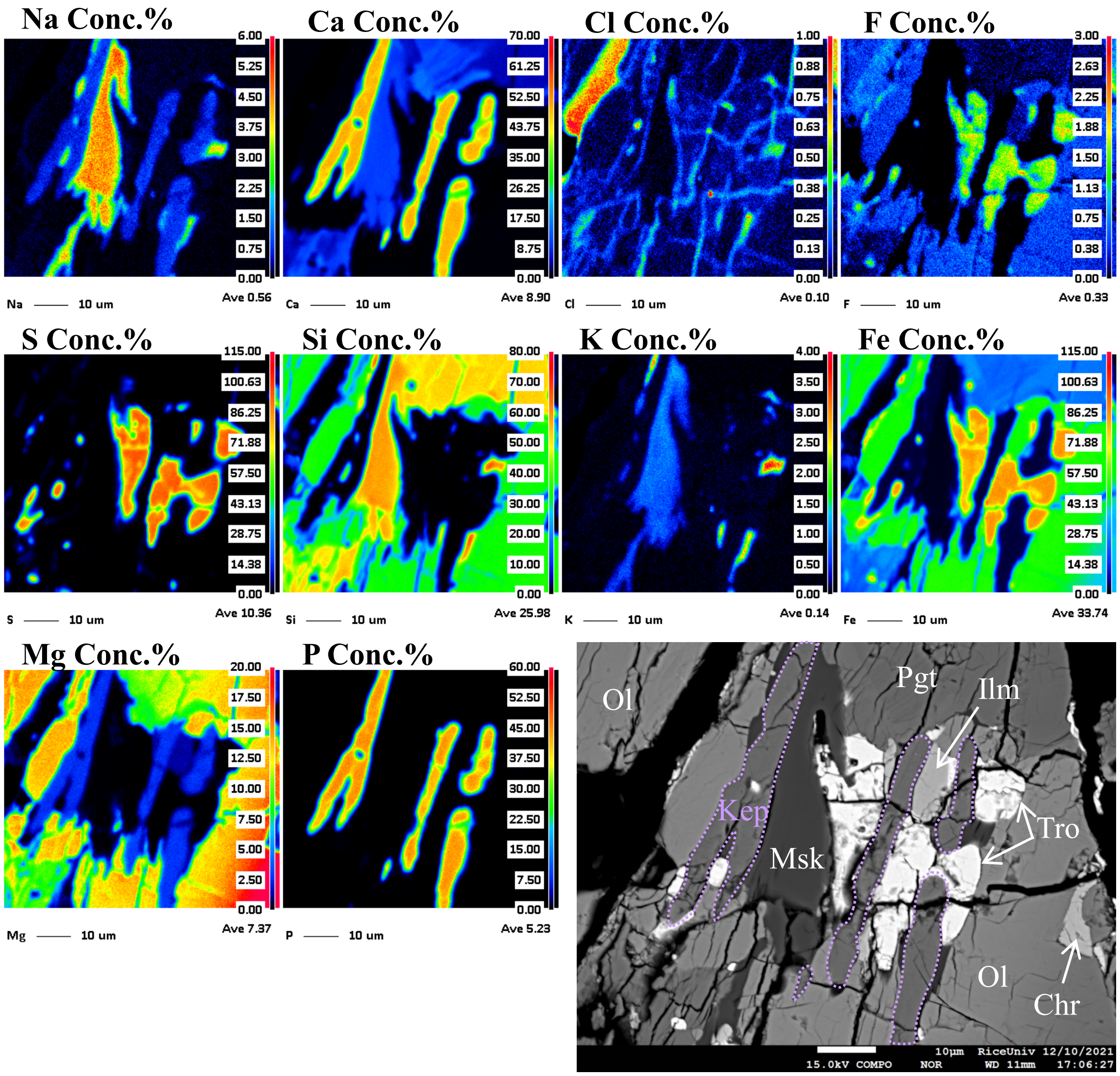

Figure 35. Quantitative WDS (Wavelength Dispersive Spectrometry) element map distribution and BSE (BackScattered Electron) image of phosphate keplerite grain #2 in Tissint. WDS element maps illustrate elemental distributions in phosphates and surrounding phases; maps are given in weight percent (wt%). WDS element maps correspond to BSE image in the bottom right-hand corner. Mineral abbreviations: Pgt = pigeonite; Tro = troilite; Ol = olivine; Msk = maskelynite; Ilm = ilmenite; Kep = keplerite; Chr = chromite. Scale bar is 10 µm in length.

4.1.3 Raman Spectroscopy

A total of four scans were collected for Raman phosphate phase analysis in Tissint: two spectra were collected for keplerite grain #1 and two were collected for keplerite grain #2. A representative scan of keplerite in Tissint are shown in Figure 36 and Figure 37; a backscattered electron (BSE) image of the analyzed keplerite grain are shown in Supplementary Figure 92. Additional information regarding each individual Raman scan can be found in the Appendix (e.g., Supplementary Figure 93; Supplementary Table 13). All scans collected exhibited comparable spectral features (i.e., peak locations). As such, the four collected scans were averaged. Averaged spectra are shown in Figure 38 and Figure 39.

Three key features were observed in measured spectra. First, doublets (i.e., "duplets"), characteristic of merrillite-subgroup members, were observed to occur at 955.7 to 958.7 cm^{-1} and 970.0 to 972.8 cm^{-1} (Figure 37, Figure 39). Second, visually resolved shoulders located at 947.5, 952.0, and 955.7 cm^{-1} were exhibited in spectra. The occurrence of these bands was associated with general peak-broadening. Third, the 923 cm^{-1} band, characteristic of HPO_4^{2-} groups (e.g., whitlockite), was not observed in any of the collected Raman spectra.

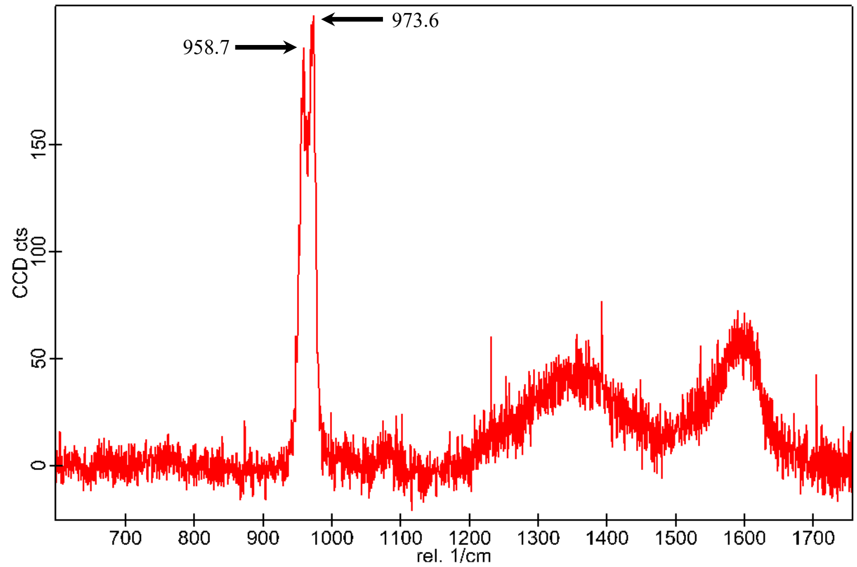

Figure 36. Representative analysis of measured Raman spectra for keplerite (grain #2) in Tissint over the 700 to 1700 cm^{-1} range. Spectrum 214. Note doublets located at 958.7 and 973.6 cm^{-1}; missing 923 cm^{-1} band (i.e., characteristic signature of HPO_4^{2-} groups); and visually resolved shoulders located in the 947.5 to 955.7 cm^{-1} region.

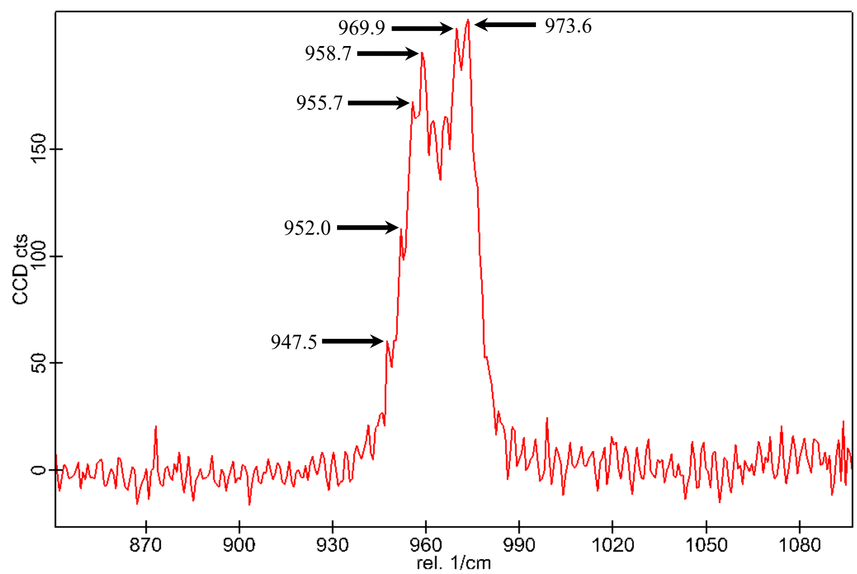

Figure 37. Representative analysis of measured Raman spectra for keplerite (grain #2) in Tissint over the 870 to 1080 cm^{-1} range. Spectrum 214. Note that keplerite displays visually resolved shoulders located at 947.5, 952.0 and 955.7 cm^{-1} which cause peak broadening. Also note the missing 923 cm^{-1} band, which is a characteristic signature of HPO_4^{2-} groups.

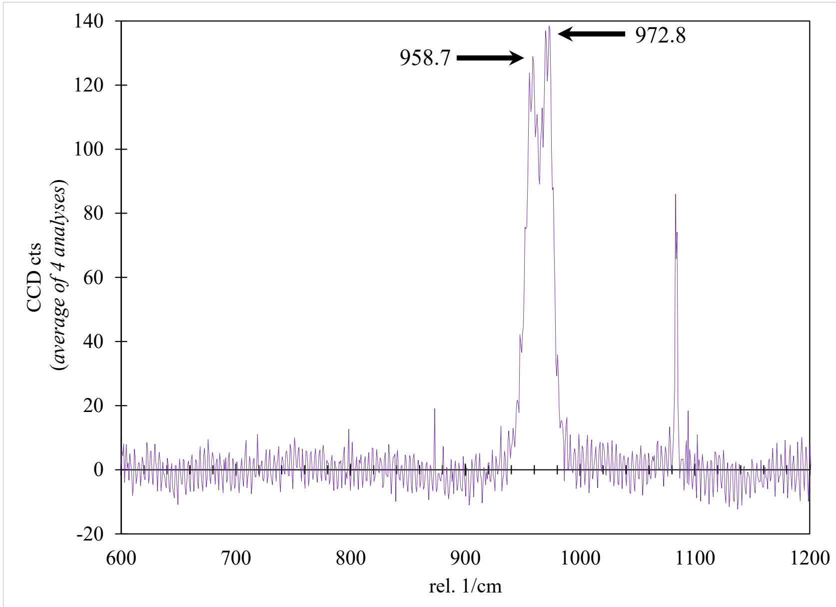

Figure 38. Averaged analysis of measured Raman spectra for keplerite grains #1 and #2 in Tissint over the 600 to 1200 cm-1 range.

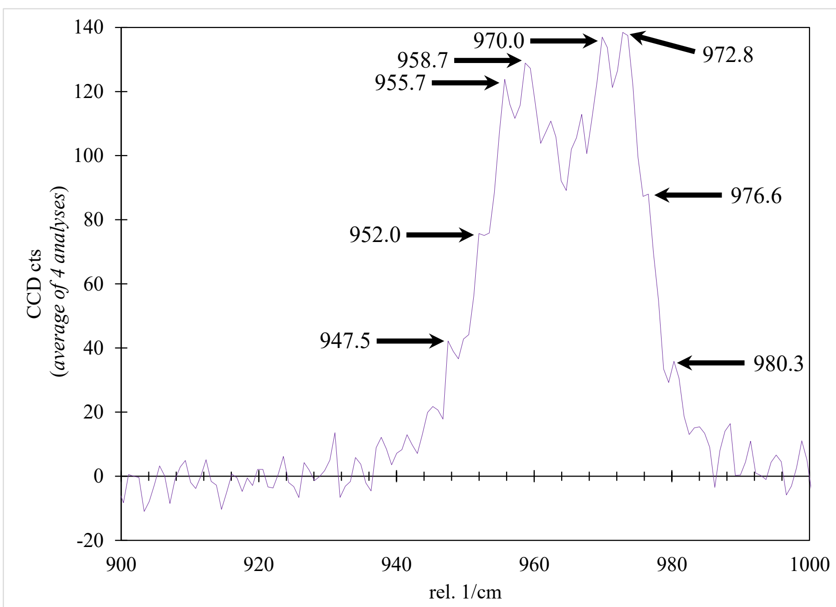

Figure 39. Averaged analysis of measured Raman spectra for keplerite grains #1 and #2 in Tissint over the 900 to 1000 cm-1 range. Note the visually resolved shoulders located at 947.5, 952.0, and 955.7 cm^{-1}. Given a local minima of 964.7 cm^{-1}; the left-most end of the curve is a distance of 17.2 cm^{-1} away from the local minima (i.e., 946.7 cm^{-1} – 957.5 cm^{-1} = 17.2 cm^{-1}). Given the same local minima of 964.7 cm^{-1}; the right-most end of the curve is a distance of 15.6 cm^{-1} away from the local minima (i.e., 980.3 cm^{-1} – 946.7 cm^{-1} = 15.6 cm^{-1}). As such, the left-most portion of the curve is more bulbous (i.e., due to the accented shoulder) than the right-most portion of the curve.

4.1.4 Electron Backscattered Diffraction (EBSD)

Keplerite grains #1 and #2 were targeted for EBSD structural analysis. Inverse pole figure (IPF) maps and electron backscatter patterns (EBSPs) (i.e., Kikuchi bands; crystal lattice projections) were collected for both keplerite grains. A total of 6 EBSPs were collected; 2 for grain #1 and 4 for grain #2.

Measured IPFs are shown in Figure 40 and Figure 41 while a representative EBSP are shown in Figure 42. Phase maps of analyzed sections can be found in the Appendix (e.g., Supplementary Figure 99). Coloring schemes used an IPF z-scheme (parallel to the z-direction) for orientation maps produced. In other words, each point on the map is colored according to which crystal direction is measured to be parallel to the z-direction of the map. Analyzed grains were found to have a merrillite-type crystal structure. Both grains exhibited similar crystal orientations as well, with the 10-10 crystal face being roughly parallel to the map surface.

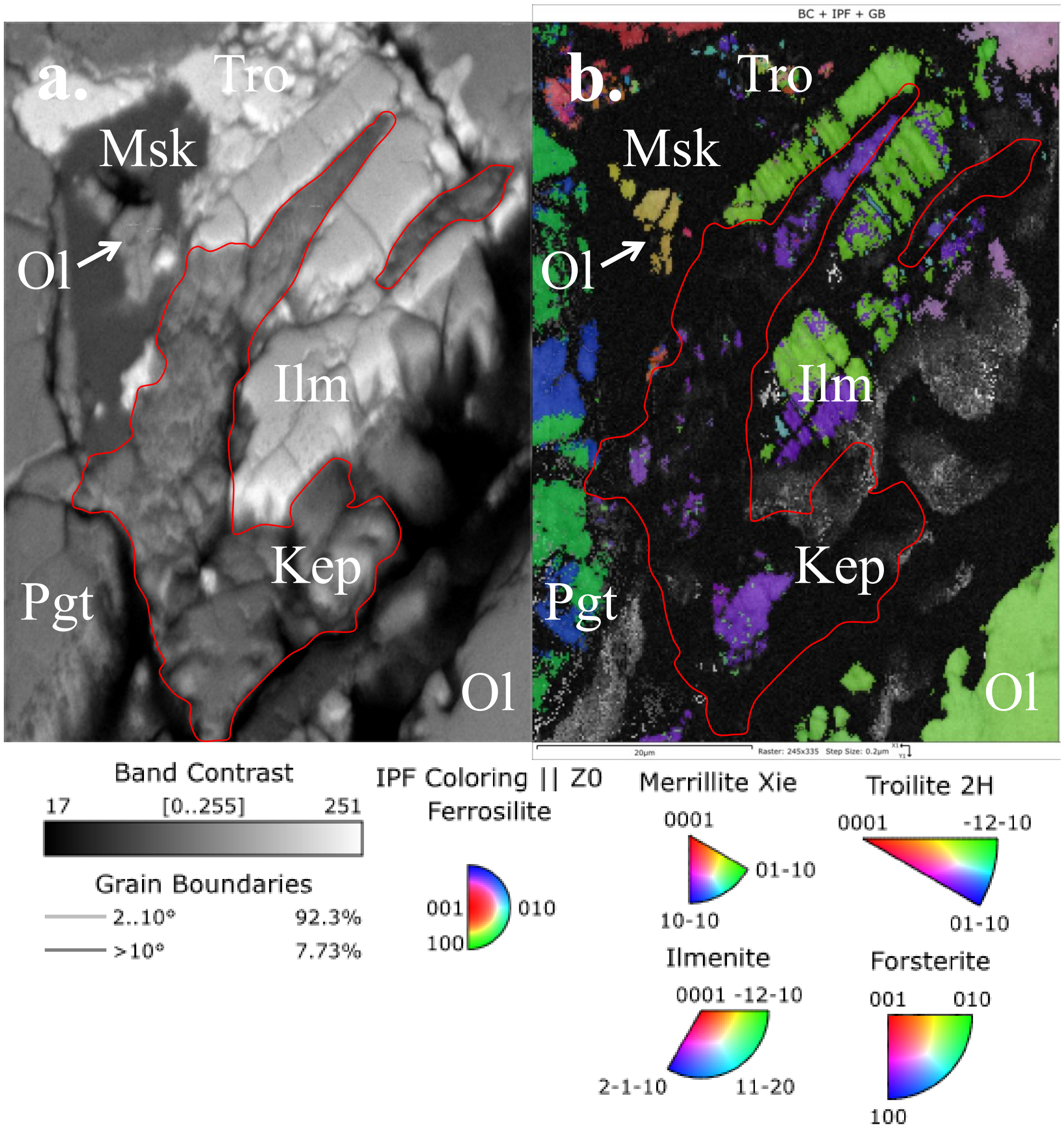

Figure 40. Backscattered electron (BSE) image and inverse pole figure (IPF) z-scheme (i.e., IPF map relative to the z direction of the image) of keplerite grain #1 in Tissint. Keplerite grain analyzed outlined in red. Note that the 10-10 face is roughly parallel to the map surface in the analyzed keplerite grain (denoted by "Merrillite Xie").

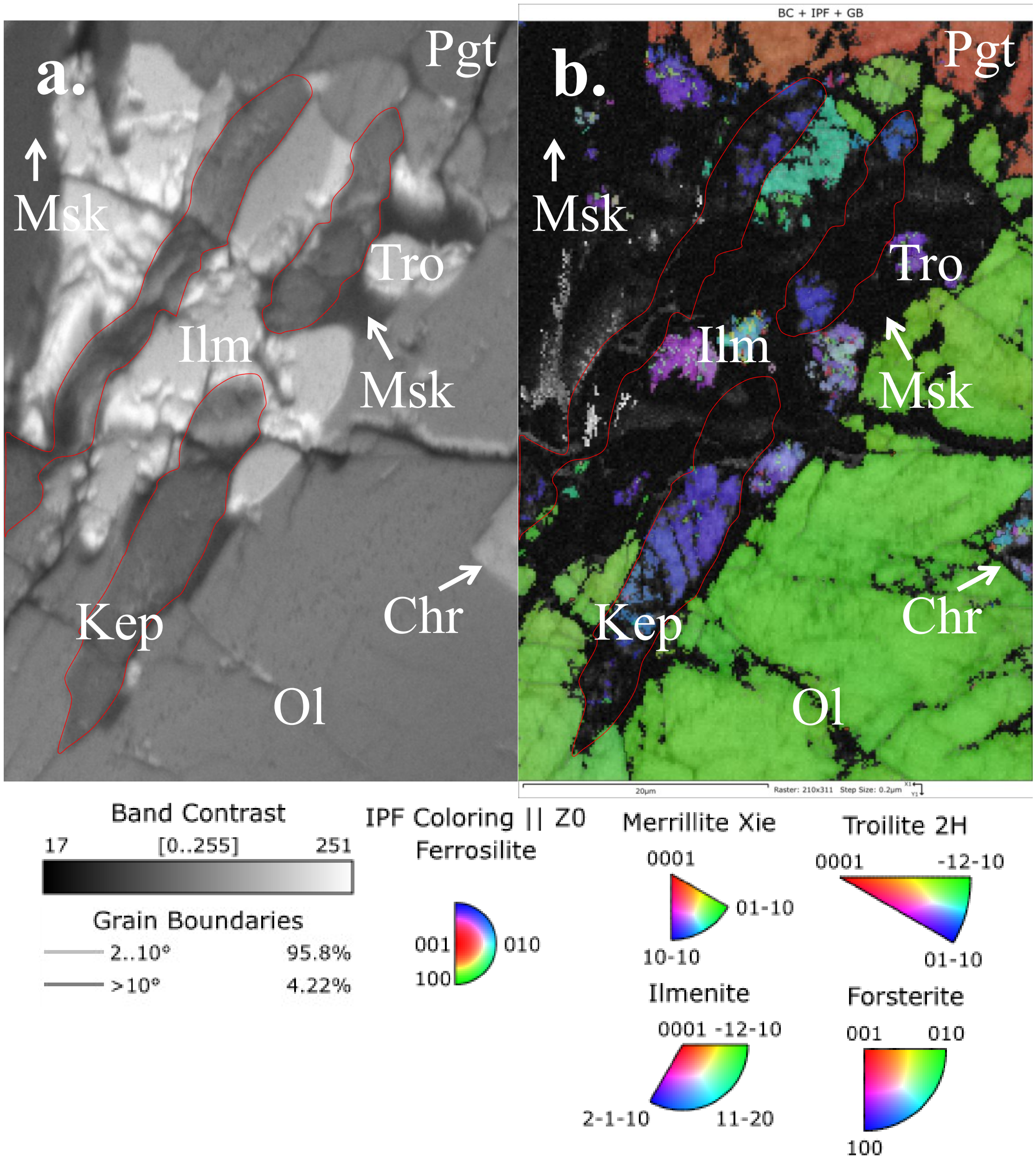

Figure 41. Backscattered electron (BSE) image and inverse pole figure (IPF) z-scheme (i.e., IPF map relative to the z direction of the image) of keplerite grain #2 in Tissint. Keplerite grain analyzed outlined in red. Note that the 10-10 face is roughly parallel to the map surface in the analyzed keplerite grain (denoted by "Merrillite Xie").

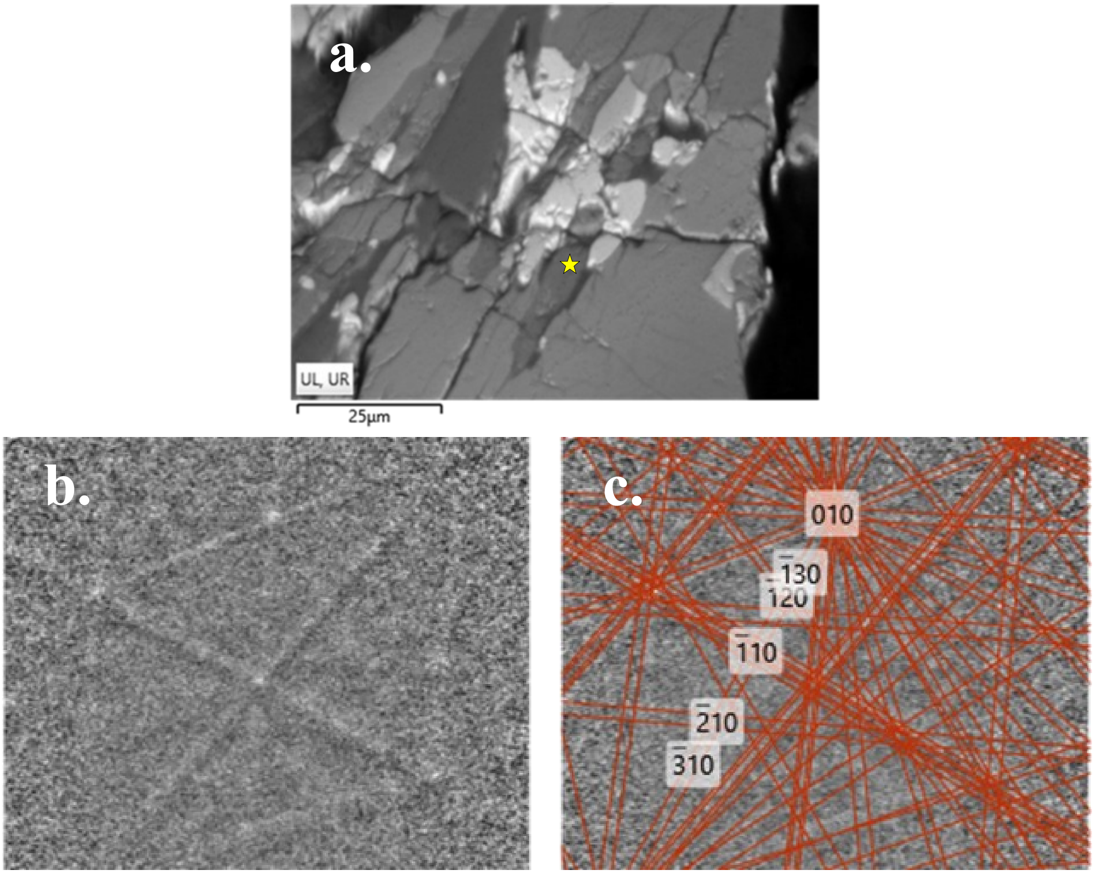

Figure 42. Backscattered electron (BSE) image and electron backscatter patterns (EBSPs) of keplerite grain #2 in Tissint. (a) BSE image of keplerite grain #2. (b) EBSP of keplerite grain #2. (c) Kikuchi bands and associated crystallographic planes superimposed on EBSP of keplerite grain #2. Yellow star denotes the location of spot analysis. Kikuchi bands are geometrical projections of crystal lattice planes.

4.2 Discussion

Through combined geochemical and structural characterization, phosphate phases in Tissint were found to have 1) compositions typical of Tissint phosphates, 2) crystal structures analogous to merrillite-subgroup members, 3) sodium deficiencies relative to that of ideal merrillite compositions ($Ca_9NaMg(PO_4)_7$), and 4) sodium deficiencies relative to merrillite-subgroup members of other meteorite groups.

As can be expected for minerals which are members of a solid-solution series, a range in measured phosphate compositions was documented in Tissint (e.g., Na_2O ranged from 0.29 to 0.98 wt%) (Supplementary Table 4). Analyzed grains were found to be moderately heterogeneous; the average sodium content of all analyzed grains was 0.61 wt% for Na_2O ($1\sigma = 0.19$, $n = 35$). However so, individual phosphate grains were generally found to be homogenous at the mineral-scale. Further, no chemical zoning was found in any of the analyzed phosphate grains (Figure 34 and Figure 35). Although shock-melt zones were not observed in this study, their influence on phosphate chemistry should not be discounted (Liu et al., 2018). Note Appendix for element-specific WDS maps.

All analyzed phosphate phases contained considerably less sodium in their structure when compared to end-member merrillite. Ideally, merrillite should accommodate 1.0 formula unit of sodium in its crystal structure for every 28 oxygens present (Xie et al., 2015). At most, the highest measured (Tissint phosphate) Na content was found to be 0.98 wt%, which corresponds to 0.34 formula units of sodium (Supplementary Table 10). Therefore, even at the highest measured value, phosphates analyzed in this study contain far too little sodium to satisfy end-member merrillite compositions.

This deficiency in sodium is reflected in the Na# as well, which was averaged at 2.32 for all analyzed phosphate grains (Table 4). When compared to end-member merrillite (which is described by an Na# of 10), it is quite clear that an intermediate merrillite-keplerite phase is present in Tissint. The following additional qualifiers are suggested to be used in conjunction with Na# to better describe intermediate merrillite-keplerite phases:

- <u>End-member keplerite</u>: for Na-number = 0.00.
- <u>Low-Na keplerite</u>: for Na-numbers between 0.01 and 2.50
- <u>High-Na keplerite</u>: for Na-numbers between 2.51 and 5.00
- <u>Low-Na merrillite</u>: for Na-numbers between 5.01 and 7.50
- <u>High-Na merrillite</u>: for Na-numbers between 7.51 and 9.99
- <u>End-member merrillite</u>: for Na-number = 10.00.

An example of the proposed Keplerite-Merrillite classification system can be given from the results of this study. The lowest Na_2O content measured in analyzed phosphates was 0.29 wt%, while the highest measured at 0.98 wt%. Using these data (along with associated chemical data; CaO, FeO, P_2O_5 wt%, etc.), normalized formula amounts (i.e., atoms per formula unit) can be calculated and then applied to the Na# equation: ($[Na_{atomic}/(Na_{atomic}+Ca_{atmoic})]*100$) (Supplementary Table 9; Supplementary Table 10).

At the lowest, sodium contents measured (0.29 wt% Na_2O), 0.10 Na atoms and 9.09 Ca atoms in analyzed grains (i.e., Point 22). Therefore, using these data the Na# is $[Na_{0.10}/(Na_{0.10}+Ca_{9.09})]*100 = 1.01$. At the highest, sodium content measured (0.98 wt% Na_2O), 0.34 Na atoms and 8.91 Ca atoms in analyzed grains (i.e., Point 210). Therefore, using these data the Na# is $[Na_{0.34}/(Na_{0.34}+Ca_{8.91})]*100 = 3.68$. At an average Na# of 2.32 (Table 4), low-end Na# of 1.01, and high-end Na# of 3.68, phosphates in Tissint were found to be generally composed of low-Na keplerite, however a few high-Na keplerite grains were found to occur as well (Supplementary Table 4). It should be noted that incorporation of sodium into the crystal structure of Tissint phosphates should be expected, simply given their occurrence with late-stage, Na-rich phases, such as maskelynite (i.e., feldspathic glass, $(Na,Ca)[(Si,Al)AlSi_2]O_8)$) (e.g., Figure 34 and Figure 35).

Likewise, Mg#, $[Mg_{atomic}/(Mg_{atomic}+Fe_{atmoic})]*100$, extrema can be calculated as well. At the lowest, magnesium contents measured (2.57 wt% MgO), 0.70 Mg atoms, 0.45 Fe atoms, and 0.16 Na atoms in analyzed grains (i.e., Point 15). Therefore, using these data the Mg# is $[Mg_{0.70}/(Mg_{0.70}+Fe_{0.45})]*100 = 60.87$ (Supplementary Table 11). At the highest, magnesium contents measured (3.32 wt% MgO), 0.90 Mg atoms, 0.27 Fe atoms, and 0.23 Na atoms in analyzed grains (i.e., Point 211) (Supplementary Table 12). Therefore, using these data the Mg# is $[Mg_{0.90}/(Mg_{0.90}+Fe_{0.27})]*100 = 76.9$. The average for the 35 analyzed points in Tissint were found to have Mg# = 63.2 with 0.21 Na atoms and 0.02 Mn atoms (per 28 O) (Table 4).

When these data are compared to the olivine-phyric phosphates of Liu et al. (2016) and the Martian phosphates of Shearer et al. (2015), it was found that all phosphates analyzed in this study exhibited chemical compositions typical of Tissint (Figure 12) with notable deficiencies in Na_2O contents when compared to phosphates in other meteorite groups (Figure 13). Additionally, when considering site-specific occupancies, analyzed phosphate grains in Tissint were found to contain excess calcium (i.e., 9.3 atoms) relative to ideal merrillite compositions (i.e., 9.0 atoms; $Ca_9NaMg(PO_4)_7$) (Table 4).

Raman spectra collected of Tissint phosphate grains also reflect intermediate merrillite–keplerite characteristics. Overall, spectra collected in this study were found to be in close approximation to the meteoritic keplerite grains analyzed in Britvin et al. (2021) (e.g., Figure 23, Figure 24). The most robust similarity between this study and that of Britvin et al. (2021) is the presence of visually-resolved shoulders and associated peak-width-broadening in all collected Raman spectra (e.g., Figure 37, Figure 39). An important note to be made here is that such visually-resolved shoulders (i.e., located at 950 and 958 cm^{-1}) have not been reported in earlier works for end-member merrillite (Britvin et al., 2021; Xie et al., 2015). As such, the presence of these additional bands further supports the presence of intermediate merrillite-keplerite phases in Tissint.

As is discussed by Britvin et al. (2021), peak width-broadening in keplerite may be attributed to phase-specific structural distortions associated with the selective bonding of $[PO_4]$ tetrahedra to the half-occupied B-site of the crystal system (Figure 10). In a more general sense, peak-width broadening of Raman spectra could also be caused by (1) general compositional variations in minerals (e.g., ionic substitutions), and (2) analyzing internally damaged minerals that have undergone shock-metamorphic alterations (e.g., due to shock-compression and mechanical stress) (Ruschel et al., 2012; Zhang et al., 2018).

The widened peaks measured in Tissint could provide diagnostic phase-specific information. The distinction between end-member merrillite and end-member keplerite can be made by taking note of two unique spectral signatures recorded in Tissint Raman spectra. First, Tissint phosphate-phase spectra recorded the presence of a visually resolved shoulder occurring between the frequencies of 950 and 958 cm^{-1}; these frequencies noted describe the shoulder locations of end-member keplerite (Britvin et al., 2021). The occurrence of a shoulder in the correct spectral range (for all measured spectra) indicates that the phosphate phase identified in Tissint is likely keplerite. Second, although collected Tissint spectra are in agreement with the general spectral properties of keplerite-type phases (e.g., observable shoulder), they do not adequately describe end-member keplerite (i.e., analyzed Tissint phosphates have additional bands at 947.5, 952.0, and 955.7 cm^{-1}). These data do, however, indicate that compositional variation in minerals (e.g., merrillite-keplerite solid solution series) can cause unique spectral signals to result in intermediate phases (e.g., peak-broadening); as was observed in Tissint phosphates. The occurrence of a skewed shoulder in the approximate spectral range then indicates that the phosphate phase identified in Tissint is actually of intermediate merrillite-keplerite composition. Therefore, Raman spectroscopic techniques explored through this study proved useful as a method to distinguish between minerals of the merrillite-keplerite solid solution series.

Along with the aforementioned geochemical and spectral analyses, a structural analysis of phosphate grains in Tissint was conducted as well by collecting inverse pole figures (IPFs) and electron backscatter patterns (EBSPs). IPFs and diffraction patterns were collected as they provide information specific to the crystallographic orientation of individual mineral grains (Černok et al., 2019). All orientation maps and diffraction patterns produced were in good agreement with one another (i.e., data were consistent between mineral grains). Orientation maps demonstrate a preference for both keplerite grains to align with the 10-10 plane. As anticipated, all keplerite grains analyzed exhibited a merrillite-type crystal structure (i.e., note Figure 17 and Figure 42). Further distinctions between merrillite and keplerite in collected EBSP data were not observed.

4.3 Implications

It is important to stay up-to-date with current nomenclature and classification schemes, as it allows for comprehensive communication between communities. As discussed, though keplerite is not a newly discovered mineral, it is a newly defined mineral. As a result of its novelty, there exists within the literature several key examples where keplerite (particularly end-member keplerite) likely existed, instead of merrillite. These examples are explored further to illustrate the implications of having a keplerite-bearing rock.

Keplerite presence in Tissint may provide insight to the conditions that might have existed at the time of phosphate crystallization (e.g., Udry et al. (2020); Figure 5). As was demonstrated by Adcock et al. (2014), stoichiometric keplerite (i.e., $Ca_{9.4}Mg_{1.1}(PO_4)_{7.0}$) was produced through the devolatilization of whitlockite (i.e., heating of whitlockite to ~1,000 ˚C). Further, the shock experiments of Adcock et al. (2017) demonstrated that the likely driver of phosphate transformation from OH-rich (e.g., whitlockite) to OH-poor phases (e.g., keplerite) is facilitated by extreme, localized, temperature spikes. These formation conditions (i.e., punctuated heating events) are consistent with the proposed formation environment of keplerite (Britvin et al., 2021). This is important considering that merrillite subgroup minerals are late-stage, volatile-rich, phases that are often used to estimate the volatile histories of magmas (Baziotis et al., 2013). Therefore, rocks which contain end-member keplerite may have originally formed in volatile-rich, hydrous environments, if shock-transformed from whitlockite (Adcock et al., 2017).

Further, if it is indeed keplerite that forms as a result of shock-related processes and not merrillite, then Na-deficiencies in analyzed Tissint grains are to be expected as keplerite itself is a Na-free mineral. However, due to its association with other late-stage phases that are Na-rich (e.g., maskelynite; Figure 34 and Figure 35), it is also not surprising that analyzed keplerite grains in Tissint accommodated variable amounts of sodium (Table 4). Additionally, chemical zonation of sodium in intermediate merrillite-keplerite phases has been observed in grains which contact impact melt (i.e., a shock metamorphic feature) (Liu et al., 2018). Therefore, shock-metamorphic conditions (i.e., elevated temperatures) and features (e.g., impact melt) can cause geochemical variations in the merrillite-keplerite mineral series.

4.4 Conclusions

Keplerite is a newly recognized phosphate mineral that forms a solid solution with merrillite. Here we show the first documented occurrence of (low-Na) keplerite in Tissint. The presence of keplerite in Tissint suggests it likely common and occurs in broader range environments (i.e., meteorite groups) than initially established (Britvin et al., 2021). End-member keplerite may be produced through the devolatilization of whitlockite (Adcock et al., 2014). Formation of keplerite from whitlockite may then indicate the presence of a volatile-rich, hydrous, source environment for those rocks which contain keplerite-bearing mineral assemblages (Adcock et al., 2017). However, care must be taken when analyzing phosphate phases, as proximity to impact melt (i.e., shock-metamorphic features) can cause compositional zonation in the merrillite-keplerite mineral series (e.g., Liu et al., 2018).

CHAPTER 5:
ALH 84001

5.1 Results

A total of 11 phosphate grains were identified in ALH 84001: two grains of Cl-rich apatite, and 9 grains of merrillite. Backscattered electron (BSE) images of all identified grains can be seen in Figure 43. All phosphates identified in ALH 84001 were associated with interstitial plagioclase and/or orthopyroxene. Two of the merrillite grains were intergrown with apatite grains; specifically, merrillite mantles a core of apatite (Figure 43a-b). Merrillite-included apatite grains were approximately 40-50 microns in diameter. The other merrillite grains are single, discrete grains associated with orthopyroxene and interstitial plagioclase (Figure 43c-d). The merrillite grains are anhedral (and irregular) to euhedral and ranged in size from 10s of microns in length (or diameter) to 100s of microns in maximum dimension. No Na-deficient merrillite (i.e., keplerite) grains were identified.

Apatite and Merrillite Chemical Composition

All 9 identified merrillite grains were targeted for quantitative analysis and 95 individual points were collected (Supplementary Table 5). Further, both identified apatite grains were targeted for quantitative analysis as well; 13 individual points were collected (Supplementary Table 7). A comprehensive summary of apatite chemical composition data is given in Table 5, while merrillite chemical composition data is given in Table 6. Normalized formula amounts were calculated from measured oxide weight percentages. Datapoints which measured abnormal oxide concentrations (e.g., low phosphorus content, like 30 wt% P_2O_5) or total percentages (e.g., total wt% $\leq$98.5%) were excluded from calculations.

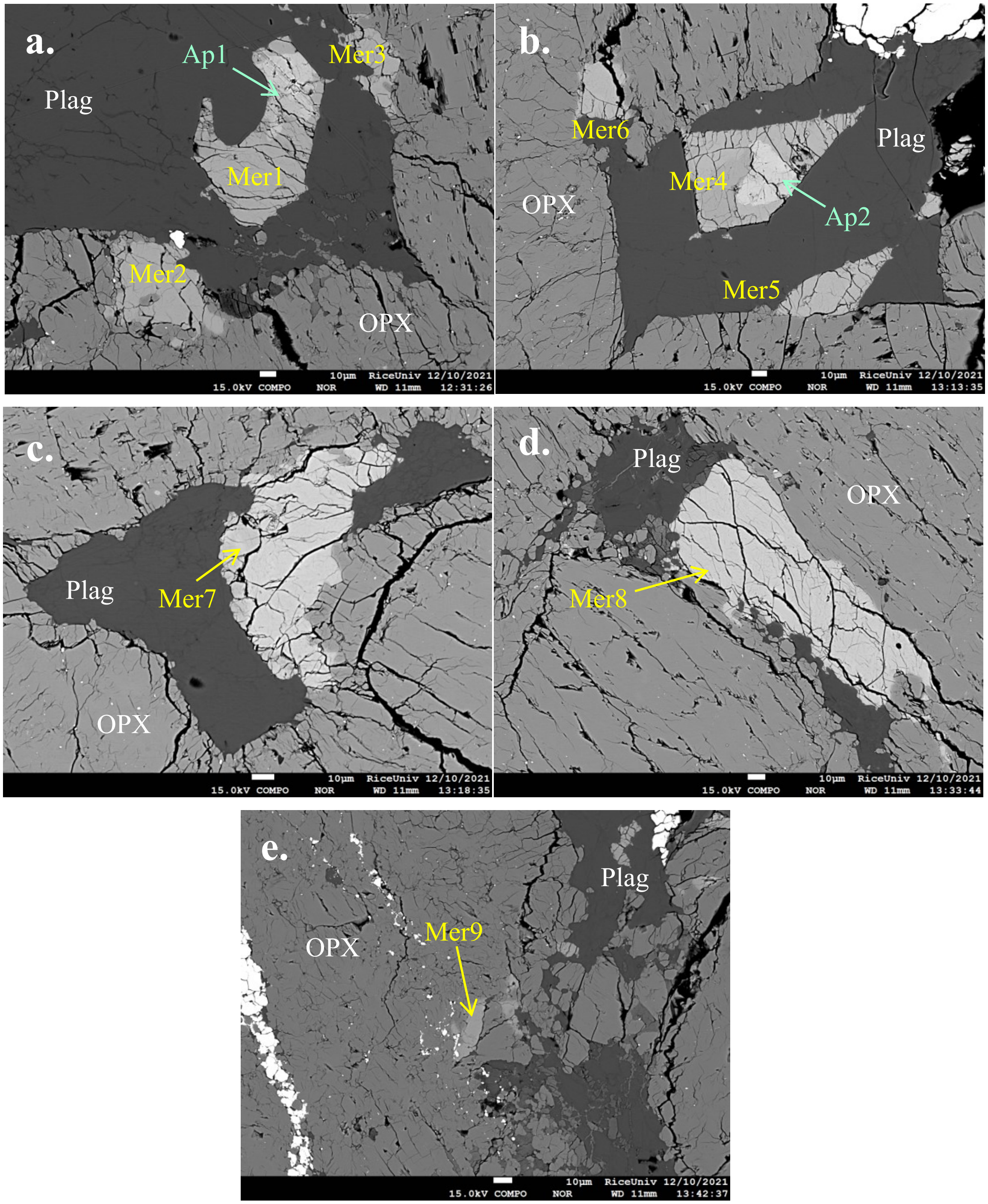

Figure 43. Backscattered electron (BSE) images of apatite grains #1-2 and merrillite grains #1-9 in ALH 84001. Mineral abbreviations: Plag = plagioclase; OPX = orthopyroxene; Ap = apatite; Mer = merrillite. Note intergrown apatite-merrillite textures and occurrence of phosphates with interstitial plagioclase and orthopyroxene. Scale bar is 10 µm in length. Note Figure 30 for location of analyzed points.

Table 5. Average chemical composition of apatite in ALH 84001.

Chemical composition of Apatite in ALH84001,146				
	wt%[a]	1σ[a]	To 8 cations	
Al_2O_3	0.04	0.06	Al	0.005
Ce_2O_3	0.02	0.02	Ce	0.001
La_2O_3	0.01	0.03	La	0.000
Nd_2O_3	0.11	0.13	Nd	0.003
FeO	0.17	0.05	Fe	0.012
MnO	0.03	0.02	Mn	0.002
MgO	0.03	0.01	Mg	0.004
CaO	53.79	0.61	Ca	4.911
Na_2O	0.26	0.04	Na	0.043
K_2O	0.01	0.01	K	0.001
P_2O_5	41.50	0.38	P	2.994
SiO_2	0.19	0.05	Si	0.016
SO_3	0.12	0.01	S	0.008
F	0.61	0.17	F	0.164
Cl	4.36	0.42	Cl	0.630
O=F,Cl	-1.24	0.11	Charge Sum	0.215
Total	**100.02**			

[a] Oxide concentrations; EPMA analyses by mass. Average of 13 analyses.

Ca-site	4.982	Includes: Al, Ce, La, Nd, Fe, Mn, Mg, Ca, Na, K
P-site	3.018	Includes: Si, P, S

Mg#	25.07	Mg ratio = 100 x Mg / (Mg + Fe)
Na#	0.88	Na ratio = 100 x Na / (Na + Ca)

Apatite Formula	$Ca_5(PO_4)_3(OH,F,Cl)$

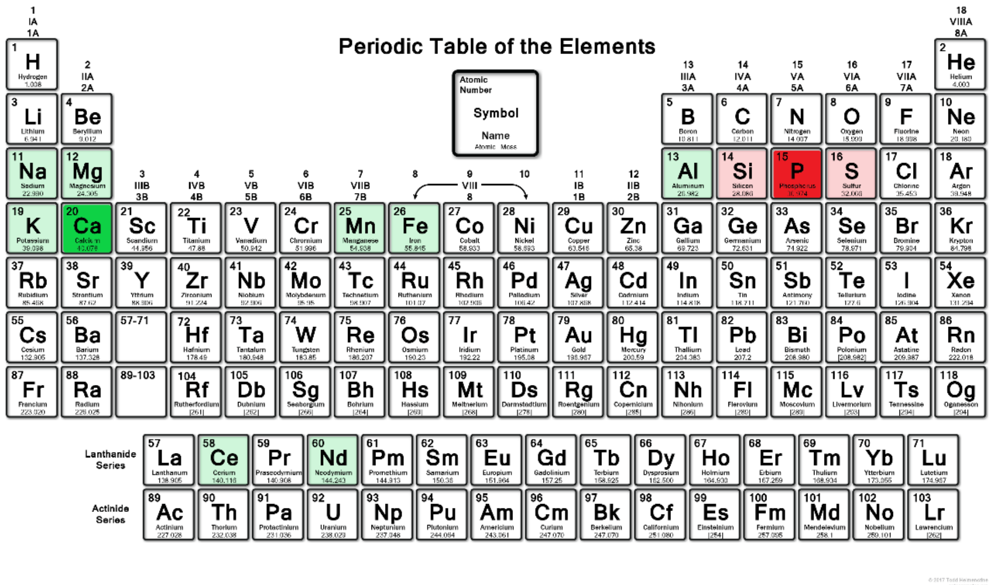

Figure 44. Periodic table of elements with Ca-Site (green) and P-site (red) assignments filled in for apatite. Source of periodic table: https://sciencenotes.org/. Data corresponds to Table 5. Opacity of colors varies with respect to relative abundances (i.e., 0.001 to 0.250 cations = 20% opacity; 0.251 to 0.500 cations = 40% opacity; 0.501 to 0.750 cations = 60% opacity; 0.751 to 1.000 cations = 80% opacity; >1.001 cations = 100% opacity).

Table 6. Average chemical composition of merrillite in ALH 84001.

Chemical composition of Merrillite in ALH84001,146				
	wt%[a]	1σ[a]	To 28 oxygens	
Al_2O_3	0.014	0.03	Al	0.003
Ce_2O_3	0.092	0.11	Ce	0.006
La_2O_3	0.094	0.18	La	0.006
Nd_2O_3	0.053	0.08	Nd	0.003
FeO	0.861	0.18	Fe	0.129
MnO	0.031	0.02	Mn	0.005
MgO	3.421	0.06	Mg	0.911
CaO	46.715	0.41	Ca	8.946
Na_2O	2.348	0.08	Na	0.814
K_2O	0.089	0.01	K	0.020
P_2O_5	46.399	0.38	P	7.021
SiO_2	0.026	0.12	Si	0.005
SO_3	0.009	0.01	S	0.001
F	0.000	0.00	F	0.000
Cl	0.004	0.00	Cl	0.001
O=F,Cl	-0.001	0.00		
Total	**100.155**			

[a] Oxide concentrations; EPMA analyses by mass. Average of 95 analyses.

Ca-site	8.966	Includes: La, Ca, Mn, Ce, Nd
Na-site	0.834	Includes: Na, K
Mg-site	1.040	Includes: Fe, Mg
P-site	7.026	Includes: Si, P, S

Mg#	87.62	Mg ratio = 100 x Mg / (Mg + Fe)
Na#	8.34	Na ratio = 100 x Na / (Na + Ca)

Merrillite Formula	$Ca_9NaMg(PO_4)_7$

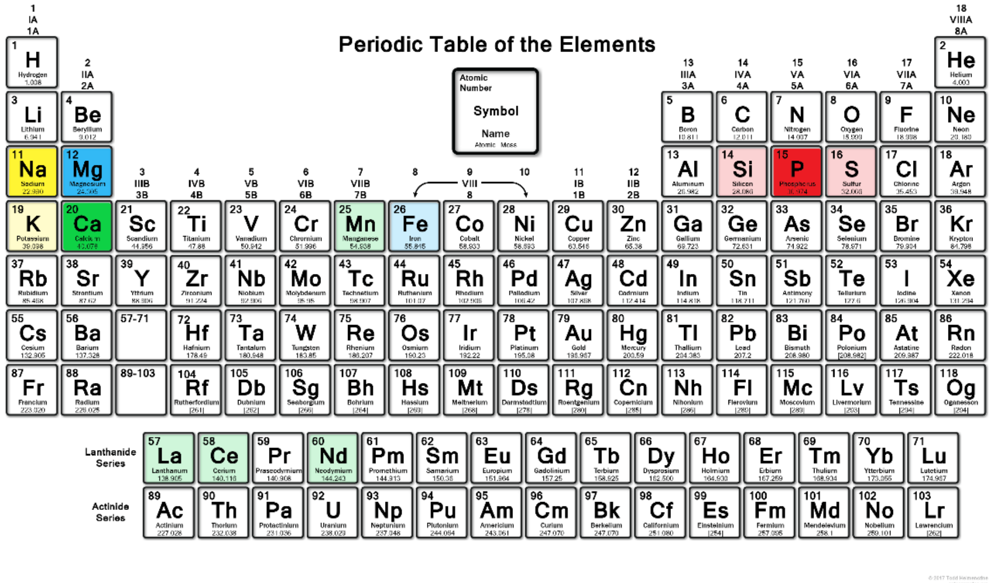

Figure 45. Periodic table of elements with Ca-Site (green), Na-site (yellow), Mg-site (blue), and P-site (red) assignments filled in for merrillite. Source of periodic table: https://sciencenotes.org/. Data corresponds to Table 6. Opacity of colors varies with respect to relative abundances (i.e., 0.001 to 0.250 cations = 20% opacity; 0.251 to 0.500 cations = 40% opacity; 0.501 to 0.750 cations = 60% opacity; 0.751 to 1.000 cations = 80% opacity; >1.001 cations = 100% opacity).

Quantitative Wavelength Dispersive Spectrometry (WDS) element map distributions of the apatite- and merrillite-bearing assemblages of ALH 84001 can be seen in Figure 46, Figure 47, and Figure 48. WDS element maps were generated for Na, Ca, Cl, F, S, Si, K, Fe, Mg, and P. Moderate Cl enrichments were observed to occur in some apatite grains (e.g., Figure 47) but not others (e.g., Figure 46). Further, isolated merrillite grains show evidence of chemical mobility; Cl-rich mineral grain fractures were observed (e.g., Figure 48). Slight chemical zoning can be seen in plagioclase (e.g., note K element map of Figure 48).

An example of homogenous mineral-assemblages can be seen in the WDS element maps of Na, Cl, and F of apatite and merrillite grains #1-3 (Figure 50, Figure 51, and Figure 52, respectively). An example of heterogenous mineral-assemblages can be seen in the WDS element maps of Na, Cl, and F of apatite and merrillite grains #4-6 (Figure 54, Figure 55, and Figure 56, respectively). Lastly, an example of selective mineral-grain enrichments be seen in the WDS element maps of Na, Cl, and F in merrillite grain #8 (Figure 58, Figure 59, and Figure 60, respectively). Note Appendix for supplementary element-specific WDS maps.

Overall, however, apatite and merrillite grains were found to be largely homogenous in composition (Table 5 and Table 6). To compare chemistries with the keplerite-bearing assemblages of Tissint, weight percentages (wt%) of select oxides for analyzed ALH 84001 merrillite grains are given. Na_2O contents ranged from 2.15 to 2.50 wt%; average = 2.35 wt% ($1\sigma = 0.08$). CaO contents ranged from 45.00 to 47.48 wt%; average = 46.72 wt% ($1\sigma = 0.41$). MgO contents ranged from 3.30 to 3.83 wt%; average = 3.42 wt% ($1\sigma = 0.06$). P_2O_5 contents ranged from 44.51 to 47.03 wt%; average = 46.40 wt% ($1\sigma = 0.38$) (Supplementary Table 5). When compared to average Tissint phosphate compositions, ALH 84001 phosphates are enriched in sodium and magnesium.

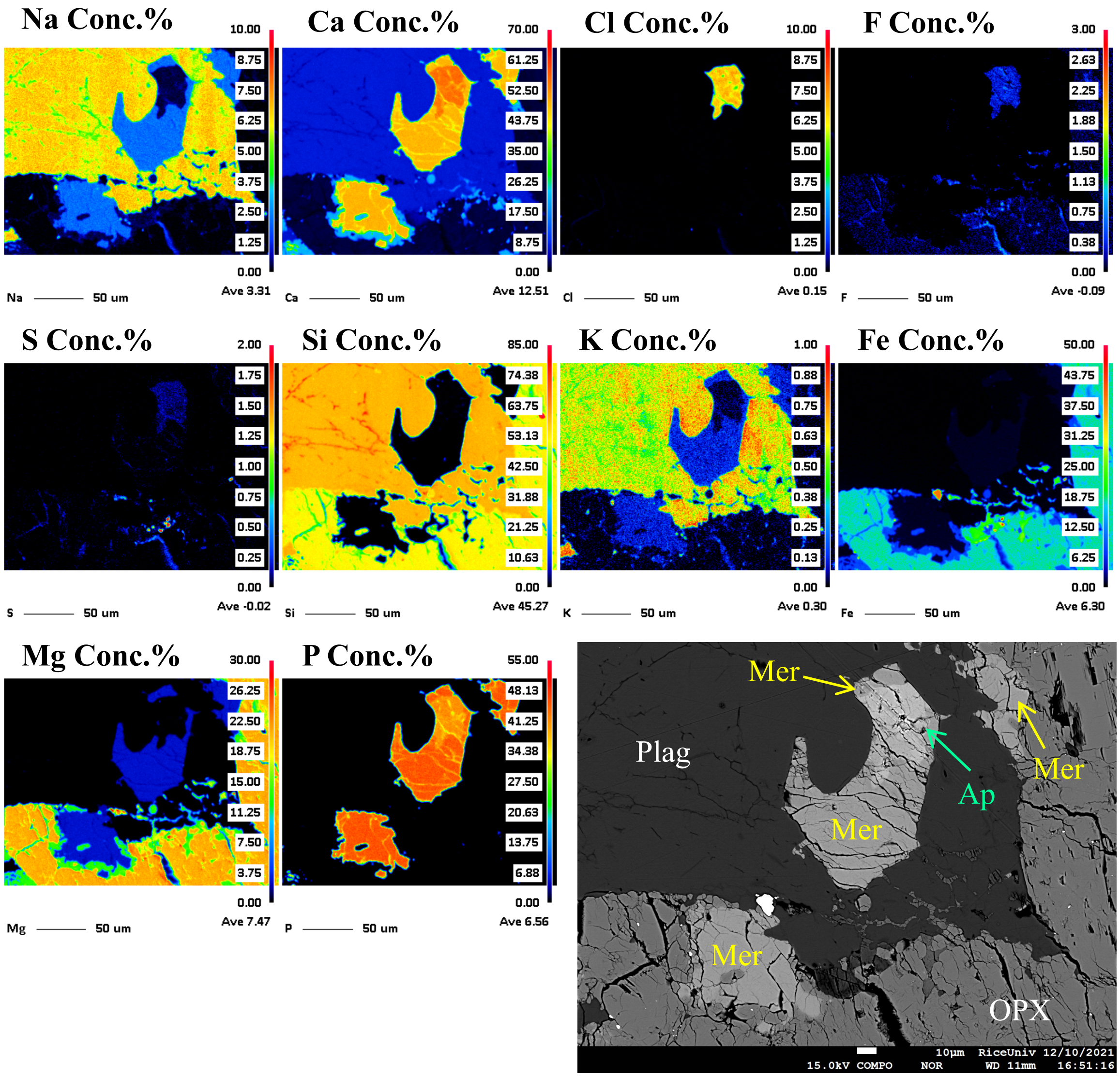

Figure 46. Quantitative WDS (Wavelength Dispersive Spectrometry) element map distribution and BSE (BackScattered Electron) image of apatite-merrillite intergrown grains #1-3 in ALH 84001. WDS element maps illustrate elemental distributions in phosphates and surrounding phases; maps are given in weight percent (wt%). WDS element maps correspond to BSE image in the bottom right-hand corner. Mineral abbreviations: Plag = plagioclase; Mer = merrillite; Ap = apatite; OPX = orthopyroxene. Note intergrown texture between apatite and merrillite (i.e., merrillite overgrowths on apatite grains) and highly fractured mineral grains. Scale bar is 10 µm in length.

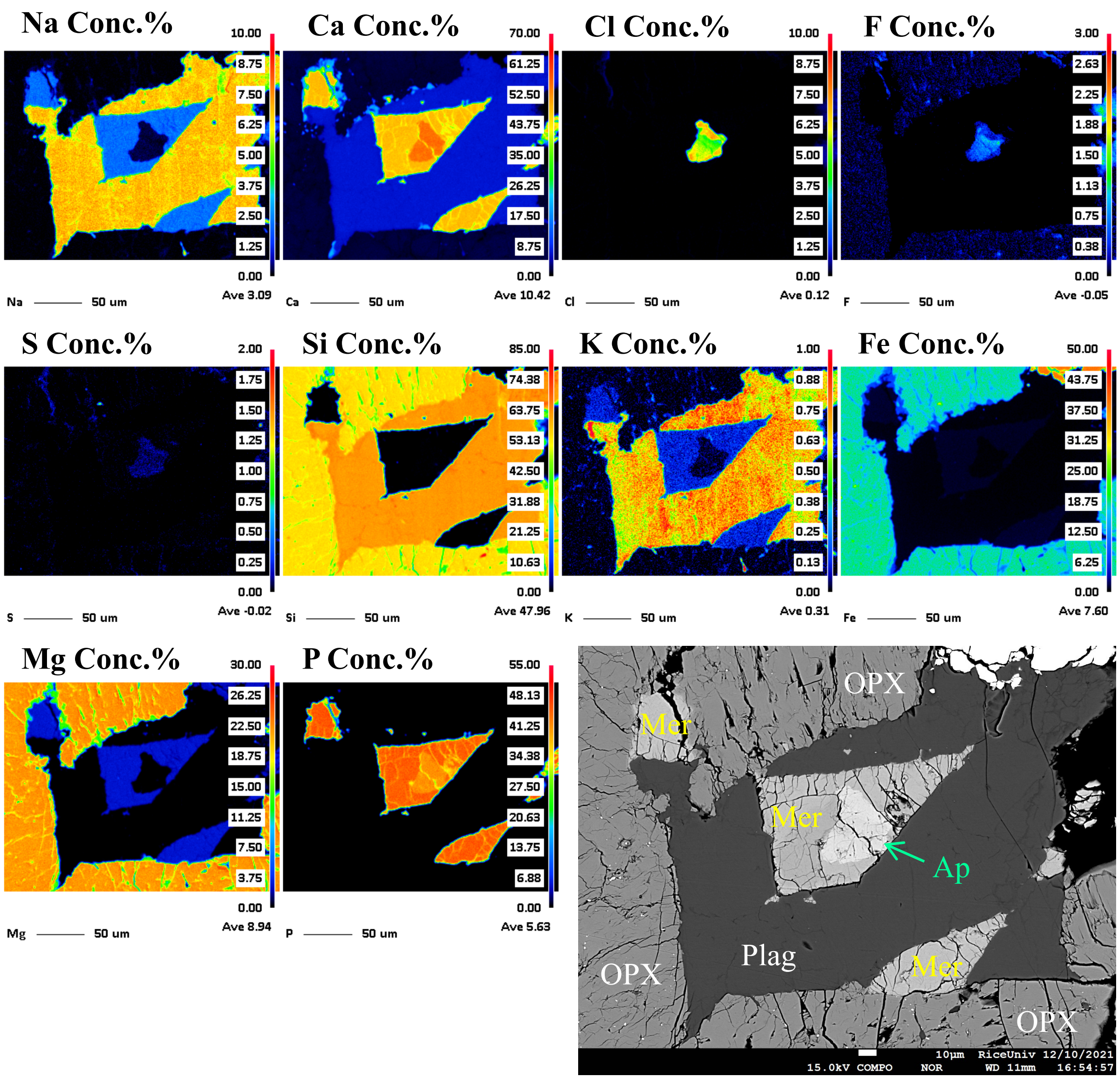

Figure 47. Quantitative WDS (Wavelength Dispersive Spectrometry) element map distribution and BSE (BackScattered Electron) image of apatite-merrillite intergrown grains #4-6 in ALH 84001. WDS element maps illustrate elemental distributions in phosphates and surrounding phases; maps are given in weight percent (wt%). WDS element maps correspond to BSE image in the bottom right-hand corner. Mineral abbreviations: Plag = plagioclase; Mer = merrillite; Ap = apatite; OPX = orthopyroxene. Note intergrown texture between apatite and merrillite (i.e., merrillite overgrowths on apatite grains) and highly fractured mineral grains. Scale bar is 10 µm in length.

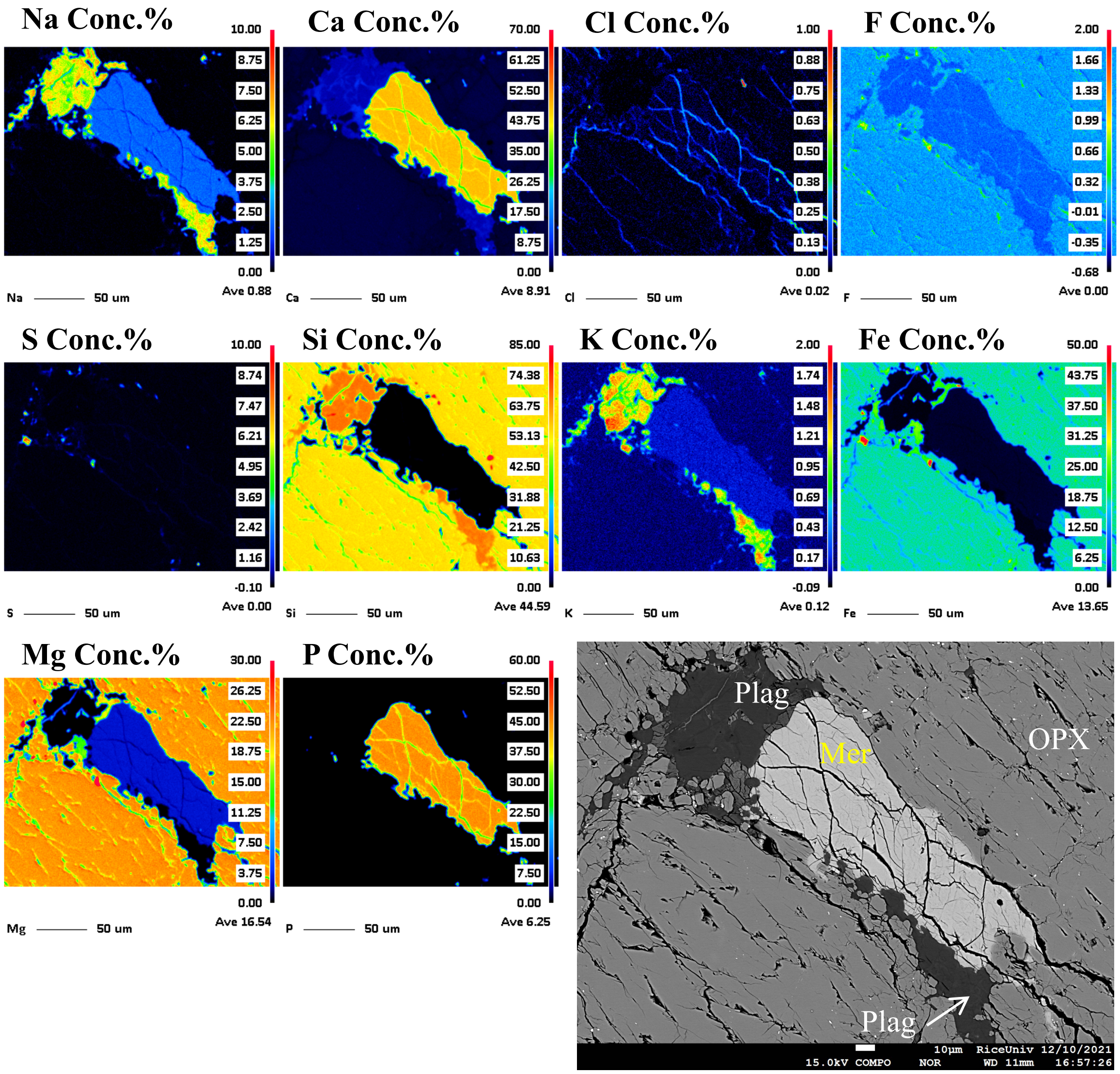

Figure 48. Quantitative WDS (Wavelength Dispersive Spectrometry) element map distribution and BSE (BackScattered Electron) image of isolated merrillite grain #8 in ALH 84001. WDS element maps illustrate elemental distributions in phosphates and surrounding phases; maps are given in weight percent (wt%). WDS element maps correspond to BSE image in the bottom right-hand corner. Mineral abbreviations: Plag = plagioclase; Mer = merrillite; OPX = orthopyroxene. Scale bar is 10 µm in length.

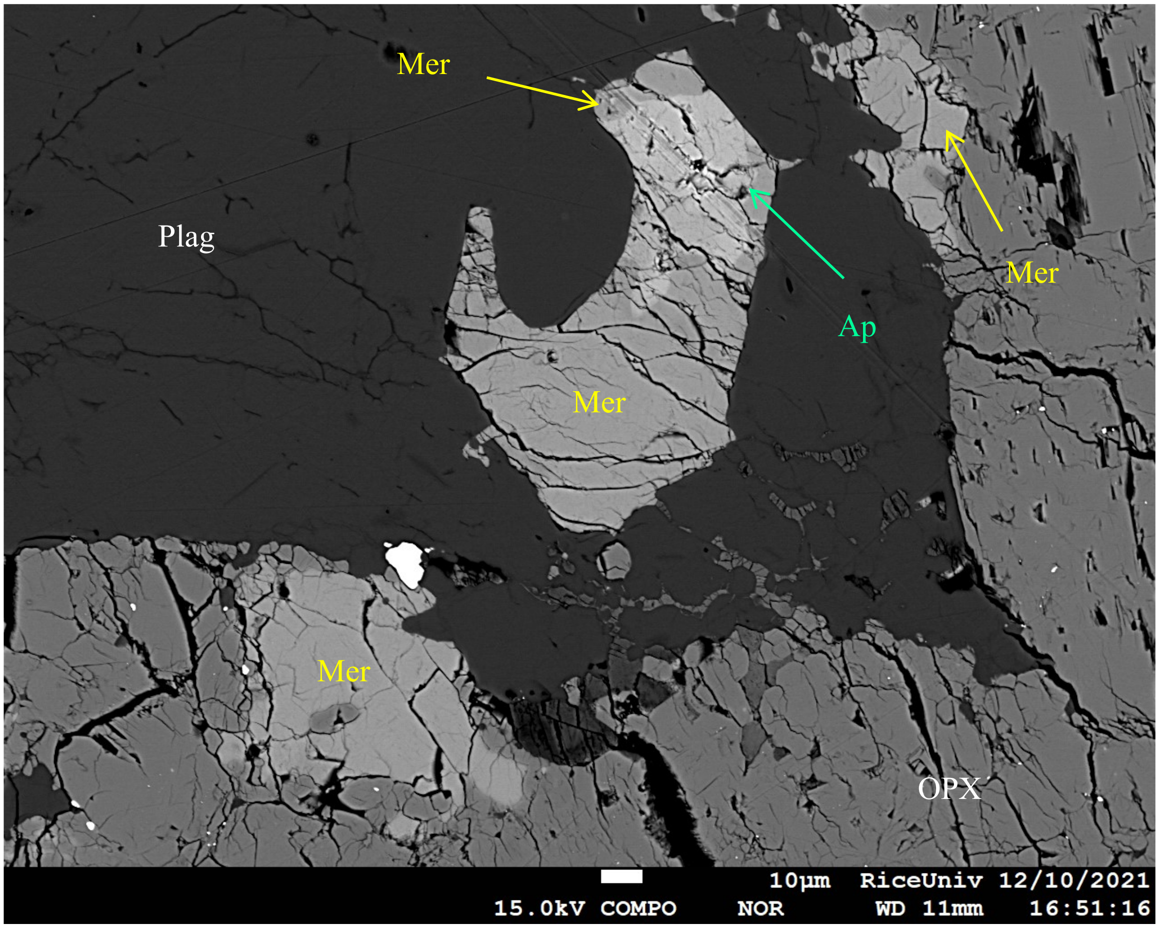

Figure 49. Detailed view of BSE (BackScattered Electron) image of apatite-merrillite intergrown grains #1-3 in ALH 84001. Mineral abbreviations: Plag = plagioclase; Mer = merrillite; Ap = apatite; OPX = orthopyroxene. Scale bar is 10 µm in length.

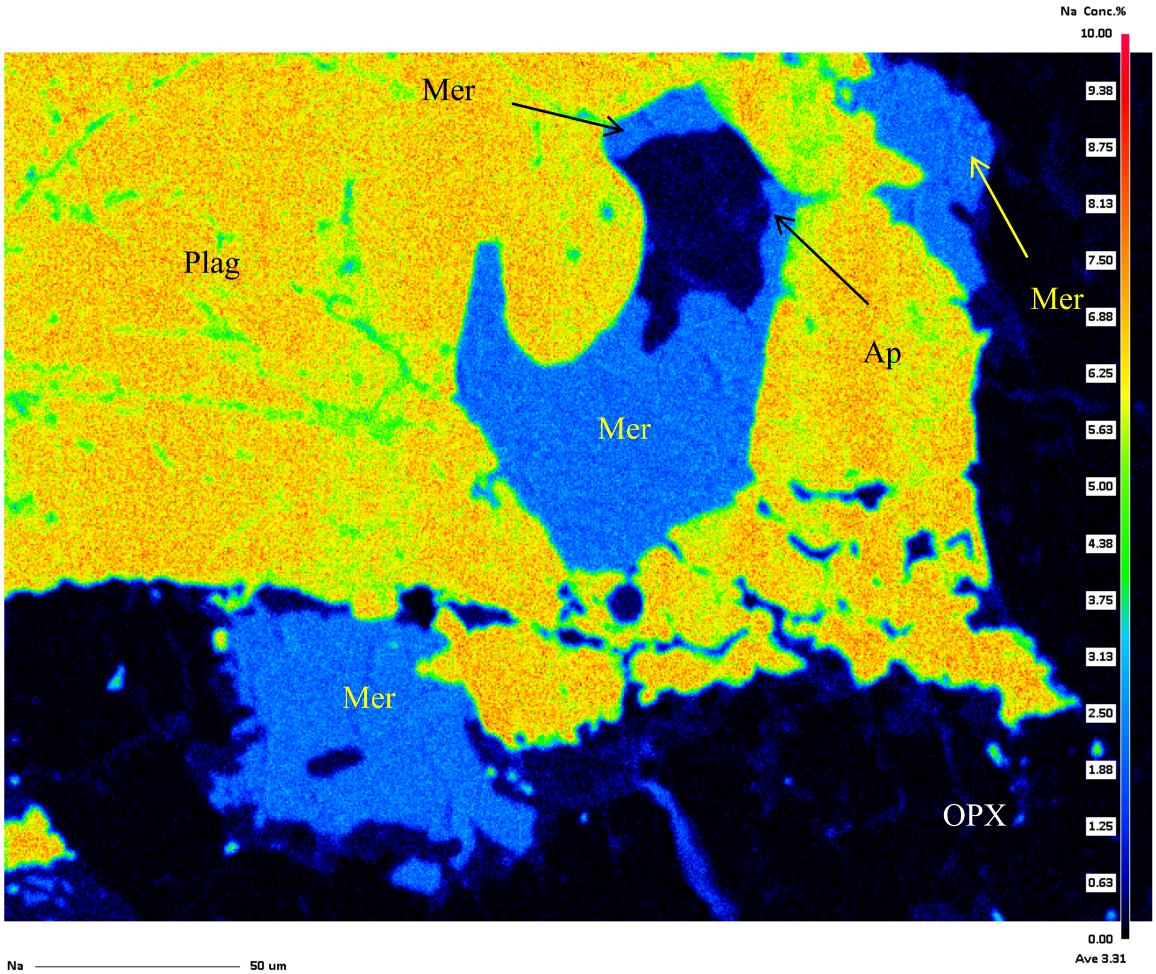

Figure 50. Quantitative WDS (Wavelength Dispersive Spectrometry) elemental map distribution of sodium (Na) in apatite-merrillite intergrown grains #1-3 in ALH 84001. WDS element maps are given in weight percent (wt%). WDS element maps correspond to BSE image from Figure 49. Plag = plagioclase; Mer = merrillite; Ap = apatite; OPX = orthopyroxene. Scale bar is 50 µm in length. Note that all minerals exhibit homogenous compositions (i.e., homogeneity based on low variance in chemical measurements).

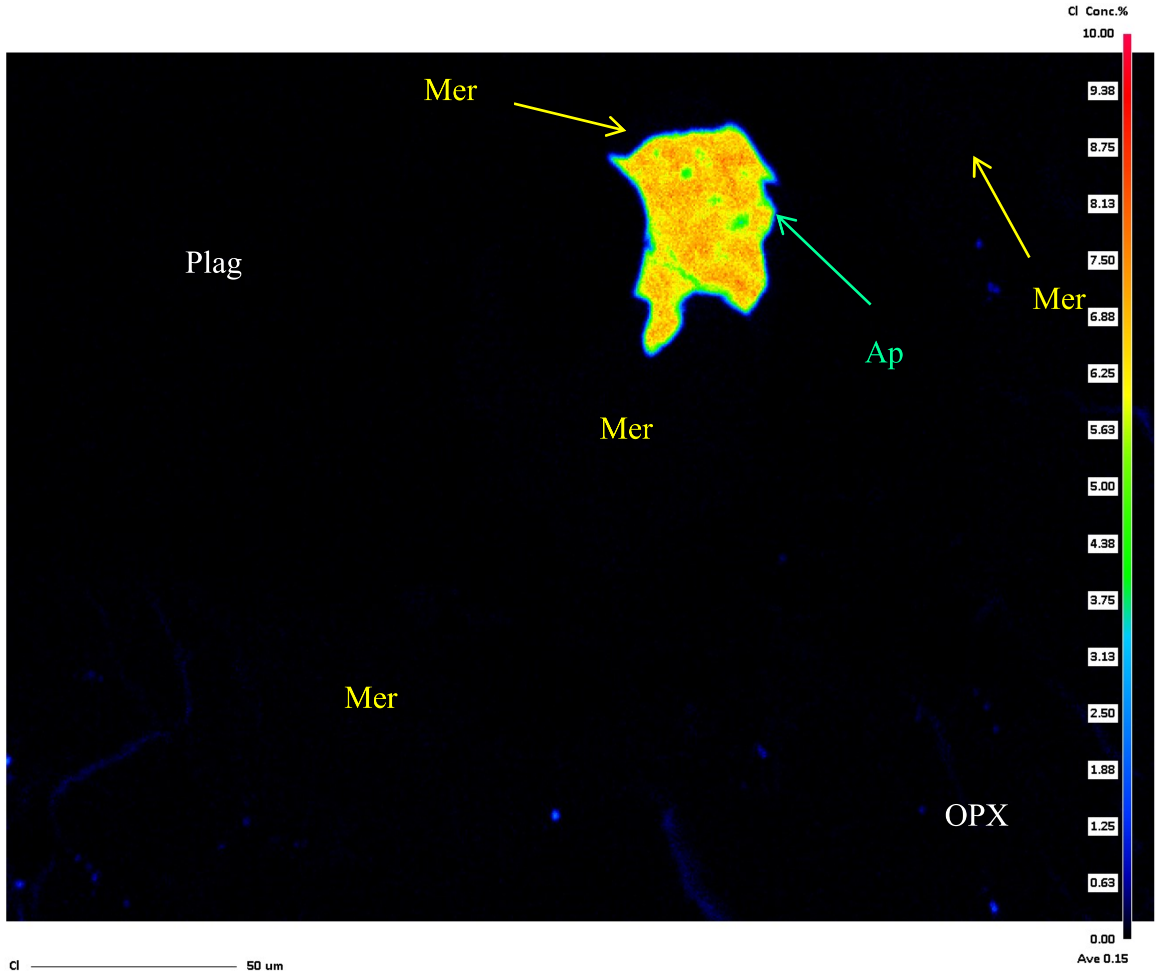

Figure 51. Quantitative WDS (Wavelength Dispersive Spectrometry) elemental map distribution of chlorine (Cl) in apatite-merrillite intergrown grains #1-3 in ALH 84001. WDS element maps are given in weight percent (wt%). WDS element maps correspond to BSE image from Figure 49. Plag = plagioclase; Mer = merrillite; Ap = apatite; OPX = orthopyroxene. Scale bar is 50 µm in length. Note that all minerals exhibit homogenous compositions.

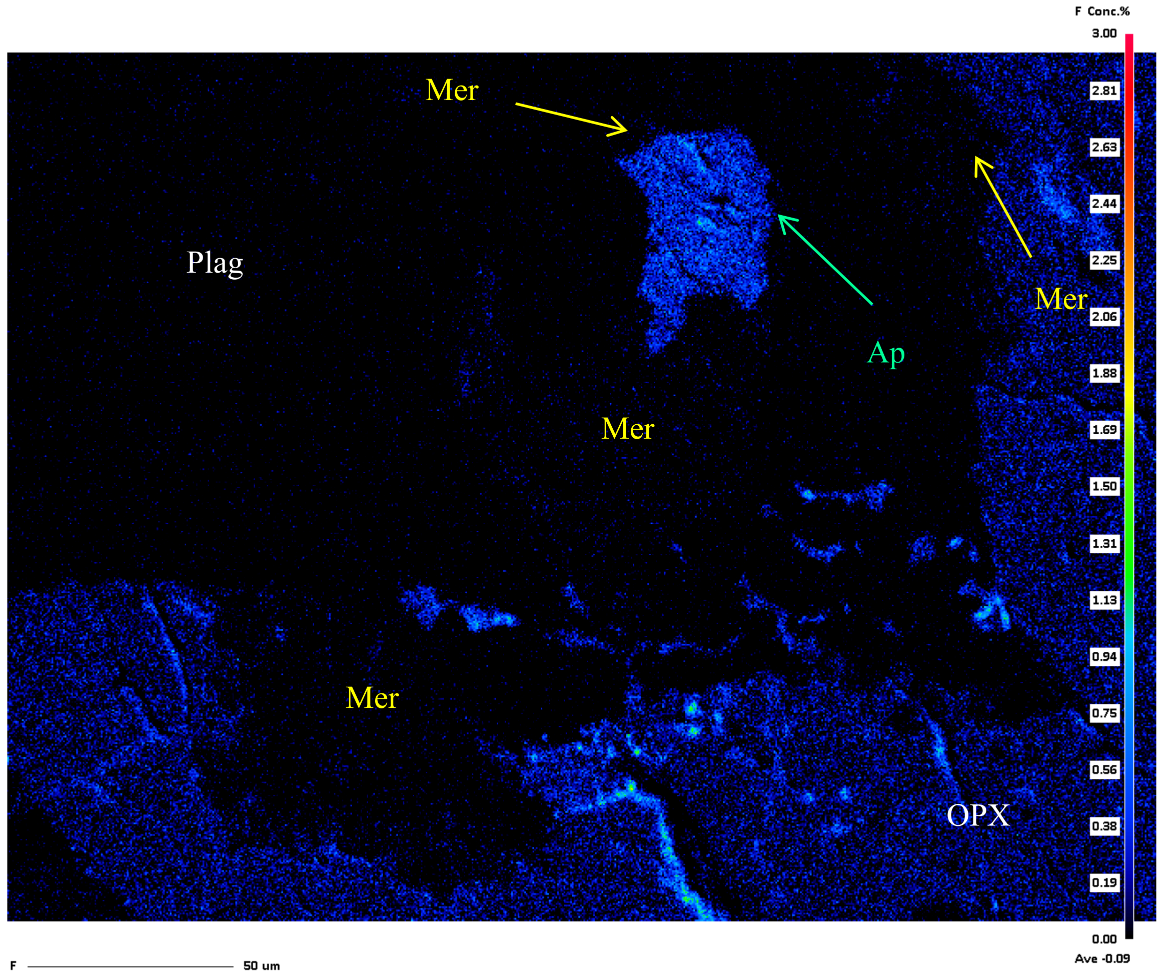

Figure 52. Quantitative WDS (Wavelength Dispersive Spectrometry) elemental map distribution of fluorine (F) in apatite-merrillite intergrown grains #1-3 in ALH 84001. WDS element maps are given in weight percent (wt%). WDS element maps correspond to BSE image from Figure 49. Plag = plagioclase; Mer = merrillite; Ap = apatite; OPX = orthopyroxene. Scale bar is 50 µm in length. Note that only apatite and orthopyroxene accommodate F incorporation. Although slight "*peaks*" is fluorine content is observed (i.e., bright patches), minerals shown here exhibit approximately homogenous compositions.

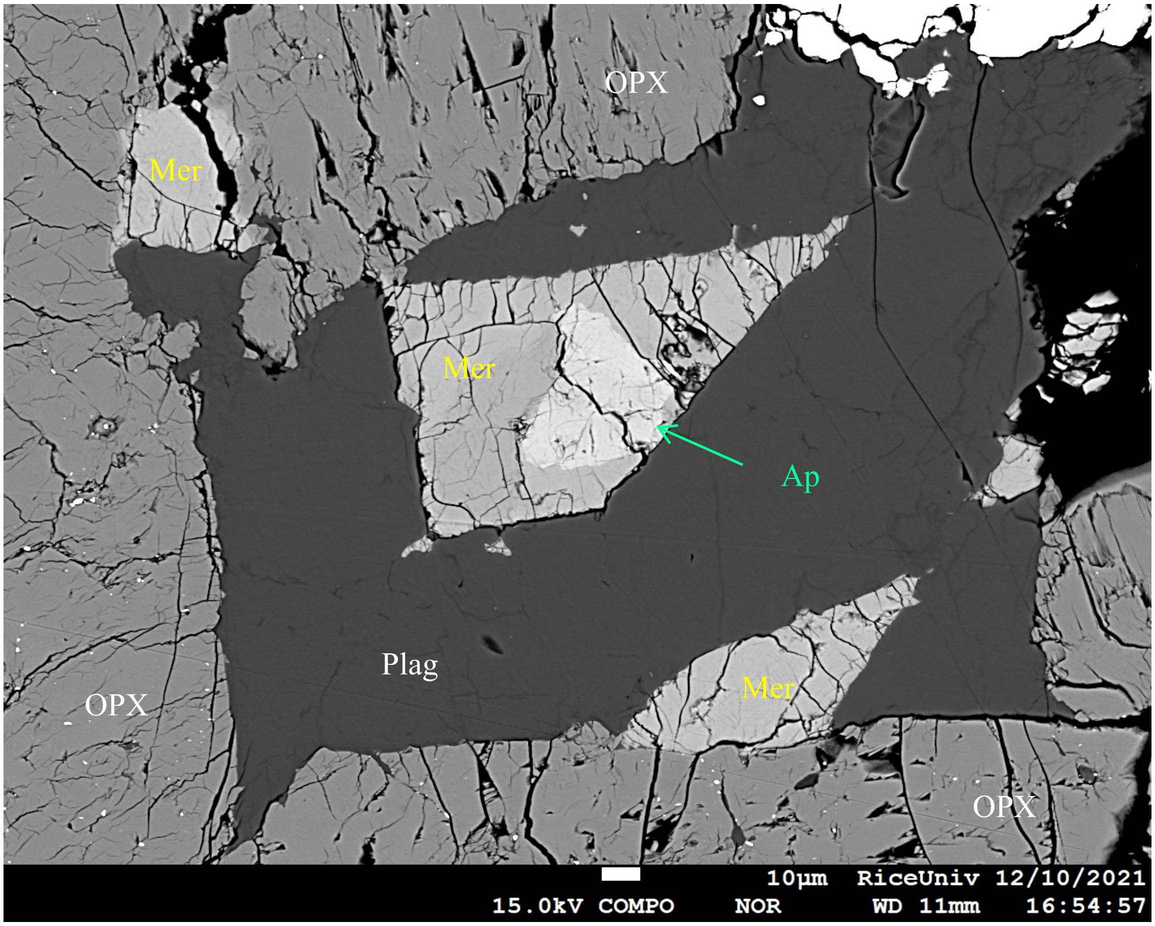

Figure 53. Detailed view of BSE (BackScattered Electron) image of apatite-merrillite intergrown grains #4-6 in ALH 84001. Mineral abbreviations: Plag = plagioclase; Mer = merrillite; Ap = apatite; OPX = orthopyroxene. Scale bar is 10 µm in length.

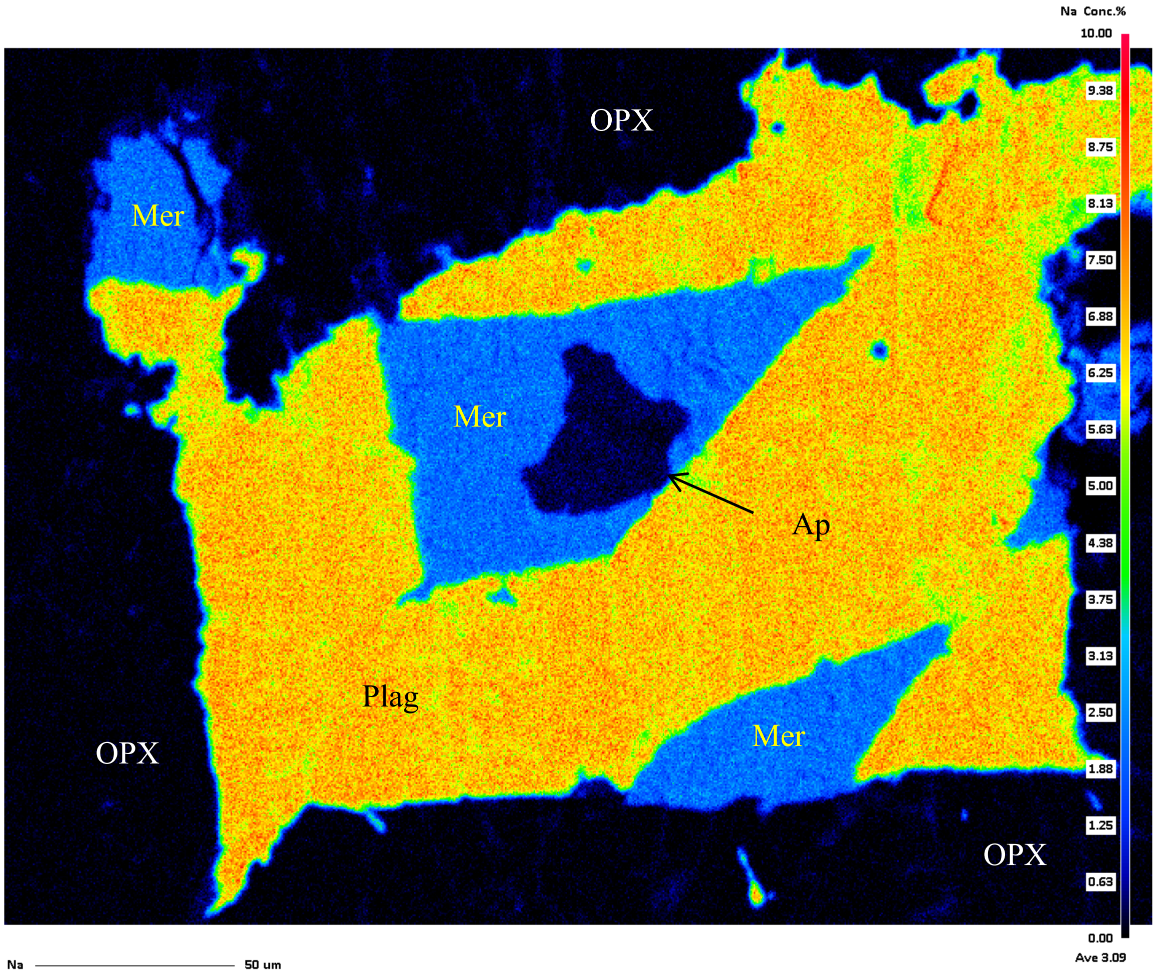

Figure 54. Quantitative WDS (Wavelength Dispersive Spectrometry) elemental map distribution of sodium (Na) in apatite-merrillite intergrown grains #4-6 in ALH 84001. WDS element maps are given in weight percent (wt%). WDS element maps correspond to BSE image from Figure 53. Plag = plagioclase; Mer = merrillite; Ap = apatite; OPX = orthopyroxene. Scale bar is 50 µm in length. Note that all minerals exhibit homogenous compositions.

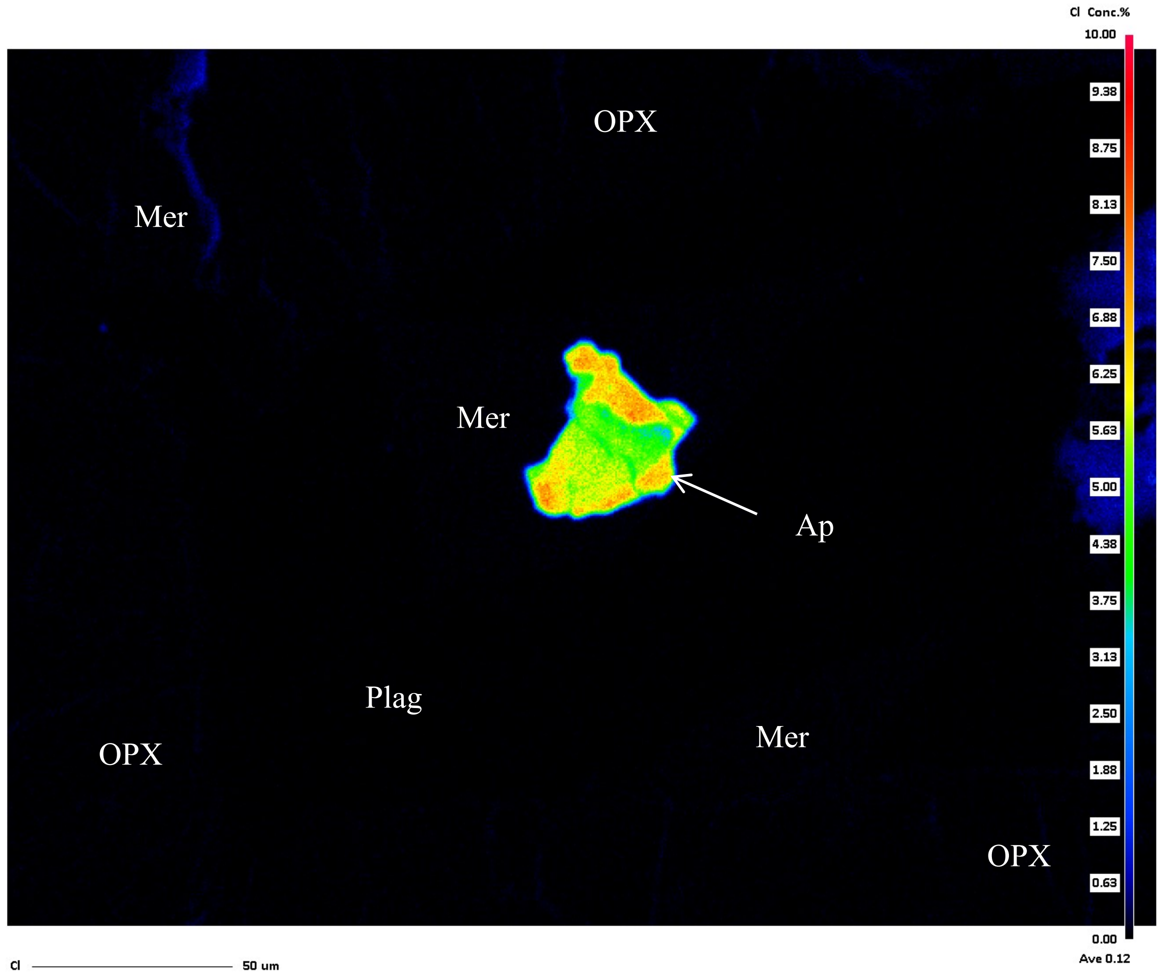

Figure 55. Quantitative WDS (Wavelength Dispersive Spectrometry) elemental map distribution of chlorine (Cl) in apatite-merrillite intergrown grains #4-6 in ALH 84001. WDS element maps are given in weight percent (wt%). WDS element maps correspond to BSE image from Figure 53. Plag = plagioclase; Mer = merrillite; Ap = apatite; OPX = orthopyroxene. Scale bar is 50 μm in length. Note heterogenous incorporation of chlorine into the apatite structure. There was no observed relationship between mineral fractures and variance in chemical composition (i.e., fractures were not associated with apparent loss or gain in chlorine).

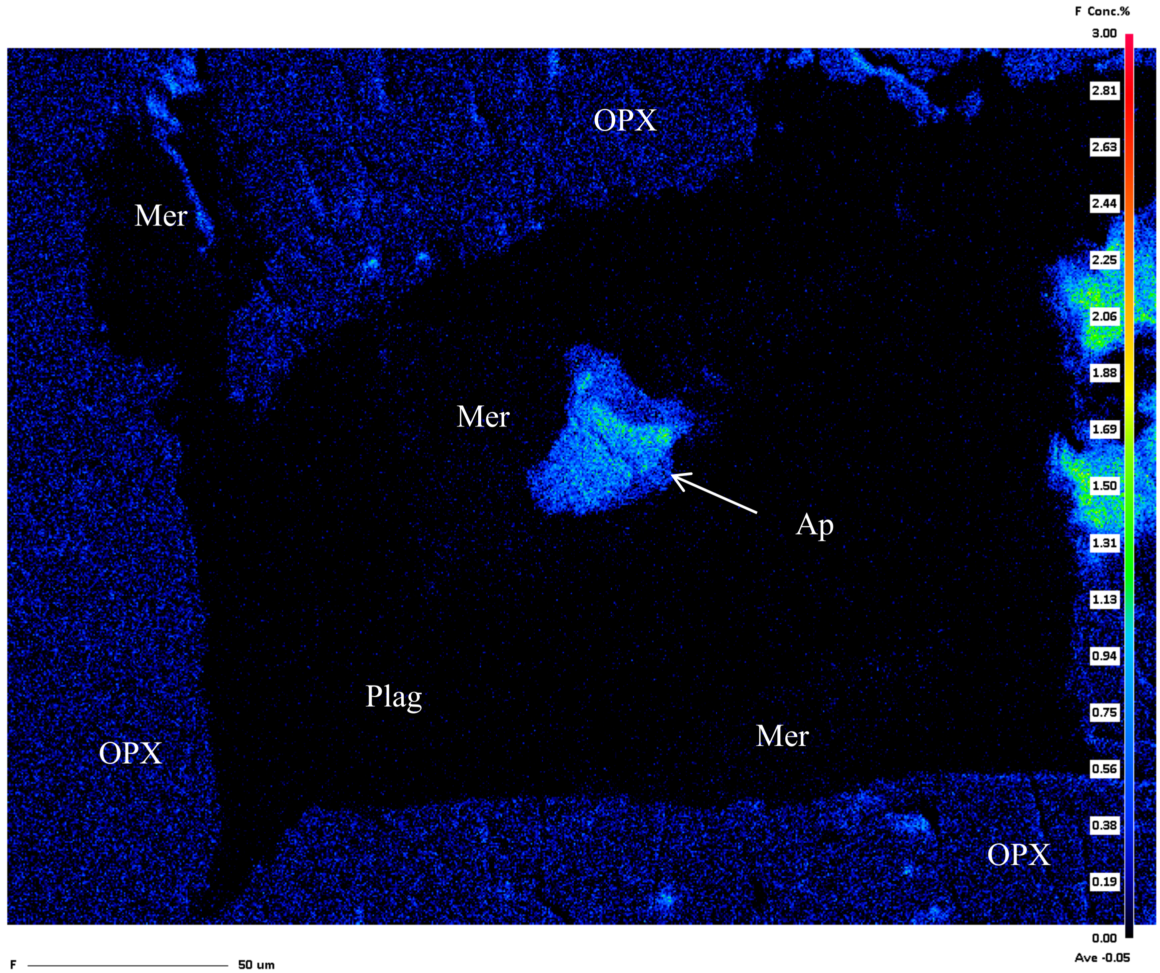

Figure 56. Quantitative WDS (Wavelength Dispersive Spectrometry) elemental map distribution of fluorine (F) in apatite-merrillite intergrown grains #4-6 in ALH 84001. WDS element maps are given in weight percent (wt%). WDS element maps correspond to BSE image from Figure 53. Plag = plagioclase; Mer = merrillite; Ap = apatite; OPX = orthopyroxene. Scale bar is 50 µm in length. Although very minimal, there is a slight enrichment in F associated with the large mineral fracture which cuts the apatite grain diagonally. Note that the F-rich "phase" to the right-end of the map is the result of epoxy, and thus not a reflection of the meteorite itself.

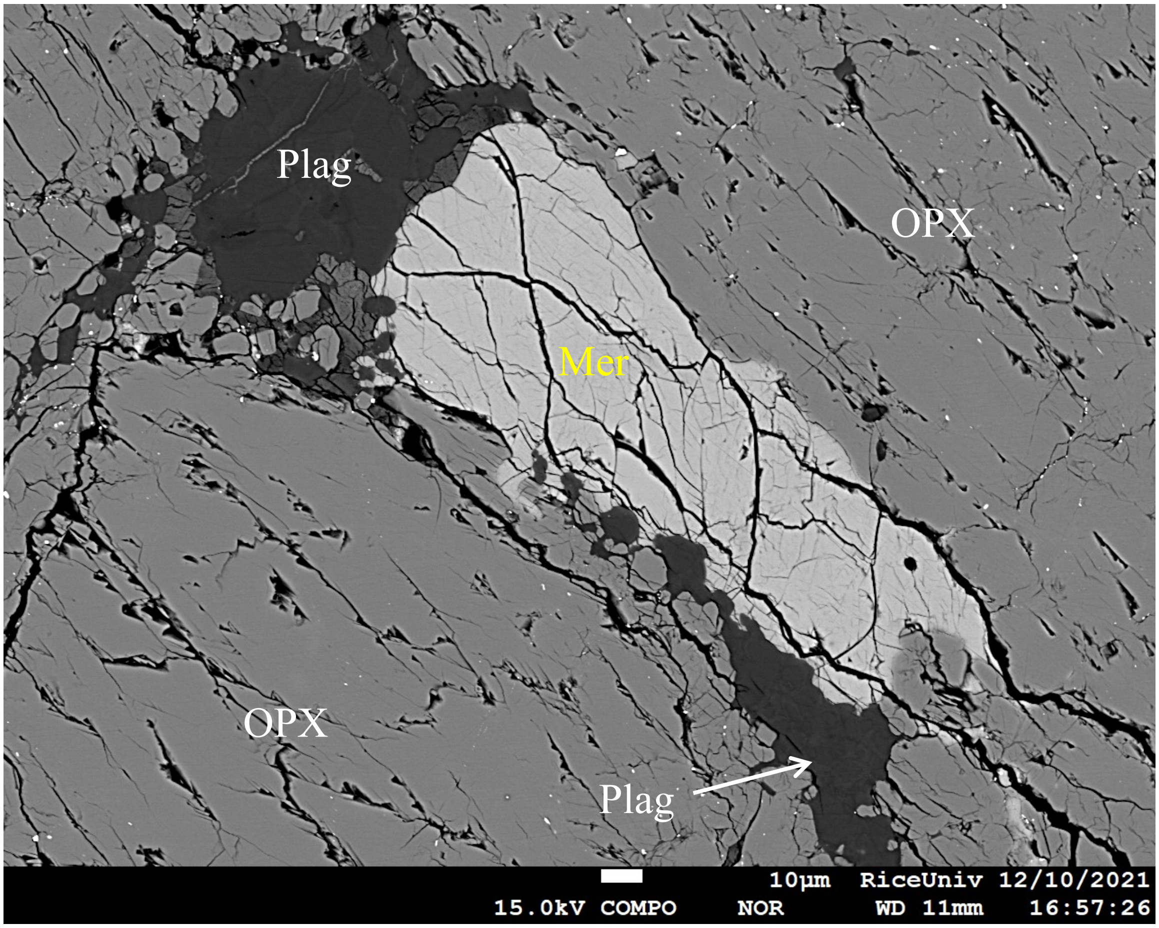

Figure 57. Detailed view of BSE (BackScattered Electron) image of merrillite grain #8 in ALH 84001. Mineral abbreviations: Plag = plagioclase; Mer = merrillite; OPX = orthopyroxene. Scale bar is 10 μm in length

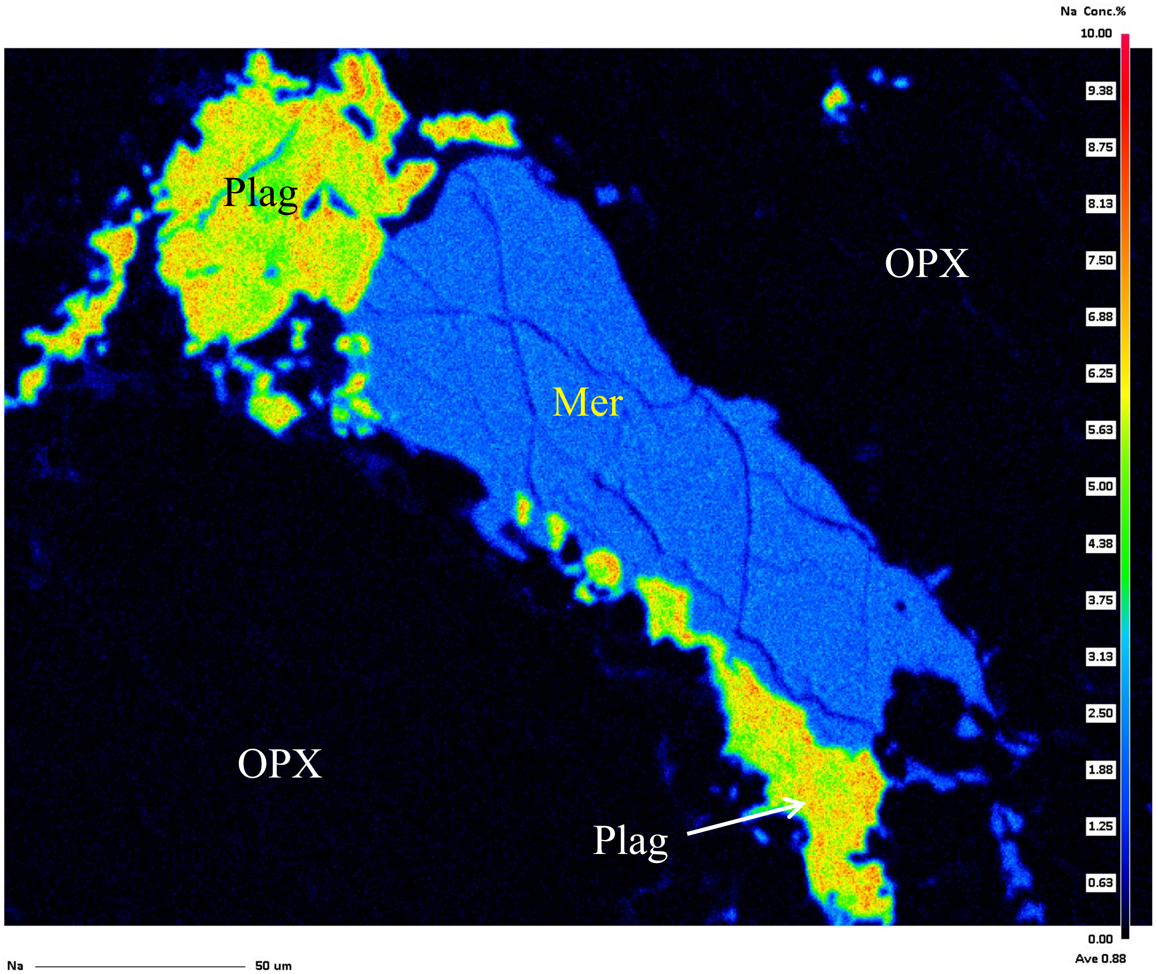

Figure 58. Quantitative WDS (Wavelength Dispersive Spectrometry) elemental map distribution of sodium (Na) in merrillite grain #8 in ALH 84001. WDS element maps are given in weight percent (wt%). WDS element maps correspond to BSE image from Figure 57. Plag = plagioclase; Mer = merrillite; Ap = apatite; OPX = orthopyroxene. Scale bar is 50 µm in length. Note that all minerals exhibit homogenous compositions.

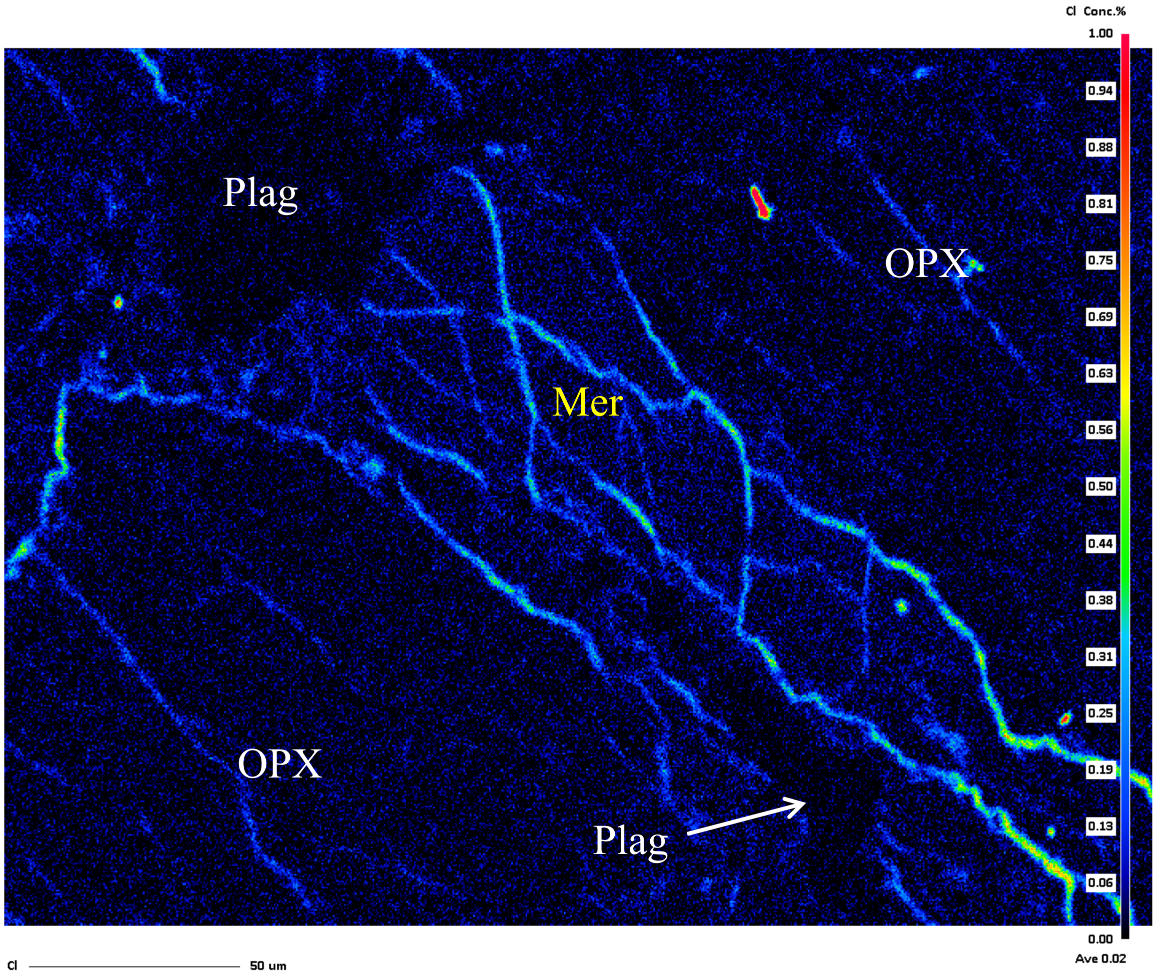

Figure 59. Quantitative WDS (Wavelength Dispersive Spectrometry) elemental map distribution of chlorine (Cl) in merrillite grain #8 in ALH 84001. WDS element maps are given in weight percent (wt%). WDS element maps correspond to BSE image from Figure 57. Plag = plagioclase; Mer = merrillite; Ap = apatite; OPX = orthopyroxene. Scale bar is 50 μm in length. Note that there is a moderate enrichment in Cl that is directly associated with mineral (i.e., merrillite) fractures.

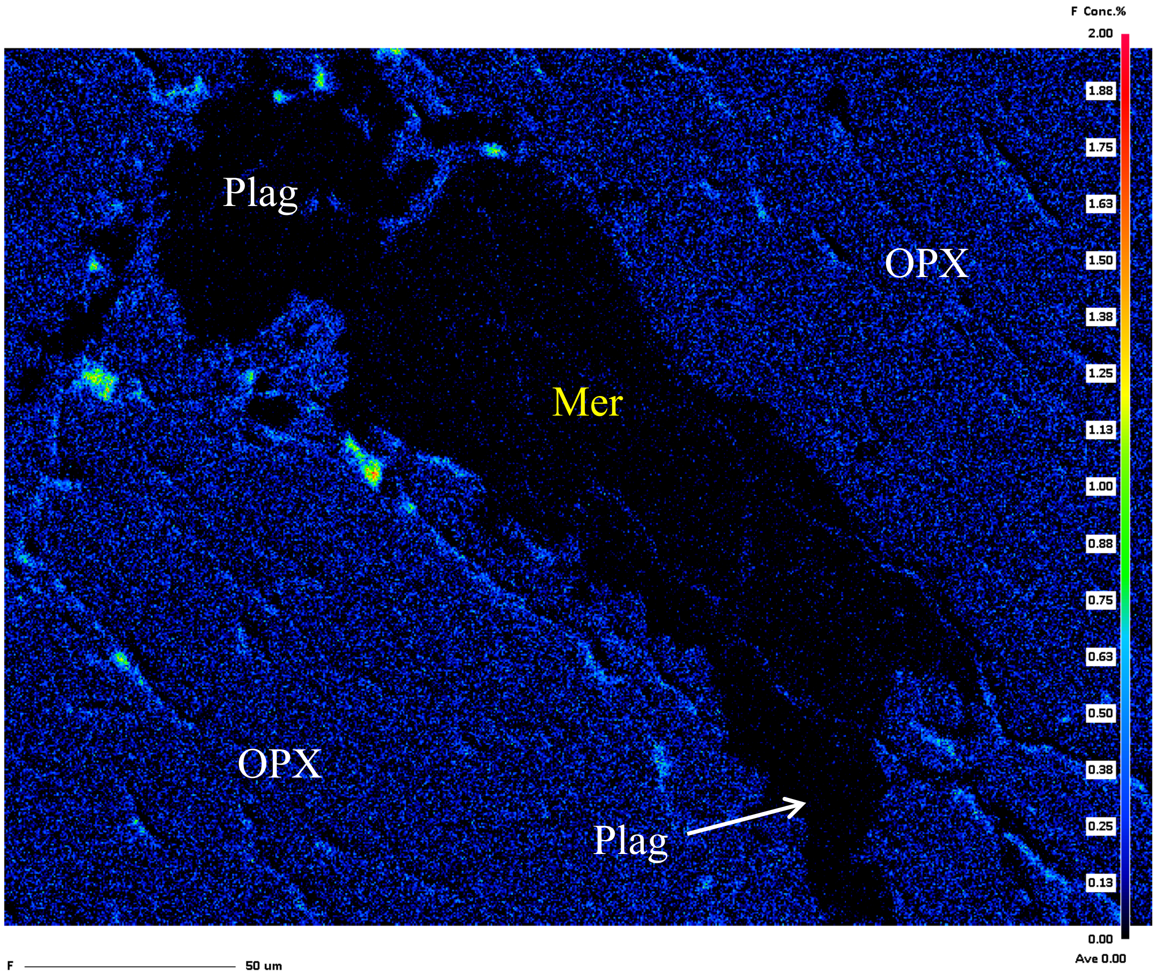

Figure 60. Quantitative WDS (Wavelength Dispersive Spectrometry) elemental map distribution of fluorine (F) in merrillite grain #8 in ALH 84001. WDS element maps are given in weight percent (wt%). WDS element maps correspond to BSE image from Figure 57. Plag = plagioclase; Mer = merrillite; Ap = apatite; OPX = orthopyroxene. Scale bar is 50 µm in length. Note that all (major) minerals exhibit homogenous compositions.

However, unlike phosphates found in Tissint, the mineral assemblage of ALH 84001 contains volatile-bearing phases (i.e., apatite). Apatite Cl and F contents in ALH 84001 grains were moderately heterogeneous in composition with Cl concentrations ranging from 3.85 – 5.05 wt% (average = 4.36 wt%; 1σ = 0.42) and F concentrations ranging from 0.30 – 0.92 wt% (average = 0.61 wt%; 1σ = 0.17) (Supplementary Table 6).

Assuming that F + Cl + OH = 1.0 structural formula unit (sfu), an indirect calculation can be made which estimates the water content of apatite. Average atoms per formula unit (apfu) of F in apatite was calculated at 0.16 while the average apfu Cl was calculated to be 0.63. Therefore, the water content of apatite is estimated at 0.21 sfu or ~21% hydroxyl apatite component (Table 5).

Magnesium# for analyzed apatite, $Ca_5(PO_4)_3(OH,F,Cl)$, grains was calculated to be 25.1 ($[Mg_{atomic}/(Mg_{atomic}+Fe_{atmoic})]*100$). Site-specific element designations were: Ca-site = 4.98; P-site = 3.02. Site designations included the following: Ca-site included Al, Ce, La, Nd, Fe, Mn, Mg, ca, Na, K; P-site included Si, P, S (Figure 44).

Magnesium# for analyzed merrillite, $Ca_9NaMg(PO_4)_7$, grains was calculated to be 87.6 ($[Mg_{atomic}/(Mg_{atomic}+Fe_{atmoic})]*100$). Sodium# was calculated to be 8.3 ($[Na_{atomic}/(Na_{atomic}+Ca_{atmoic})]*100$). Site-specific element designations were: Ca-site = 8.97; Na-site = 0.83; Mg-site = 1.04; P-site = 7.03. Site designations included the following: Ca-site included La, Ca, Mn, Ce, Nd; Na-site included Na, K; Mg-site included Fe, Mg; P-site included Si, P, S (Figure 45). Finally, although granular bands are a well-documented feature in ALH 84001 (Treiman, 1995, 1998, 2021), they were not identified in the analyzed section. Therefore, no phosphates were identified or analyzed from the granular zones within ALH 84001.

5.2 Discussion

A geochemical investigation of ALH 84001 phosphate phases revealed 1) intergrown apatite-merrillite textures, 2) Cl-rich, OH-poor, apatite grains, 3) moderate Cl-enrichment in merrillite mineral fractures, and 4) moderate Cl-enrichment in select apatite grains. When compared to end-member merrillite compositions ($Ca_9NaMg(PO_4)_7$), merrillite in ALH 84001 was found to have slight deficiencies in sodium. Average Na_2O contents measured 2.35 wt% ($1\sigma = 0.08$) and 0.81 formula amounts (per 28 O) (

Table 6). When the chemical composition (i.e., Na apfu; Mn apfu; Mg#) of merrillite in ALH 84001 was compared to the olivine-phyric phosphates of Liu et al. (2016)

and the Martian phosphates of Shearer et al. (2015), all analyzed phosphates in this study exhibited chemical signatures characteristic of ALH 84001 (e.g., Na- and Mg-contents: Figure 12, Figure 13, Figure 14).

Analyzed apatite grains also reflect typical chemical compositions measured in Martian meteorites (Figure 9); however, grains analyzed in ALH 84001 exhibited slightly higher Cl contents. At 0.16 apfu F and 0.63 apfu Cl, the hydroxyl component calculated in apatite accounted for 0.21 sfu or ~21%. These results are consistent with that of Filiberto and Treiman (2009) who propose that Martian magmas are depleted in water but enriched in chlorine.

Textural relationships observed between apatite and merrillite (Figure 46, Figure 47) suggest that processes related to shock-metamorphism (e.g., punctuated pressure spikes) likely played an important role in the chemical evolution of ALH 84001 phosphates. Crystallization sequences of apatite-merrillite intergrowths are oftentimes ambiguous in Martian meteorites, as the textural relationship between the two phases can be complex (i.e., inclusions and intergrowths of one phase in the other) (Bellucci et al., 2017; Darling et al., 2021; Greenwood et al., 2003; Greenwood et al., 2008; Howarth et al., 2015; Hwang et al., 2019; Shearer et al., 2011) (Figure 21). However, it is proposed that ALH 84001 results provide clear textural evidence for the following crystallization sequence:

1. Magmatic apatite crystallizes first from a Cl-rich, late-stage, melt or fluid.
2. Devolatilization of apatite grains occurs following multiple cataclysmic shock events.
3. Volatile-free merrillite replaces shocked, devolatilized, apatite grains.
4. Mobilized volatiles (i.e., chlorine) move from the apatite system to concentrate in:

i. *the mineral fractures of merrillite* (e.g., Figure 59). In this scenario, the entire apatite system has been devolatilized due to a shock event; chlorine is mobilized, and becomes concentrated along newly generated (shock-induced) cracks and fractures of the original apatite grain. The recrystallization of apatite to merrillite proceeds to completion (i.e., complete transformation from apatite to merrillite occurs), and residual chlorine becomes concentrated in the fractures of merrillite (i.e., a volatile-free phase).

ii. *low-fracture zones within apatite* (e.g., Figure 55). In this scenario, the apatite system has been partially devolatilized due to a shock event; chlorine is mobilized, and becomes concentrated in "pockets" within the apatite mineral system. The recrystallization of apatite to merrillite proceeds and mobilized chlorine becomes enriched in the apatite mineral system present.

The counterargument for this scenario would be one in which merrillite was the magmatic phase (instead of apatite). In this counter case, the observed texture produced would be created predominately through interaction with Cl-rich fluids or melt, instead of resulting from shock-metamorphism. This scenario seems unlikely for ALH 84001 though, which has had an extensive shock history (i.e., granular bands in ALH formed between 45-50 GPa; carbonates in ALH fractured at 25-45 GPa; ALH underwent a maximum of 16 GPa when it was ejected from Mars) (North et al., 2023). As such, although there may have been some alteration related to fluid-based interactions, it is proposed that the chemical variation observed in the intergrown texture of apatite and merrillite in ALH 84001 formed as a result of extensive devolatilization related to extensive shock-metamorphic processes.

5.3 Implications

The Cl-rich nature of apatite in ALH 84001 supports the interpretation that Martian parental magmas contained little water but were enriched in other volatiles, such as chlorine (Filiberto and Treiman, 2009). The major implication of these findings is that ancient eruptions of Cl-rich, OH-poor, magmas contributed very little water to the Martian surface (Filiberto and Treiman, 2009). Further, shock-induced chemical variations were found to occur in the magmatic (e.g., apatite devolatilization) and nonmagmatic (e.g., chlorine enrichment in merrillite fractures) phosphate phases of ALH 84001. Therefore, careful consideration must be taken when investigating phosphates that have undergone physical and chemical changes resulting from shock-metamorphism.

5.4 Conclusions

Intergrown merrillite-apatite phases were found to occur in ALH 84001. Analyzed apatite grains contain variable volatile contents but are generally enriched in Cl, while merrillite grains are largely homogenous in composition. In contrast to previous reports (Howarth et al., 2015; Shearer et al., 2011), textures observed in this study provide unambiguous support for a proposed phosphate crystallization history involving magmatic apatite and merrillite recrystallization. Evidence of shock-induced chemical alterations was observed in the fractures of merrillite grains (i.e., Cl-rich fractures) and within unfractured regions of apatite grains. Chemical variations are linked to shock-induced metamorphic events (i.e., meteorite impacts). As was concluded for Tissint, careful consideration must be taken when analyzing grains that show evidence of alteration by shock, as shock metamorphism can drive element mobility in phosphate phases.

REFERENCES

Adcock, C.T., Hausrath, E.M., Forster, P.M., Tschauner, O. and Sefein, K.J. (2014) Synthesis and characterization of the Mars-relevant phosphate minerals Fe-and Mg-whitlockite and merrillite and a possible mechanism that maintains charge balance during whitlockite to merrillite transformation. American Mineralogist 99, 1221-1232.

Adcock, C.T., Tschauner, O., Hausrath, E.M., Udry, A., Luo, S., Cai, Y., Ren, M., Lanzirotti, A., Newville, M. and Kunz, M. (2017) Shock-transformation of whitlockite to merrillite and the implications for meteoritic phosphate. Nature communications 8, 1-8.

Aoudjehane, H.C., Avice, G., Barrat, J.-A., Boudouma, O., Chen, G., Duke, M., Franchi, I., Gattacceca, J., Grady, M. and Greenwood, R. (2012) Tissint martian meteorite: A fresh look at the interior, surface, and atmosphere of Mars. Science 338, 785-788.

Balta, J.B., Sanborn, M.E., Udry, A., Wadhwa, M. and McSween, H.Y. (2015) Petrology and trace element geochemistry of Tissint, the newest shergottite fall. Meteoritics & Planetary Science 50, 63-85.

Barrat, J.A., Jambon, A., Ferrière, L., Bollinger, C., Langlade, J.A., Liorzou, C., Boudouma, O. and Fialin, M. (2014) No Martian soil component in shergottite meteorites. Geochimica et Cosmochimica Acta 125, 23-33.

Baziotis, I.P., Liu, Y., DeCarli, P.S., Jay Melosh, H., McSween, H.Y., Bodnar, R.J. and Taylor, L.A. (2013) The Tissint Martian meteorite as evidence for the largest impact excavation. Nature Communications 4, 1404.

Bellucci, J., Whitehouse, M., John, T., Nemchin, A., Snape, J., Bland, P. and Benedix, G. (2017) Halogen and Cl isotopic systematics in Martian phosphates: Implications for the Cl cycle and surface halogen reservoirs on Mars. Earth and Planetary Science Letters 458, 192-202.

Britvin, S.N., Galuskina, I.O., Vlasenko, N.S., Vereshchagin, O.S., Bocharov, V.N., Krzhizhanovskaya, M.G., Shilovskikh, V.V., Galuskin, E.V., Vapnik, Y. and Obolonskaya, E.V. (2021) Keplerite, $Ca9(Ca0.5\square0.5)Mg(PO4)7$, a new meteoritic and terrestrial phosphate isomorphous with merrillite, $Ca9NaMg(PO4)7$. American Mineralogist 106, 1917-1927.

Buseck, P.R. and Holdsworth, E. (1977) Phosphate minerals in pallasite meteorites. Mineralogical Magazine 41, 91-102.

Capitelli, F., Bosi, F., Capelli, S.C., Radica, F. and Della Ventura, G. (2021) Neutron and XRD Single-Crystal Diffraction Study and Vibrational Properties of Whitlockite, the Natural Counterpart of Synthetic Tricalcium Phosphate. Crystals 11, 225.

Černok, A., White, L.F., Darling, J., Dunlop, J. and Anand, M. (2019) Shock-induced microtextures in lunar apatite and merrillite. Meteoritics & Planetary Science 54, 1262-1282.

Cox, M.A., Erickson, T.M., Schmieder, M., Christoffersen, R., Ross, D.K., Cavosie, A.J., Bland, P.A., Kring, D.A. and Scientists, I.I.E. (2020) High-resolution microstructural and compositional analyses of shock deformed apatite from the peak ring of the Chicxulub impact crater. Meteoritics & Planetary Science 55.

Crozaz, G. and McKay, G. (1990) Rare earth elements in Angra dos Reis and Lewis Cliff 86010, two meteorites with similar but distinct magma evolutions. Earth and Planetary Science Letters 97, 369-381.

Darling, J., White, L., Kizovski, T., Černok, A., Moser, D.E., Tait, K., Dunlop, J., Langelier, B., Douglas, J. and Zhao, X. (2021) The shocking state of apatite and merrillite in shergottite Northwest Africa 5298 and extreme nanoscale chlorine isotope variability revealed by atom probe tomography. Geochimica et Cosmochimica Acta 293, 422-437.

Dasgupta, S. and Bhowmik, S.K. (2021) Types of Metamorphism, in: Alderton, D., Elias, S.A. (Eds.), Encyclopedia of Geology (Second Edition). Academic Press, Oxford, pp. 354-365.

DeCarli, P.S. (2005) SHOCK METAMORPHISM, in: Selley, R.C., Cocks, L.R.M., Plimer, I.R. (Eds.), Encyclopedia of Geology. Elsevier, Oxford, pp. 179-184.

Dowty, E. (1977) Phosphate in Angra dos Reis: Structure and composition of the Ca3(PO4)2 minerals. Earth and Planetary Science Letters 35, 347-351.

Ferrière, L. and Osinski, G.R. (2013) Shock metamorphism. Impact cratering: Processes and products, 106-124.

Filiberto, J., Baratoux, D., Beaty, D., Breuer, D., Farcy, B.J., Grott, M., Jones, J.H., Kiefer, W.S., Mane, P. and McCubbin, F.M. (2016) A review of volatiles in the Martian interior. Meteoritics & Planetary Science 51, 1935-1958.

Filiberto, J. and Treiman, A.H. (2009) Martian magmas contained abundant chlorine, but little water. Geology 37, 1087-1090.

French, B.M. (1998) Traces of catastrophe: A handbook of shock-metamorphic effects in terrestrial meteorite impact structures. Lunar and Planetary Institute (Contribution CB-954), Houston, Texas.

Fritz, J., Artemieva, N. and Greshake, A. (2005) Ejection of Martian meteorites. Meteoritics & Planetary Science 40, 1393-1411.

Greenwood, J.P., Blake, R.E. and Coath, C.D. (2003) Ion microprobe measurements of 18O/16O ratios of phosphate minerals in the Martian meteorites ALH84001 and Los Angeles. Geochimica et Cosmochimica Acta 67, 2289-2298.

Greenwood, J.P., Itoh, S., Sakamoto, N., Vicenzi, E.P. and Yurimoto, H. (2008) Hydrogen isotope evidence for loss of water from Mars through time. Geophysical Research Letters 35.

Howarth, G.H., Pernet-Fisher, J.F., Bodnar, R.J. and Taylor, L.A. (2015) Evidence for the exsolution of Cl-rich fluids in martian magmas: Apatite petrogenesis in the enriched lherzolitic shergottite Northwest Africa 7755. Geochimica et Cosmochimica Acta 166, 234-248.

Hughes, J. and Rakovan, J. (2002) The crystal structure of apatite, Ca-5(PO4)(3)(F,OH,Cl). Reviews in Mineralogy and Geochemistry 48, 1-12.

Hughes, J.M. and Rakovan, J.F. (2015) Structurally robust, chemically diverse: apatite and apatite supergroup minerals. Elements 11, 165-170.

Hwang, S.-L., Shen, P., Chu, H.-T., Yui, T.-F., Varela, M.-E. and Iizuka, Y. (2019) New minerals tsangpoite Ca5 (PO4) 2 (SiO4) and matyhite Ca9 (Ca0. 5□ 0.5) Fe (PO4) 7 from the D'Orbigny angrite. Mineralogical Magazine 83, 293-313.
Irving, A., Kuehner, S., Tanaka, R., Herd, C., Chen, G. and Lapen, T. (2012) The Tissint depleted permafic olivine-phyric Shergottite: Petrologic, elemental and isotopic characterization of a recent Martian Fall in Morocco, Lunar Planet. Sci. Conf, p. 2510.
Jolliff, B., Freeman, J. and Wopenka, B. (1996) Structural comparison of lunar, terrestrial, and synthetic whitlockite using laser Raman microprobe spectroscopy, Lunar and Planetary Science Conference.
Jolliff, B.L., Hughes, J.M., Freeman, J.J. and Zeigler, R.A. (2006) Crystal chemistry of lunar merrillite and comparison to other meteoritic and planetary suites of whitlockite and merrillite. American Mineralogist 91, 1583-1595.
Keil, K., Prinz, M., Hlava, P., Gomes, C., Curvello, W., Wasserburg, G., Tera, F., Papanastassiou, D., Huneke, J. and Murali, A. (1976) Progress by the consorts of Angra dos Reis (The Adorables), Lunar and Planetary Science Conference.
Kenny, G.G., Karlsson, A., Schmieder, M., Whitehouse, M.J., Nemchin, A.A. and Bellucci, J.J. (2019) Recrystallization and chemical changes in apatite in response to hypervelocity impact. Geology 48, 19-23.
Kizovski, T.V., Tait, K.T., Di Cecco, V.E., White, L.F. and Moser, D.E. (2019) Detailed mineralogy and petrology of highly shocked poikilitic shergottite Northwest Africa 6342. Meteoritics & Planetary Science 54, 768-784.
Krot, A., Keil, K., Scott, E., Goodrich, C. and Weisberg, M. (2014) Classification of meteorites and their genetic relationships. Meteorites and cosmochemical processes 1, 1-63.
Langenhorst, F. and Deutsch, A. (2012) Shock metamorphism of minerals. Elements 8, 31-36.
Lapen, T.J., Righter, M., Brandon, A.D., Debaille, V., Beard, B.L., Shafer, J.T. and Peslier, A.H. (2010) A Younger Age for ALH84001 and Its Geochemical Link to Shergottite Sources in Mars. Science 328, 347-351.
Liu, Q., Huang, S., Matinlinna, J.P., Chen, Z. and Pan, H. (2013) Insight into Biological Apatite: Physiochemical Properties and Preparation Approaches. BioMed Research International 2013, 1-13.
Liu, Y., Baziotis, I.P., Asimow, P.D., Bodnar, R.J. and Taylor, L.A. (2016) Mineral chemistry of the Tissint meteorite: Indications of two-stage crystallization in a closed system. Meteoritics & Planetary Science 51, 2293-2315.
Liu, Y., Chen, Y., Guan, Y., Ma, C., Rossman, G.R., Eiler, J.M. and Zhang, Y. (2018) Impact-melt hygrometer for Mars: The case of shergottite Elephant Moraine (EETA) 79001. Earth and Planetary Science Letters 490, 206-215.
Ma, C., Tschauner, O., Beckett, J.R., Liu, Y., Rossman, G.R., Zhuravlev, K., Prakapenka, V., Dera, P. and Taylor, L.A. (2015) Tissintite,(Ca, Na,□) AlSi2O6, a highly-defective, shock-induced, high-pressure clinopyroxene in the Tissint martian meteorite. Earth and Planetary Science Letters 422, 194-205.

Mari, N., Hallis, L. and Lee, M. (2019) Chlorine Abundance in the Shergottite Parental Melt Amphibole and Apatite in Tissint and Zagami, 82nd Annual Meeting of The Meteoritical Society, p. 6041.

McCubbin, F.M. and Jones, R.H. (2015) Extraterrestrial apatite: Planetary geochemistry to astrobiology. Elements 11, 183-188.

McCubbin, F.M., Shearer, C.K., Burger, P.V., Hauri, E.H., Wang, J., Elardo, S.M. and Papike, J.J. (2014) Volatile abundances of coexisting merrillite and apatite in the martian meteorite Shergotty: Implications for merrillite in hydrous magmas. American Mineralogist 99, 1347-1354.

McKay, D.S., Gibson, E.K., Thomas-Keprta, K.L., Vali, H., Romanek, C.S., Clemett, S.J., Chillier, X.D.F., Maechling, C.R. and Zare, R.N. (1996) Search for Past Life on Mars: Possible Relic Biogenic Activity in Martian Meteorite ALH84001. Science 273, 924-930.

Meyer, C. (2012) Martian Meteorite Compendium [Available at http://curator.jsc.nasa.gov/antmet/mmc/.]. Technical Report, NASA.

Min, K., Farah, A.E., Lee, S.R. and Lee, J.I. (2017) (U-Th)/He ages of phosphates from Zagami and ALHA77005 Martian meteorites: Implications to shock temperatures. Geochimica et Cosmochimica Acta 196, 160-178.

Mittlefehldt, D. (2014) 1.6—Achondrites. Treatise on Geochemistry 2, 235-266.

Morlok, A., Koike, C., Tomeoka, K., Mason, A., Lisse, C., Anand, M. and Grady, M. (2012) Mid-infrared spectra of differentiated meteorites (achondrites): Comparison with astronomical observations of dust in protoplanetary and debris disks. Icarus 219, 48-56.

North, T.L., Collins, G.S., Davison, T.M., Muxworthy, A.R., Steele, S.C. and Fu, R.R. (2023) The heterogeneous response of Martian meteorite Allan Hills 84001 to planar shock. Icarus 390, 115322.

Pan, Y. and Fleet, M.E. (2002) Compositions of the apatite-group minerals: substitution mechanisms and controlling factors. Reviews in Mineralogy and Geochemistry 48, 13-49.

Rakovan, J. (2002) Growth and surface properties of apatite. Reviews in Mineralogy and Geochemistry 48, 51-86.

Ruschel, K., Nasdala, L., Kronz, A., Hanchar, J.M., Többens, D.M., Škoda, R., Finger, F. and Möller, A. (2012) A Raman spectroscopic study on the structural disorder of monazite–(Ce). Mineralogy and Petrology 105, 41-55.

Schulz, T., Povinec, P.P., Ferrière, L., Jull, A.J.T., Kováčik, A., Sýkora, I., Tusch, J., Münker, C., Topa, D. and Koeberl, C. (2020) The history of the Tissint meteorite, from its crystallization on Mars to its exposure in space: New geochemical, isotopic, and cosmogenic nuclide data. Meteoritics & Planetary Science 55, 294-311.

Shearer, C., Burger, P., Papike, J., McCubbin, F. and Bell, A. (2015) Crystal chemistry of merrillite from Martian meteorites: Mineralogical recorders of magmatic processes and planetary differentiation. Meteoritics & Planetary Science 50, 649-673.

Shearer, C.K., Burger, P.V., Papike, J.J., Sharp, Z.D. and McKEEGAN, K.D. (2011) Fluids on differentiated asteroids: Evidence from phosphates in differentiated meteorites GRA 06128 and GRA 06129. Meteoritics & Planetary Science 46, 1345-1362.

Suarez, S., Lapen, T., Righter, M., Beard, B. and Irving, A. (2022) Isotopic and trace element data of Tissint indicate a homogeneous strewn field, mobilization of Sr, REE, and Pb during shock metamorphism, and limits on the incorporation of martian surficial materials in impact melt glass. Geochimica et Cosmochimica Acta 327, 137-157.

Treiman, A.H. (1995) A petrographic history of martian meteorite ALH84001: Two shocks and an ancient age. Meteoritics 30, 294-302.

Treiman, A.H. (1998) The history of Allan Hills 84001 revised: Multiple shock events. Meteoritics & Planetary Science 33, 753-764.

Treiman, A.H. (2021) Uninhabitable and potentially habitable environments on Mars: Evidence from Meteorite ALH 84001. Astrobiology 21, 940-953.

Udry, A., Howarth, G.H., Herd, C.D.K., Day, J.M.D., Lapen, T.J. and Filiberto, J. (2020) What Martian Meteorites Reveal About the Interior and Surface of Mars. Journal of Geophysical Research: Planets 125.

Walton, E.L., Irving, A.J., Bunch, T.E. and Herd, C.D.K. (2012) Northwest Africa 4797: A strongly shocked ultramafic poikilitic shergottite related to compositionally intermediate Martian meteorites. Meteoritics & Planetary Science 47, 1449-1474.

Walton, E.L., Sharp, T., Hu, J. and Filiberto, J. (2014) Heterogeneous mineral assemblages in Martian meteorite Tissint as a result of a recent small impact event on Mars. Geochimica et Cosmochimica Acta 140, 334-348.

Xie, X., Yang, H., Gu, X. and Downs, R.T. (2015) Chemical composition and crystal structure of merrillite from the Suizhou meteorite. American Mineralogist 100, 2753-2756.

Zhang, B., Shieh, S.R., Withers, A.C. and Bouvier, A. (2018) Raman spectroscopy of shocked enstatite-rich meteorites. Meteoritics & Planetary Science 53, 2067-2077.

APPENDIX A:

INSTRUMENT CONDITIONS

JEOL JXA-8530F Hyperprobe

Supplementary Table 1. JEOL JXA 8530F Hyperprobe spectrometer settings, and average standard deviation SD (1σ) and detection limits DL (in ppm).

Element	**X-ray**	**Crystal**	**Peak Pos. (mm)**	**BG_L**	**BG_U**	**SD**	**DL**
Na	Ka	TAP	129.771	5	5	12.657	138.729
Si	Ka	TAP	77.987	6	6	103.990	105.793
La	La	PETJ	85.483	5	5	46.563	1706.268
K	Ka	PETJ	119.993	5	5.5	467.067	101.278
Ca	Ka	PETJ	107.771	5	6	0.350	104.818
Fe	Ka	LIF	134.833	5	5	189.667	310.395
Cl	Ka	PETH	151.477	5.5	5	63.803	61.667
P	Ka	PETH	197.081	6	6	0.490	65.173
S	Ka	PETH	172.102	5	5	3.220	30.034
F	Ka	LDE1	85.61	5	5	1.737	307.000
Mg	Ka	TAP	107.491	6	6	100.000	45.831
Al	Ka	TAP	90.635	5	5	189.110	84.152
Mn	Ka	LIFL	145.493	5	5	49.100	127.269
Ce	La	LIFL	177.428	3	5	12.873	177.015
Nd	La	LIFL	164.888	5.3	5	273.017	1297.458

Supplementary Table 2. JEOL JXA 8530F Hyperprobe counting times and detector settings. *Source of the standards: SPI: SPI Sullpies; Smth: Smithsonian standards; Mode**: Int=integral; Dif=differential

		Counting time (sec)		Detector setting				
Element	**Standard**	Peak	Back	Gain	High.V	Base.Line	Window (V)	Mode**
Na	Plagioclase_SPI*	10	5	32	1651	0.7	0	Int
Si	Olivine_SPI	10	5	32	1651	0.7	9.3	Dif
La	Monazite_SPI	30	20	16	1700	0.7	0	Int
K	Biotite_SPI	10	5	64	1676	0.7	0	Int
Ca	Apatite_SPI	10	5	64	1676	0.7	0	Int
Fe	Olivine_SPI	10	5	32	1716	0.7	0	Int
Cl	Tugtupite_SPI	10	5	64	1660	0.7	0	Int
P	Apatite_SPI	10	5	64	1660	0.7	0	Int
S	Apatite_SPI	30	20	64	1660	0.7	0	Int
F	Apatite_SPI	10	5	64	1690	0.7	9.3	Dif
Mg	Biotite_SPI	30	20	32	1644	0.7	0	Int
Al	Plagioclase_SPI	10	5	32	1644	0.7	0	Int
Mn	Rhodonite_SPI	10	5	32	1700	0.5	0	Int
Ce	CePO4_Smth*	30	20	32	1700	0.5	0	Int
Nd	NdPO4_Smth	30	20	32	1700	0.5	0	Int

Mafic silicates

The analytical conditions used were 15 kV accelerating voltage, 20 nA beam current, spot beam (~300 nm diameter). The standards used are shown in Supplementary Table 3. The counting time was 20 seconds for each element (10 sec per peak and 5 sec per each lower and upper background, respectively), except for Ni, where the counting time was 70 sec (30 per peak and 20 sec per each lower and upper background, respectively). PRZ (JEOL) matrix correction was employed for quantification.

Supplementary Table 3. JEOL JXA 8530F Hyperprobe standards used in mafic silicate analysis.

Element	Standard
Na	Jadeite_SPI
Si	Olivine_SPI
K	Biotite_SPI
Ca	Plagioclase_SPI
Fe	Almandine_SPI
Ti	Rutile_SPI
Ni	Olivine_SPI
Al	Almandine_SPI
Mg	Olivine_SPI
Cr	Chromite_SPI
Mn	Rhodonite_SPI

Trace elements analysis in phosphates

The analytical conditions used were 15 kV accelerating voltage, 150 nA beam current, and a 3-micron beam diameter. The analyzed X-ray line analyzed was Lα X-ray for Sm, Eu, Ce, Nd, Gd, and the Mα X for U and Th. The standards used were Smithsonian REE phosphate standards. For U and Th, pure metal and monazite standards were used, respectively. The counting time for each element was 200 sec (80 sec per peak and 60 sec per each lower and upper background, respectively). The PRZ (JEOL) matrix correction was used for quantification). The average detection limits were 30 ppm for Sm, 40 ppm for Eu, 34 ppm for Ce, 19 ppm for Gd, 25 ppm for Th, and 19 ppm for U. Gd, Th and U show analytical standard deviation mostly above 100%, showing that the concentration of these elements is below the detection limit, except for few analyses. For details regarding the standard deviation for each element/analysis see Table X (Trace Element Analysis) in Appendix Y. The interference between Nd and Ce was corrected as follows:

$(\text{Nd cps})_{\text{corrected}} = (\text{Nd Net})_{\textit{measured}} - k \times (\text{Ce Net})_{\textit{measured}}$

Where the "fake" Nd counts produced by the interference of Ce were first counted on pure $CePO_4$ standard, then the correction coefficient k (=0.00223) was calculated and applied in the correction of Nd in the trace element analysis of the Martian phosphates.

APPENDIX B:

QUANTITATIVE POINT ANALYSES

Supplementary Table 4. Summarized quantitative point analyses for keplerite in Tissint. Data used to calculate average wt% (weight percent) and formula amounts included data collected at Rice University (JEOL JXA-8530F Hyperprobe) and JSC (JEOL JXA-8530F Field Emission Electron Probe). Note that TiO2 was not analyzed at Rice University; these data were only collected at JSC. Comments denote mineral names given at time of data collection.

Data Collection	Point	Comment	Na2O	SiO2	La2O3	K2O	CaO	FeO	Cl	P2O5	SO3	F
Rice Uni.	207	Tissint_merr1_1	0.660	0.054	0.000	0.008	47.482	2.338	0.008	46.127	0.031	0.000
Rice Uni.	208	Tissint_merr1_2	0.720	0.128	0.000	0.033	47.136	2.234	0.003	45.922	0.019	0.000
Rice Uni.	209	Tissint_merr1_3	0.652	0.110	0.423	0.011	47.170	2.398	0.004	46.227	0.028	0.000
Rice Uni.	210	Tissint_merr1_4	0.981	0.618	0.000	0.050	46.423	2.387	0.003	46.127	0.147	0.000
Rice Uni.	211	Tissint_merr1_5	0.638	0.011	0.000	0.062	47.111	1.763	0.017	45.387	0.040	0.000
Rice Uni.	212	Tissint_merr1_6	0.688	0.021	0.000	0.027	46.713	2.201	0.019	45.352	0.032	0.000
Rice Uni.	213	Tissint_merr1_7	0.824	0.047	0.187	0.020	47.433	2.660	0.010	46.502	0.023	0.000
Rice Uni.	214	Tissint_merr1_8	0.816	0.266	0.000	0.034	47.387	2.556	0.001	46.773	0.034	0.000
Rice Uni.	215	Tissint_merr1_9	0.880	0.662	0.000	0.050	47.187	2.551	0.006	46.600	0.011	0.000
Rice Uni.	217	Tissint_merr2_1	0.777	0.276	0.000	0.052	47.527	2.888	0.008	46.712	0.076	0.000
Rice Uni.	218	Tissint_merr2_2	0.855	1.336	0.331	0.074	46.609	2.843	0.005	46.250	0.043	0.000
Rice Uni.	219	Tissint_merr2_3	0.871	0.386	0.000	0.055	47.542	2.711	0.013	46.505	0.044	0.000
Rice Uni.	220	Tissint_merr2_4	0.887	0.885	0.000	0.093	47.060	3.017	0.017	46.432	0.687	0.000
Rice Uni.	221	Tissint_merr2_5	0.830	1.428	0.263	0.104	47.579	2.816	0.008	46.126	0.060	0.000
Rice Uni.	223	Tissint_merr2_7	0.772	0.583	0.000	0.066	47.191	2.701	0.047	45.673	0.166	0.000
JSC-ARES	10	Kep5a	0.520	0.347	0.000	0.035	46.814	3.005	0.021	45.198	0.053	0.000
JSC-ARES	11	Kep5b	0.458	0.338	0.000	0.031	47.120	2.879	0.000	45.273	0.046	0.000
JSC-ARES	12	Kep5c	0.542	0.303	0.000	0.059	46.511	3.031	0.006	45.200	0.036	0.000
JSC-ARES	13	Kep5d	0.440	0.344	0.000	0.053	47.099	3.044	0.004	45.136	0.061	0.000
JSC-ARES	14	Kep5e	0.512	0.365	0.000	0.057	46.907	2.929	0.016	45.289	0.208	0.000
JSC-ARES	15	Kep5f	0.453	0.352	0.000	0.053	46.960	2.931	0.000	45.001	0.015	0.000
JSC-ARES	18	Kep8a	0.787	1.701	0.011	0.044	45.078	2.992	0.019	44.002	0.428	0.000
JSC-ARES	19	Kep8b	0.530	0.075	0.023	0.043	46.994	2.959	0.013	45.513	0.040	0.000
JSC-ARES	20	Kep8c	0.837	1.513	0.019	0.077	45.861	3.018	0.017	44.208	0.147	0.000
JSC-ARES	21	Kep8d	0.692	1.063	0.000	0.050	46.284	2.888	0.000	44.605	0.070	0.000
JSC-ARES	22	Kep9a	0.291	0.119	0.000	0.019	46.381	3.583	0.000	45.353	0.034	0.000
JSC-ARES	23	Kep9b	0.350	0.135	0.000	0.038	46.794	3.582	0.000	45.917	0.024	0.000
JSC-ARES	24	Kep9c	0.385	0.310	0.016	0.068	46.369	3.470	0.001	45.218	0.031	0.000
JSC-ARES	25	Kep9d	0.415	0.722	0.000	0.049	46.627	3.464	0.013	45.294	0.023	0.000
JSC-ARES	33	Kep10b	0.383	2.668	0.000	0.026	44.529	4.561	0.012	43.385	0.110	0.000
JSC-ARES	32	Kep10a	0.389	0.188	0.000	0.029	46.442	3.579	0.005	45.969	0.081	0.000
JSC-ARES	26	Kep12a	0.469	0.056	0.000	0.049	46.567	3.484	0.000	45.287	0.066	0.000
JSC-ARES	27	Kep12b	0.400	0.232	0.000	0.024	46.443	3.536	0.007	44.985	0.134	0.000
JSC-ARES	28	Kep12c	0.325	0.129	0.000	0.053	46.575	3.581	0.003	45.557	0.037	0.000
JSC-ARES	31	Kep12f	0.475	1.253	0.000	0.094	45.499	3.722	0.005	44.368	0.052	0.000
		Average	**0.614**	**0.544**	**0.036**	**0.048**	**46.726**	**2.980**	**0.009**	**45.528**	**0.090**	**0.000**
		Min	*0.291*	*0.011*	*0.000*	*0.008*	*44.529*	*1.763*	*0.000*	*43.385*	*0.011*	*0.000*
		Max	*0.981*	*2.668*	*0.423*	*0.104*	*47.579*	*4.561*	*0.047*	*46.773*	*0.687*	*0.000*
		StDev	0.199	0.600	0.101	0.023	0.679	0.542	0.009	0.798	0.130	0.000

Data Collection	Point	Comment	MgO	Al2O3	MnO	Ce2O3	Nd2O3	TiO2	Total	O=F,Cl	-O=F2	-O=Cl2	Total recalc
Rice Uni.	207	Tissint_merr1_1	3.192	0.001	0.143	0.050	0.000	*	100.094	0.002	0.000	0.002	100.092
Rice Uni.	208	Tissint_merr1_2	3.149	0.063	0.140	0.036	0.000	*	99.583	0.001	0.000	0.001	99.582
Rice Uni.	209	Tissint_merr1_3	3.217	0.073	0.119	0.000	0.000	*	100.432	0.001	0.000	0.001	100.431
Rice Uni.	210	Tissint_merr1_4	3.196	0.361	0.115	0.000	0.192	*	100.600	0.001	0.000	0.001	100.599
Rice Uni.	211	Tissint_merr1_5	3.323	0.061	0.104	0.000	0.133	*	98.650	0.004	0.000	0.004	98.646
Rice Uni.	212	Tissint_merr1_6	3.270	0.070	0.176	0.097	0.114	*	98.780	0.004	0.000	0.004	98.776
Rice Uni.	213	Tissint_merr1_7	2.962	0.032	0.131	0.023	0.000	*	100.854	0.002	0.000	0.002	100.852
Rice Uni.	214	Tissint_merr1_8	3.033	0.120	0.149	0.053	0.213	*	101.435	0.000	0.000	0.000	101.435
Rice Uni.	215	Tissint_merr1_9	3.039	0.382	0.159	0.008	0.066	*	101.601	0.001	0.000	0.001	101.600
Rice Uni.	217	Tissint_merr2_1	3.215	0.083	0.141	0.053	0.000	*	101.808	0.002	0.000	0.002	101.806
Rice Uni.	218	Tissint_merr2_2	3.203	0.301	0.157	0.031	0.052	*	102.090	0.001	0.000	0.001	102.089
Rice Uni.	219	Tissint_merr2_3	3.200	0.058	0.109	0.076	0.023	*	101.593	0.003	0.000	0.003	101.590
Rice Uni.	220	Tissint_merr2_4	3.135	0.229	0.096	0.041	0.000	*	102.579	0.004	0.000	0.004	102.575
Rice Uni.	221	Tissint_merr2_5	3.213	0.284	0.118	0.023	0.253	*	103.105	0.002	0.000	0.002	103.103
Rice Uni.	223	Tissint_merr2_7	3.192	0.237	0.176	0.012	0.000	*	100.816	0.011	0.000	0.011	100.805
JSC-ARES	10	Kep5a	2.625	0.035	0.087	0.000	0.000	0.023	98.763	0.005	0.000	0.005	98.758
JSC-ARES	11	Kep5b	2.672	0.013	0.122	0.055	0.042	0.086	99.135	0.000	0.000	0.000	99.135
JSC-ARES	12	Kep5c	2.611	0.037	0.141	0.041	0.000	0.000	98.518	0.001	0.000	0.001	98.517
JSC-ARES	13	Kep5d	2.613	0.059	0.123	0.016	0.000	0.027	99.019	0.001	0.000	0.001	99.018
JSC-ARES	14	Kep5e	2.704	0.068	0.117	0.032	0.000	0.059	99.263	0.004	0.000	0.004	99.259
JSC-ARES	15	Kep5f	2.567	0.021	0.158	0.063	0.010	0.029	98.613	0.000	0.000	0.000	98.613
JSC-ARES	18	Kep8a	2.697	0.753	0.130	0.069	0.000	0.001	98.712	0.004	0.000	0.004	98.708
JSC-ARES	19	Kep8b	2.781	0.024	0.149	0.000	0.058	0.008	99.210	0.003	0.000	0.003	99.207
JSC-ARES	20	Kep8c	2.815	0.226	0.137	0.062	0.033	0.030	99.000	0.004	0.000	0.004	98.996
JSC-ARES	21	Kep8d	2.642	0.550	0.155	0.058	0.000	0.018	99.075	0.000	0.000	0.000	99.075
JSC-ARES	22	Kep9a	2.583	0.022	0.168	0.002	0.029	0.000	98.584	0.000	0.000	0.000	98.584
JSC-ARES	23	Kep9b	2.633	0.028	0.155	0.039	0.000	0.000	99.695	0.000	0.000	0.000	99.695
JSC-ARES	24	Kep9c	2.572	0.082	0.184	0.029	0.001	0.030	98.766	0.000	0.000	0.000	98.766
JSC-ARES	25	Kep9d	2.595	0.323	0.106	0.048	0.000	0.000	99.679	0.003	0.000	0.003	99.676
JSC-ARES	33	Kep10b	2.950	0.062	0.175	0.028	0.000	0.052	98.941	0.003	0.000	0.003	98.938
JSC-ARES	32	Kep10a	2.616	0.000	0.190	0.029	0.000	0.005	99.522	0.001	0.000	0.001	99.521
JSC-ARES	26	Kep12a	2.579	0.030	0.173	0.004	0.000	0.008	98.772	0.000	0.000	0.000	98.772
JSC-ARES	27	Kep12b	2.628	0.049	0.118	0.043	0.000	0.042	98.641	0.002	0.000	0.002	98.639
JSC-ARES	28	Kep12c	2.621	0.010	0.164	0.006	0.007	0.000	99.068	0.001	0.000	0.001	99.067
JSC-ARES	31	Kep12f	2.607	0.165	0.191	0.069	0.015	0.035	98.550	0.001	0.000	0.001	98.549
		Average	**2.876**	**0.140**	**0.142**	**0.034**	**0.035**	**0.023**	**99.816**	**0.002**	**0.000**	**0.002**	**99.814**
		Min	*2.567*	*0.000*	*0.087*	*0.000*	*0.000*	*0.000*	*98.518*	*0.000*	*0.000*	*0.000*	*98.517*
		Max	*3.323*	*0.753*	*0.191*	*0.097*	*0.253*	*0.086*	*103.105*	*0.011*	*0.000*	*0.011*	*103.103*
		StDev	0.274	0.171	0.028	0.026	0.066	0.024	1.315	0.002	0.000	0.002	1.315

Supplementary Table 5. Summarized quantitative point analyses for merrillite in ALH 84001. Data used to calculate average wt% and formula amounts were collected at Rice University (JEOL JXA-8530F Hyperprobe). Comments denote mineral names given at time of data collection.

Data Collection	Point	Comment	Na2O	SiO2	La2O3	K2O	CaO	FeO	Cl	P2O5	SO3	F
Rice Uni.	92	ALH84001_Ap1_gray_7	2.317	0.000	0.000	0.087	46.709	0.786	0.002	46.583	0.011	0.000
Rice Uni.	93	ALH84001_Ap1_gray_8	2.268	0.000	0.052	0.080	46.670	0.748	0.004	46.563	0.009	0.000
Rice Uni.	94	ALH84001_Ap1_gray_9	2.429	0.000	0.000	0.103	47.106	0.765	0.000	46.760	0.000	0.000
Rice Uni.	95	ALH84001_Ap1_gray_10	2.254	0.000	0.000	0.093	47.261	0.769	0.000	46.412	0.007	0.000
Rice Uni.	96	ALH84001_Ap1_gray_11	2.331	0.000	0.000	0.084	46.364	0.795	0.002	46.471	0.007	0.000
Rice Uni.	97	ALH84001_Ap1_gray_12	2.409	0.000	0.000	0.077	46.898	0.625	0.000	46.880	0.000	0.000
Rice Uni.	98	ALH84001_Ap1_gray_13	2.296	0.000	0.000	0.085	46.444	0.782	0.005	46.191	0.011	0.000
Rice Uni.	99	ALH84001_Ap1_gray_14	2.378	0.000	0.000	0.102	47.125	0.685	0.000	46.852	0.029	0.000
Rice Uni.	100	ALH84001_Ap1_gray_15	2.326	0.045	0.000	0.099	46.939	0.711	0.000	46.268	0.015	0.000
Rice Uni.	101	ALH84001_Ap1_gray_16	2.382	0.000	0.000	0.111	47.050	0.662	0.000	46.308	0.003	0.000
Rice Uni.	102	ALH84001_Ap2_gray_1	2.296	0.026	0.000	0.098	46.719	0.725	0.009	46.177	0.004	0.000
Rice Uni.	103	ALH84001_Ap2_gray_2	2.291	0.000	0.112	0.100	46.600	0.618	0.002	46.403	0.001	0.000
Rice Uni.	104	ALH84001_Ap2_gray_3	2.189	0.016	0.000	0.084	46.437	0.662	0.000	46.222	0.003	0.000
Rice Uni.	105	ALH84001_Ap2_gray_4	2.323	0.000	0.000	0.090	47.199	0.809	0.005	46.571	0.000	0.000
Rice Uni.	106	ALH84001_Ap2_gray_5	2.422	0.000	0.000	0.093	47.021	0.715	0.000	46.518	0.009	0.000
Rice Uni.	107	ALH84001_Ap2_gray_6	2.429	0.000	0.000	0.083	47.019	0.785	0.006	46.964	0.000	0.000
Rice Uni.	108	ALH84001_Ap2_gray_7	2.360	0.000	0.000	0.083	47.050	0.785	0.002	46.118	0.008	0.000
Rice Uni.	109	ALH84001_Ap3_1	2.416	0.000	0.000	0.098	46.971	0.846	0.001	46.342	0.016	0.000
Rice Uni.	110	ALH84001_Ap3_2	2.388	0.000	0.000	0.087	46.809	0.728	0.000	46.391	0.012	0.000
Rice Uni.	111	ALH84001_Ap3_3	2.275	0.000	0.000	0.085	46.724	0.688	0.000	46.392	0.008	0.000
Rice Uni.	112	ALH84001_Ap3_4	2.353	0.000	0.000	0.092	46.620	0.652	0.006	46.637	0.021	0.000
Rice Uni.	113	ALH84001_Ap3_5	2.394	0.000	0.000	0.076	47.127	0.789	0.008	46.735	0.014	0.000
Rice Uni.	114	ALH84001_Ap3_6	2.350	0.000	0.194	0.059	46.929	0.682	0.003	46.373	0.000	0.000
Rice Uni.	116	ALH84001_Ap3_8	2.407	0.000	0.000	0.112	46.181	0.942	0.001	46.547	0.011	0.000
Rice Uni.	117	ALH84001_Ap3_9	2.325	0.036	0.000	0.105	46.974	0.955	0.004	46.333	0.014	0.000
Rice Uni.	118	ALH84001_Ap3_10	2.386	0.000	0.175	0.090	46.949	0.808	0.006	46.590	0.000	0.000
Rice Uni.	119	ALH84001_Ap3_11	2.425	0.000	0.000	0.089	46.676	0.752	0.000	46.545	0.011	0.000
Rice Uni.	120	ALH84001_Ap3_12	2.149	0.000	0.000	0.077	46.968	0.649	0.001	46.471	0.005	0.000
Rice Uni.	121	ALH84001_Ap3_13	2.346	0.000	0.000	0.077	46.626	0.649	0.006	46.076	0.015	0.000
Rice Uni.	122	ALH84001_Ap3_14	2.395	0.000	0.332	0.110	47.083	0.843	0.011	46.320	0.000	0.000
Rice Uni.	123	ALH84001_Ap3_15	2.368	0.000	0.000	0.071	46.944	0.799	0.000	46.530	0.018	0.000
Rice Uni.	124	ALH84001_Ap3_trail_1	2.304	0.000	0.000	0.072	46.132	0.852	0.006	45.150	0.016	0.000
Rice Uni.	125	ALH84001_Ap3_trail_2	2.375	0.021	0.000	0.085	46.770	0.943	0.000	46.431	0.001	0.000

Data Collection	Point	Comment	Na2O	SiO2	La2O3	K2O	CaO	FeO	Cl	P2O5	SO3	F
Rice Uni.	126	ALH84001_Ap3_trail_3	2.423	0.037	0.000	0.101	46.960	1.096	0.011	46.385	0.014	0.000
Rice Uni.	127	ALH84001_Ap3_trail_4	2.367	0.068	0.140	0.080	46.662	0.949	0.007	46.865	0.001	0.000
Rice Uni.	128	ALH84001_Ap3_trail_5	2.329	0.095	0.318	0.096	46.837	0.946	0.004	46.483	0.012	0.000
Rice Uni.	129	ALH84001_Ap3_trail_6	2.389	0.089	0.000	0.115	46.901	0.809	0.000	45.765	0.000	0.000
Rice Uni.	139	ALH84001_Ap4_gray_3	2.361	0.000	0.000	0.106	46.757	0.782	0.008	46.346	0.019	0.000
Rice Uni.	140	ALH84001_Ap4_gray_4	2.444	0.000	0.000	0.100	46.922	0.646	0.004	46.691	0.000	0.000
Rice Uni.	142	ALH84001_Ap4_gray_6	2.433	0.000	0.000	0.091	46.620	0.836	0.007	46.731	0.008	0.000
Rice Uni.	143	ALH84001_Ap4_gray_7	2.396	0.000	0.000	0.072	46.755	0.655	0.005	46.328	0.012	0.000
Rice Uni.	144	ALH84001_Ap4_gray_8	2.248	0.000	0.000	0.083	46.605	0.776	0.003	46.291	0.019	0.000
Rice Uni.	145	ALH84001_Ap4_gray_9	2.337	0.000	0.180	0.095	46.355	0.769	0.000	46.275	0.002	0.000
Rice Uni.	146	ALH84001_Ap4_gray_10	2.240	0.024	0.000	0.088	45.812	0.682	0.010	45.335	0.026	0.000
Rice Uni.	147	ALH84001_Ap4_gray_11	2.449	0.000	0.000	0.105	47.013	0.672	0.017	46.766	0.005	0.000
Rice Uni.	148	ALH84001_Ap4_gray_12	2.477	0.009	0.405	0.094	46.813	0.879	0.014	46.864	0.006	0.000
Rice Uni.	149	ALH84001_Ap5_1	2.504	0.019	0.000	0.090	46.805	0.898	0.000	46.211	0.002	0.000
Rice Uni.	150	ALH84001_Ap5_2	2.282	0.000	0.000	0.103	46.756	0.792	0.009	46.576	0.006	0.000
Rice Uni.	151	ALH84001_Ap5_3	2.431	0.001	0.000	0.096	46.618	0.802	0.000	46.451	0.011	0.000
Rice Uni.	152	ALH84001_Ap5_4	2.399	0.000	0.000	0.106	46.864	1.102	0.003	46.159	0.014	0.000
Rice Uni.	153	ALH84001_Ap5_5	2.429	0.000	0.000	0.078	46.623	0.959	0.010	46.286	0.013	0.000
Rice Uni.	154	ALH84001_Ap5_6	2.338	0.031	0.000	0.080	46.736	1.015	0.005	46.377	0.003	0.000
Rice Uni.	155	ALH84001_Ap5_7	2.340	0.000	0.000	0.074	46.730	0.865	0.006	46.498	0.004	0.000
Rice Uni.	156	ALH84001_Ap5_8	2.362	0.000	0.049	0.107	46.594	0.995	0.000	46.446	0.000	0.000
Rice Uni.	157	ALH84001_Ap6_1	2.404	0.000	0.000	0.102	47.170	1.108	0.000	46.859	0.000	0.000
Rice Uni.	158	ALH84001_Ap6_2	2.318	0.000	0.000	0.094	47.055	1.019	0.001	46.397	0.003	0.000
Rice Uni.	159	ALH84001_Ap6_3	2.302	0.000	0.034	0.107	47.020	0.929	0.000	46.465	0.004	0.000
Rice Uni.	160	ALH84001_Ap6_4	2.391	0.000	0.215	0.083	47.249	0.878	0.009	46.750	0.011	0.000
Rice Uni.	163	ALH84001_Ap6_7	2.353	0.000	0.000	0.095	47.360	0.859	0.002	46.860	0.011	0.000
Rice Uni.	164	ALH84001_Ap6_8	2.408	0.000	0.000	0.084	46.744	0.935	0.000	46.565	0.016	0.000
Rice Uni.	165	ALH84001_Ap6_9	2.312	0.007	0.000	0.082	47.000	0.992	0.007	46.282	0.017	0.000
Rice Uni.	166	ALH84001_Ap6_10	2.407	0.000	0.000	0.098	47.112	0.849	0.007	46.651	0.021	0.000
Rice Uni.	167	ALH84001_Ap7_1	2.467	0.000	0.000	0.085	47.182	0.822	0.000	46.817	0.002	0.000
Rice Uni.	168	ALH84001_Ap7_2	2.359	0.000	0.000	0.056	46.925	0.825	0.000	46.602	0.003	0.000
Rice Uni.	169	ALH84001_Ap7_3	2.464	0.000	0.000	0.094	47.167	0.968	0.000	46.498	0.014	0.000
Rice Uni.	170	ALH84001_Ap7_4	2.323	0.000	0.496	0.101	47.188	0.784	0.005	46.585	0.000	0.000
Data Collection	**Point**	**Comment**	**Na2O**	**SiO2**	**La2O3**	**K2O**	**CaO**	**FeO**	**Cl**	**P2O5**	**SO3**	**F**
Rice Uni.	171	ALH84001_Ap7_5	2.402	0.000	0.000	0.087	47.477	0.919	0.004	46.808	0.002	0.000
Rice Uni.	172	ALH84001_Ap7_6	2.358	0.000	0.087	0.098	47.005	0.775	0.007	46.859	0.009	0.000
Rice Uni.	173	ALH84001_Ap7_7	2.273	0.000	0.239	0.089	46.975	0.838	0.004	45.913	0.015	0.000
Rice Uni.	174	ALH84001_Ap7_8	2.431	0.000	0.000	0.091	46.910	0.859	0.000	46.502	0.016	0.000
Rice Uni.	175	ALH84001_Ap7_9	2.328	0.041	0.000	0.079	46.329	0.911	0.000	45.940	0.030	0.000
Rice Uni.	176	ALH84001_Ap7_10	2.480	0.025	0.000	0.103	46.263	0.958	0.004	47.031	0.005	0.000
Rice Uni.	177	ALH84001_Ap7_11	2.382	0.000	0.000	0.097	46.831	0.638	0.000	46.848	0.004	0.000
Rice Uni.	178	ALH84001_Ap7_12	2.406	0.000	0.227	0.094	46.798	0.818	0.008	46.814	0.019	0.000
Rice Uni.	179	ALH84001_Ap7_13	2.345	0.000	0.230	0.082	46.985	0.864	0.003	46.092	0.007	0.000
Rice Uni.	180	ALH84001_Ap7_14	2.432	0.000	0.000	0.077	46.939	0.865	0.000	46.520	0.000	0.000
Rice Uni.	181	ALH84001_Ap7_15	2.366	0.039	0.000	0.113	47.144	0.812	0.000	46.463	0.004	0.000
Rice Uni.	182	ALH84001_Ap8_1	2.234	0.000	0.207	0.095	46.244	0.834	0.014	46.147	0.003	0.000
Rice Uni.	183	ALH84001_Ap8_2	2.335	0.000	0.017	0.090	46.077	0.737	0.005	45.346	0.018	0.000
Rice Uni.	186	ALH84001_Ap8_5	2.212	0.000	0.512	0.056	45.751	0.874	0.007	46.203	0.027	0.000
Rice Uni.	187	ALH84001_Ap8_6	2.239	0.000	0.288	0.085	46.164	0.831	0.007	46.581	0.019	0.000
Rice Uni.	189	ALH84001_Ap8_8	2.291	0.000	0.347	0.064	46.197	0.857	0.000	46.561	0.017	0.000
Rice Uni.	190	ALH84001_Ap8_9	2.190	0.000	0.931	0.078	46.386	0.800	0.000	46.237	0.008	0.000
Rice Uni.	192	ALH84001_Ap8_11	2.156	0.000	0.411	0.078	46.022	0.847	0.000	46.080	0.000	0.000
Rice Uni.	194	ALH84001_Ap8_13	2.205	0.000	0.438	0.066	46.134	0.964	0.003	46.094	0.011	0.000
Rice Uni.	196	ALH84001_Ap8_15	2.223	0.000	0.187	0.092	46.484	0.868	0.007	46.410	0.003	0.000
Rice Uni.	197	ALH84001_Ap8_16	2.230	0.009	0.390	0.073	46.126	1.005	0.000	46.047	0.000	0.000
Rice Uni.	198	ALH84001_Ap8_17	2.204	0.000	0.917	0.109	45.791	1.010	0.007	46.240	0.017	0.000
Rice Uni.	200	ALH84001_Ap9_in_OPX_1	2.422	0.047	0.120	0.092	46.204	1.235	0.002	46.511	0.006	0.000
Rice Uni.	201	ALH84001_Ap9_in_OPX_2	2.349	0.055	0.218	0.087	46.521	1.181	0.003	46.344	0.000	0.000
Rice Uni.	202	ALH84001_Ap9_in_OPX_3	2.466	0.075	0.139	0.067	45.980	1.241	0.007	46.108	0.009	0.000
Rice Uni.	203	ALH84001_Ap9_in_OPX_4	2.324	0.064	0.180	0.089	46.454	1.068	0.004	46.598	0.009	0.000
Rice Uni.	204	ALH84001_Ap9_in_OPX_5	2.297	0.370	0.007	0.113	46.829	1.265	0.010	46.034	0.000	0.000
Rice Uni.	205	ALH84001_Ap9_in_OPX_6	2.216	1.094	0.151	0.099	45.001	1.853	0.001	44.511	0.001	0.000
Rice Uni.	206	ALH84001_Ap9_in_OPX_7	2.426	0.090	0.000	0.072	46.913	1.215	0.000	46.473	0.015	0.000
		Average	**2.348**	**0.026**	**0.094**	**0.089**	**46.715**	**0.861**	**0.004**	**46.399**	**0.009**	**0.000**
		Min	*2.149*	*0.000*	*0.000*	*0.056*	*45.001*	*0.618*	*0.000*	*44.511*	*0.000*	*0.000*
		Max	*2.504*	*1.094*	*0.931*	*0.115*	*47.477*	*1.853*	*0.017*	*47.031*	*0.030*	*0.000*
		StDev	0.079	0.119	0.180	0.013	0.412	0.178	0.004	0.383	0.008	0.000

Data Collection	Point	Comment	MgO	Al2O3	MnO	Ce2O3	Nd2O3	Total	O=F,Cl	-O=F2	-O=Cl2	Total recalc
Rice Uni.	92	ALH84001_Ap1_gray_7	3.383	0.000	0.063	0.029	0.000	99.970	0.000	0.000	0.000	*99.970*
Rice Uni.	93	ALH84001_Ap1_gray_8	3.384	0.000	0.047	0.056	0.000	99.881	0.001	0.000	0.001	*99.880*
Rice Uni.	94	ALH84001_Ap1_gray_9	3.430	0.000	0.039	0.065	0.436	101.133	0.000	0.000	0.000	*101.133*
Rice Uni.	95	ALH84001_Ap1_gray_10	3.316	0.000	0.018	0.043	0.016	100.189	0.000	0.000	0.000	*100.189*
Rice Uni.	96	ALH84001_Ap1_gray_11	3.365	0.021	0.050	0.025	0.000	99.515	0.000	0.000	0.000	*99.515*
Rice Uni.	97	ALH84001_Ap1_gray_12	3.341	0.000	0.000	0.080	0.000	100.310	0.000	0.000	0.000	*100.310*
Rice Uni.	98	ALH84001_Ap1_gray_13	3.380	0.026	0.046	0.043	0.000	99.309	0.001	0.000	0.001	*99.308*
Rice Uni.	99	ALH84001_Ap1_gray_14	3.415	0.000	0.061	0.046	0.000	100.693	0.000	0.000	0.000	*100.693*
Rice Uni.	100	ALH84001_Ap1_gray_15	3.455	0.002	0.025	0.058	0.000	99.943	0.000	0.000	0.000	*99.943*
Rice Uni.	101	ALH84001_Ap1_gray_16	3.444	0.020	0.001	0.057	0.046	100.084	0.000	0.000	0.000	*100.084*
Rice Uni.	102	ALH84001_Ap2_gray_1	3.447	0.000	0.022	0.041	0.033	99.597	0.002	0.000	0.002	*99.595*
Rice Uni.	103	ALH84001_Ap2_gray_2	3.416	0.000	0.030	0.010	0.000	99.583	0.000	0.000	0.000	*99.583*
Rice Uni.	104	ALH84001_Ap2_gray_3	3.496	0.205	0.007	0.032	0.000	99.353	0.000	0.000	0.000	*99.353*
Rice Uni.	105	ALH84001_Ap2_gray_4	3.393	0.000	0.040	0.046	0.000	100.476	0.001	0.000	0.001	*100.475*
Rice Uni.	106	ALH84001_Ap2_gray_5	3.405	0.001	0.040	0.027	0.000	100.251	0.000	0.000	0.000	*100.251*
Rice Uni.	107	ALH84001_Ap2_gray_6	3.392	0.009	0.026	0.000	0.234	100.947	0.001	0.000	0.001	*100.946*
Rice Uni.	108	ALH84001_Ap2_gray_7	3.417	0.000	0.008	0.071	0.000	99.902	0.000	0.000	0.000	*99.902*
Rice Uni.	109	ALH84001_Ap3_1	3.363	0.001	0.005	0.040	0.000	100.099	0.000	0.000	0.000	*100.099*
Rice Uni.	110	ALH84001_Ap3_2	3.452	0.000	0.000	0.048	0.160	100.075	0.000	0.000	0.000	*100.075*
Rice Uni.	111	ALH84001_Ap3_3	3.416	0.050	0.029	0.066	0.000	99.733	0.000	0.000	0.000	*99.733*
Rice Uni.	112	ALH84001_Ap3_4	3.398	0.000	0.020	0.010	0.111	99.920	0.001	0.000	0.001	*99.919*
Rice Uni.	113	ALH84001_Ap3_5	3.439	0.000	0.052	0.030	0.059	100.723	0.002	0.000	0.002	*100.721*
Rice Uni.	114	ALH84001_Ap3_6	3.502	0.000	0.000	0.012	0.000	100.104	0.001	0.000	0.001	*100.103*
Rice Uni.	116	ALH84001_Ap3_8	3.454	0.026	0.024	0.050	0.000	99.755	0.000	0.000	0.000	*99.755*
Rice Uni.	117	ALH84001_Ap3_9	3.499	0.038	0.049	0.029	0.049	100.410	0.001	0.000	0.001	*100.409*
Rice Uni.	118	ALH84001_Ap3_10	3.457	0.028	0.028	0.029	0.000	100.546	0.001	0.000	0.001	*100.545*
Rice Uni.	119	ALH84001_Ap3_11	3.484	0.006	0.006	0.000	0.000	99.994	0.000	0.000	0.000	*99.994*
Rice Uni.	120	ALH84001_Ap3_12	3.469	0.000	0.027	0.027	0.006	99.849	0.000	0.000	0.000	*99.849*
Rice Uni.	121	ALH84001_Ap3_13	3.489	0.000	0.030	0.015	0.000	99.329	0.001	0.000	0.001	*99.328*
Rice Uni.	122	ALH84001_Ap3_14	3.420	0.004	0.033	0.041	0.189	100.781	0.002	0.000	0.002	*100.779*
Rice Uni.	123	ALH84001_Ap3_15	3.403	0.000	0.022	0.047	0.026	100.228	0.000	0.000	0.000	*100.228*
Rice Uni.	124	ALH84001_Ap3_trail_1	3.375	0.013	0.039	0.000	0.044	98.003	0.001	0.000	0.001	*98.002*
Rice Uni.	125	ALH84001_Ap3_trail_2	3.414	0.009	0.028	0.013	0.000	100.090	0.000	0.000	0.000	*100.090*
Data Collection	**Point**	**Comment**	**MgO**	**Al2O3**	**MnO**	**Ce2O3**	**Nd2O3**	**Total**	**O=F,Cl**	**-O=F2**	**-O=Cl2**	**Total recalc**
Rice Uni.	126	ALH84001_Ap3_trail_3	3.432	0.014	0.028	0.046	0.000	100.547	0.002	0.000	0.002	*100.545*
Rice Uni.	127	ALH84001_Ap3_trail_4	3.377	0.000	0.031	0.062	0.000	100.609	0.002	0.000	0.002	*100.607*
Rice Uni.	128	ALH84001_Ap3_trail_5	3.399	0.000	0.011	0.062	0.000	100.592	0.001	0.000	0.001	*100.591*
Rice Uni.	129	ALH84001_Ap3_trail_6	3.490	0.046	0.036	0.058	0.135	99.833	0.000	0.000	0.000	*99.833*
Rice Uni.	139	ALH84001_Ap4_gray_3	3.373	0.001	0.056	0.047	0.000	99.856	0.002	0.000	0.002	*99.854*
Rice Uni.	140	ALH84001_Ap4_gray_4	3.465	0.075	0.067	0.000	0.000	100.414	0.001	0.000	0.001	*100.413*
Rice Uni.	142	ALH84001_Ap4_gray_6	3.446	0.000	0.023	0.070	0.000	100.265	0.002	0.000	0.002	*100.263*
Rice Uni.	143	ALH84001_Ap4_gray_7	3.416	0.031	0.042	0.035	0.251	99.998	0.001	0.000	0.001	*99.997*
Rice Uni.	144	ALH84001_Ap4_gray_8	3.368	0.025	0.000	0.035	0.000	99.453	0.001	0.000	0.001	*99.452*
Rice Uni.	145	ALH84001_Ap4_gray_9	3.408	0.040	0.042	0.030	0.025	99.558	0.000	0.000	0.000	*99.558*
Rice Uni.	146	ALH84001_Ap4_gray_10	3.449	0.052	0.000	0.053	0.163	97.934	0.002	0.000	0.002	*97.932*
Rice Uni.	147	ALH84001_Ap4_gray_11	3.366	0.004	0.028	0.078	0.113	100.616	0.004	0.000	0.004	*100.612*
Rice Uni.	148	ALH84001_Ap4_gray_12	3.409	0.016	0.085	0.040	0.102	101.213	0.003	0.000	0.003	*101.210*
Rice Uni.	149	ALH84001_Ap5_1	3.427	0.007	0.018	0.098	0.286	100.365	0.000	0.000	0.000	*100.365*
Rice Uni.	150	ALH84001_Ap5_2	3.450	0.000	0.044	0.040	0.313	100.371	0.002	0.000	0.002	*100.369*
Rice Uni.	151	ALH84001_Ap5_3	3.361	0.000	0.000	0.054	0.210	100.035	0.000	0.000	0.000	*100.035*
Rice Uni.	152	ALH84001_Ap5_4	3.357	0.019	0.022	0.048	0.000	100.093	0.001	0.000	0.001	*100.092*
Rice Uni.	153	ALH84001_Ap5_5	3.404	0.001	0.003	0.010	0.000	99.816	0.002	0.000	0.002	*99.814*
Rice Uni.	154	ALH84001_Ap5_6	3.402	0.000	0.058	0.083	0.000	100.128	0.001	0.000	0.001	*100.127*
Rice Uni.	155	ALH84001_Ap5_7	3.393	0.017	0.000	0.015	0.068	100.010	0.001	0.000	0.001	*100.009*
Rice Uni.	156	ALH84001_Ap5_8	3.461	0.000	0.050	0.058	0.128	100.250	0.000	0.000	0.000	*100.250*
Rice Uni.	157	ALH84001_Ap6_1	3.433	0.000	0.043	0.046	0.000	101.165	0.000	0.000	0.000	*101.165*
Rice Uni.	158	ALH84001_Ap6_2	3.499	0.000	0.025	0.031	0.000	100.442	0.000	0.000	0.000	*100.442*
Rice Uni.	159	ALH84001_Ap6_3	3.445	0.000	0.042	0.063	0.035	100.446	0.000	0.000	0.000	*100.446*
Rice Uni.	160	ALH84001_Ap6_4	3.438	0.000	0.031	0.059	0.000	101.114	0.002	0.000	0.002	*101.112*
Rice Uni.	163	ALH84001_Ap6_7	3.424	0.000	0.073	0.033	0.000	101.070	0.000	0.000	0.000	*101.070*
Rice Uni.	164	ALH84001_Ap6_8	3.423	0.000	0.021	0.027	0.144	100.367	0.000	0.000	0.000	*100.367*
Rice Uni.	165	ALH84001_Ap6_9	3.407	0.006	0.042	0.010	0.108	100.272	0.002	0.000	0.002	*100.270*
Rice Uni.	166	ALH84001_Ap6_10	3.462	0.000	0.012	0.044	0.000	100.663	0.002	0.000	0.002	*100.661*
Rice Uni.	167	ALH84001_Ap7_1	3.394	0.000	0.025	0.058	0.000	100.852	0.000	0.000	0.000	*100.852*
Rice Uni.	168	ALH84001_Ap7_2	3.415	0.016	0.033	0.000	0.143	100.377	0.000	0.000	0.000	*100.377*
Rice Uni.	169	ALH84001_Ap7_3	3.393	0.009	0.033	0.021	0.138	100.799	0.000	0.000	0.000	*100.799*
Rice Uni.	170	ALH84001_Ap7_4	3.374	0.000	0.046	0.043	0.093	101.038	0.001	0.000	0.001	*101.037*

Data Collection	Point	Comment	MgO	Al2O3	MnO	Ce2O3	Nd2O3	Total	O=F,Cl	-O=F2	-O=Cl2	Total recalc
Rice Uni.	171	ALH84001_Ap7_5	3.397	0.000	0.028	0.051	0.000	101.175	0.001	0.000	0.001	*101.174*
Rice Uni.	172	ALH84001_Ap7_6	3.408	0.000	0.010	0.026	0.000	100.642	0.002	0.000	0.002	*100.640*
Rice Uni.	173	ALH84001_Ap7_7	3.433	0.000	0.017	0.065	0.000	99.861	0.001	0.000	0.001	*99.860*
Rice Uni.	174	ALH84001_Ap7_8	3.398	0.004	0.029	0.046	0.093	100.379	0.000	0.000	0.000	*100.379*
Rice Uni.	175	ALH84001_Ap7_9	3.348	0.213	0.026	0.060	0.000	99.305	0.000	0.000	0.000	*99.305*
Rice Uni.	176	ALH84001_Ap7_10	3.431	0.021	0.071	0.046	0.000	100.438	0.001	0.000	0.001	*100.437*
Rice Uni.	177	ALH84001_Ap7_11	3.362	0.000	0.054	0.084	0.117	100.417	0.000	0.000	0.000	*100.417*
Rice Uni.	178	ALH84001_Ap7_12	3.405	0.003	0.017	0.010	0.149	100.768	0.002	0.000	0.002	*100.766*
Rice Uni.	179	ALH84001_Ap7_13	3.385	0.022	0.038	0.058	0.200	100.311	0.001	0.000	0.001	*100.310*
Rice Uni.	180	ALH84001_Ap7_14	3.369	0.031	0.025	0.069	0.000	100.327	0.000	0.000	0.000	*100.327*
Rice Uni.	181	ALH84001_Ap7_15	3.432	0.018	0.000	0.021	0.000	100.412	0.000	0.000	0.000	*100.412*
Rice Uni.	182	ALH84001_Ap8_1	3.361	0.016	0.026	0.356	0.158	99.695	0.003	0.000	0.003	*99.692*
Rice Uni.	183	ALH84001_Ap8_2	3.367	0.025	0.073	0.387	0.000	98.477	0.001	0.000	0.001	*98.476*
Rice Uni.	186	ALH84001_Ap8_5	3.349	0.001	0.026	0.443	0.000	99.461	0.002	0.000	0.002	*99.459*
Rice Uni.	187	ALH84001_Ap8_6	3.456	0.000	0.047	0.363	0.000	100.080	0.002	0.000	0.002	*100.078*
Rice Uni.	189	ALH84001_Ap8_8	3.362	0.004	0.000	0.343	0.000	100.043	0.000	0.000	0.000	*100.043*
Rice Uni.	190	ALH84001_Ap8_9	3.403	0.000	0.001	0.319	0.000	100.353	0.000	0.000	0.000	*100.353*
Rice Uni.	192	ALH84001_Ap8_11	3.404	0.008	0.025	0.393	0.000	99.424	0.000	0.000	0.000	*99.424*
Rice Uni.	194	ALH84001_Ap8_13	3.458	0.000	0.018	0.382	0.055	99.828	0.001	0.000	0.001	*99.827*
Rice Uni.	196	ALH84001_Ap8_15	3.416	0.000	0.028	0.376	0.112	100.206	0.002	0.000	0.002	*100.204*
Rice Uni.	197	ALH84001_Ap8_16	3.374	0.032	0.032	0.329	0.000	99.647	0.000	0.000	0.000	*99.647*
Rice Uni.	198	ALH84001_Ap8_17	3.296	0.011	0.037	0.398	0.000	100.037	0.002	0.000	0.002	*100.035*
Rice Uni.	200	ALH84001_Ap9_in_OPX_1	3.442	0.000	0.026	0.180	0.000	100.287	0.000	0.000	0.000	*100.287*
Rice Uni.	201	ALH84001_Ap9_in_OPX_2	3.456	0.000	0.069	0.231	0.000	100.514	0.001	0.000	0.001	*100.513*
Rice Uni.	202	ALH84001_Ap9_in_OPX_3	3.453	0.009	0.016	0.241	0.000	99.811	0.002	0.000	0.002	*99.809*
Rice Uni.	203	ALH84001_Ap9_in_OPX_4	3.497	0.000	0.072	0.199	0.095	100.653	0.001	0.000	0.001	*100.652*
Rice Uni.	204	ALH84001_Ap9_in_OPX_5	3.542	0.000	0.043	0.197	0.062	100.769	0.002	0.000	0.002	*100.767*
Rice Uni.	205	ALH84001_Ap9_in_OPX_6	3.827	0.119	0.039	0.241	0.140	99.293	0.000	0.000	0.000	*99.293*
Rice Uni.	206	ALH84001_Ap9_in_OPX_7	3.456	0.000	0.032	0.202	0.000	100.894	0.000	0.000	0.000	*100.894*
		Average	**3.421**	**0.014**	**0.031**	**0.092**	**0.053**	**100.156**	**0.001**	**0.000**	**0.001**	**100.155**
		Min	*3.296*	*0.000*	*0.000*	*0.000*	*0.000*	*97.934*	*0.000*	*0.000*	*0.000*	*97.932*
		Max	*3.827*	*0.213*	*0.085*	*0.443*	*0.436*	*101.213*	*0.004*	*0.000*	*0.004*	*101.210*
		StDev	0.061	0.034	0.020	0.114	0.085	0.602	0.001	0.000	0.001	0.602

Supplementary Table 6. Summarized quantitative point analyses for apatite in ALH 84001. Data used to calculate average wt% and formula amounts were collected at Rice University (JEOL JXA-8530F Hyperprobe). Comments denote mineral names given at time of data collection.

Data Collection	Point	Comment	Na2O	SiO2	La2O3	K2O	CaO	FeO	Cl	P2O5	SO3	F
Rice Uni.	86	ALH84001_Ap1_bright_1	0.287	0.162	0.000	0.022	53.897	0.233	4.797	41.527	0.150	0.669
Rice Uni.	87	ALH84001_Ap1_bright_2	0.259	0.240	0.000	0.006	53.819	0.230	4.165	41.290	0.121	0.553
Rice Uni.	88	ALH84001_Ap1_bright_3	0.248	0.224	0.000	0.003	54.872	0.187	3.884	41.612	0.142	0.339
Rice Uni.	89	ALH84001_Ap1_bright_4	0.276	0.249	0.000	0.000	54.203	0.170	4.337	41.292	0.135	0.488
Rice Uni.	90	ALH84001_Ap1_bright_5	0.211	0.186	0.000	0.013	53.595	0.107	5.045	41.071	0.112	0.573
Rice Uni.	91	ALH84001_Ap1_bright_6	0.331	0.305	0.000	0.025	52.733	0.194	4.953	40.613	0.124	0.300
Rice Uni.	130	ALH84001_Ap4_bright_1	0.319	0.128	0.000	0.000	54.656	0.073	3.904	41.798	0.120	0.548
Rice Uni.	131	ALH84001_Ap4_bright_2	0.256	0.161	0.000	0.039	54.358	0.207	3.848	42.127	0.111	0.685
Rice Uni.	132	ALH84001_Ap4_bright_3	0.268	0.148	0.000	0.015	53.263	0.130	4.252	41.654	0.118	0.763
Rice Uni.	133	ALH84001_Ap4_bright_4	0.234	0.212	0.102	0.008	53.254	0.164	4.724	41.477	0.108	0.666
Rice Uni.	134	ALH84001_Ap4_bright_5	0.184	0.155	0.000	0.000	53.513	0.167	4.005	41.477	0.115	0.787
Rice Uni.	135	ALH84001_Ap4_bright_6	0.283	0.183	0.000	0.000	53.232	0.197	4.232	41.708	0.106	0.919
Rice Uni.	136	ALH84001_Ap4_bright_7	0.259	0.126	0.000	0.017	53.815	0.110	4.569	41.796	0.140	0.606
		Average	**0.263**	**0.191**	**0.008**	**0.011**	**53.785**	**0.167**	**4.363**	**41.496**	**0.123**	**0.607**
		Min	*0.184*	*0.126*	*0.000*	*0.000*	*52.733*	*0.073*	*3.848*	*40.613*	*0.106*	*0.300*
		Max	*0.331*	*0.305*	*0.102*	*0.039*	*54.872*	*0.233*	*5.045*	*42.127*	*0.150*	*0.919*
		StDev	0.040	0.053	0.028	0.012	0.615	0.049	0.416	0.377	0.014	0.172

Data Collection	Point	Comment	MgO	Al2O3	MnO	Ce2O3	Nd2O3	Total	O=F,Cl	-O=F2	-O=Cl2	Total recalc
Rice Uni.	86	ALH84001_Ap1_bright_1	0.043	0.020	0.068	0.047	0.100	102.022	1.364	0.282	1.082	*100.658*
Rice Uni.	87	ALH84001_Ap1_bright_2	0.047	0.008	0.049	0.000	0.224	101.011	1.173	0.233	0.940	*99.838*
Rice Uni.	88	ALH84001_Ap1_bright_3	0.008	0.000	0.060	0.038	0.000	101.617	1.019	0.143	0.876	*100.598*
Rice Uni.	89	ALH84001_Ap1_bright_4	0.031	0.008	0.035	0.022	0.000	101.246	1.184	0.205	0.979	*100.062*
Rice Uni.	90	ALH84001_Ap1_bright_5	0.011	0.000	0.012	0.000	0.183	101.119	1.380	0.241	1.138	*99.739*
Rice Uni.	91	ALH84001_Ap1_bright_6	0.050	0.175	0.020	0.000	0.000	99.823	1.244	0.126	1.118	*98.579*
Rice Uni.	130	ALH84001_Ap4_bright_1	0.033	0.000	0.004	0.016	0.373	101.972	1.112	0.231	0.881	*100.860*
Rice Uni.	131	ALH84001_Ap4_bright_2	0.023	0.100	0.021	0.040	0.121	102.097	1.157	0.288	0.868	*100.940*
Rice Uni.	132	ALH84001_Ap4_bright_3	0.026	0.052	0.022	0.035	0.303	101.049	1.281	0.321	0.959	*99.768*
Rice Uni.	133	ALH84001_Ap4_bright_4	0.028	0.003	0.019	0.052	0.000	101.051	1.346	0.280	1.066	*99.705*
Rice Uni.	134	ALH84001_Ap4_bright_5	0.039	0.052	0.058	0.025	0.000	100.577	1.235	0.331	0.904	*99.342*
Rice Uni.	135	ALH84001_Ap4_bright_6	0.035	0.161	0.000	0.016	0.150	101.222	1.342	0.387	0.955	*99.880*
Rice Uni.	136	ALH84001_Ap4_bright_7	0.033	0.004	0.040	0.030	0.000	101.545	1.286	0.255	1.031	*100.259*
		Average	**0.031**	**0.045**	**0.031**	**0.025**	**0.112**	**101.258**	**1.240**	**0.256**	**0.984**	**100.018**
		Min	*0.008*	*0.000*	*0.000*	*0.000*	*0.000*	*99.823*	*1.019*	*0.126*	*0.868*	*98.579*
		Max	*0.050*	*0.175*	*0.068*	*0.052*	*0.373*	*102.097*	*1.380*	*0.387*	*1.138*	*100.940*
		StDev	0.012	0.062	0.022	0.018	0.129	0.626	0.108	0.072	0.094	0.657

Supplementary Table 7. Summarized quantitative point analyses for apatite (contained within CPX) in NWA 998. Data used to calculate average wt% and formula amounts were collected at Rice University (JEOL JXA-8530F Hyperprobe). Comments denote mineral names given at time of data collection.

Data Collection	Point	Comment	Na2O	SiO2	La2O3	K2O	CaO	FeO	Cl	P2O5	SO3	F
Rice Uni.	34	NWA998_Ap3_in_CPX_1	0.042	0.553	0.733	0.012	53.378	0.670	3.626	41.272	0.029	1.234
Rice Uni.	35	NWA998_Ap3_in_CPX_2	0.007	0.564	0.208	0.000	53.378	0.864	3.376	40.886	0.056	1.262
Rice Uni.	36	NWA998_Ap3_in_CPX_3	0.063	0.589	0.592	0.000	53.893	0.807	3.511	40.807	0.040	1.406
Rice Uni.	37	NWA998_Ap3_in_CPX_4	0.023	0.563	0.501	0.000	54.236	0.814	3.060	40.816	0.029	1.230
		Average	**0.034**	**0.567**	**0.509**	**0.003**	**53.721**	**0.789**	**3.393**	**40.945**	**0.039**	**1.283**
		Min	*0.007*	*0.553*	*0.208*	*0.000*	*53.378*	*0.670*	*3.060*	*40.807*	*0.029*	*1.230*
		Max	*0.063*	*0.589*	*0.733*	*0.012*	*54.236*	*0.864*	*3.626*	*41.272*	*0.056*	*1.406*
		StDev	0.024	0.015	0.222	0.006	0.420	0.083	0.245	0.221	0.013	0.083

Data Collection	Point	Comment	MgO	Al2O3	MnO	Ce2O3	Nd2O3	Total	O=F,Cl	-O=F2	-O=Cl2	Total recalc
Rice Uni.	34	NWA998_Ap3_in_CPX_1	0.048	0.000	0.103	0.233	0.154	102.087	1.338	0.520	0.818	*100.749*
Rice Uni.	35	NWA998_Ap3_in_CPX_2	0.054	0.000	0.087	0.300	0.000	101.042	1.293	0.531	0.762	*99.749*
Rice Uni.	36	NWA998_Ap3_in_CPX_3	0.049	0.000	0.091	0.276	0.092	102.216	1.384	0.592	0.792	*100.832*
Rice Uni.	37	NWA998_Ap3_in_CPX_4	0.043	0.009	0.088	0.298	0.000	101.710	1.208	0.518	0.690	*100.502*
		Average	**0.049**	**0.002**	**0.092**	**0.277**	**0.062**	**101.764**	**1.306**	**0.540**	**0.766**	**100.458**
		Min	*0.043*	*0.000*	*0.087*	*0.233*	*0.000*	*101.042*	*1.208*	*0.518*	*0.690*	*99.749*
		Max	*0.054*	*0.009*	*0.103*	*0.300*	*0.154*	*102.216*	*1.384*	*0.592*	*0.818*	*100.832*
		StDev	0.005	0.005	0.007	0.031	0.075	0.527	0.075	0.035	0.055	0.493

Supplementary Table 8. Summarized quantitative point analyses for apatite in NWA 998. Data used to calculate average wt% and formula amounts were collected at Rice University (JEOL JXA-8530F Hyperprobe). Comments denote mineral names given at time of data collection.

Data Collection	Point	Comment	Na2O	SiO2	La2O3	K2O	CaO	FeO	Cl	P2O5	SO3	F
Rice Uni.	4	NWA998_Ap1_1	0.050	0.250	0.298	0.055	54.674	0.638	2.942	41.704	0.024	1.188
Rice Uni.	5	NWA998_Ap1_2	0.076	0.349	0.268	0.044	54.717	0.645	2.979	41.307	0.009	1.098
Rice Uni.	6	NWA998_Ap1_3	0.062	0.374	0.363	0.035	55.093	0.595	2.700	41.421	0.000	1.070
Rice Uni.	7	NWA998_Ap1_4	0.097	0.251	1.122	0.044	54.833	0.468	2.844	41.266	0.013	1.117
Rice Uni.	9	NWA998_Ap1_6	0.074	0.234	0.252	0.085	54.464	0.467	2.961	41.421	0.015	1.155
Rice Uni.	10	NWA998_Ap1_7	0.046	0.174	0.192	0.034	54.212	0.675	2.812	41.543	0.060	1.313
Rice Uni.	11	NWA998_Ap1_8	0.040	0.222	0.173	0.046	54.445	0.665	2.920	41.568	0.011	1.160
Rice Uni.	12	NWA998_Ap1_9	0.070	0.208	0.601	0.054	55.143	0.655	2.624	41.256	0.003	1.129
Rice Uni.	13	NWA998_Ap1_10	0.106	0.160	0.000	0.011	54.599	0.605	2.722	41.838	0.067	1.161
Rice Uni.	14	NWA998_Ap1_11	0.072	0.301	0.382	0.038	54.576	0.581	2.810	41.672	0.000	1.191
Rice Uni.	15	NWA998_Ap1_12	0.095	0.164	0.920	0.038	54.370	0.741	2.773	41.352	0.078	0.980
Rice Uni.	16	NWA998_Ap1_13	0.088	0.170	0.383	0.079	54.483	0.594	3.245	41.270	0.019	1.369
Rice Uni.	17	NWA998_Ap1_14	0.094	0.293	0.376	0.083	54.009	0.684	3.043	40.950	0.031	1.192
Rice Uni.	18	NWA998_Ap1_15	0.074	0.126	0.350	0.038	55.340	0.738	2.423	41.150	0.123	0.954
Rice Uni.	19	NWA998_Ap1_16	0.067	0.189	0.387	0.073	53.275	0.701	3.517	40.922	0.060	1.391
Rice Uni.	20	NWA998_Ap1_17	0.029	0.311	0.000	0.125	53.928	0.691	3.335	41.219	0.017	1.525
Rice Uni.	21	NWA998_Ap1_18	0.130	0.400	0.226	0.153	53.469	0.778	3.045	40.453	0.257	1.490
Rice Uni.	22	NWA998_Ap2_1	0.019	0.082	0.279	0.000	54.457	0.517	3.167	41.726	0.012	1.792
Rice Uni.	23	NWA998_Ap2_2	0.058	0.125	0.357	0.017	54.099	0.647	3.226	41.264	0.011	1.508
Rice Uni.	24	NWA998_Ap2_3	0.082	0.074	0.000	0.000	53.810	0.614	3.069	41.010	0.058	1.715
Rice Uni.	25	NWA998_Ap2_4	0.052	0.254	0.404	0.004	53.801	0.711	3.285	41.360	0.046	1.598
Rice Uni.	26	NWA998_Ap2_5	0.104	0.080	0.317	0.003	54.329	0.531	3.241	41.504	0.003	1.704
Rice Uni.	27	NWA998_Ap2_6	0.000	0.154	0.223	0.002	54.084	0.577	3.171	41.788	0.000	1.750
Rice Uni.	28	NWA998_Ap2_7	0.100	0.100	0.038	0.000	54.354	0.627	3.277	41.706	0.000	1.733
Rice Uni.	29	NWA998_Ap2_8	0.016	0.174	0.163	0.000	51.240	0.587	3.246	40.499	0.013	2.061
Rice Uni.	30	NWA998_Ap2_9	0.080	0.175	0.000	0.004	53.765	0.497	3.442	41.765	0.004	1.759
Rice Uni.	31	NWA998_Ap2_10	0.042	0.181	0.191	0.008	54.019	0.547	3.312	41.425	0.000	1.842
Rice Uni.	32	NWA998_Ap2_11	0.060	0.184	0.000	0.015	54.444	0.481	2.942	41.493	0.008	1.528
Rice Uni.	33	NWA998_Ap2_12	0.102	0.122	0.182	0.008	54.298	0.474	3.273	41.922	0.013	1.702
Rice Uni.	39	NWA998_Ap4_2	0.031	0.304	0.196	0.045	53.624	0.544	3.287	40.962	0.047	1.308
Rice Uni.	40	NWA998_Ap4_3	0.071	0.228	0.464	0.021	53.121	0.567	3.228	41.192	0.048	1.320
Rice Uni.	41	NWA998_Ap4_4	0.076	0.272	0.177	0.014	51.980	0.734	3.311	40.581	0.065	1.351
Rice Uni.	42	NWA998_Ap4_5	0.029	0.207	0.293	0.017	52.824	0.721	3.024	40.160	0.085	1.245
Rice Uni.	43	NWA998_Ap4_6	0.043	0.408	0.406	0.004	53.145	0.933	3.470	40.738	0.042	1.210
Rice Uni.	44	NWA998_Ap4_7	0.052	0.400	0.067	0.004	53.101	1.187	3.485	41.126	0.007	1.179
Rice Uni.	45	NWA998_Ap4_8	0.065	0.278	0.738	0.000	53.103	1.283	3.297	41.379	0.029	1.253

Data Collection	Point	Comment	Na2O	SiO2	La2O3	K2O	CaO	FeO	Cl	P2O5	SO3	F
Rice Uni.	46	NWA998_Ap4_9	0.070	0.385	0.364	0.025	53.050	1.020	3.344	41.115	0.032	1.209
Rice Uni.	47	NWA998_Ap4_10	0.051	0.362	0.149	0.000	53.458	1.100	3.466	40.824	0.026	1.394
Rice Uni.	48	NWA998_Ap5_1	0.071	0.173	0.331	0.051	53.684	0.647	3.231	42.017	0.015	1.264
Rice Uni.	49	NWA998_Ap5_2	0.078	0.138	0.396	0.027	53.404	0.624	3.458	41.377	0.005	1.274
Rice Uni.	50	NWA998_Ap5_3	0.033	0.154	0.121	0.002	53.503	0.730	3.621	41.276	0.024	1.180
Rice Uni.	51	NWA998_Ap5_4	0.068	0.173	0.244	0.020	53.418	0.704	3.139	40.099	0.111	1.455
Rice Uni.	52	NWA998_Ap5_5	0.080	0.370	0.000	0.044	53.146	0.768	3.189	40.569	0.074	1.461
Rice Uni.	53	NWA998_Ap5_6	0.083	0.245	0.089	0.053	53.510	0.728	3.261	40.794	0.100	1.350
Rice Uni.	54	NWA998_Ap5_7	0.036	0.631	0.341	0.060	52.248	0.910	3.347	40.342	0.065	1.176
Rice Uni.	57	NWA998_Ap5_10	0.064	0.626	0.000	0.172	53.741	0.661	3.456	41.253	0.010	1.234
Rice Uni.	59	NWA998_Ap5_12	0.112	0.586	0.000	0.116	52.525	0.997	3.122	40.392	0.187	1.373
Rice Uni.	60	NWA998_Ap6_1	0.069	0.170	0.000	0.015	53.180	0.630	3.656	41.261	0.012	1.163
Rice Uni.	61	NWA998_Ap6_2	0.024	0.784	0.615	0.117	52.986	0.553	3.453	41.124	0.016	1.187
Rice Uni.	62	NWA998_Ap6_3	0.139	0.165	0.227	0.022	53.474	0.554	3.222	41.331	0.140	1.261
Rice Uni.	63	NWA998_Ap6_4	0.044	0.158	0.097	0.055	54.014	0.364	3.476	41.490	0.013	1.340
Rice Uni.	64	NWA998_Ap6_5	0.063	0.901	0.000	0.133	53.497	0.507	3.404	41.082	0.010	1.250
Rice Uni.	65	NWA998_Ap6_6	0.078	0.281	0.753	0.047	53.379	0.443	3.337	41.773	0.006	1.382
Rice Uni.	66	NWA998_Ap6_7	0.043	0.474	0.273	0.104	52.580	0.524	3.410	40.436	0.039	1.168
Rice Uni.	67	NWA998_Ap6_8	0.059	0.272	0.415	0.088	53.823	0.527	3.410	41.646	0.031	1.388
Rice Uni.	68	NWA998_Ap6_9	0.114	0.200	0.211	0.062	53.856	0.697	3.214	41.306	0.084	1.358
Rice Uni.	71	NWA998_Ap6_12	0.090	0.324	0.266	0.095	53.261	0.877	3.431	41.336	0.000	1.465
Rice Uni.	72	NWA998_Ap6_13	0.070	0.259	0.459	0.104	53.736	0.907	3.267	41.013	0.009	1.361
Rice Uni.	73	NWA998_Ap6_14	0.066	0.260	0.511	0.083	53.929	0.787	3.271	41.228	0.007	1.393
Rice Uni.	74	NWA998_Ap6_15	0.067	0.286	0.094	0.099	53.723	0.807	3.224	41.376	0.006	1.382
Rice Uni.	77	NWA998_Ap7_3	0.073	0.550	0.000	0.049	54.006	0.634	3.471	41.038	0.035	1.291
Rice Uni.	78	NWA998_Ap8_1	0.032	0.572	0.000	0.006	53.616	0.896	3.667	40.968	0.000	1.238
Rice Uni.	79	NWA998_Ap8_2	0.071	0.593	0.175	0.000	53.613	0.773	3.843	41.135	0.008	1.261
Rice Uni.	80	NWA998_Ap8_3	0.023	0.648	0.432	0.006	53.339	0.720	3.693	40.776	0.009	1.246
Rice Uni.	81	NWA998_Ap8_4	0.080	0.563	0.521	0.011	53.174	0.926	3.756	40.685	0.020	1.256
Rice Uni.	82	NWA998_Ap8_5	0.039	0.560	0.596	0.023	53.825	0.843	3.867	40.794	0.004	1.373
Rice Uni.	83	NWA998_Ap8_6	0.126	1.437	0.009	0.198	52.995	0.647	3.614	40.771	0.018	1.334
Rice Uni.	84	NWA998_Ap8_7	0.079	0.444	0.000	0.164	53.096	0.787	3.306	40.417	0.040	1.574
		Average	**0.067**	**0.319**	**0.272**	**0.048**	**53.706**	**0.691**	**3.251**	**41.161**	**0.036**	**1.354**
		Min	*0.000*	*0.074*	*0.000*	*0.000*	*51.240*	*0.364*	*2.423*	*40.099*	*0.000*	*0.954*
		Max	*0.139*	*1.437*	*1.122*	*0.198*	*55.340*	*1.283*	*3.867*	*42.017*	*0.257*	*2.061*
		StDev	0.028	0.225	0.233	0.048	0.741	0.176	0.288	0.440	0.046	0.216

Data Collection	Point	Comment	MgO	Al2O3	MnO	Ce2O3	Nd2O3	Total	O=F,Cl	-O=F2	-O=Cl2	Total recalc
Rice Uni.	4	NWA998_Ap1_1	0.042	0.000	0.066	0.126	0.000	102.057	1.164	0.500	0.664	*100.893*
Rice Uni.	5	NWA998_Ap1_2	0.054	0.000	0.077	0.245	0.011	101.879	1.135	0.462	0.672	*100.744*
Rice Uni.	6	NWA998_Ap1_3	0.051	0.000	0.085	0.219	0.000	102.068	1.060	0.451	0.609	*101.008*
Rice Uni.	7	NWA998_Ap1_4	0.052	0.000	0.111	0.239	0.021	102.478	1.112	0.470	0.642	*101.366*
Rice Uni.	9	NWA998_Ap1_6	0.061	0.000	0.117	0.196	0.282	101.784	1.155	0.486	0.668	*100.630*
Rice Uni.	10	NWA998_Ap1_7	0.045	0.018	0.125	0.136	0.000	101.385	1.187	0.553	0.634	*100.198*
Rice Uni.	11	NWA998_Ap1_8	0.062	0.000	0.065	0.277	0.000	101.654	1.147	0.488	0.659	*100.507*
Rice Uni.	12	NWA998_Ap1_9	0.043	0.011	0.059	0.174	0.000	102.030	1.068	0.475	0.592	*100.963*
Rice Uni.	13	NWA998_Ap1_10	0.045	0.000	0.097	0.182	0.000	101.593	1.103	0.489	0.614	*100.490*
Rice Uni.	14	NWA998_Ap1_11	0.048	0.040	0.082	0.125	0.012	101.930	1.136	0.501	0.634	*100.794*
Rice Uni.	15	NWA998_Ap1_12	0.065	0.000	0.127	0.148	0.000	101.851	1.038	0.413	0.626	*100.813*
Rice Uni.	16	NWA998_Ap1_13	0.039	0.000	0.080	0.153	0.000	101.972	1.309	0.576	0.732	*100.663*
Rice Uni.	17	NWA998_Ap1_14	0.046	0.000	0.116	0.190	0.000	101.107	1.189	0.502	0.687	*99.918*
Rice Uni.	18	NWA998_Ap1_15	0.069	0.000	0.124	0.215	0.000	101.724	0.948	0.402	0.547	*100.776*
Rice Uni.	19	NWA998_Ap1_16	0.032	0.000	0.084	0.183	0.000	100.881	1.379	0.586	0.794	*99.502*
Rice Uni.	20	NWA998_Ap1_17	0.025	0.035	0.119	0.181	0.232	101.772	1.395	0.642	0.752	*100.377*
Rice Uni.	21	NWA998_Ap1_18	0.020	0.000	0.258	0.246	0.000	100.925	1.315	0.627	0.687	*99.611*
Rice Uni.	22	NWA998_Ap2_1	0.025	0.000	0.078	0.116	0.000	102.270	1.469	0.755	0.715	*100.801*
Rice Uni.	23	NWA998_Ap2_2	0.050	0.000	0.071	0.162	0.111	101.706	1.363	0.635	0.728	*100.343*
Rice Uni.	24	NWA998_Ap2_3	0.045	0.000	0.095	0.119	0.000	100.691	1.415	0.722	0.692	*99.276*
Rice Uni.	25	NWA998_Ap2_4	0.050	0.021	0.060	0.229	0.005	101.880	1.414	0.673	0.741	*100.466*
Rice Uni.	26	NWA998_Ap2_5	0.064	0.000	0.084	0.209	0.000	102.173	1.449	0.718	0.731	*100.724*
Rice Uni.	27	NWA998_Ap2_6	0.037	0.000	0.122	0.150	0.000	102.058	1.452	0.737	0.715	*100.606*
Rice Uni.	28	NWA998_Ap2_7	0.059	0.000	0.106	0.154	0.043	102.297	1.469	0.730	0.739	*100.828*
Rice Uni.	29	NWA998_Ap2_8	0.084	1.399	0.096	0.172	0.050	99.800	1.600	0.868	0.732	*98.200*
Rice Uni.	30	NWA998_Ap2_9	0.063	0.026	0.109	0.182	0.000	101.871	1.517	0.741	0.777	*100.354*
Rice Uni.	31	NWA998_Ap2_10	0.054	0.000	0.109	0.263	0.237	102.230	1.523	0.776	0.747	*100.707*
Rice Uni.	32	NWA998_Ap2_11	0.060	0.029	0.089	0.173	0.371	101.877	1.307	0.643	0.664	*100.570*
Rice Uni.	33	NWA998_Ap2_12	0.074	0.000	0.103	0.171	0.135	102.579	1.455	0.717	0.739	*101.124*
Rice Uni.	39	NWA998_Ap4_2	0.063	0.000	0.115	0.211	0.107	100.844	1.292	0.551	0.742	*99.552*
Rice Uni.	40	NWA998_Ap4_3	0.076	0.014	0.078	0.197	0.000	100.625	1.284	0.556	0.728	*99.341*
Rice Uni.	41	NWA998_Ap4_4	0.064	0.000	0.105	0.161	0.101	98.992	1.316	0.569	0.747	*97.676*
Rice Uni.	42	NWA998_Ap4_5	0.052	0.001	0.131	0.182	0.000	98.971	1.207	0.524	0.682	*97.764*
Rice Uni.	43	NWA998_Ap4_6	0.067	0.000	0.061	0.306	0.092	100.925	1.293	0.509	0.783	*99.633*
Rice Uni.	44	NWA998_Ap4_7	0.046	0.000	0.082	0.250	0.000	100.986	1.283	0.496	0.786	*99.703*
Rice Uni.	45	NWA998_Ap4_8	0.045	0.000	0.071	0.166	0.000	101.707	1.272	0.528	0.744	*100.435*

Data Collection	Point	Comment	MgO	Al2O3	MnO	Ce2O3	Nd2O3	Total	O=F,Cl	-O=F2	-O=Cl2	Total recalc
Rice Uni.	46	NWA998_Ap4_9	0.057	0.000	0.086	0.276	0.095	101.128	1.264	0.509	0.755	*99.864*
Rice Uni.	47	NWA998_Ap4_10	0.073	0.000	0.097	0.208	0.017	101.225	1.369	0.587	0.782	*99.856*
Rice Uni.	48	NWA998_Ap5_1	0.058	0.007	0.090	0.128	0.000	101.767	1.261	0.532	0.729	*100.506*
Rice Uni.	49	NWA998_Ap5_2	0.050	0.005	0.111	0.129	0.008	101.084	1.317	0.536	0.780	*99.767*
Rice Uni.	50	NWA998_Ap5_3	0.034	0.000	0.091	0.119	0.024	100.912	1.314	0.497	0.817	*99.598*
Rice Uni.	51	NWA998_Ap5_4	0.065	0.017	0.100	0.176	0.000	99.789	1.321	0.613	0.708	*98.468*
Rice Uni.	52	NWA998_Ap5_5	0.097	0.000	0.099	0.147	0.000	100.044	1.335	0.615	0.720	*98.709*
Rice Uni.	53	NWA998_Ap5_6	0.089	0.000	0.139	0.171	0.005	100.617	1.304	0.568	0.736	*99.313*
Rice Uni.	54	NWA998_Ap5_7	0.106	0.077	0.123	0.152	0.000	99.614	1.250	0.495	0.755	*98.364*
Rice Uni.	57	NWA998_Ap5_10	0.074	0.059	0.084	0.169	0.000	101.603	1.299	0.520	0.780	*100.304*
Rice Uni.	59	NWA998_Ap5_12	0.162	0.061	0.195	0.104	0.037	99.969	1.283	0.578	0.704	*98.686*
Rice Uni.	60	NWA998_Ap6_1	0.036	0.000	0.109	0.175	0.000	100.476	1.315	0.490	0.825	*99.161*
Rice Uni.	61	NWA998_Ap6_2	0.036	0.115	0.138	0.183	0.032	101.363	1.279	0.500	0.779	*100.084*
Rice Uni.	62	NWA998_Ap6_3	0.047	0.000	0.155	0.182	0.086	101.005	1.258	0.531	0.727	*99.747*
Rice Uni.	63	NWA998_Ap6_4	0.040	0.000	0.047	0.096	0.000	101.234	1.349	0.564	0.784	*99.885*
Rice Uni.	64	NWA998_Ap6_5	0.049	0.104	0.070	0.154	0.134	101.358	1.294	0.526	0.768	*100.064*
Rice Uni.	65	NWA998_Ap6_6	0.038	0.018	0.115	0.244	0.000	101.894	1.335	0.582	0.753	*100.559*
Rice Uni.	66	NWA998_Ap6_7	0.033	0.033	0.070	0.262	0.000	99.449	1.261	0.492	0.769	*98.188*
Rice Uni.	67	NWA998_Ap6_8	0.048	0.000	0.091	0.160	0.000	101.958	1.354	0.584	0.769	*100.604*
Rice Uni.	68	NWA998_Ap6_9	0.033	0.005	0.098	0.183	0.060	101.481	1.297	0.572	0.725	*100.184*
Rice Uni.	71	NWA998_Ap6_12	0.041	0.036	0.043	0.166	0.000	101.431	1.391	0.617	0.774	*100.040*
Rice Uni.	72	NWA998_Ap6_13	0.046	0.045	0.084	0.175	0.000	101.535	1.310	0.573	0.737	*100.225*
Rice Uni.	73	NWA998_Ap6_14	0.052	0.000	0.049	0.205	0.000	101.841	1.325	0.587	0.738	*100.516*
Rice Uni.	74	NWA998_Ap6_15	0.043	0.039	0.085	0.176	0.102	101.509	1.309	0.582	0.727	*100.200*
Rice Uni.	77	NWA998_Ap7_3	0.059	0.033	0.105	0.030	0.158	101.532	1.327	0.544	0.783	*100.205*
Rice Uni.	78	NWA998_Ap8_1	0.043	0.000	0.095	0.285	0.000	101.418	1.349	0.521	0.827	*100.069*
Rice Uni.	79	NWA998_Ap8_2	0.054	0.013	0.123	0.304	0.040	102.006	1.398	0.531	0.867	*100.608*
Rice Uni.	80	NWA998_Ap8_3	0.042	0.000	0.087	0.240	0.000	101.261	1.358	0.525	0.833	*99.903*
Rice Uni.	81	NWA998_Ap8_4	0.045	0.039	0.093	0.259	0.186	101.614	1.376	0.529	0.847	*100.238*
Rice Uni.	82	NWA998_Ap8_5	0.040	0.027	0.106	0.253	0.000	102.350	1.451	0.578	0.873	*100.899*
Rice Uni.	83	NWA998_Ap8_6	0.064	0.336	0.105	0.211	0.000	101.865	1.377	0.562	0.815	*100.488*
Rice Uni.	84	NWA998_Ap8_7	0.045	0.108	0.043	0.142	0.000	100.245	1.409	0.663	0.746	*98.836*
		Average	**0.054**	**0.041**	**0.098**	**0.186**	**0.041**	**101.326**	**1.304**	**0.570**	**0.734**	**100.022**
		Min	*0.020*	*0.000*	*0.043*	*0.030*	*0.000*	*98.971*	*0.948*	*0.402*	*0.547*	97.676
		Max	*0.162*	*1.399*	*0.258*	*0.306*	*0.371*	*102.579*	*1.600*	*0.868*	*0.873*	101.366
		StDev	0.021	0.174	0.033	0.053	0.076	0.822	0.121	0.091	0.065	0.833

Supplementary Table 9. Normalized formula amount calculation for datapoint 22 ("Kep9a"). Calculated formula amounts noted in table were derived from the quantitate point analysis datapoint which exhibited the lowest content of sodium.

Data Collection: JSC-ARES - Point 22 - Kep9a - Normalized to 28 O (apfu)									
Oxide	**wt%**	**molecular weight of oxide**	**molecular proportion of oxide**	**number of oxygen atoms in oxide concerned**	**atomic proportion of oxygen from each molecule**	**no. of anions on the basis of X# (O,OH)**	**no. atoms per oxygen**	**no. of ions in formula**	
Na_2O	0.291	61.979	0.005	1	0.005	0.052	2	**0.10**	***Na***
CaO	46.381	56.077	0.827	1	0.827	9.091	1	**9.09**	***Ca***
MgO	2.583	40.304	0.064	1	0.064	0.704	1	**0.70**	***Mg***
FeO	3.583	71.844	0.050	1	0.050	0.548	1	**0.55**	***Fe***
P_2O_5	45.353	141.940	0.320	5	1.598	17.561	0.4	**7.02**	***P***
SiO2	0.119	60.080	0.002	2	0.004	0.044	0.5	**0.02**	***Si***
Total	**98.310**				**2.547**	**28**		**17.49**	
					28.000	*Normalized to 28 O for merrillite, keplerite			
					2.547				
					10.992				

Mg#	56.00	Mg ratio = 100 x Mg / (Mg + Fe)
Na#	1.09	Na ratio = 100 x Na / (Na + Ca)

Supplementary Table 10. Normalized formula amount calculation for Datapoint 210 ("Tissint_merrl_4"). Calculated formula amounts noted in table were derived from the quantitate point analysis datapoint which exhibited the highest content of sodium.

Data Collection: Rice Uni. - Point 210 - Tissint_merr1_4 - Normalized to 28 O (apfu)									
Oxide	**wt%**	**molecular weight of oxide**	**molecular proportion of oxide**	**number of oxygen atoms in oxide concerned**	**atomic proportion of oxygen from each molecule**	**no. of anions on the basis of X# (O,OH)**	**no. atoms per oxygen**	**no. of ions in formula**	
Na_2O	0.981	61.979	0.016	1	0.016	0.170	2	**0.34**	***Na***
CaO	46.423	56.077	0.828	1	0.828	8.910	1	**8.91**	***Ca***
MgO	3.196	40.304	0.079	1	0.079	0.853	1	**0.85**	***Mg***
FeO	2.387	71.844	0.033	1	0.033	0.358	1	**0.36**	***Fe***
P_2O_5	46.127	141.940	0.325	5	1.625	17.488	0.4	**7.00**	***P***
SiO2	0.618	60.080	0.010	2	0.021	0.221	0.5	**0.11**	***Si***
Total	**99.732**				**2.602**	**28**		**17.57**	
					28.000	*Normalized to 28 O for merrillite, keplerite			
					2.602				
					10.762				

Mg#	70.23	Mg ratio = 100 x Mg / (Mg + Fe)
Na#	3.68	Na ratio = 100 x Na / (Na + Ca)

Supplementary Table 11. Normalized formula amount calculation for datapoint 15 ("Kep5f"). Calculated formula amounts noted in table were derived from the quantitate point analysis datapoint which exhibited the lowest content of magnesium.

Data Collection: JSC-ARES - Point 15 - Kep5f - Normalized to 28 O (apfu)									
Oxide	**wt%**	**molecular weight of oxide**	**molecular proportion of oxide**	**number of oxygen atoms in oxide concerned**	**atomic proportion of oxygen from each molecule**	**no. of anions on the basis of X# (O,OH)**	**no. atoms per oxygen**	**no. of ions in formula**	
Na_2O	0.453	61.979	0.007	1	0.007	0.080	2	**0.16**	***Na***
CaO	46.960	56.077	0.837	1	0.837	9.209	1	**9.21**	***Ca***
MgO	2.567	40.304	0.064	1	0.064	0.700	1	**0.70**	***Mg***
FeO	2.931	71.844	0.041	1	0.041	0.449	1	**0.45**	***Fe***
P_2O_5	45.001	141.940	0.317	5	1.585	17.433	0.4	**6.97**	***P***
SiO2	0.352	60.080	0.006	2	0.012	0.129	0.5	**0.06**	***Si***
Total	**98.264**				**2.546**	**28**		**17.56**	
					28.000	*Normalized to 28 O for merrillite, keplerite			
					2.546				
					10.997				

Mg#	60.87	Mg ratio = 100 x Mg / (Mg + Fe)
Na#	7.71	Na ratio = 100 x Na / (Na + Ca)

Supplementary Table 12. Normalized formula amount calculation for datapoint 211 (“Tissint_merr1_5”). Calculated formula amounts noted in table were derived from the quantitate point analysis datapoint which exhibited the highest content of magnesium.

Data Collection: Rice Uni. - Point 211 - Tissint_merr1_5 - Normalized to 28 O (apfu)									
Oxide	**wt%**	**molecular weight of oxide**	**molecular proportion of oxide**	**number of oxygen atoms in oxide concerned**	**atomic proportion of oxygen from each molecule**	**no. of anions on the basis of X# (O,OH)**	**no. atoms per oxygen**	**no. of ions in formula**	
Na_2O	0.638	61.979	0.010	1	0.010	0.113	2	**0.23**	***Na***
CaO	47.111	56.077	0.840	1	0.840	9.201	1	**9.20**	***Ca***
MgO	3.323	40.304	0.082	1	0.082	0.903	1	**0.90**	***Mg***
FeO	1.763	71.844	0.025	1	0.025	0.269	1	**0.27**	***Fe***
P_2O_5	45.387	141.940	0.320	5	1.599	17.510	0.4	**7.00**	***P***
SiO2	0.011	60.080	0.000	2	0.000	0.004	0.5	**0.00**	***Si***
Total	**98.233**				**2.557**	**28**		**17.60**	
					28	*Normalized to 28 O for merrillite, keplerite			
					2.557				
					10.952				

Mg#	76.92
Na#	2.44

Mg ratio = 100 x Mg / (Mg + Fe)
Na ratio = 100 x Na / (Na + Ca)

APPENDIX C:

WAVELENGTH DISPERSIVE SPECTROMETRY (WDS)

Tissint

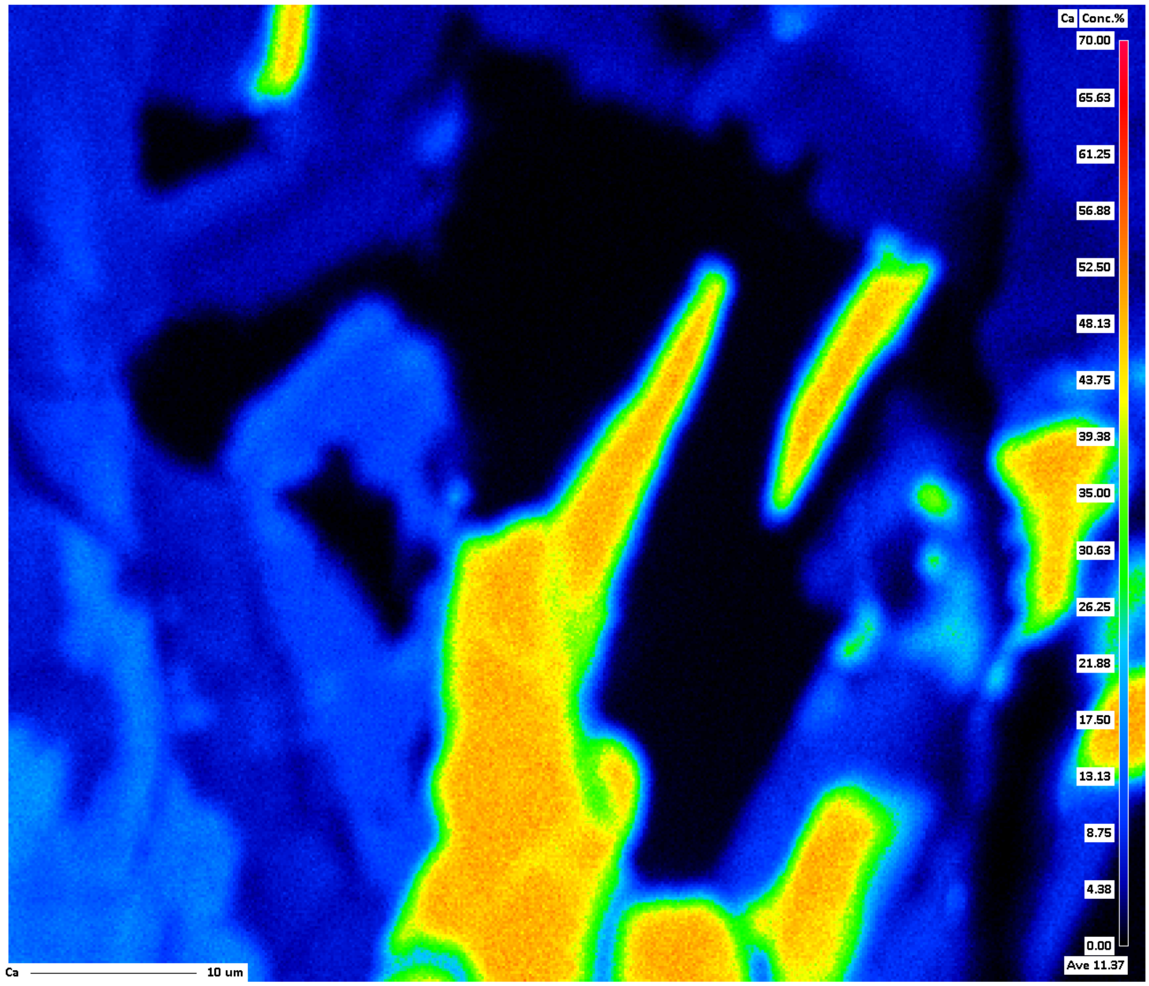

Supplementary Figure 1. Quantitative WDS (Wavelength Dispersive Spectrometry) elemental map distribution of calcium (Ca) in keplerite grain #1 in Tissint. WDS element maps are given in weight percent (wt%). WDS element maps correspond to BSE image from Figure 31. Plag = plagioclase; Mer = merrillite; Ap = apatite; OPX = orthopyroxene. Scale bar is 50 µm in length.

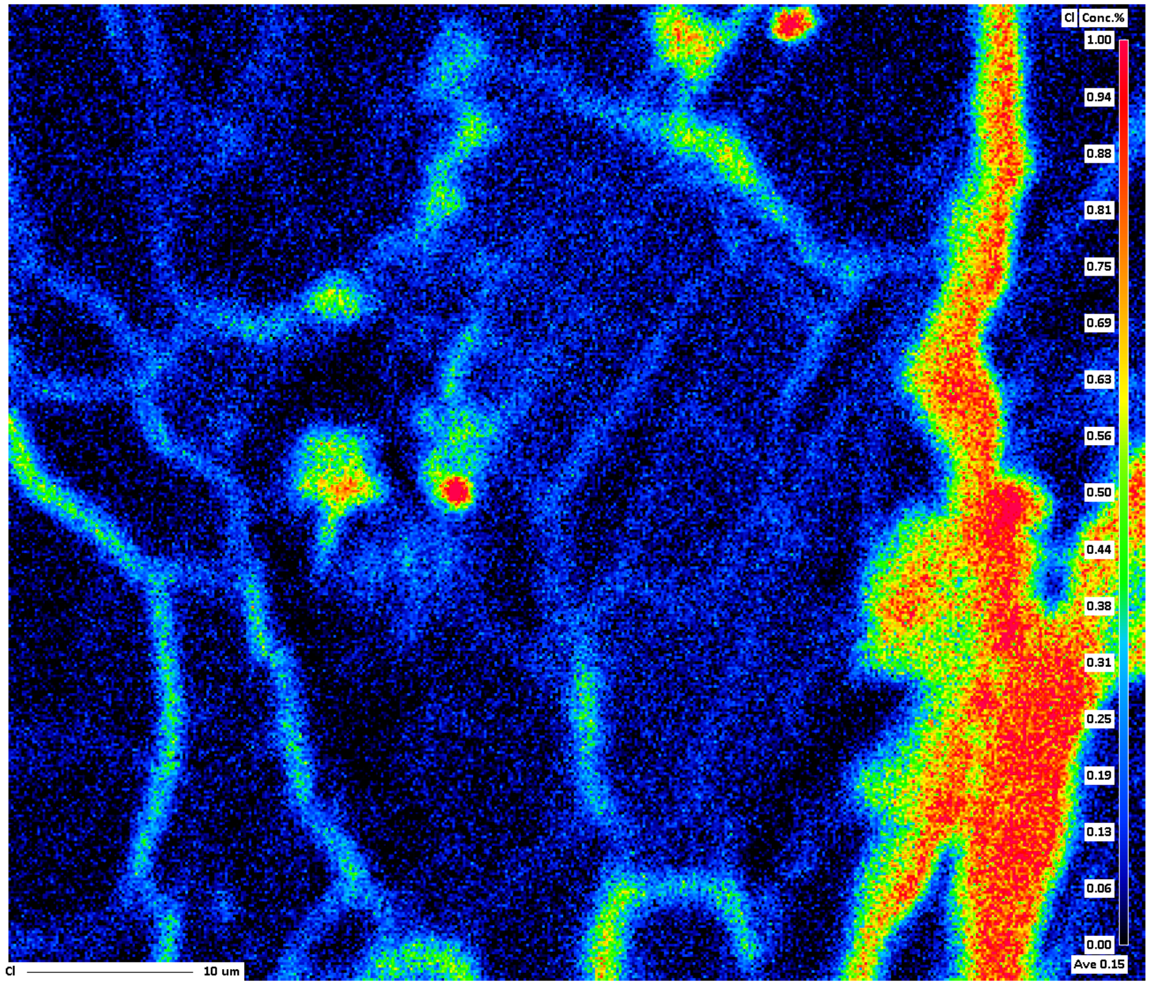

Supplementary Figure 2. Quantitative WDS (Wavelength Dispersive Spectrometry) elemental map distribution of chlorine (Cl) in keplerite grain #1 in Tissint. WDS element maps are given in weight percent (wt%). WDS element maps correspond to BSE image from Figure 31. Plag = plagioclase; Mer = merrillite; Ap = apatite; OPX = orthopyroxene. Scale bar is 50 µm in length.

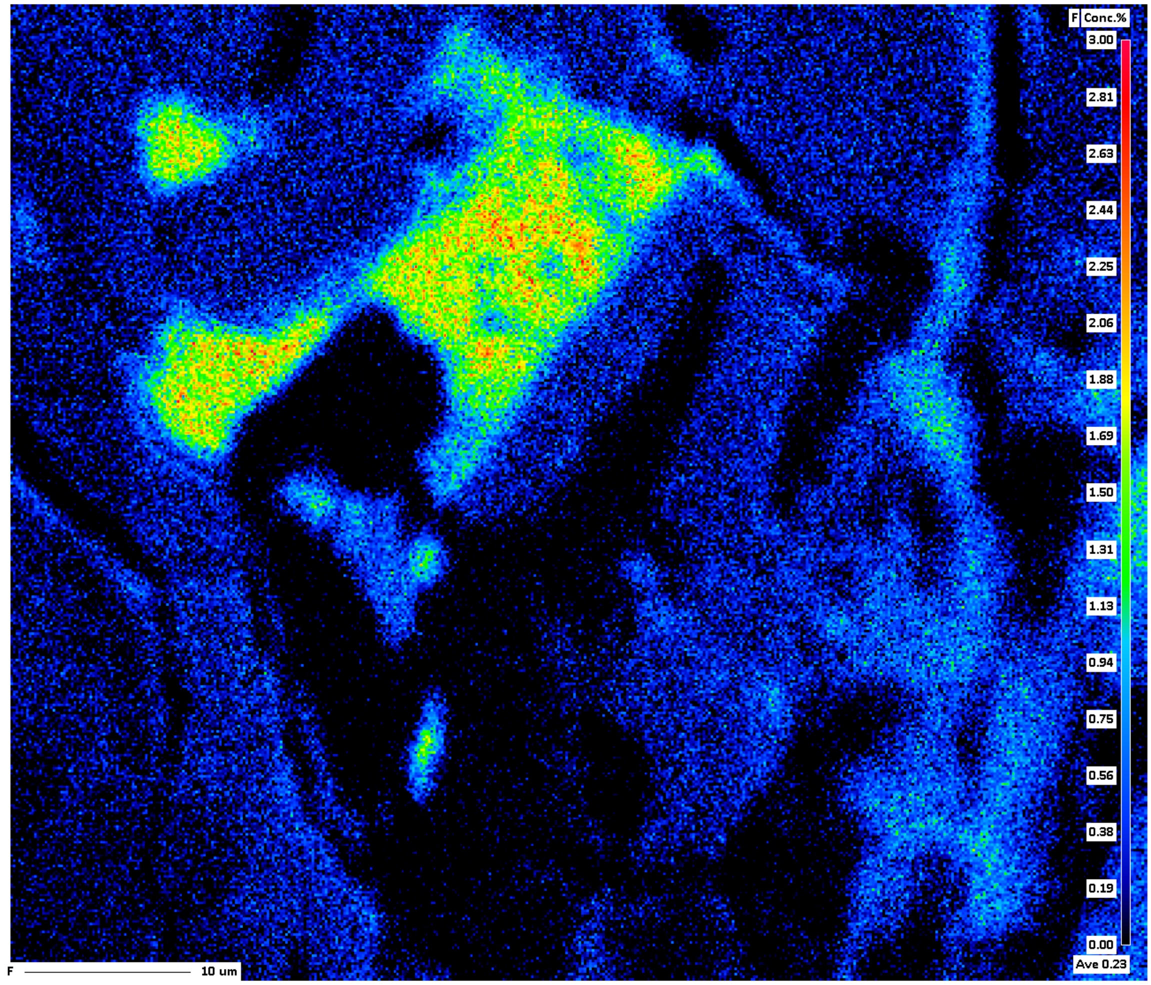

Supplementary Figure 3. Quantitative WDS (Wavelength Dispersive Spectrometry) elemental map distribution of fluorine (F) in keplerite grain #1 in Tissint. WDS element maps are given in weight percent (wt%). WDS element maps correspond to BSE image from Figure 31. Plag = plagioclase; Mer = merrillite; Ap = apatite; OPX = orthopyroxene. Scale bar is 50 µm in length.

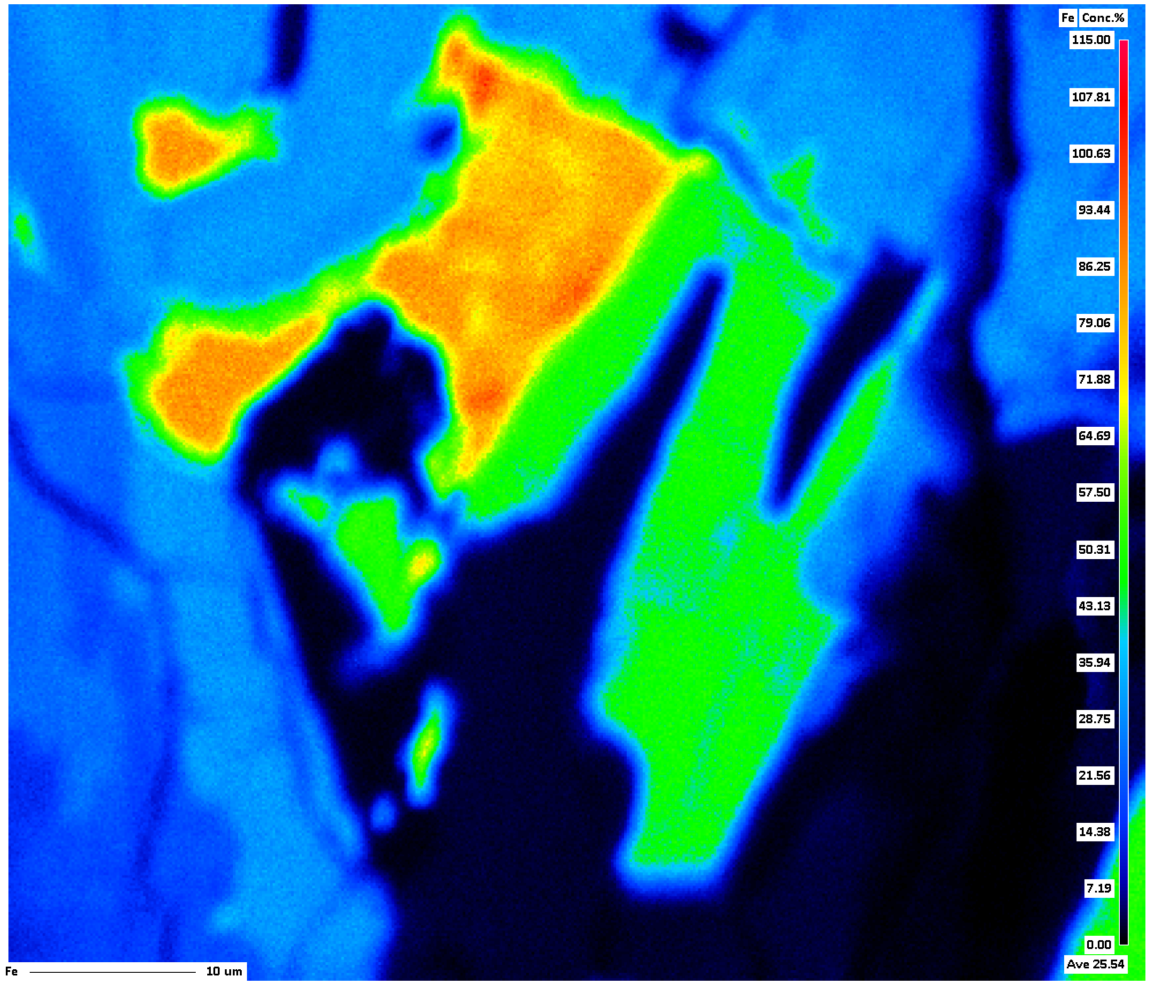

Supplementary Figure 4. Quantitative WDS (Wavelength Dispersive Spectrometry) elemental map distribution of iron (Fe) in keplerite grain #1 in Tissint. WDS element maps are given in weight percent (wt%). WDS element maps correspond to BSE image from Figure 31. Plag = plagioclase; Mer = merrillite; Ap = apatite; OPX = orthopyroxene. Scale bar is 50 μm in length.

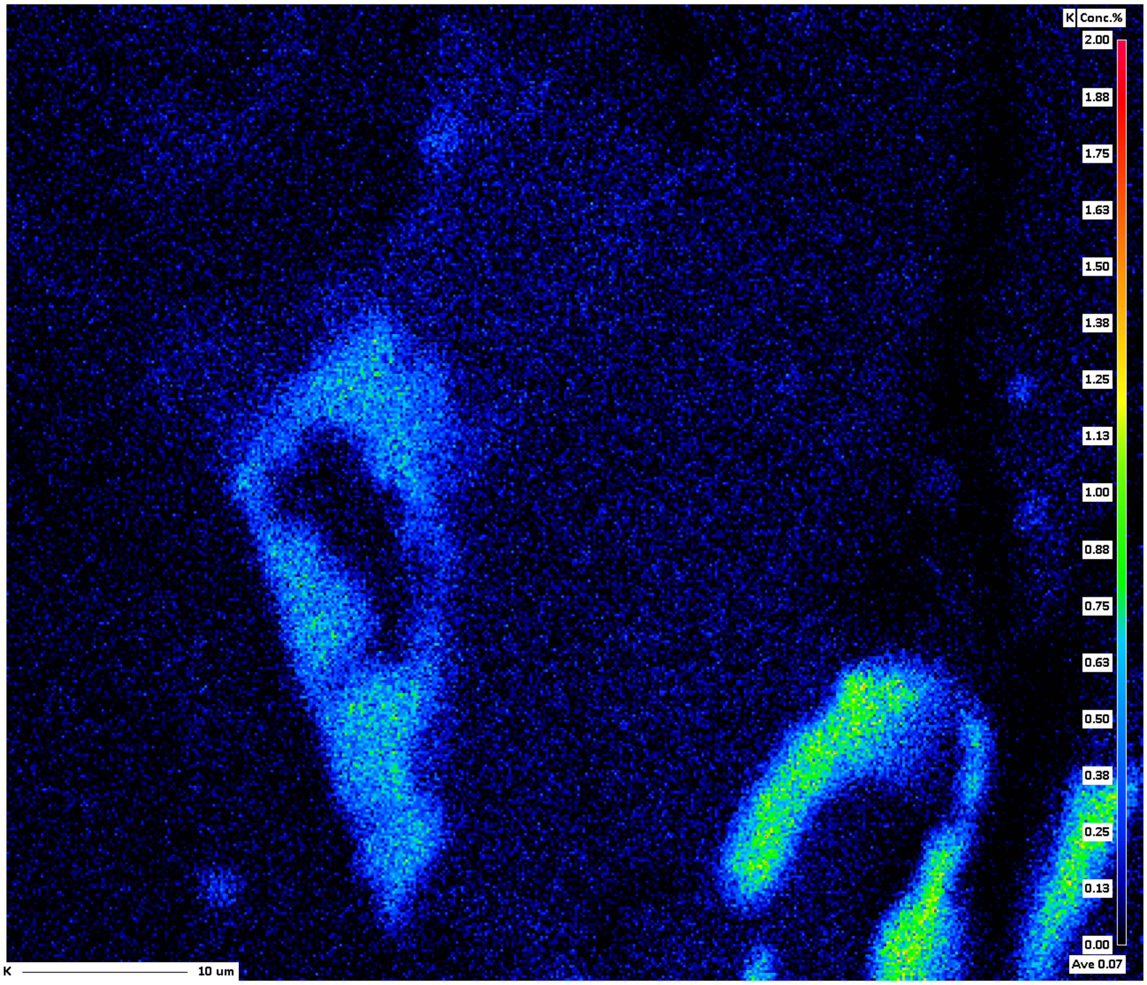

Supplementary Figure 5. Quantitative WDS (Wavelength Dispersive Spectrometry) elemental map distribution of potassium (K) in keplerite grain #1 in Tissint. WDS element maps are given in weight percent (wt%). WDS element maps correspond to BSE image from Figure 31. Plag = plagioclase; Mer = merrillite; Ap = apatite; OPX = orthopyroxene. Scale bar is 50 μm in length.

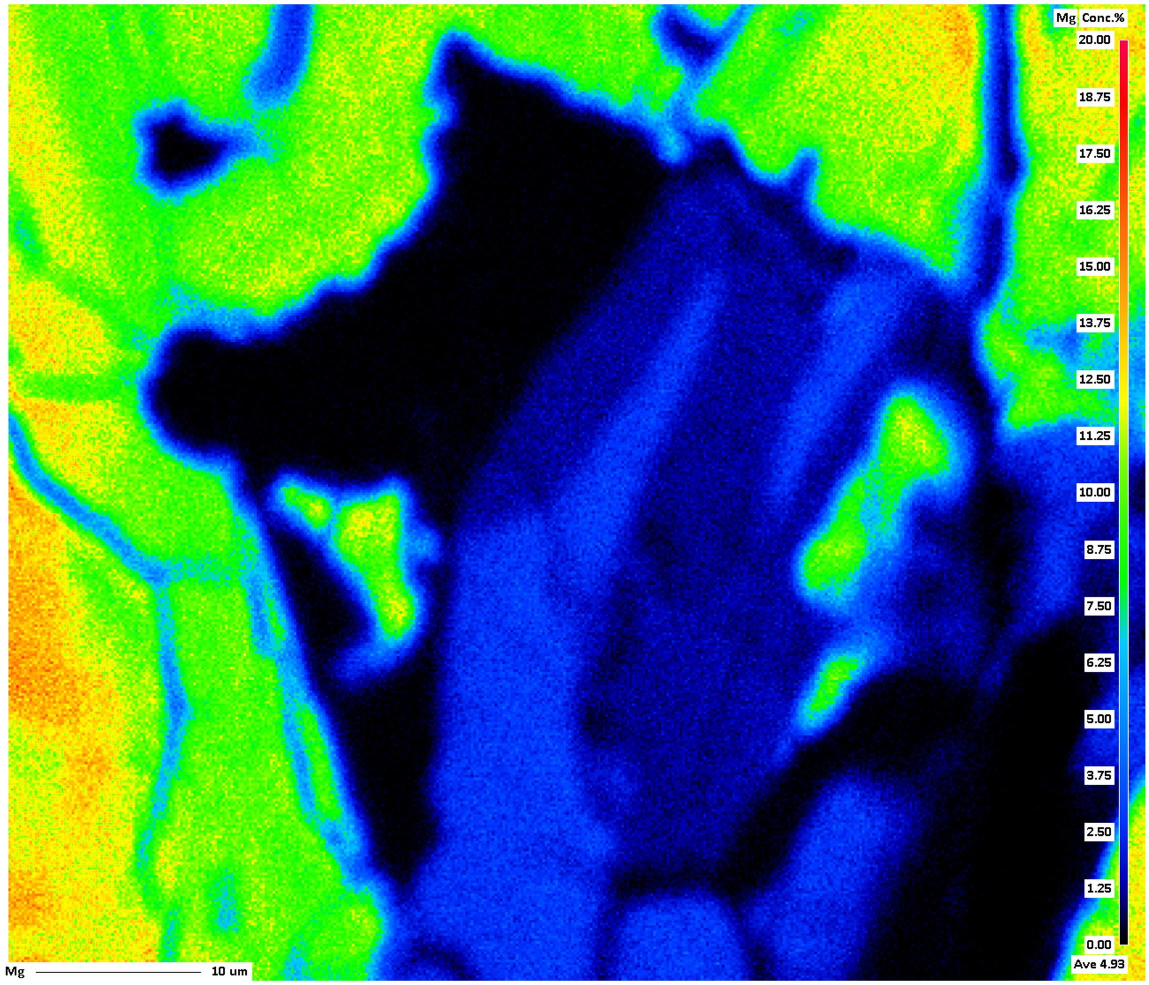

Supplementary Figure 6. Quantitative WDS (Wavelength Dispersive Spectrometry) elemental map distribution of magnesium (Mg) in keplerite grain #1 in Tissint. WDS element maps are given in weight percent (wt%). WDS element maps correspond to BSE image from Figure 31. Plag = plagioclase; Mer = merrillite; Ap = apatite; OPX = orthopyroxene. Scale bar is 50 μm in length.

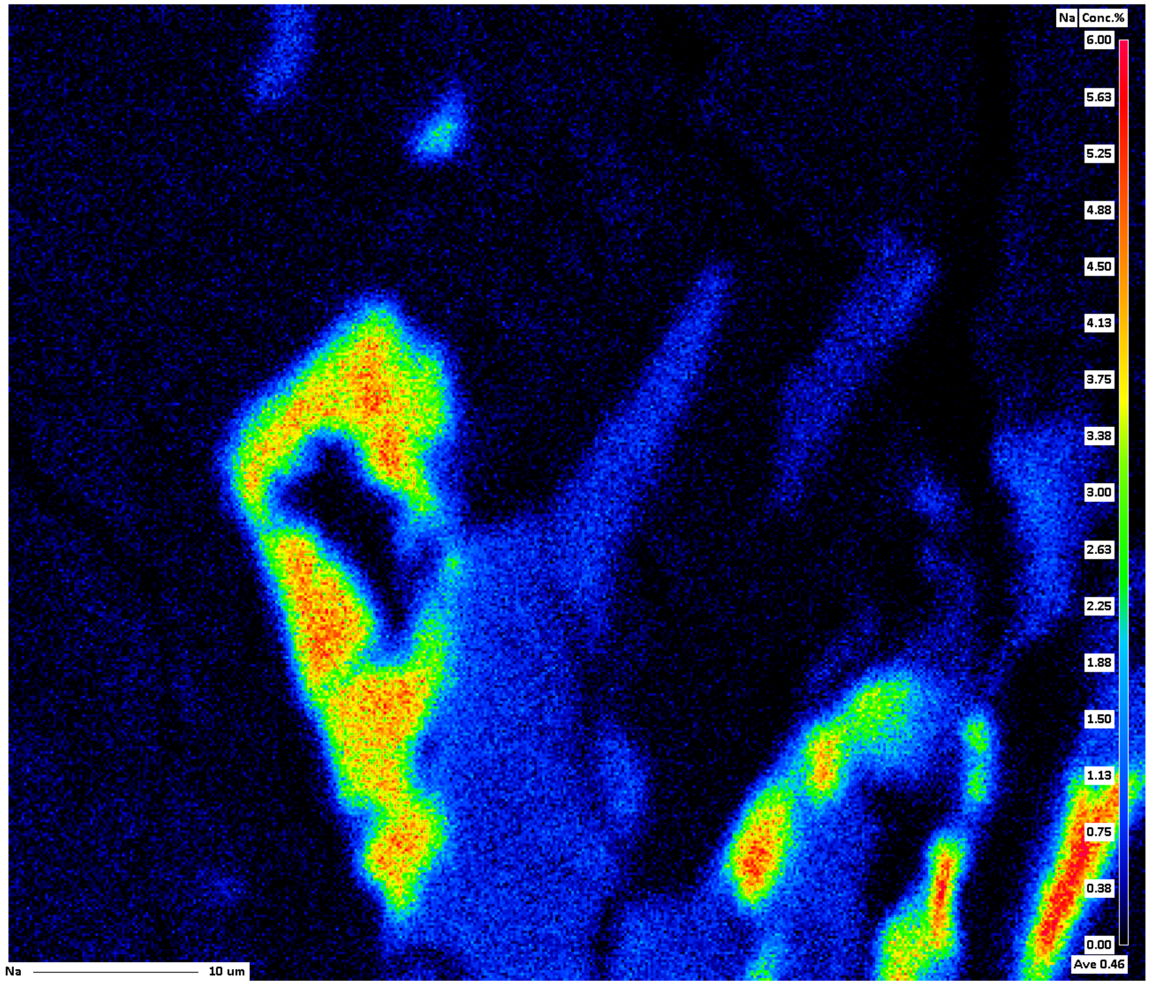

Supplementary Figure 7. Quantitative WDS (Wavelength Dispersive Spectrometry) elemental map distribution of sodium (Na) in keplerite grain #1 in Tissint. WDS element maps are given in weight percent (wt%). WDS element maps correspond to BSE image from Figure 31. Plag = plagioclase; Mer = merrillite; Ap = apatite; OPX = orthopyroxene. Scale bar is 50 µm in length.

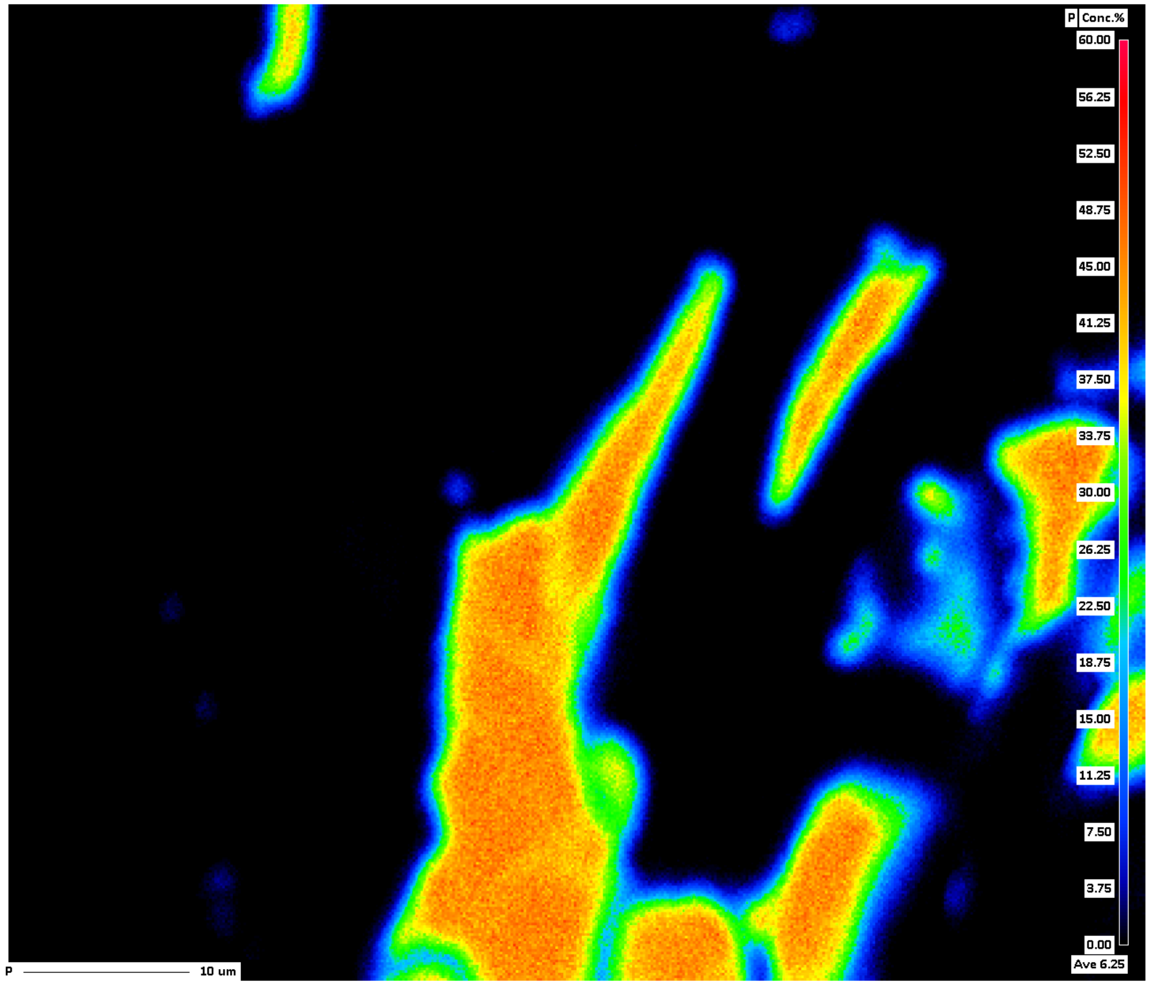

Supplementary Figure 8. Quantitative WDS (Wavelength Dispersive Spectrometry) elemental map distribution of phosphorous (P) in keplerite grain #1 in Tissint. WDS element maps are given in weight percent (wt%). WDS element maps correspond to BSE image from Figure 31. Plag = plagioclase; Mer = merrillite; Ap = apatite; OPX = orthopyroxene. Scale bar is 50 μm in length.

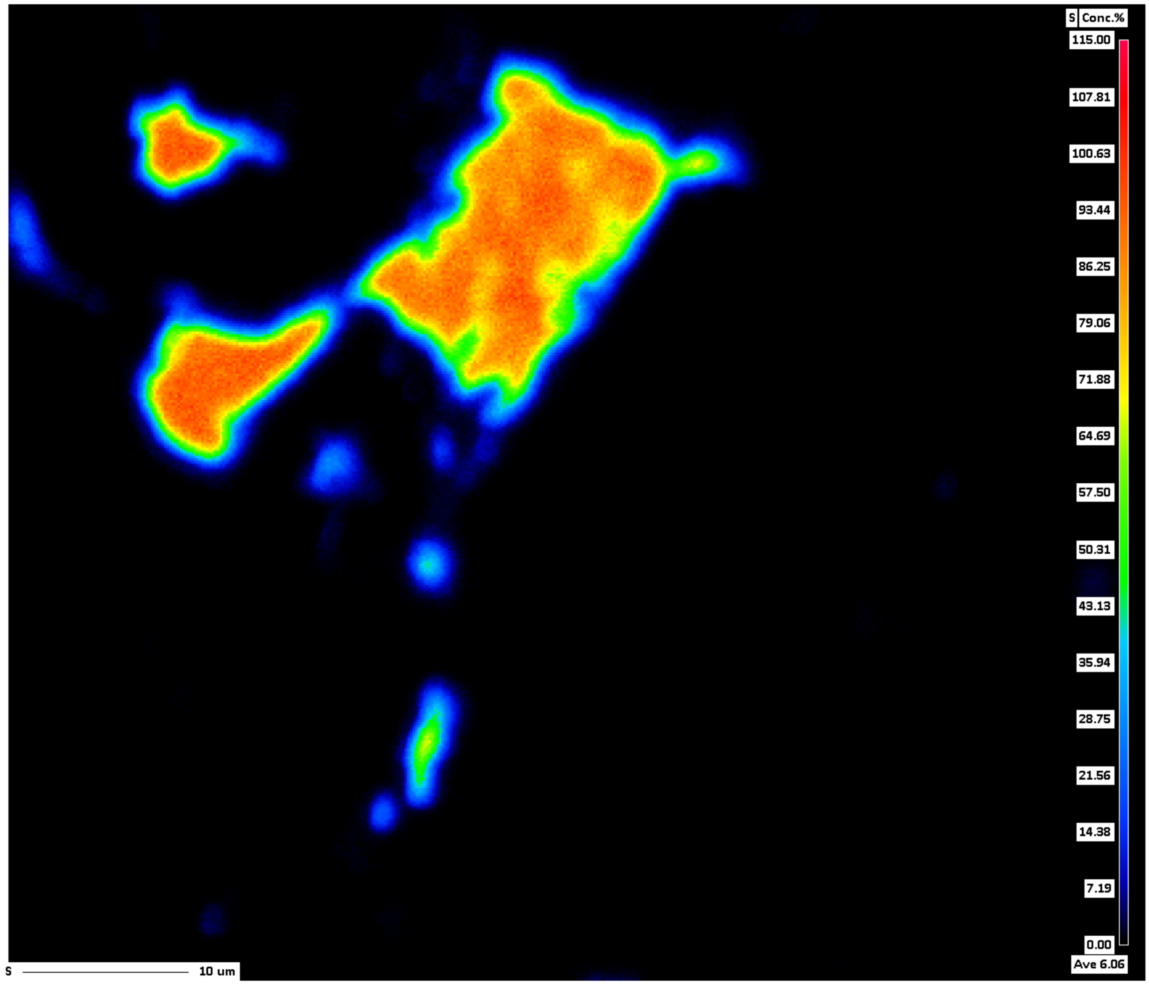

Supplementary Figure 9. Quantitative WDS (Wavelength Dispersive Spectrometry) elemental map distribution of sulfur (S) in keplerite grain #1 in Tissint. WDS element maps are given in weight percent (wt%). WDS element maps correspond to BSE image from Figure 31. Plag = plagioclase; Mer = merrillite; Ap = apatite; OPX = orthopyroxene. Scale bar is 50 µm in length.

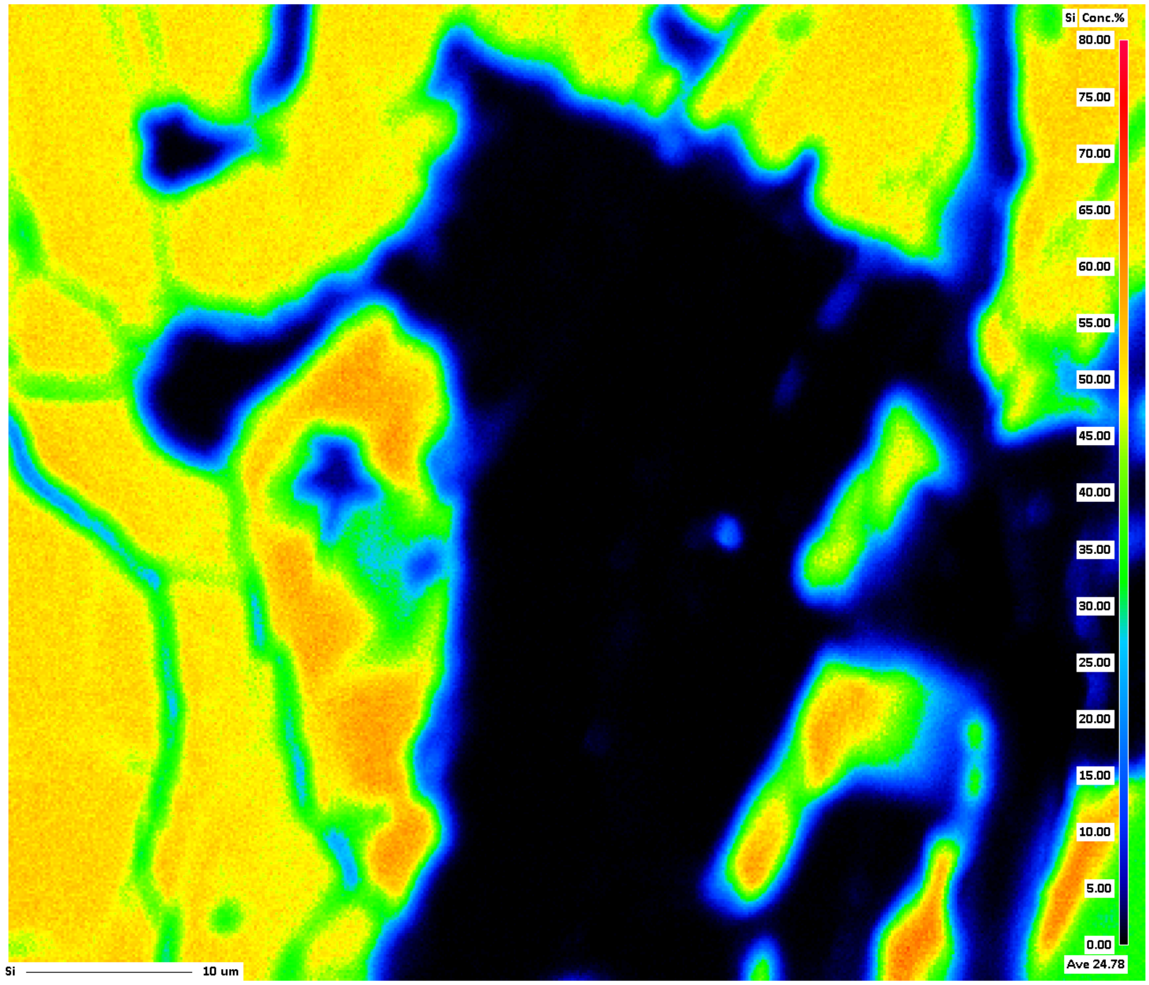

Supplementary Figure 10. Quantitative WDS (Wavelength Dispersive Spectrometry) elemental map distribution of silicon (Si) in keplerite grain #1 in Tissint. WDS element maps are given in weight percent (wt%). WDS element maps correspond to BSE image from Figure 31. Plag = plagioclase; Mer = merrillite; Ap = apatite; OPX = orthopyroxene. Scale bar is 50 µm in length.

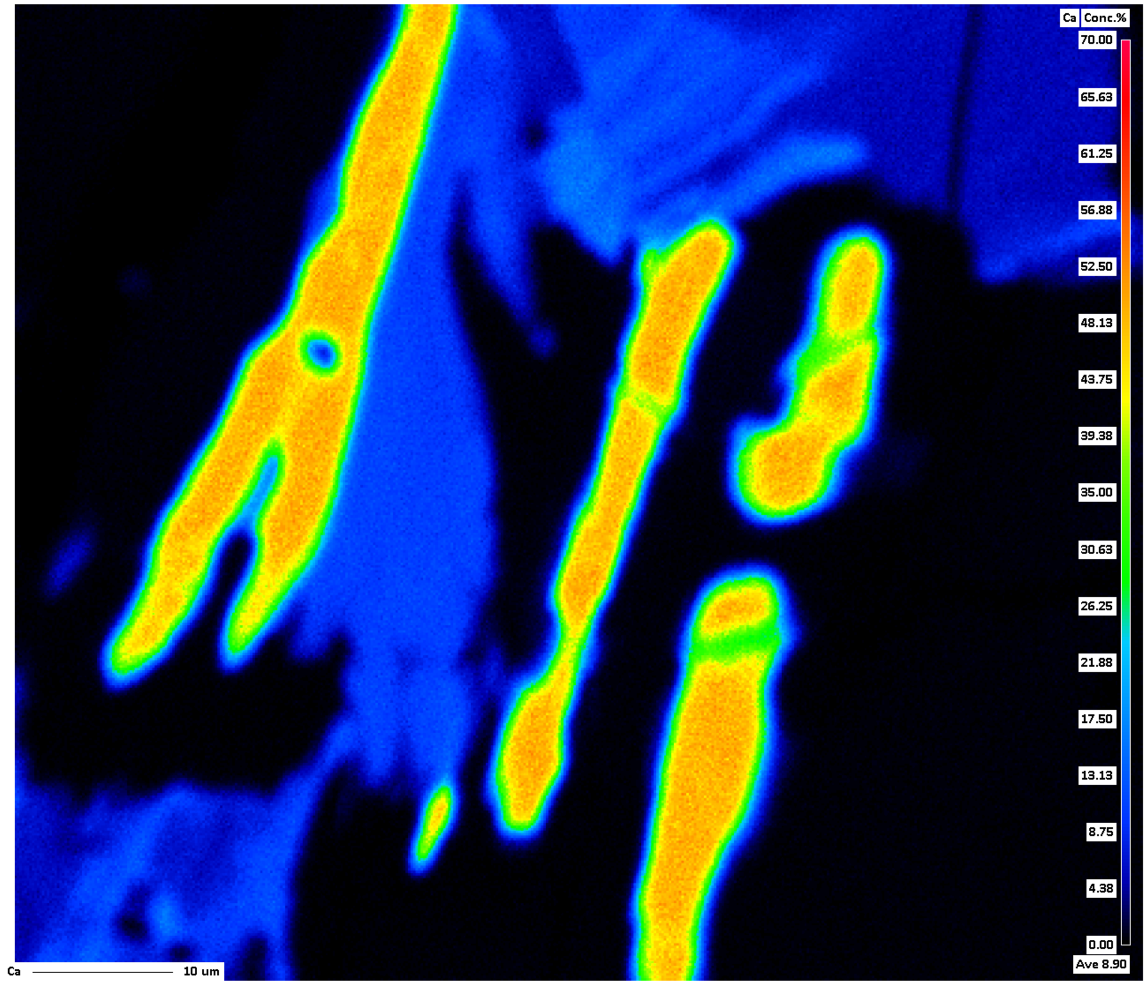

Supplementary Figure 11. Quantitative WDS (Wavelength Dispersive Spectrometry) elemental map distribution of calcium (Ca) in keplerite grain #2 in Tissint. WDS element maps are given in weight percent (wt%). WDS element maps correspond to BSE image from Figure 31. Plag = plagioclase; Mer = merrillite; Ap = apatite; OPX = orthopyroxene. Scale bar is 50 μm in length.

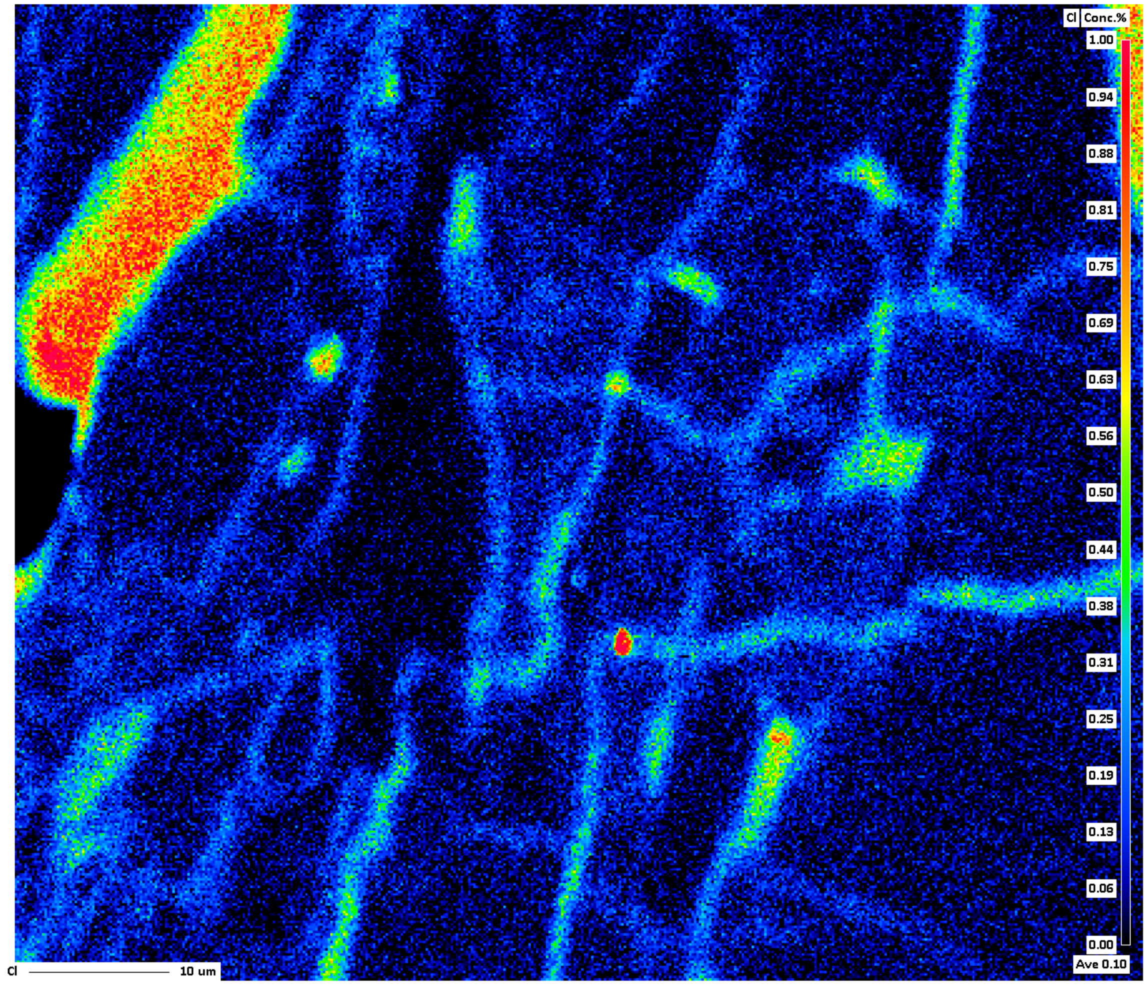

Supplementary Figure 12. Quantitative WDS (Wavelength Dispersive Spectrometry) elemental map distribution of chlorine (Cl) in keplerite grain #2 in Tissint. WDS element maps are given in weight percent (wt%). WDS element maps correspond to BSE image from Figure 31. Plag = plagioclase; Mer = merrillite; Ap = apatite; OPX = orthopyroxene. Scale bar is 50 µm in length.

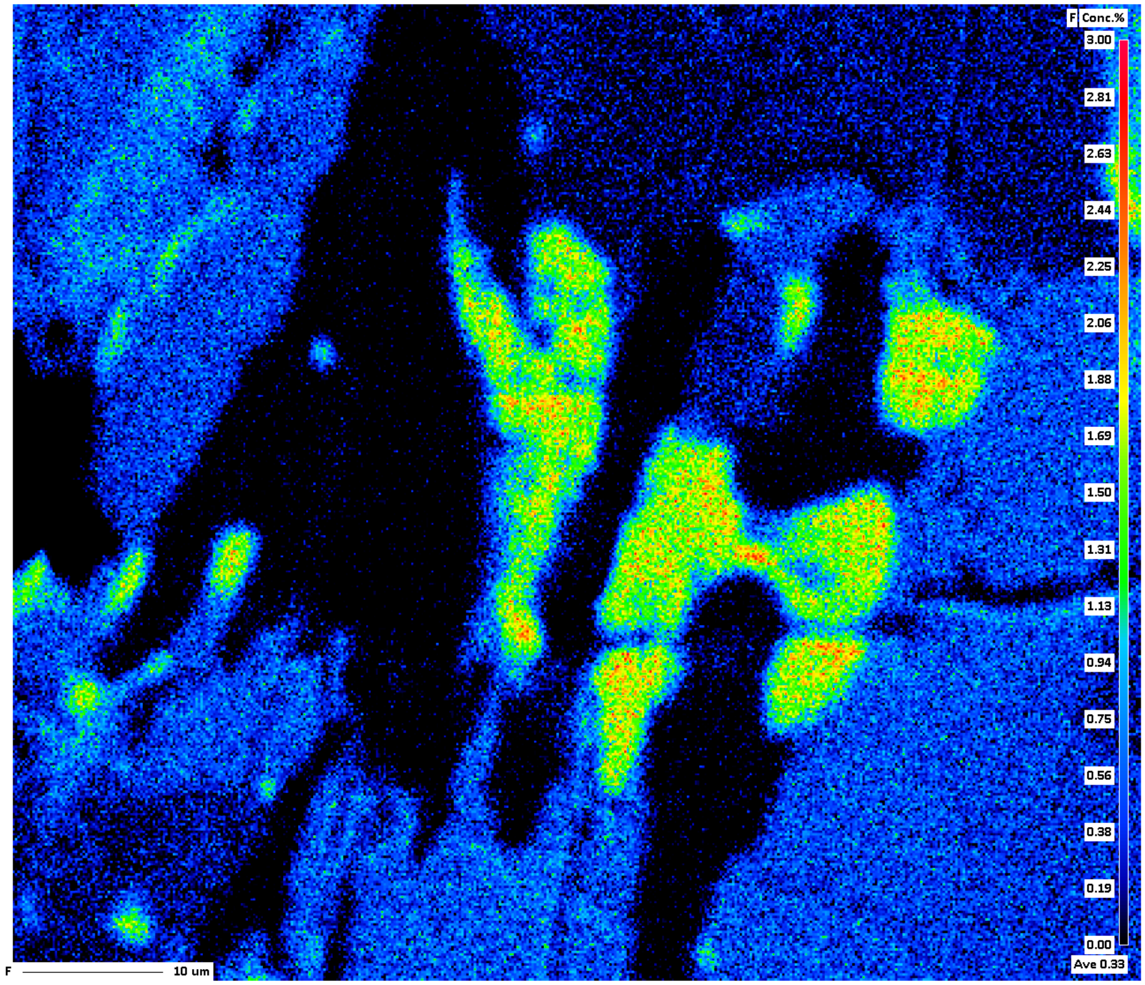

Supplementary Figure 13. Quantitative WDS (Wavelength Dispersive Spectrometry) elemental map distribution of fluorine (F) in keplerite grain #2 in Tissint. WDS element maps are given in weight percent (wt%). WDS element maps correspond to BSE image from Figure 31. Plag = plagioclase; Mer = merrillite; Ap = apatite; OPX = orthopyroxene. Scale bar is 50 μm in length.

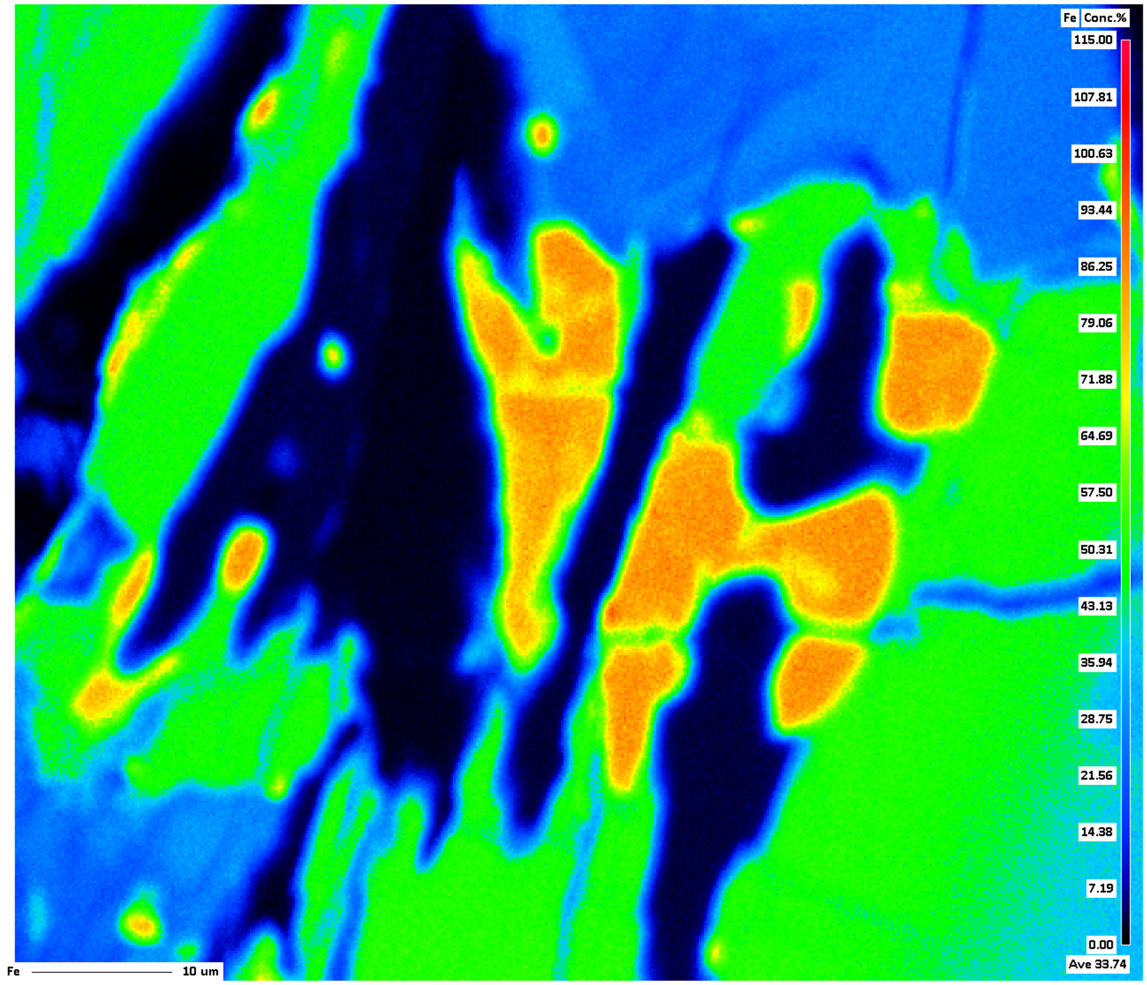

Supplementary Figure 14. Quantitative WDS (Wavelength Dispersive Spectrometry) elemental map distribution of iron (Fe) in keplerite grain #2 in Tissint. WDS element maps are given in weight percent (wt%). WDS element maps correspond to BSE image from Figure 31. Plag = plagioclase; Mer = merrillite; Ap = apatite; OPX = orthopyroxene. Scale bar is 50 μm in length.

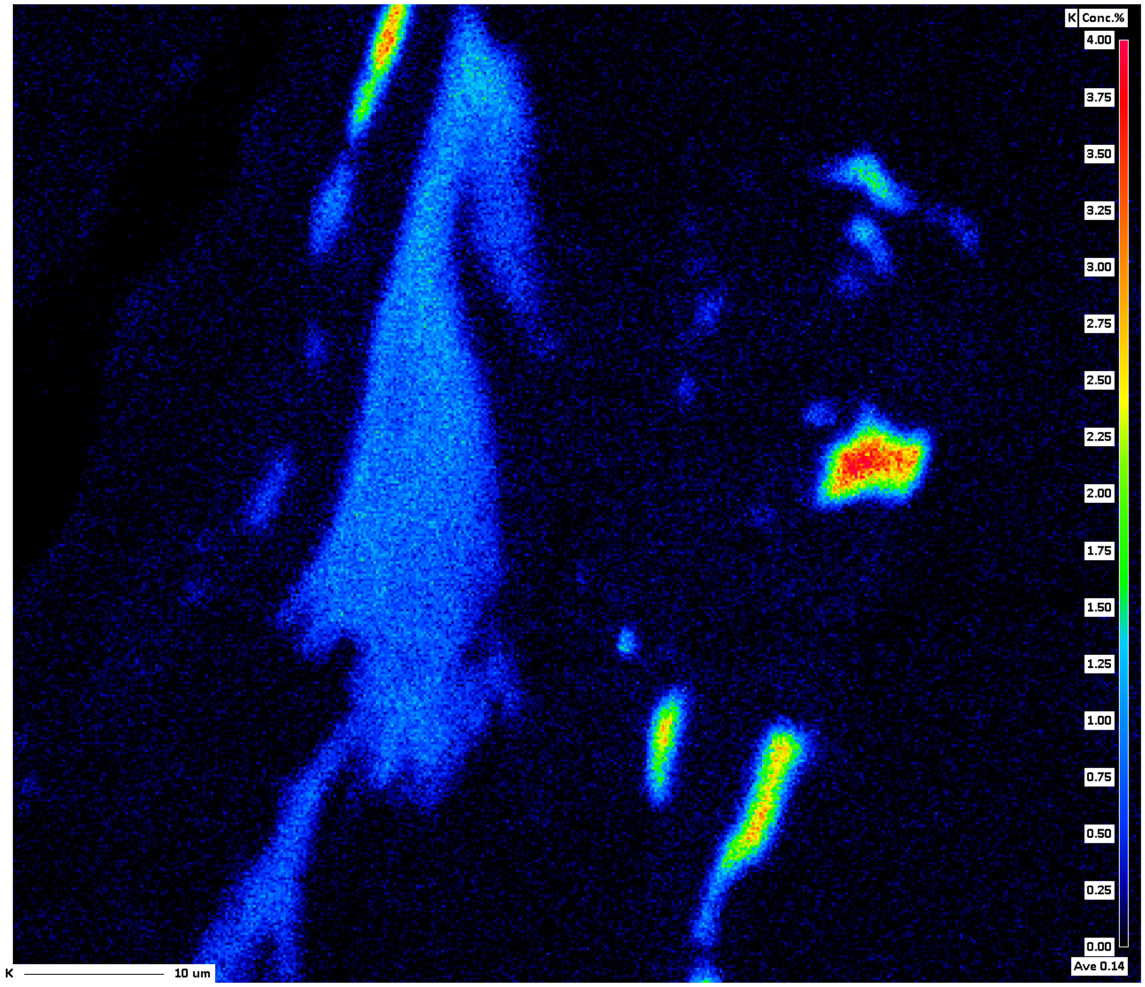

Supplementary Figure 15. Quantitative WDS (Wavelength Dispersive Spectrometry) elemental map distribution of potassium (K) in keplerite grain #2 in Tissint. WDS element maps are given in weight percent (wt%). WDS element maps correspond to BSE image from Figure 31. Plag = plagioclase; Mer = merrillite; Ap = apatite; OPX = orthopyroxene. Scale bar is 50 μm in length.

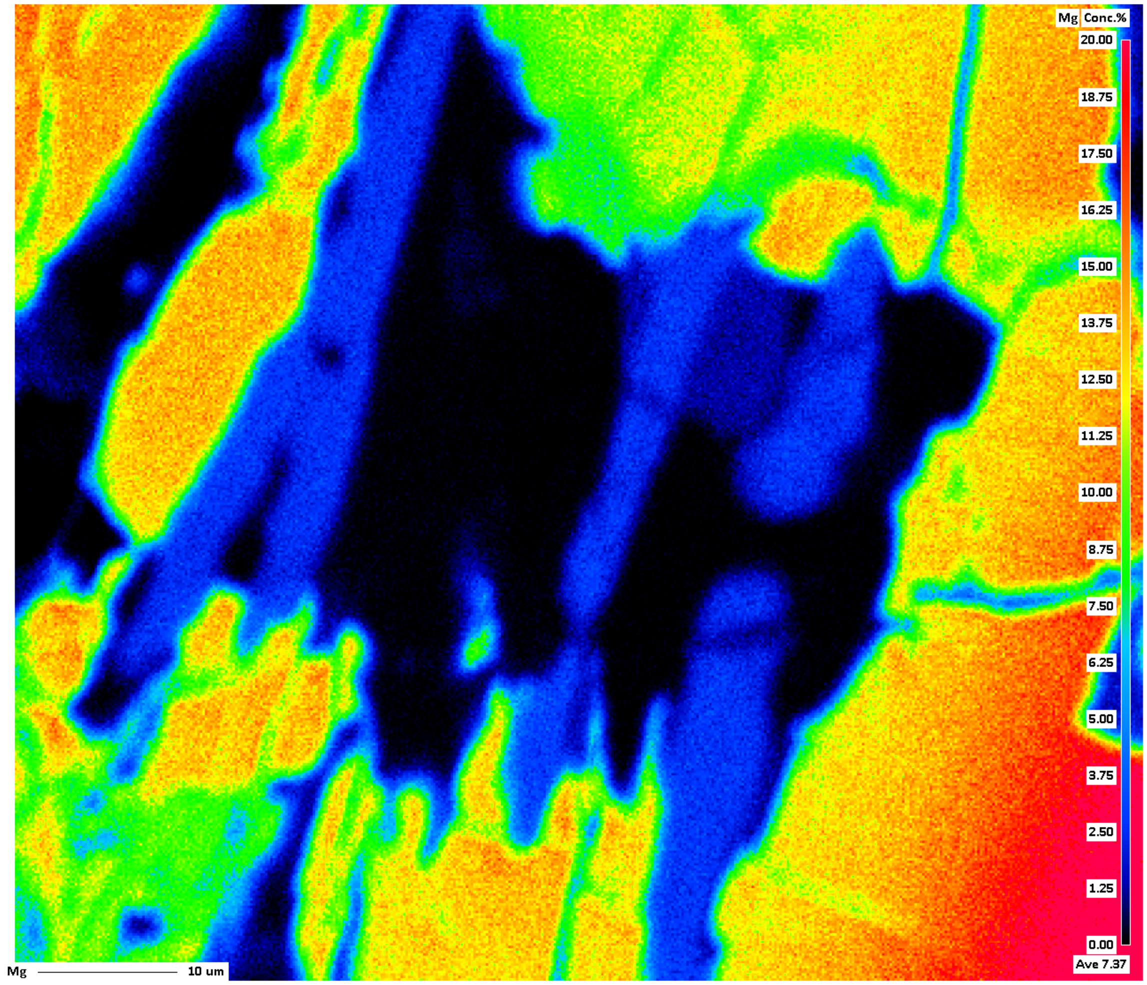

Supplementary Figure 16. Quantitative WDS (Wavelength Dispersive Spectrometry) elemental map distribution of magnesium (Mg) in keplerite grain #2 in Tissint. WDS element maps are given in weight percent (wt%). WDS element maps correspond to BSE image from Figure 31. Plag = plagioclase; Mer = merrillite; Ap = apatite; OPX = orthopyroxene. Scale bar is 50 µm in length.

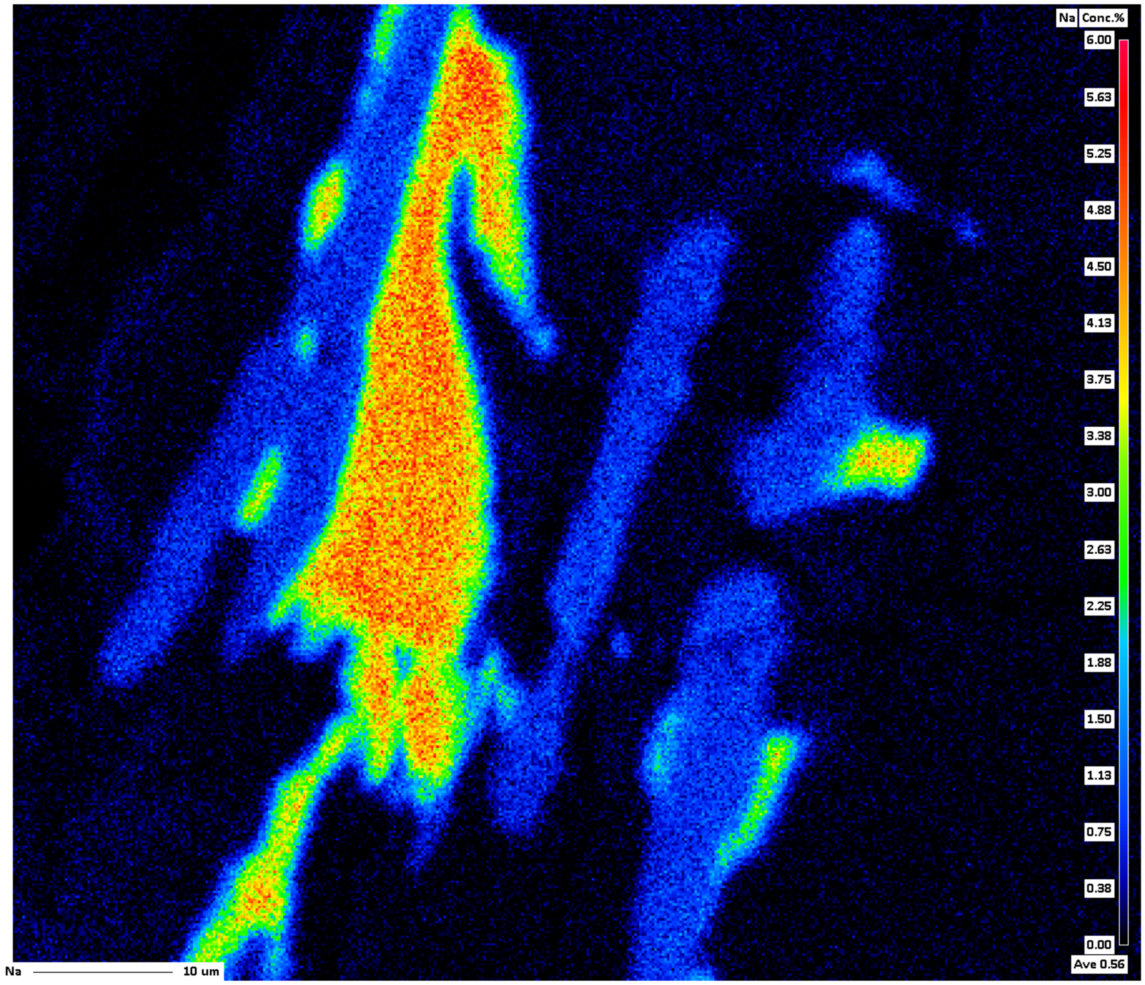

Supplementary Figure 17. Quantitative WDS (Wavelength Dispersive Spectrometry) elemental map distribution of sodium (Na) in keplerite grain #2 in Tissint. WDS element maps are given in weight percent (wt%). WDS element maps correspond to BSE image from Figure 31. Plag = plagioclase; Mer = merrillite; Ap = apatite; OPX = orthopyroxene. Scale bar is 50 μm in length.

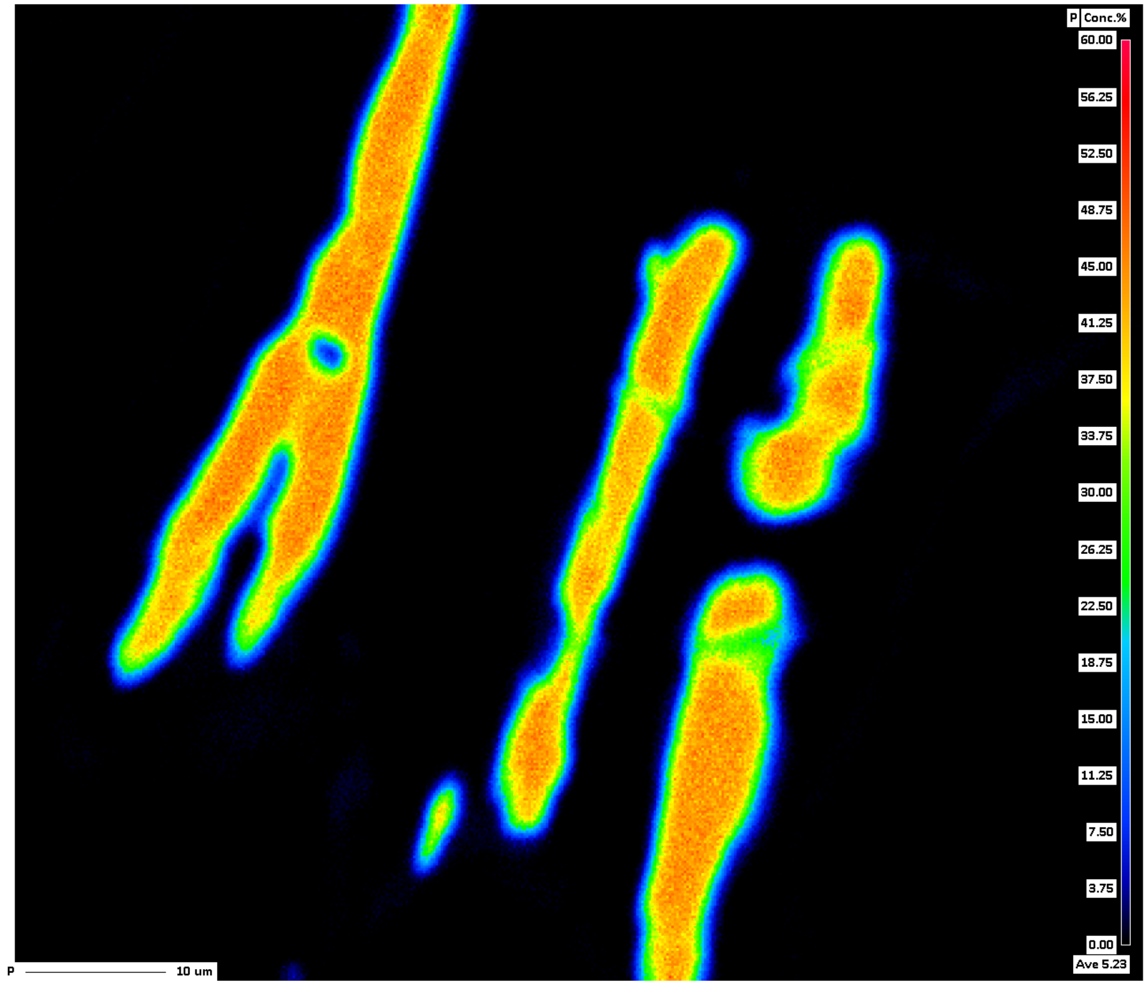

Supplementary Figure 18. Quantitative WDS (Wavelength Dispersive Spectrometry) elemental map distribution of phosphorous (P) in keplerite grain #2 in Tissint. WDS element maps are given in weight percent (wt%). WDS element maps correspond to BSE image from Figure 31. Plag = plagioclase; Mer = merrillite; Ap = apatite; OPX = orthopyroxene. Scale bar is 50 μm in length.

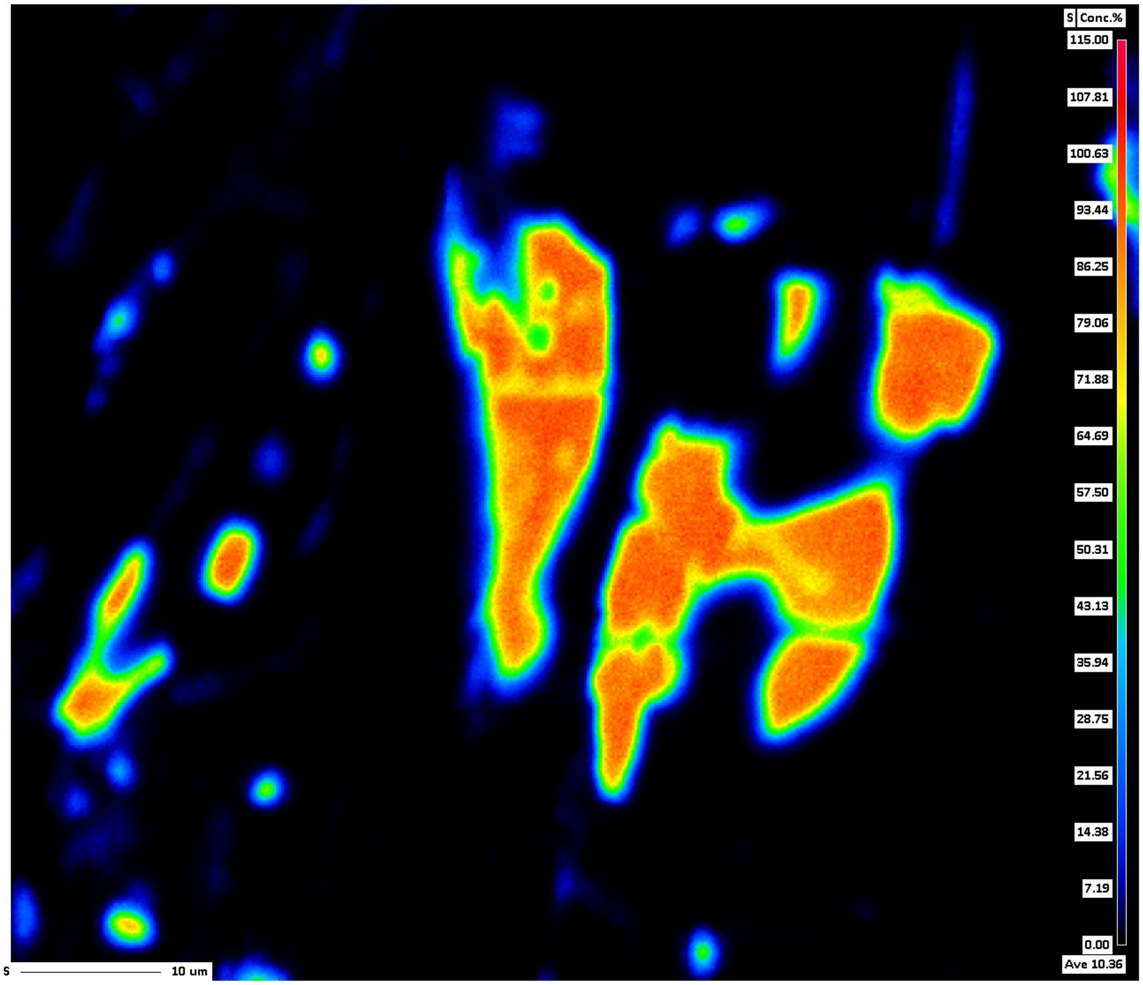

Supplementary Figure 19. Quantitative WDS (Wavelength Dispersive Spectrometry) elemental map distribution of sulfur (S) in keplerite grain #2 in Tissint. WDS element maps are given in weight percent (wt%). WDS element maps correspond to BSE image from Figure 31. Plag = plagioclase; Mer = merrillite; Ap = apatite; OPX = orthopyroxene. Scale bar is 50 µm in length.

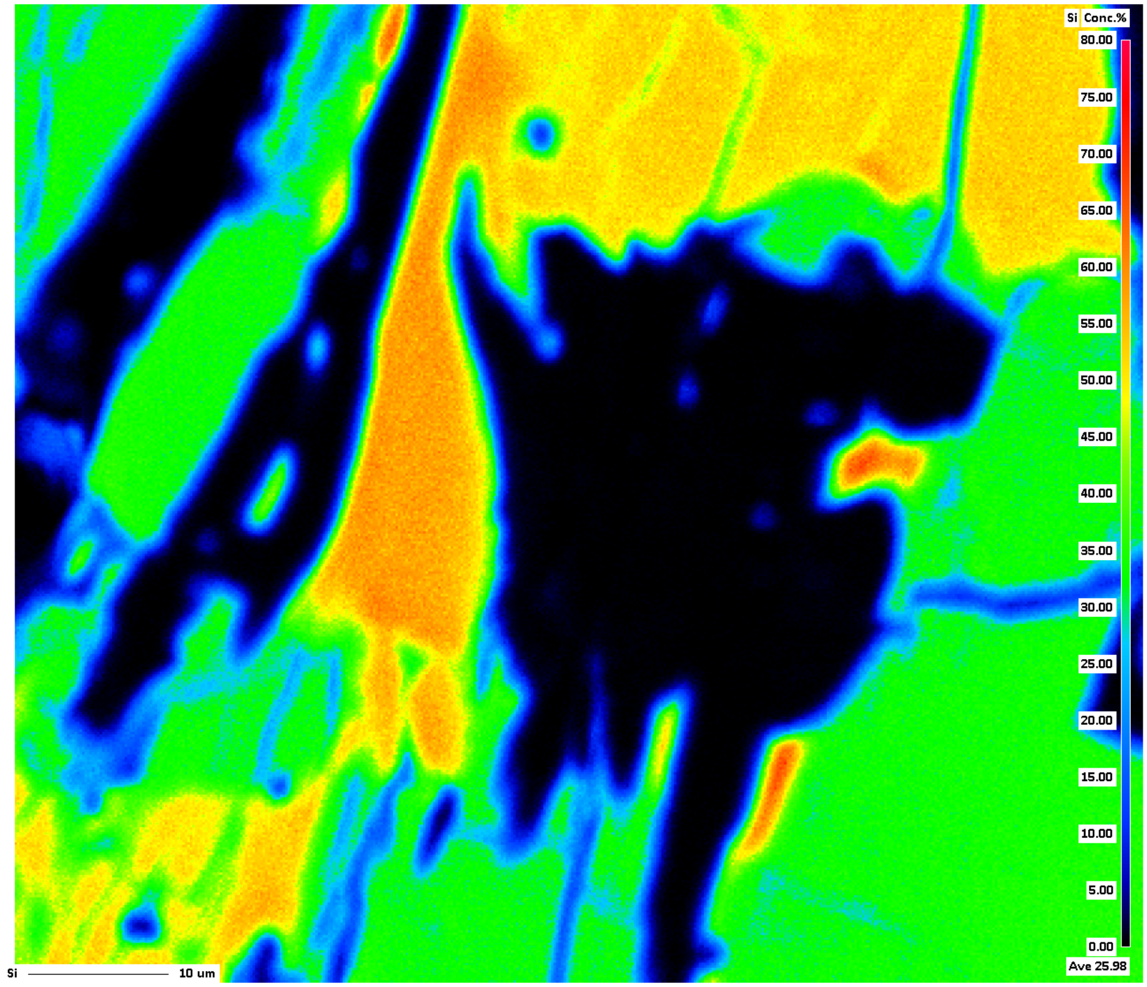

Supplementary Figure 20. Quantitative WDS (Wavelength Dispersive Spectrometry) elemental map distribution of silicon (Si) in keplerite grain #2 in Tissint. WDS element maps are given in weight percent (wt%). WDS element maps correspond to BSE image from Figure 31. Plag = plagioclase; Mer = merrillite; Ap = apatite; OPX = orthopyroxene. Scale bar is 50 μm in length.

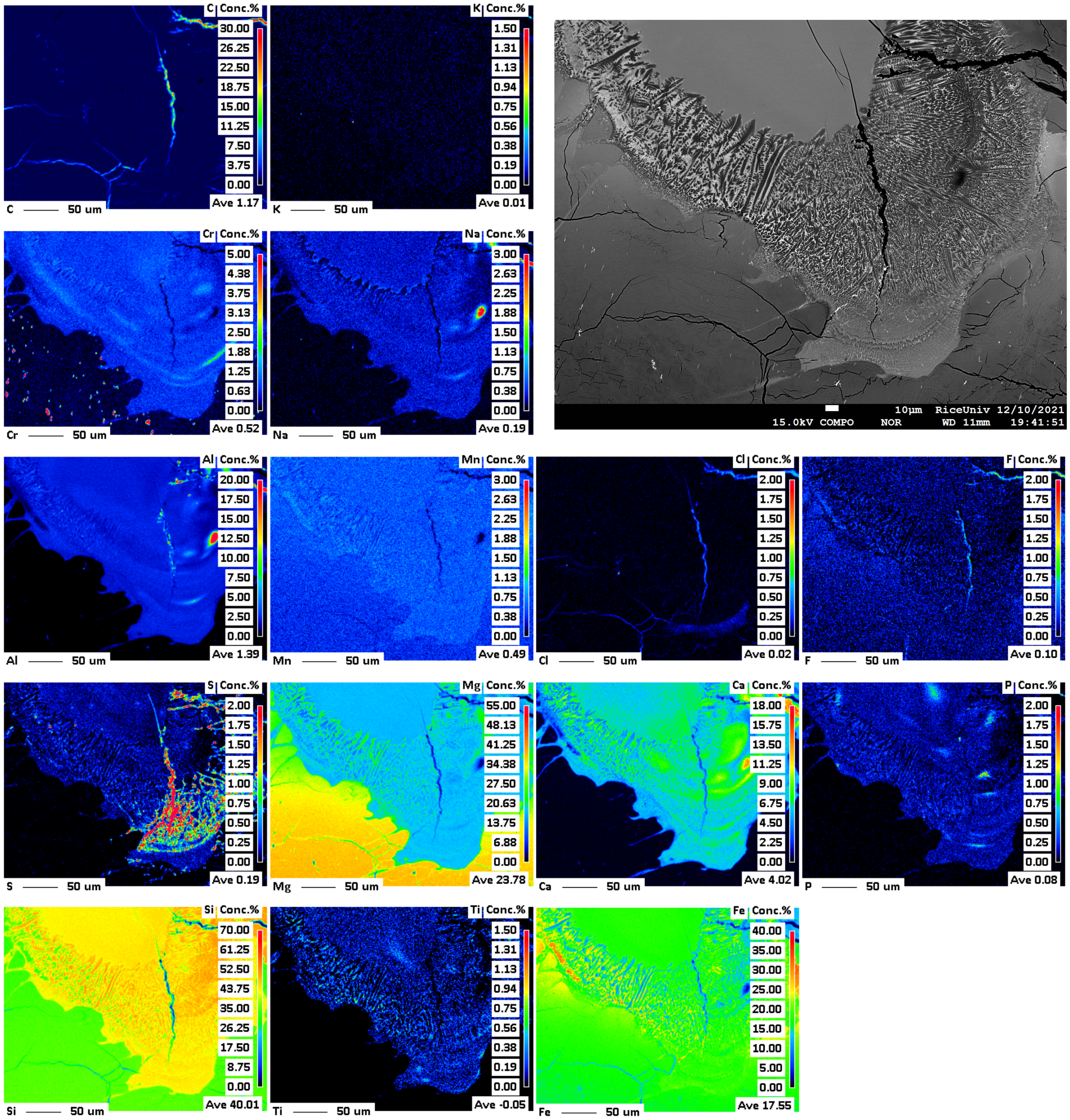

Supplementary Figure 21. Quantitative WDS (Wavelength Dispersive Spectrometry) element map distribution and BSE (BackScattered Electron) image of symplectite in Tissint. WDS element maps illustrate elemental distributions in symplectite and surrounding phases; maps are given in weight percent (wt%). WDS element maps correspond to BSE image in the top right-hand corner.

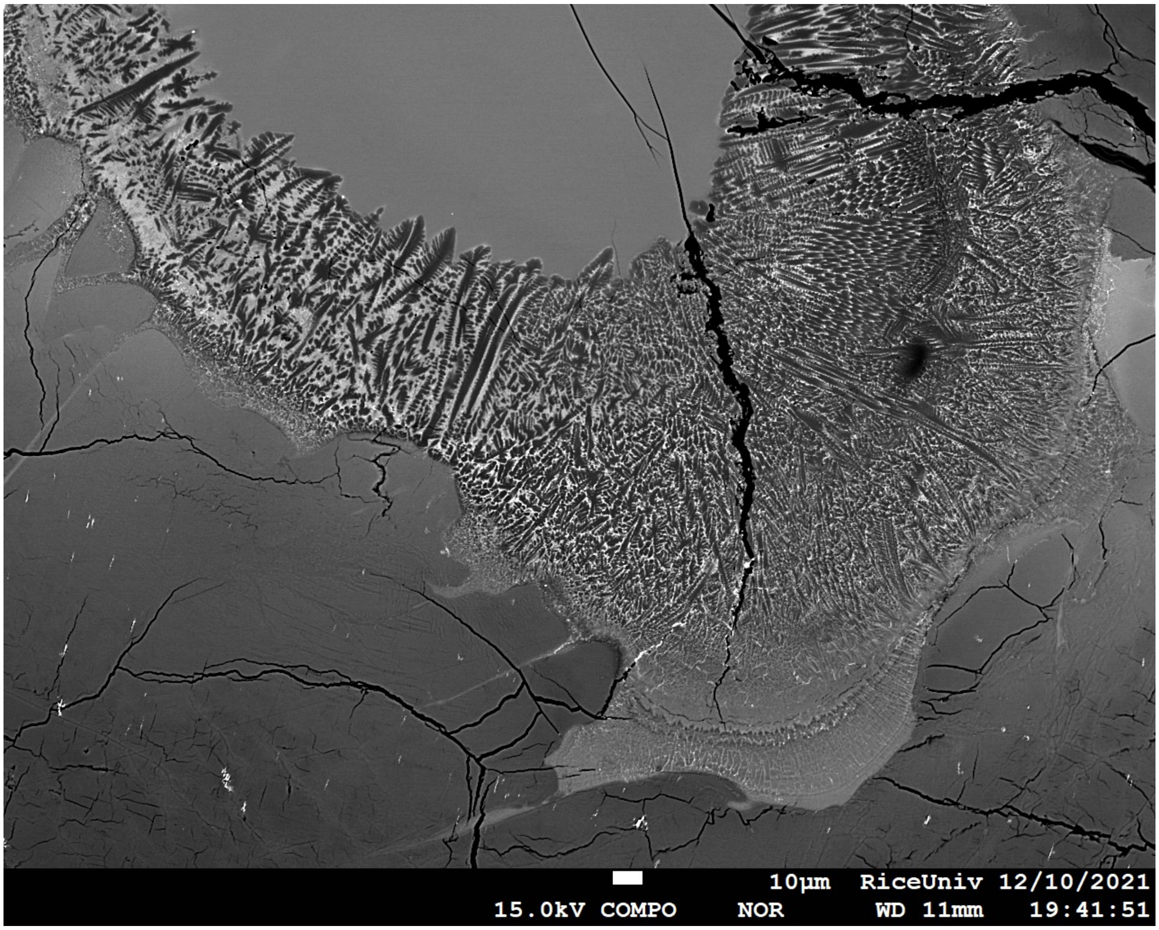
10μm RiceUniv 12/10/2021
15.0kV COMPO NOR WD 11mm 19:41:51

Supplementary Figure 22. BSE (BackScattered Electron) image of symplectite in Tissint.

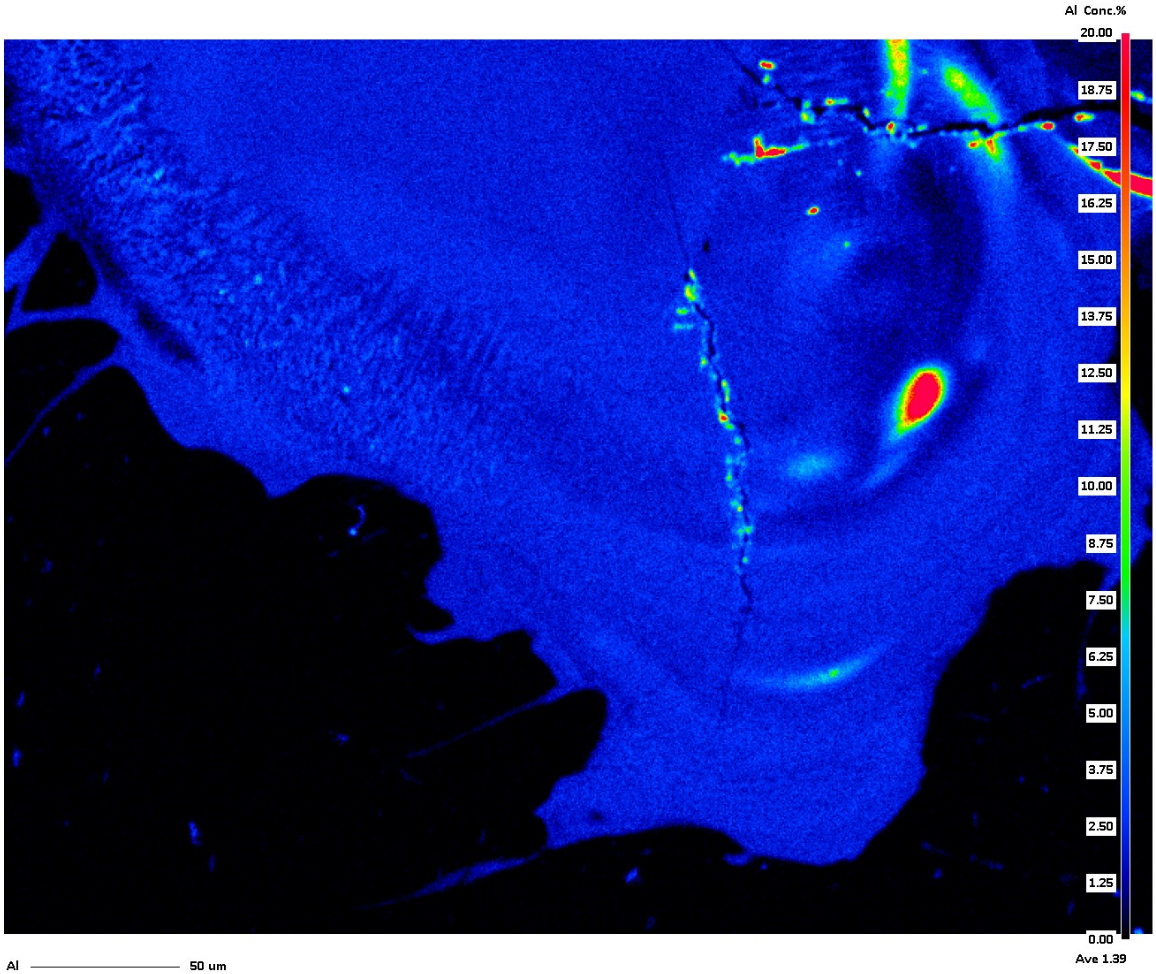

Supplementary Figure 23. Quantitative WDS (Wavelength Dispersive Spectrometry) elemental map distribution of aluminum (Al) in the symplectite of Tissint. WDS element maps are given in weight percent (wt%). WDS element maps correspond to BSE image from Supplementary Figure 22. Plag = plagioclase; Mer = merrillite; Ap = apatite; OPX = orthopyroxene. Scale bar is 50 µm in length.

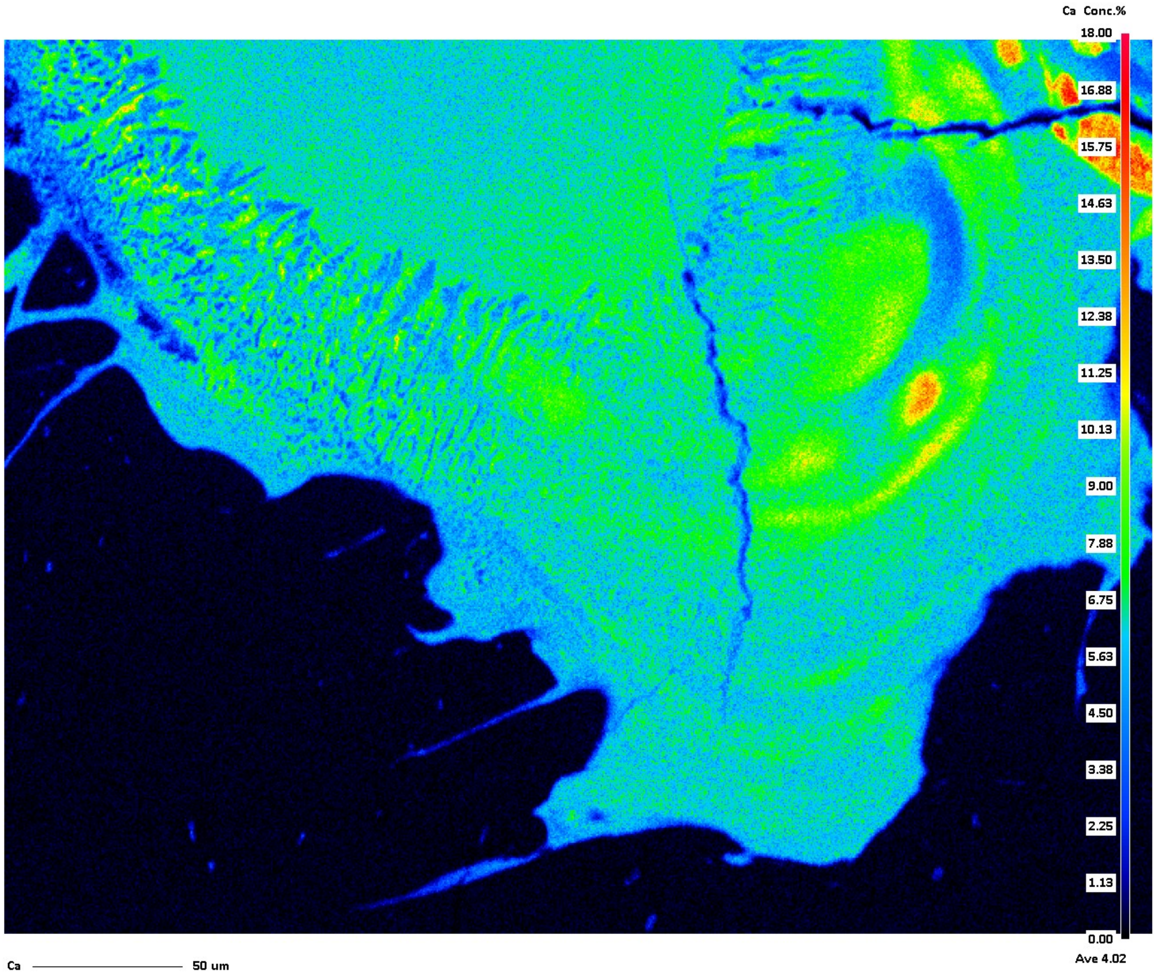

Supplementary Figure 24. Quantitative WDS (Wavelength Dispersive Spectrometry) elemental map distribution of calcium (Ca) in the symplectite of Tissint. WDS element maps are given in weight percent (wt%). WDS element maps correspond to BSE image from Supplementary Figure 22. Plag = plagioclase; Mer = merrillite; Ap = apatite; OPX = orthopyroxene. Scale bar is 50 μm in length.

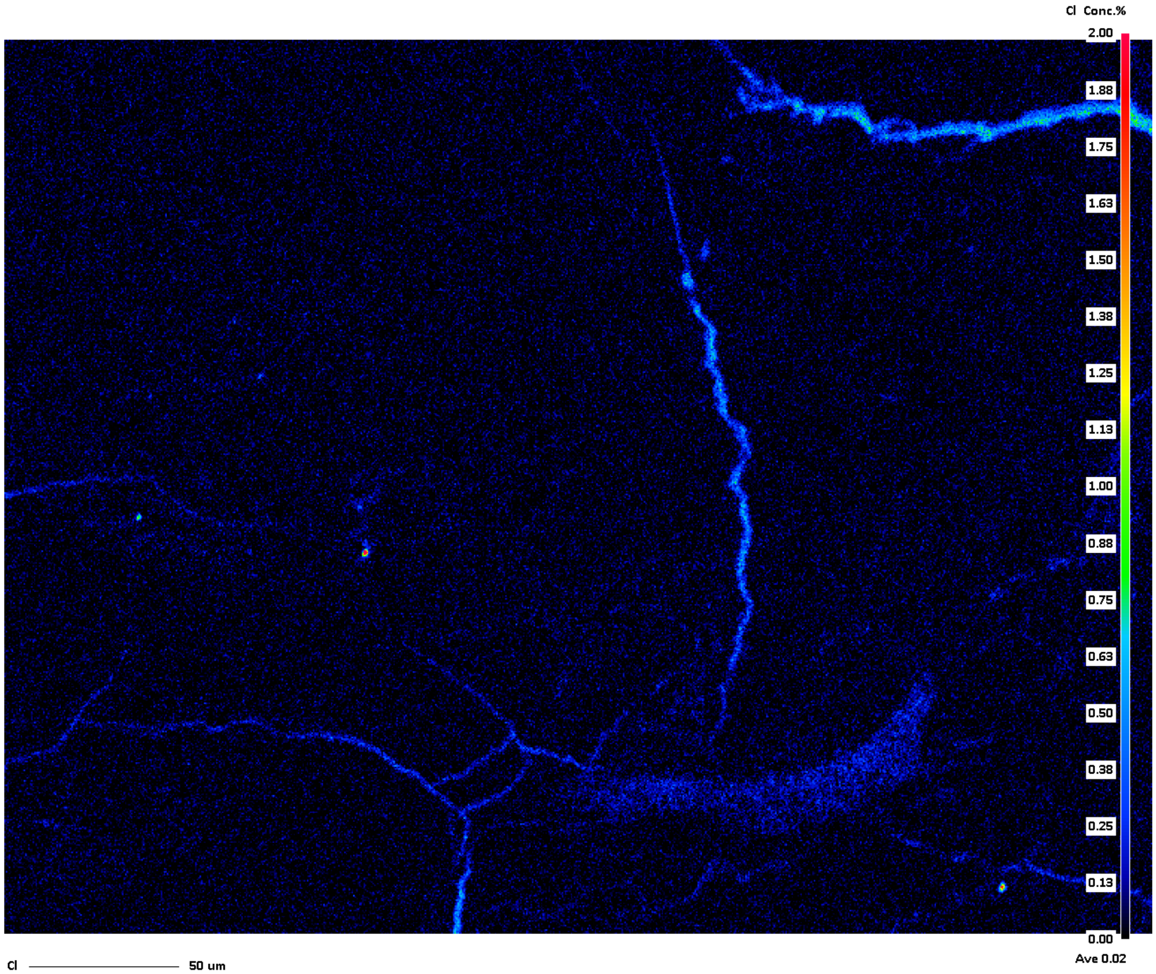

Supplementary Figure 25. Quantitative WDS (Wavelength Dispersive Spectrometry) elemental map distribution of chlorine (Cl) in the symplectite of Tissint. WDS element maps are given in weight percent (wt%). WDS element maps correspond to BSE image from Supplementary Figure 22. Plag = plagioclase; Mer = merrillite; Ap = apatite; OPX = orthopyroxene. Scale bar is 50 µm in length.

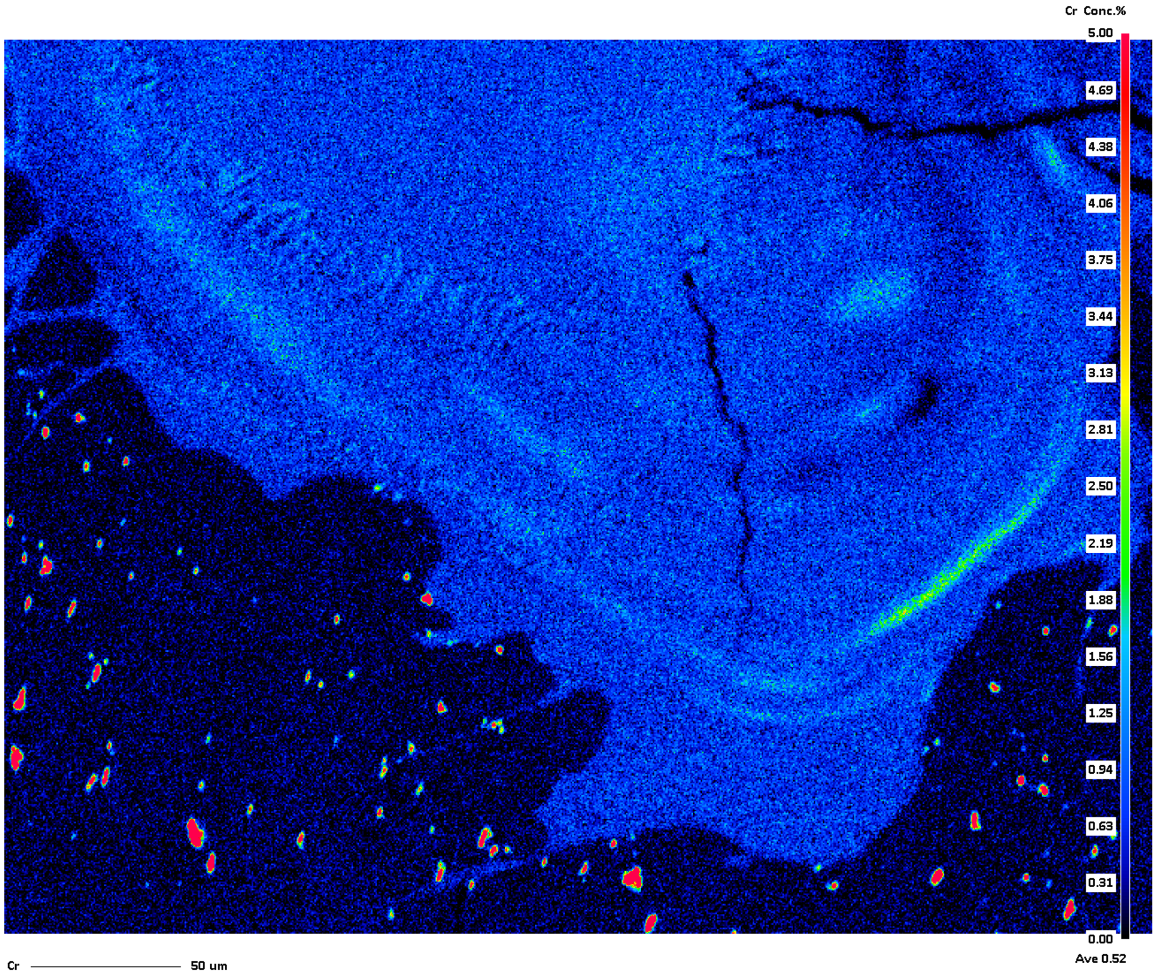

Supplementary Figure 26. Quantitative WDS (Wavelength Dispersive Spectrometry) elemental map distribution of chromium (Cr) in the symplectite of Tissint. WDS element maps are given in weight percent (wt%). WDS element maps correspond to BSE image from Supplementary Figure 22. Plag = plagioclase; Mer = merrillite; Ap = apatite; OPX = orthopyroxene. Scale bar is 50 µm in length.

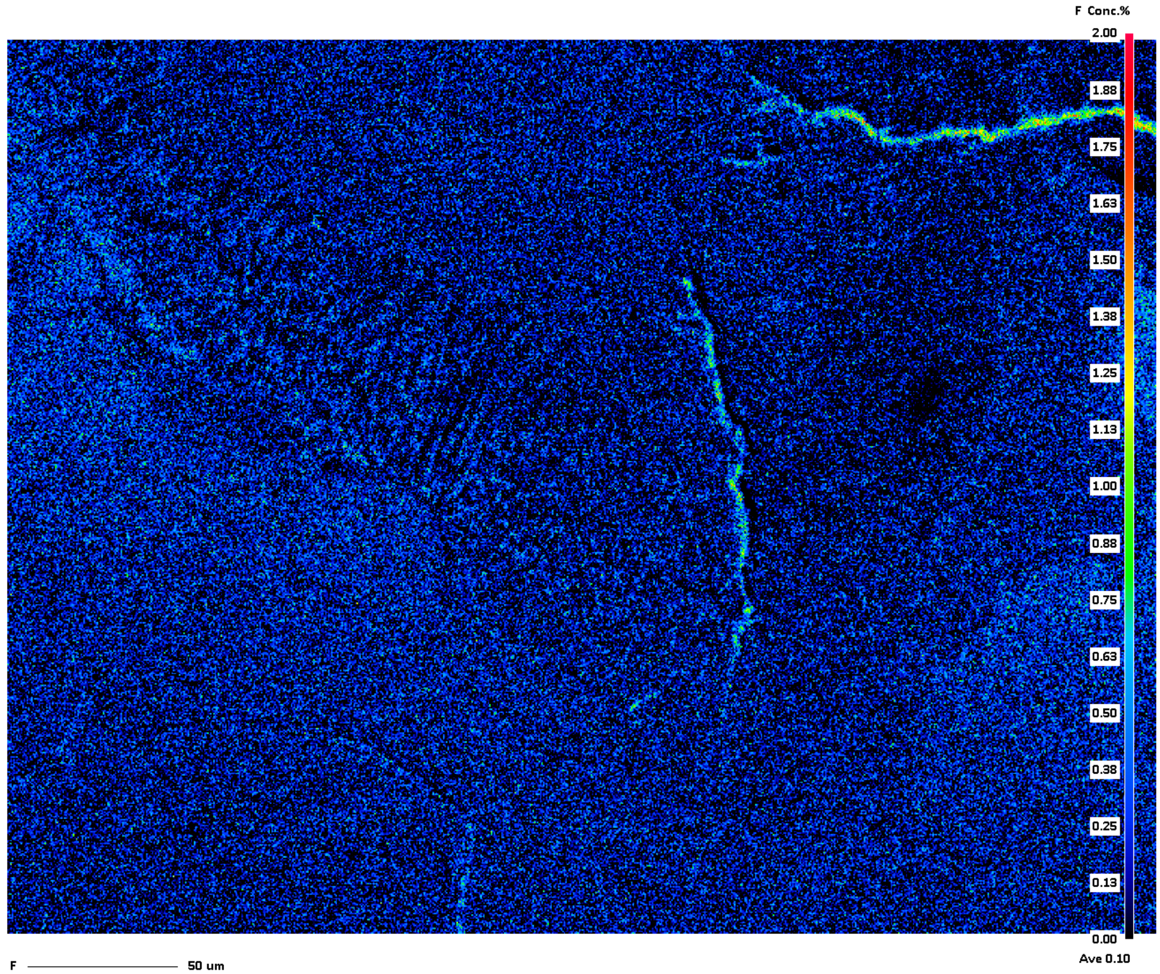

Supplementary Figure 27. Quantitative WDS (Wavelength Dispersive Spectrometry) elemental map distribution of fluorine (F) in the symplectite of Tissint. WDS element maps are given in weight percent (wt%). WDS element maps correspond to BSE image from Supplementary Figure 22. Plag = plagioclase; Mer = merrillite; Ap = apatite; OPX = orthopyroxene. Scale bar is 50 μm in length.

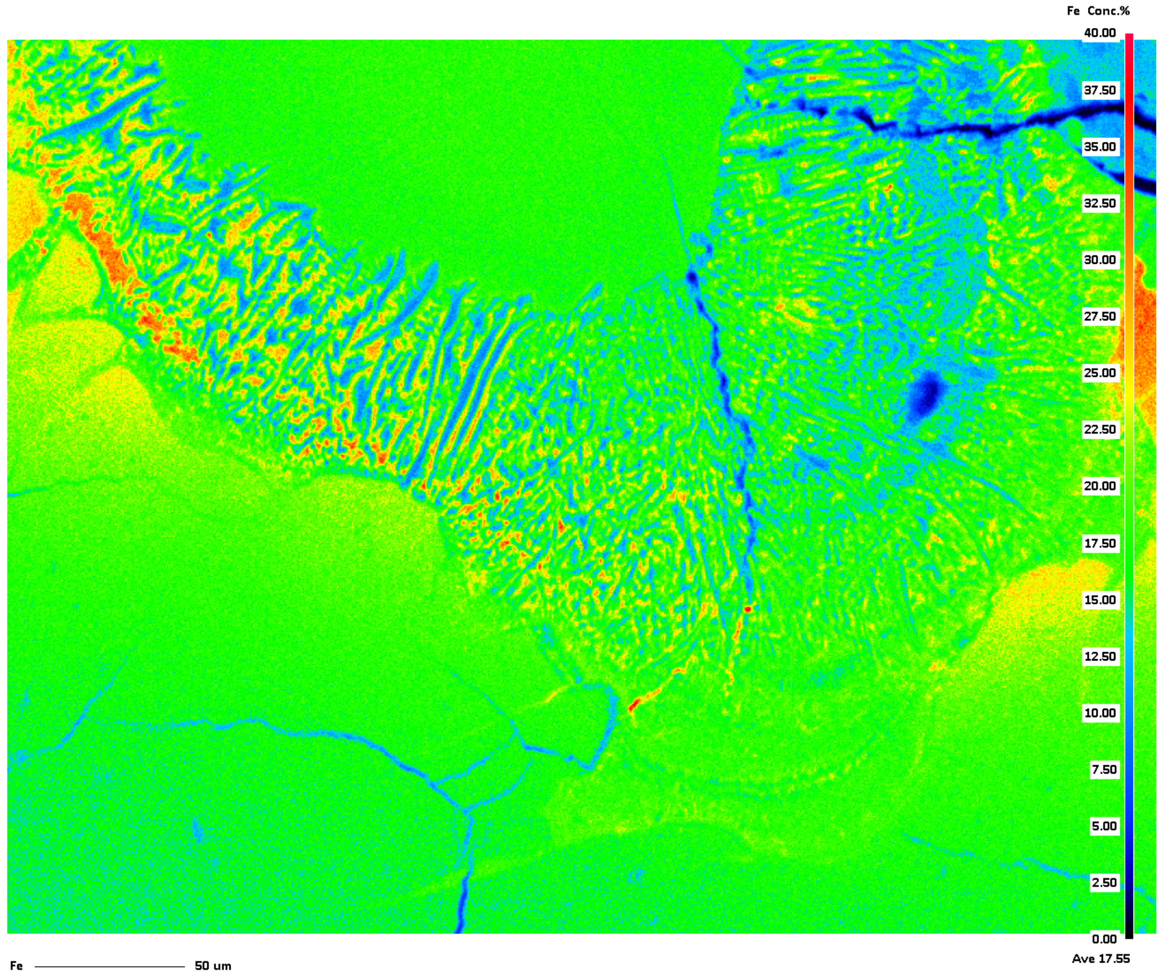

Supplementary Figure 28. Quantitative WDS (Wavelength Dispersive Spectrometry) elemental map distribution of iron (Fe) in the symplectite of Tissint. WDS element maps are given in weight percent (wt%). WDS element maps correspond to BSE image from Supplementary Figure 22. Plag = plagioclase; Mer = merrillite; Ap = apatite; OPX = orthopyroxene. Scale bar is 50 μm in length.

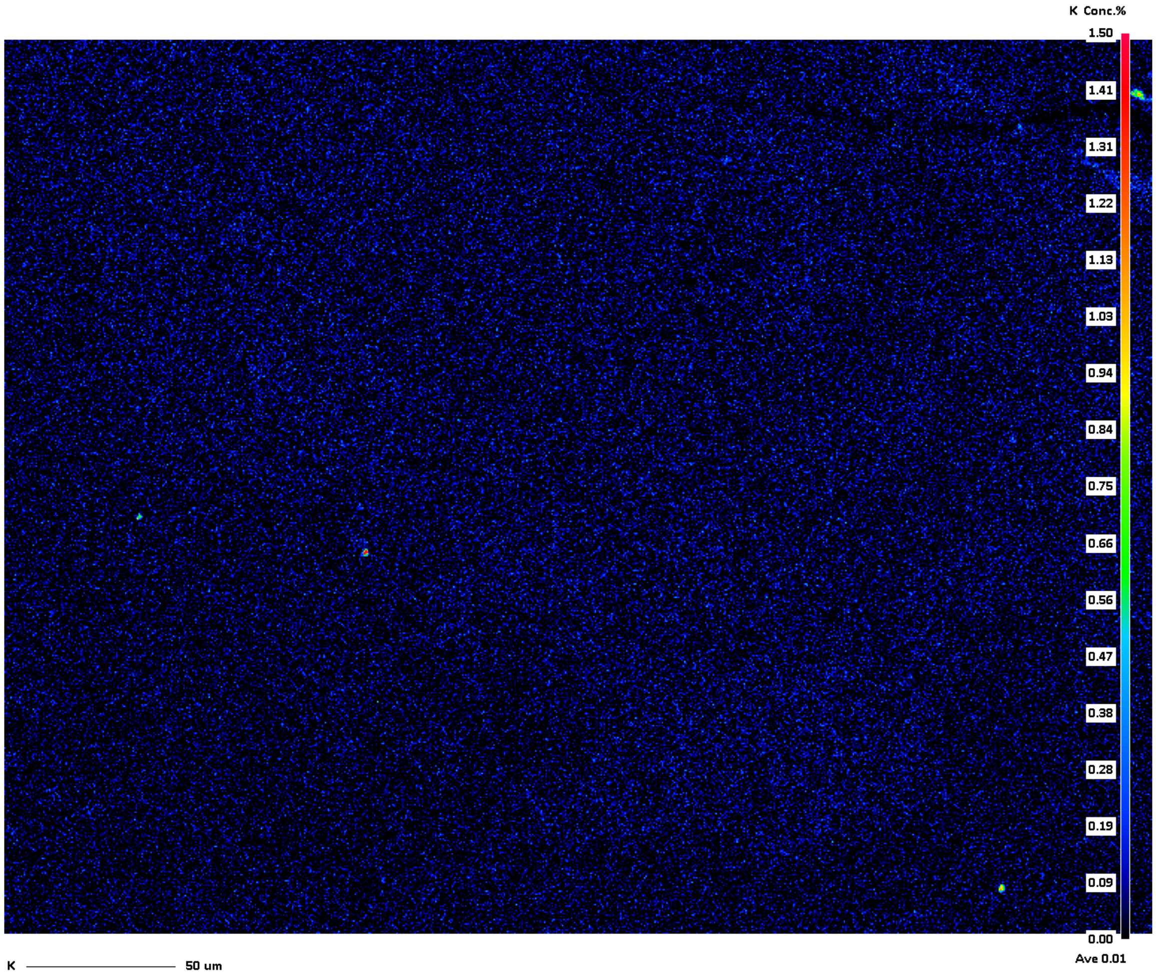

Supplementary Figure 29. Quantitative WDS (Wavelength Dispersive Spectrometry) elemental map distribution of potassium (K) in the symplectite of Tissint. WDS element maps are given in weight percent (wt%). WDS element maps correspond to BSE image from Supplementary Figure 22. Plag = plagioclase; Mer = merrillite; Ap = apatite; OPX = orthopyroxene. Scale bar is 50 µm in length.

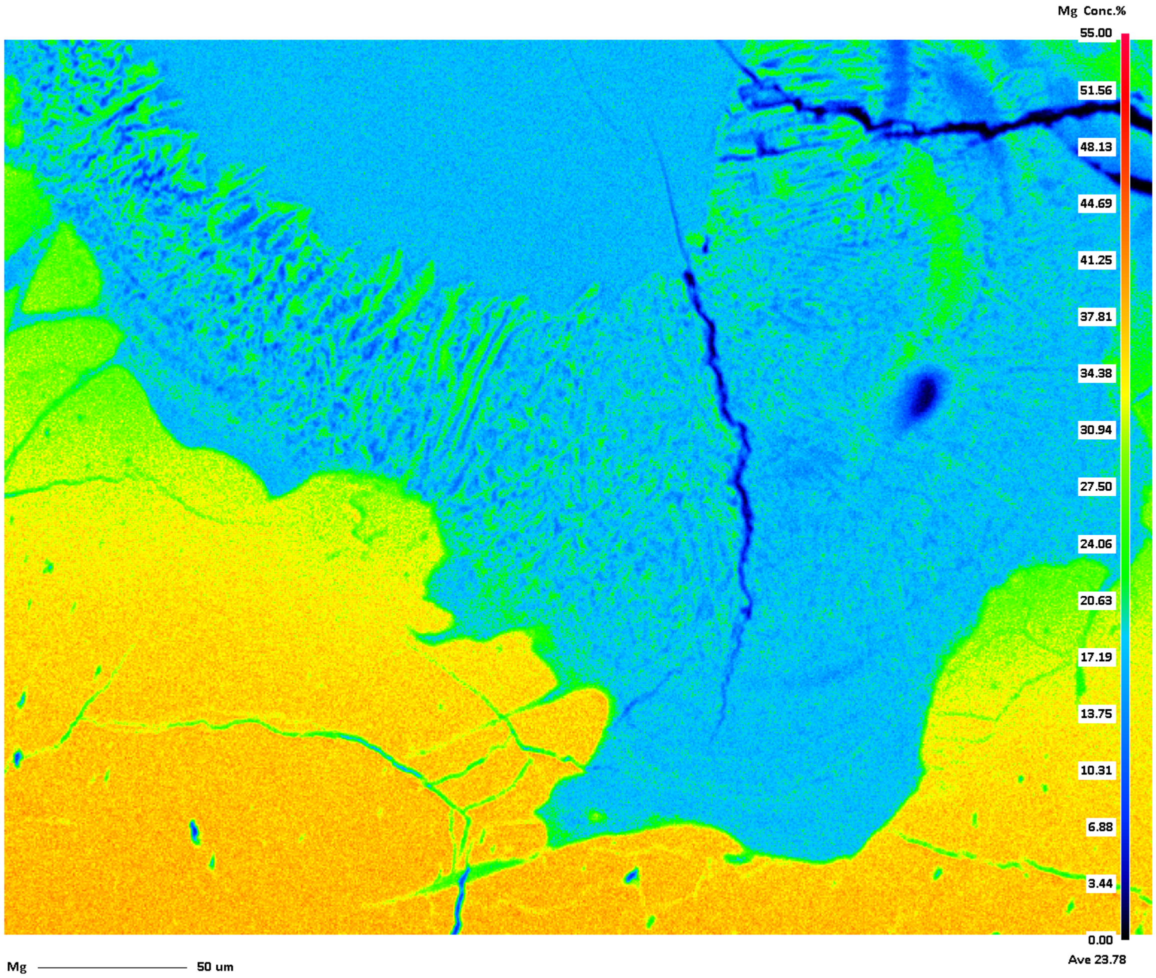

Supplementary Figure 30. Quantitative WDS (Wavelength Dispersive Spectrometry) elemental map distribution of magnesium (Mg) in the symplectite of Tissint. WDS element maps are given in weight percent (wt%). WDS element maps correspond to BSE image from Supplementary Figure 22. Plag = plagioclase; Mer = merrillite; Ap = apatite; OPX = orthopyroxene. Scale bar is 50 µm in length.

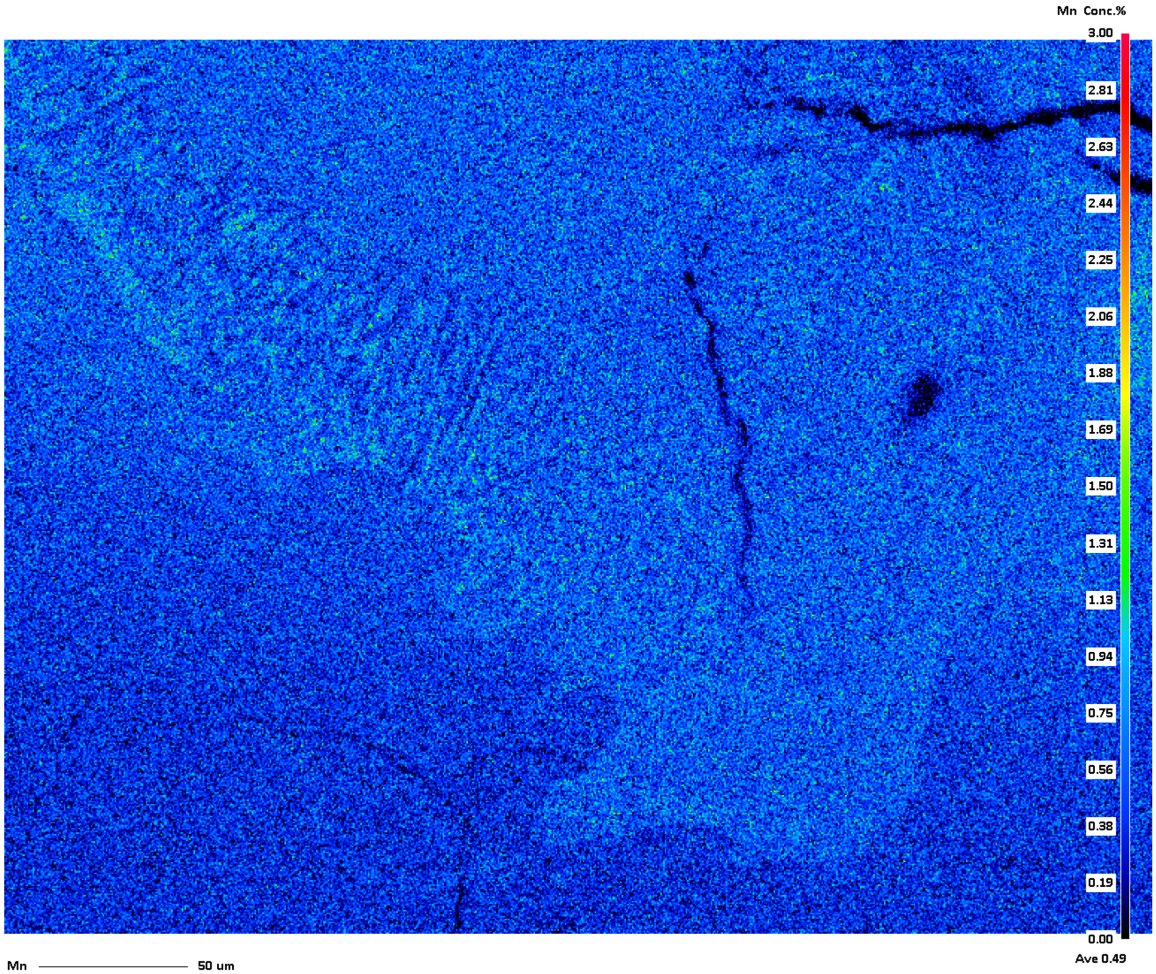

Supplementary Figure 31. Quantitative WDS (Wavelength Dispersive Spectrometry) elemental map distribution of manganese (Mn) in the symplectite of Tissint. WDS element maps are given in weight percent (wt%). WDS element maps correspond to BSE image from Supplementary Figure 22. Plag = plagioclase; Mer = merrillite; Ap = apatite; OPX = orthopyroxene. Scale bar is 50 µm in length.

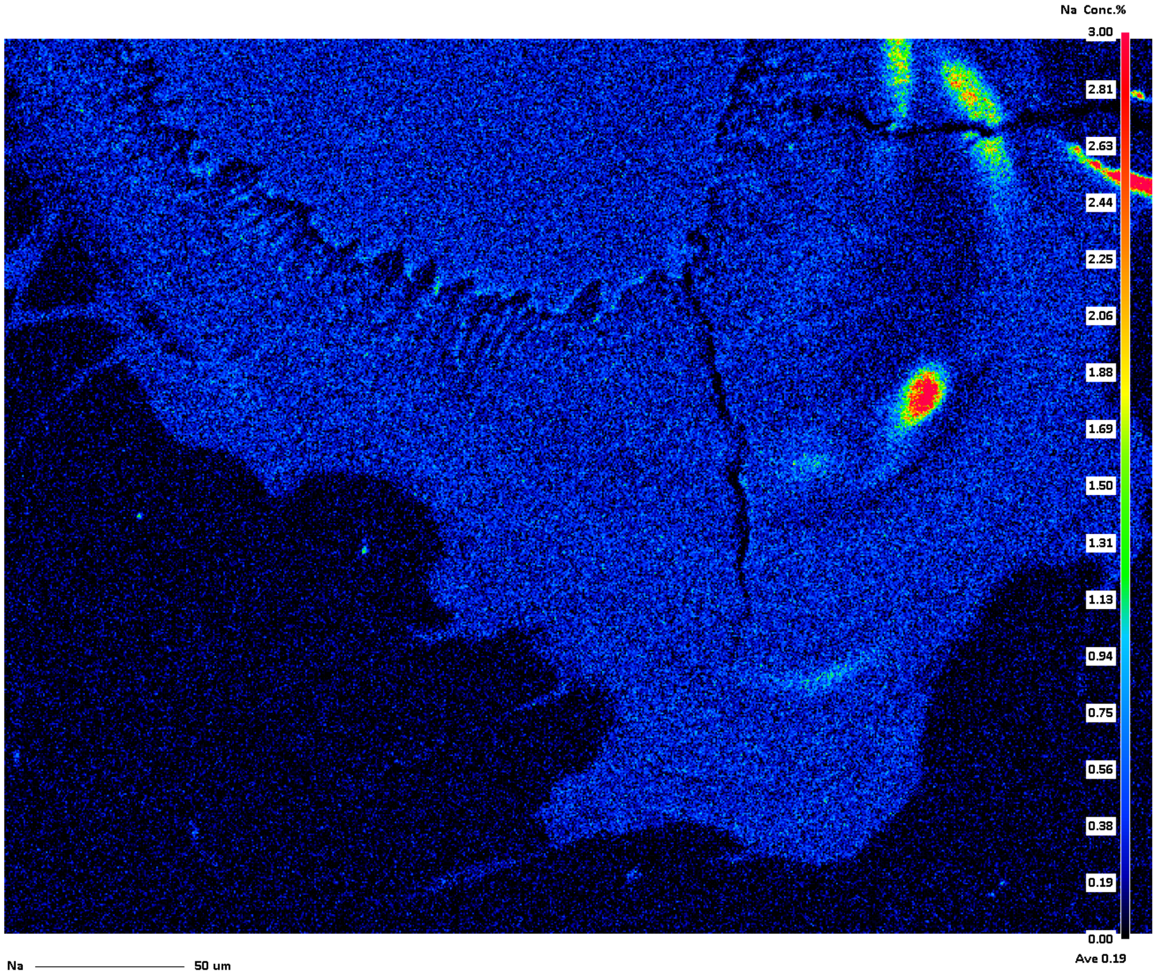

Supplementary Figure 32. Quantitative WDS (Wavelength Dispersive Spectrometry) elemental map distribution of sodium (Na) in the symplectite of Tissint. WDS element maps are given in weight percent (wt%). WDS element maps correspond to BSE image from Supplementary Figure 22. Plag = plagioclase; Mer = merrillite; Ap = apatite; OPX = orthopyroxene. Scale bar is 50 µm in length.

ALH 84001

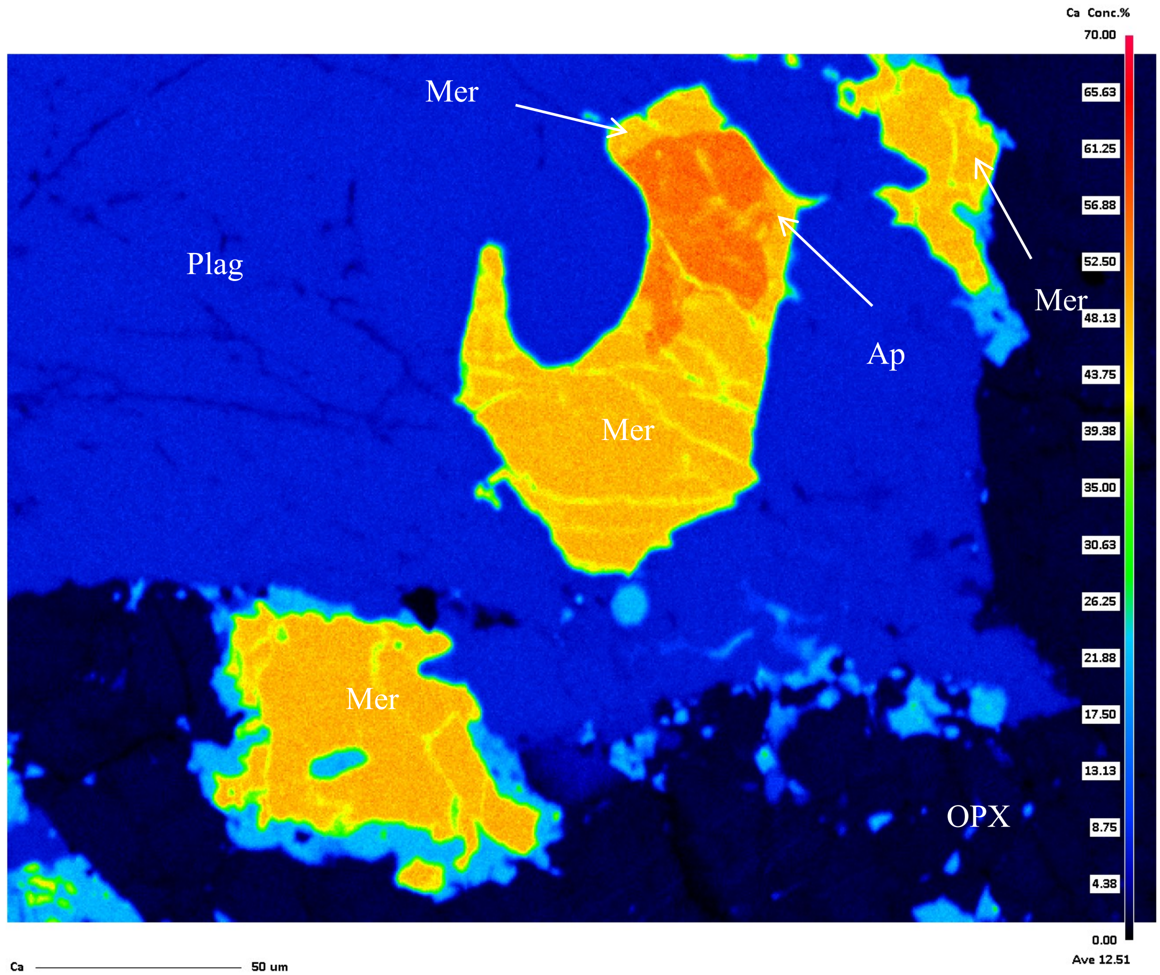

Supplementary Figure 33. Quantitative WDS (Wavelength Dispersive Spectrometry) elemental map distribution of calcium (Ca) in apatite-merrillite intergrown grains #1-3 in ALH 84001. WDS element maps are given in weight percent (wt%). WDS element maps correspond to BSE image from Figure 49. Plag = plagioclase; Mer = merrillite; Ap = apatite; OPX = orthopyroxene. Scale bar is 50 µm in length.

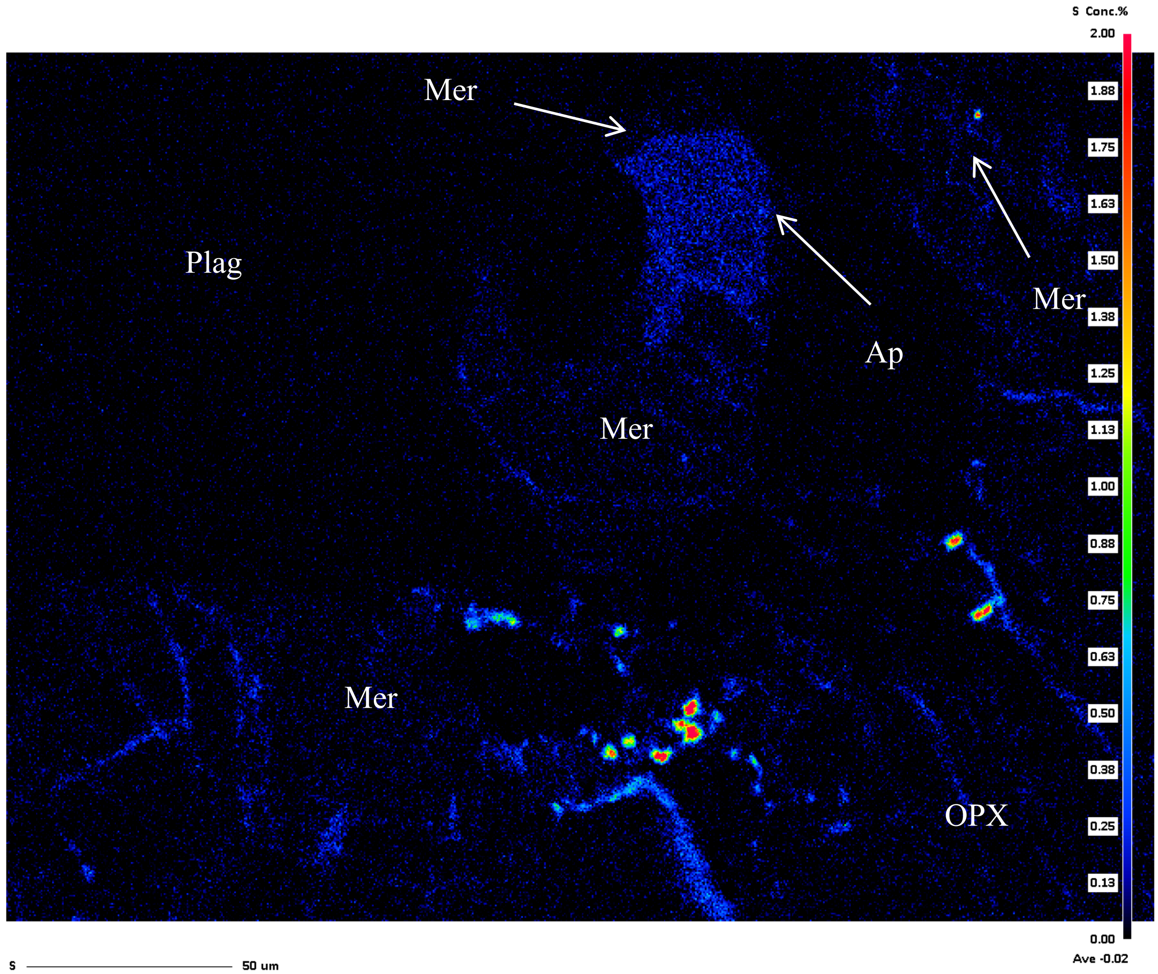

Supplementary Figure 34. Quantitative WDS (Wavelength Dispersive Spectrometry) elemental map distribution of sulfur (S) in apatite-merrillite intergrown grains #1-3 in ALH 84001. WDS element maps are given in weight percent (wt%). WDS element maps correspond to BSE image from Figure 49. Plag = plagioclase; Mer = merrillite; Ap = apatite; OPX = orthopyroxene. Scale bar is 50 µm in length.

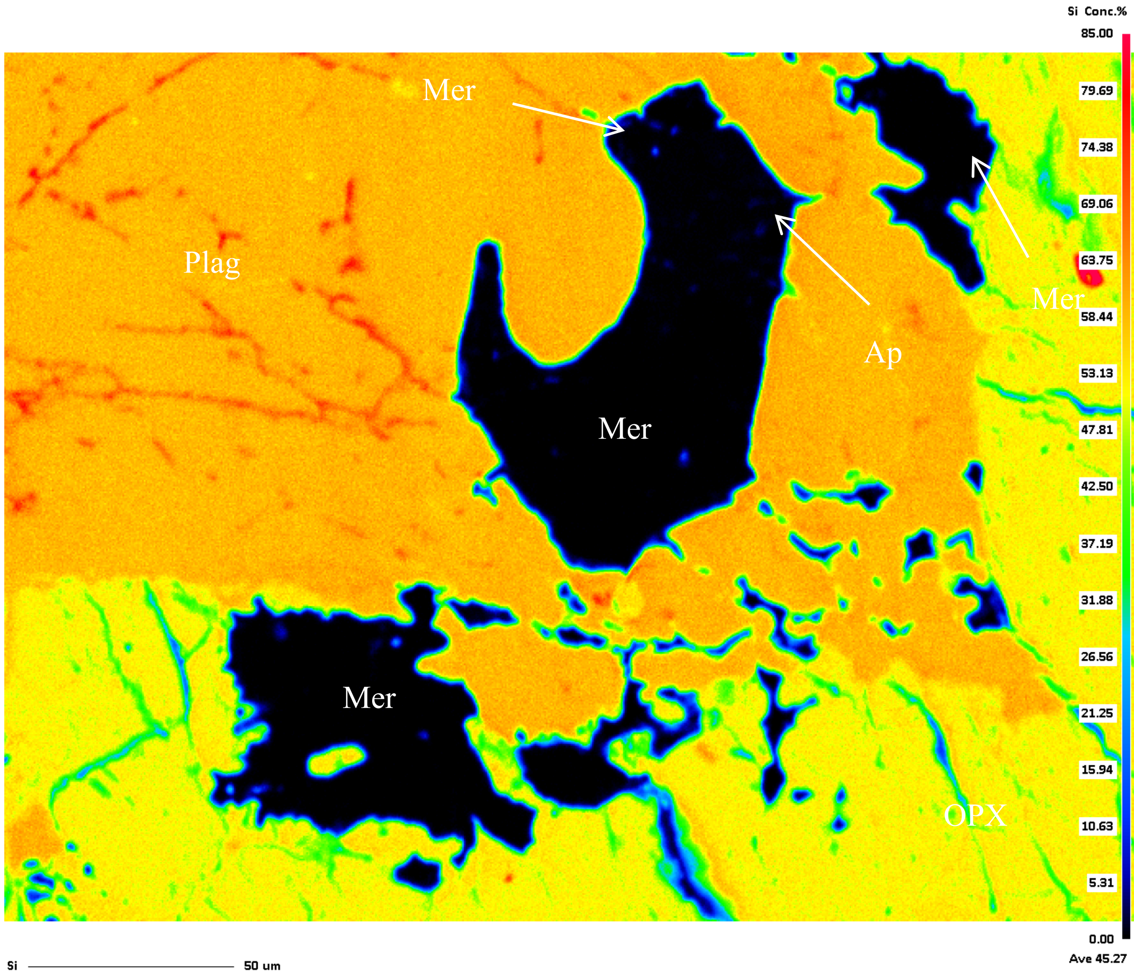

Supplementary Figure 35. Quantitative WDS (Wavelength Dispersive Spectrometry) elemental map distribution of silicon (Si) in apatite-merrillite intergrown grains #1-3 in ALH 84001. WDS element maps are given in weight percent (wt%). WDS element maps correspond to BSE image from Figure 49. Plag = plagioclase; Mer = merrillite; Ap = apatite; OPX = orthopyroxene. Scale bar is 50 μm in length.

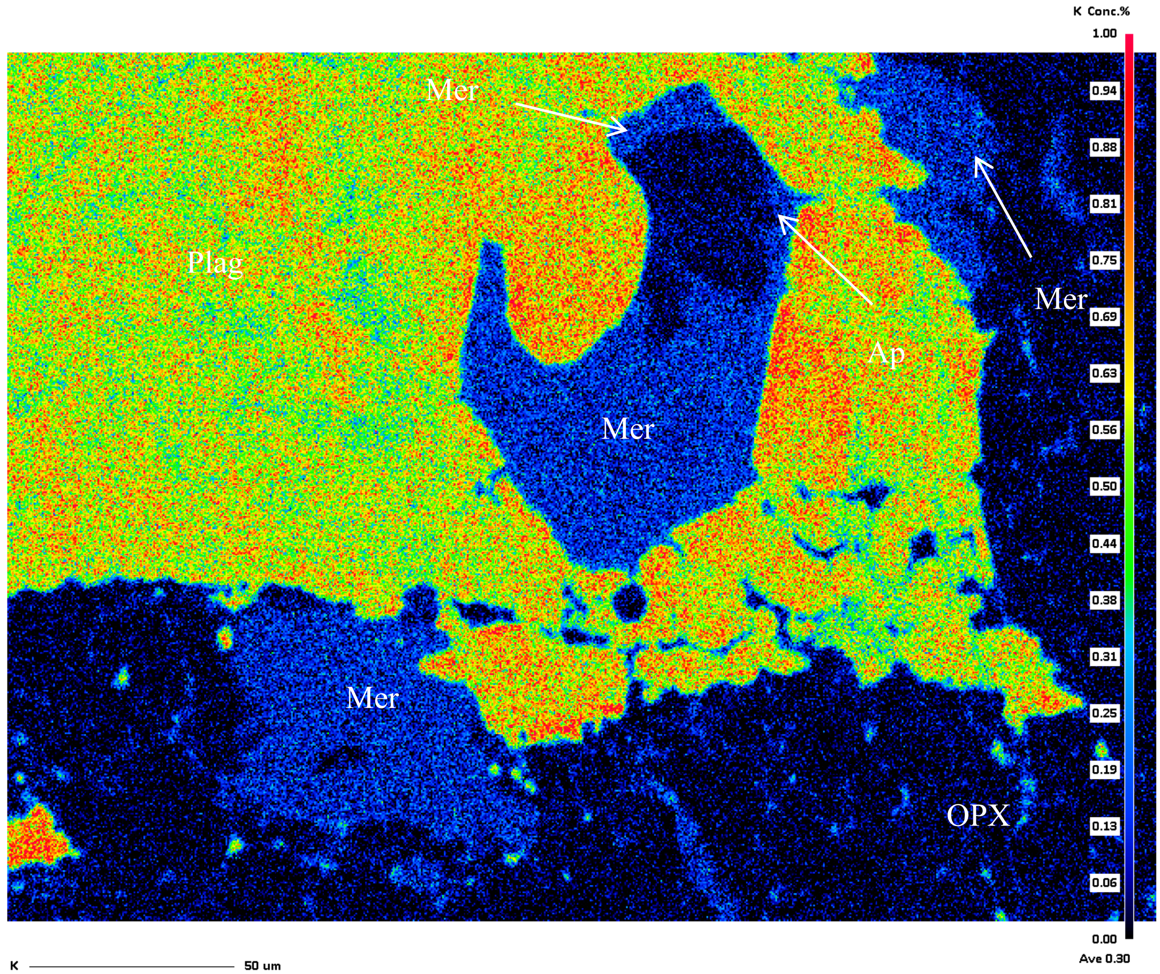

Supplementary Figure 36. Quantitative WDS (Wavelength Dispersive Spectrometry) elemental map distribution of potassium (K) in apatite-merrillite intergrown grains #1-3 in ALH 84001. WDS element maps are given in weight percent (wt%). WDS element maps correspond to BSE image from Figure 49. Plag = plagioclase; Mer = merrillite; Ap = apatite; OPX = orthopyroxene. Scale bar is 50 μm in length.

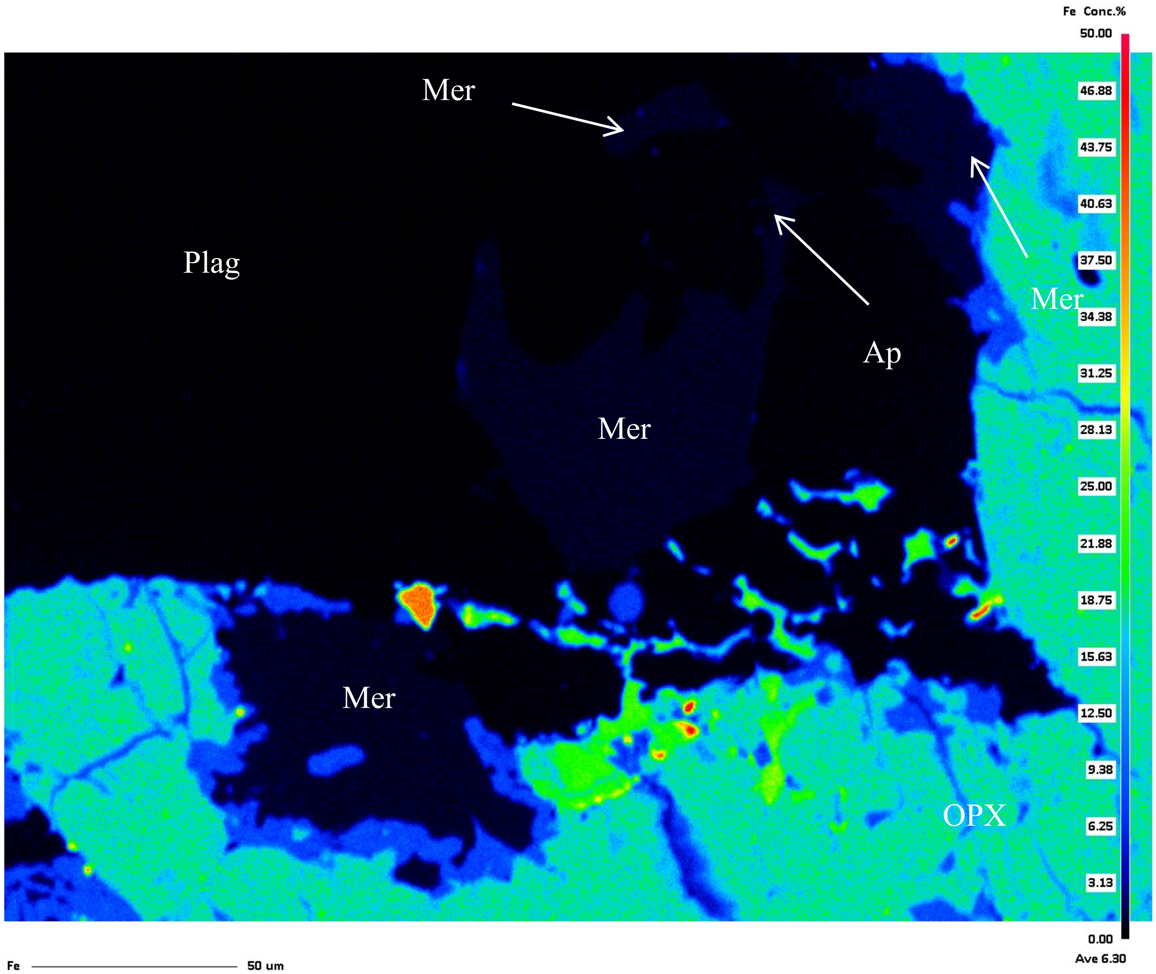

Supplementary Figure 37. Quantitative WDS (Wavelength Dispersive Spectrometry) elemental map distribution of iron (Fe) in apatite-merrillite intergrown grains #1-3 in ALH 84001. WDS element maps are given in weight percent (wt%). WDS element maps correspond to BSE image from Figure 49. Plag = plagioclase; Mer = merrillite; Ap = apatite; OPX = orthopyroxene. Scale bar is 50 µm in length.

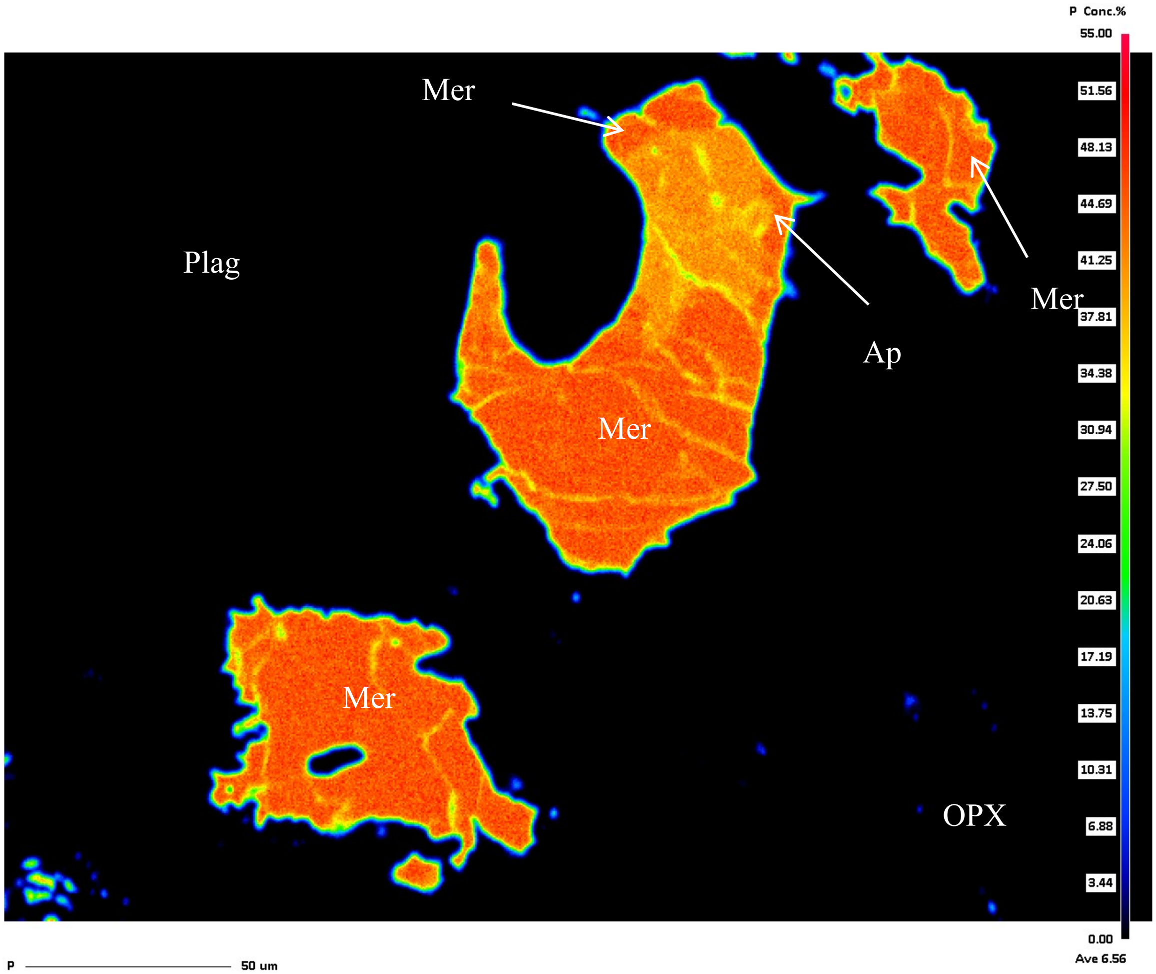

Supplementary Figure 38. Quantitative WDS (Wavelength Dispersive Spectrometry) elemental map distribution of phosphorus (P) in apatite-merrillite intergrown grains #1-3 in ALH 84001. WDS element maps are given in weight percent (wt%). WDS element maps correspond to BSE image from Figure 49. Plag = plagioclase; Mer = merrillite; Ap = apatite; OPX = orthopyroxene. Scale bar is 50 μm in length.

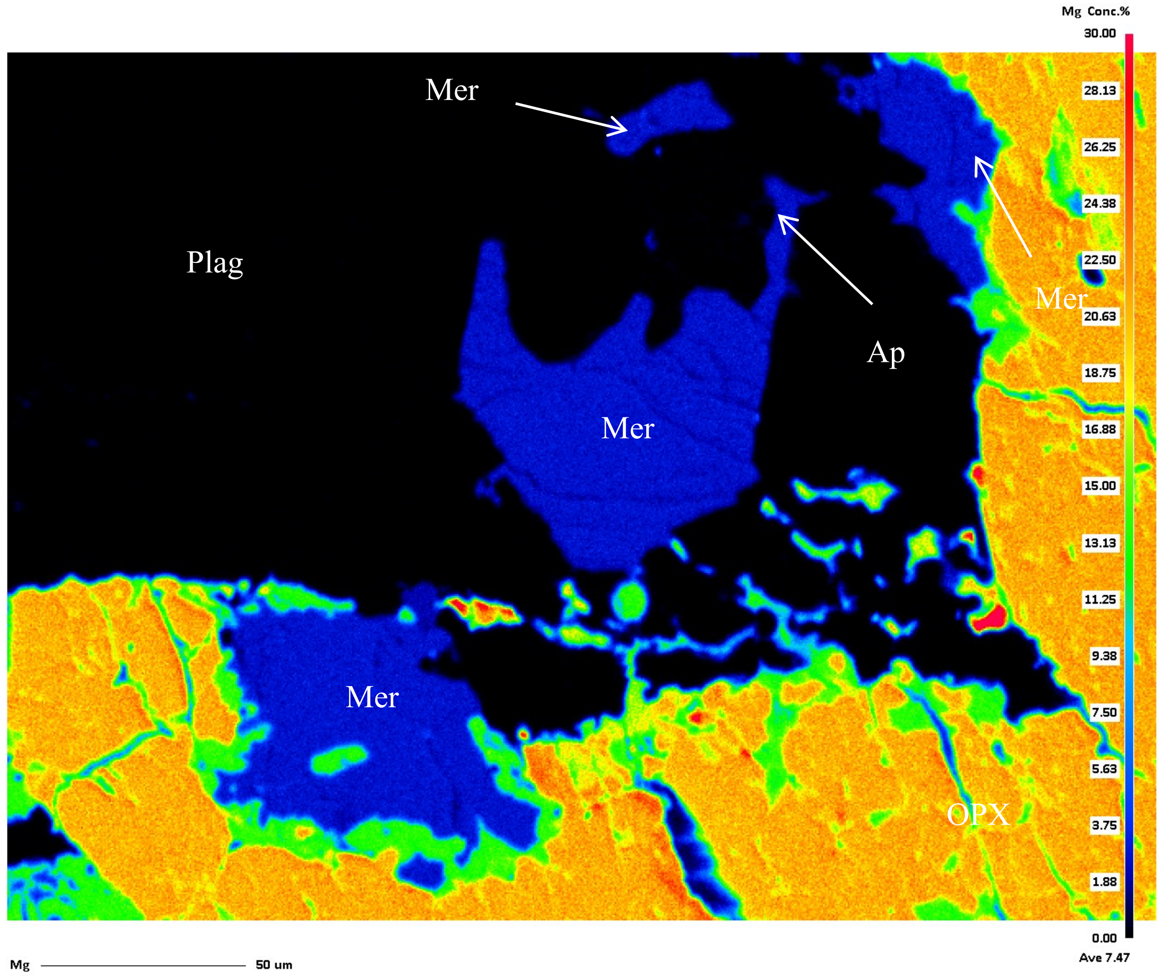

Supplementary Figure 39. Quantitative WDS (Wavelength Dispersive Spectrometry) elemental map distribution of magnesium (Mg) in apatite-merrillite intergrown grains #1-3 in ALH 84001. WDS element maps are given in weight percent (wt%). WDS element maps correspond to BSE image from Figure 49. Plag = plagioclase; Mer = merrillite; Ap = apatite; OPX = orthopyroxene. Scale bar is 50 μm in length.

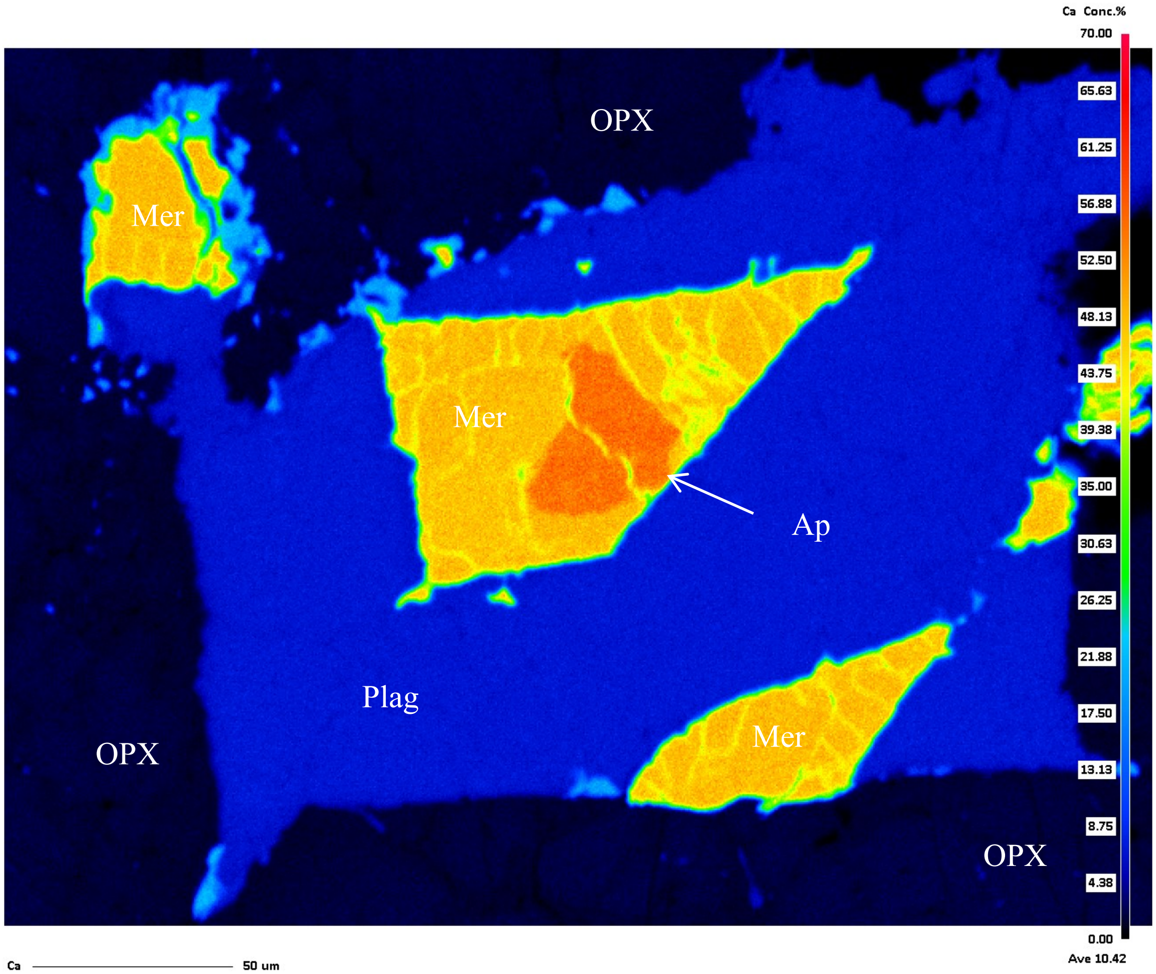

Supplementary Figure 40. Quantitative WDS (Wavelength Dispersive Spectrometry) elemental map distribution of calcium (Ca) in apatite-merrillite intergrown grains #4-6 in ALH 84001. WDS element maps are given in weight percent (wt%). WDS element maps correspond to BSE image from Figure 49. Plag = plagioclase; Mer = merrillite; Ap = apatite; OPX = orthopyroxene. Scale bar is 50 μm in length.

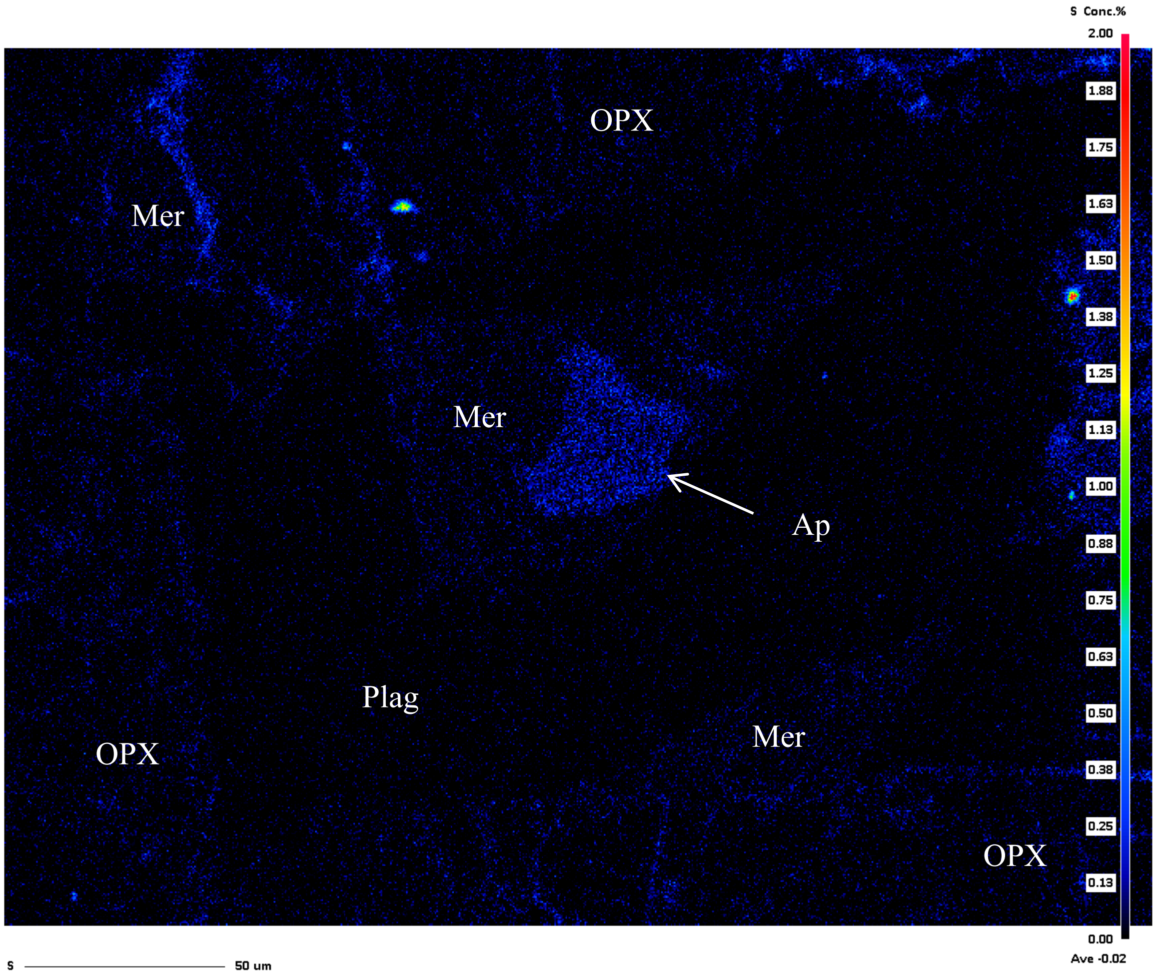

Supplementary Figure 41. Quantitative WDS (Wavelength Dispersive Spectrometry) elemental map distribution of sulfur (S) in apatite-merrillite intergrown grains #1-3 in ALH 84001. WDS element maps are given in weight percent (wt%). WDS element maps correspond to BSE image from Figure 49. Plag = plagioclase; Mer = merrillite; Ap = apatite; OPX = orthopyroxene. Scale bar is 50 μm in length.

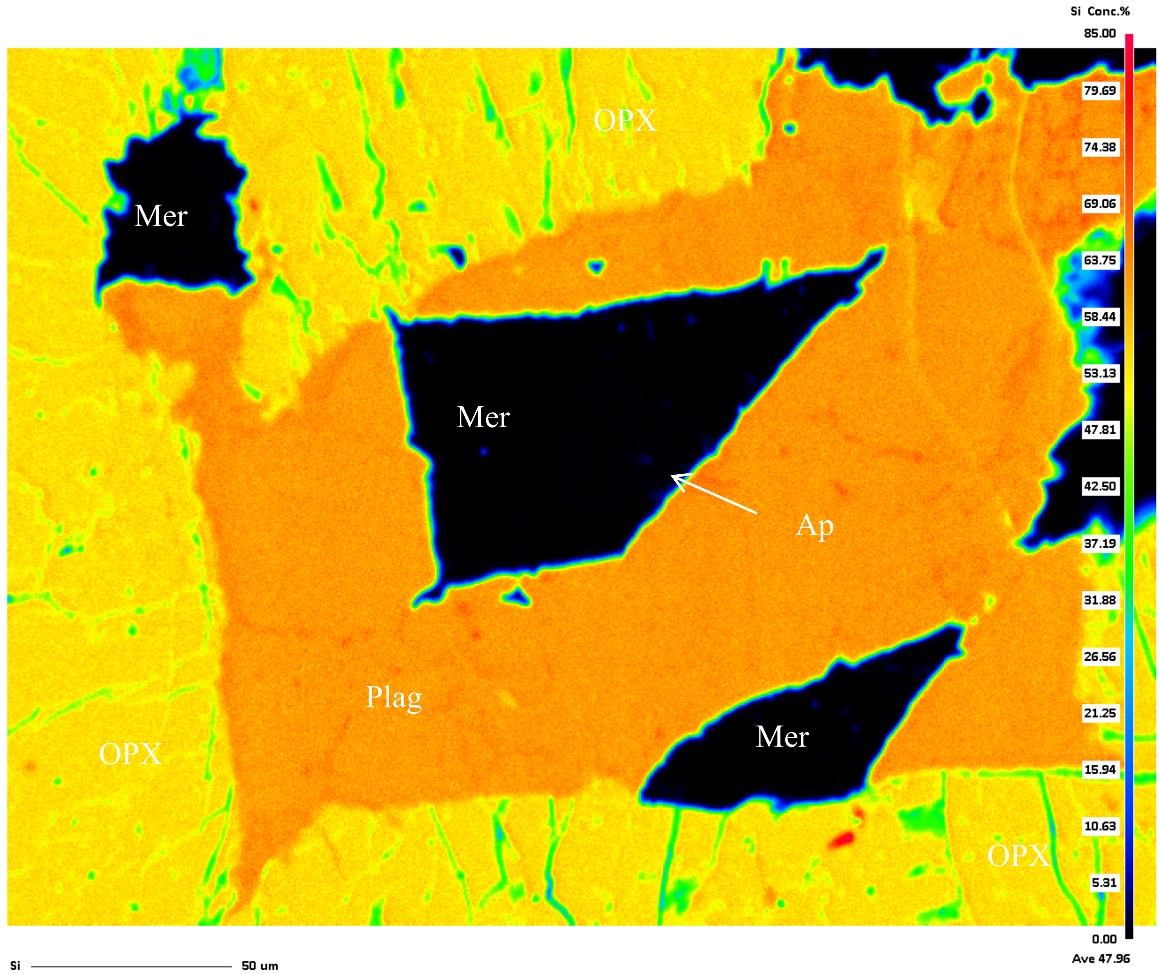

Supplementary Figure 42. Quantitative WDS (Wavelength Dispersive Spectrometry) elemental map distribution of silicon (Si) in apatite-merrillite intergrown grains #1-3 in ALH 84001. WDS element maps are given in weight percent (wt%). WDS element maps correspond to BSE image from Figure 53. Plag = plagioclase; Mer = merrillite; Ap = apatite; OPX = orthopyroxene. Scale bar is 50 μm in length.

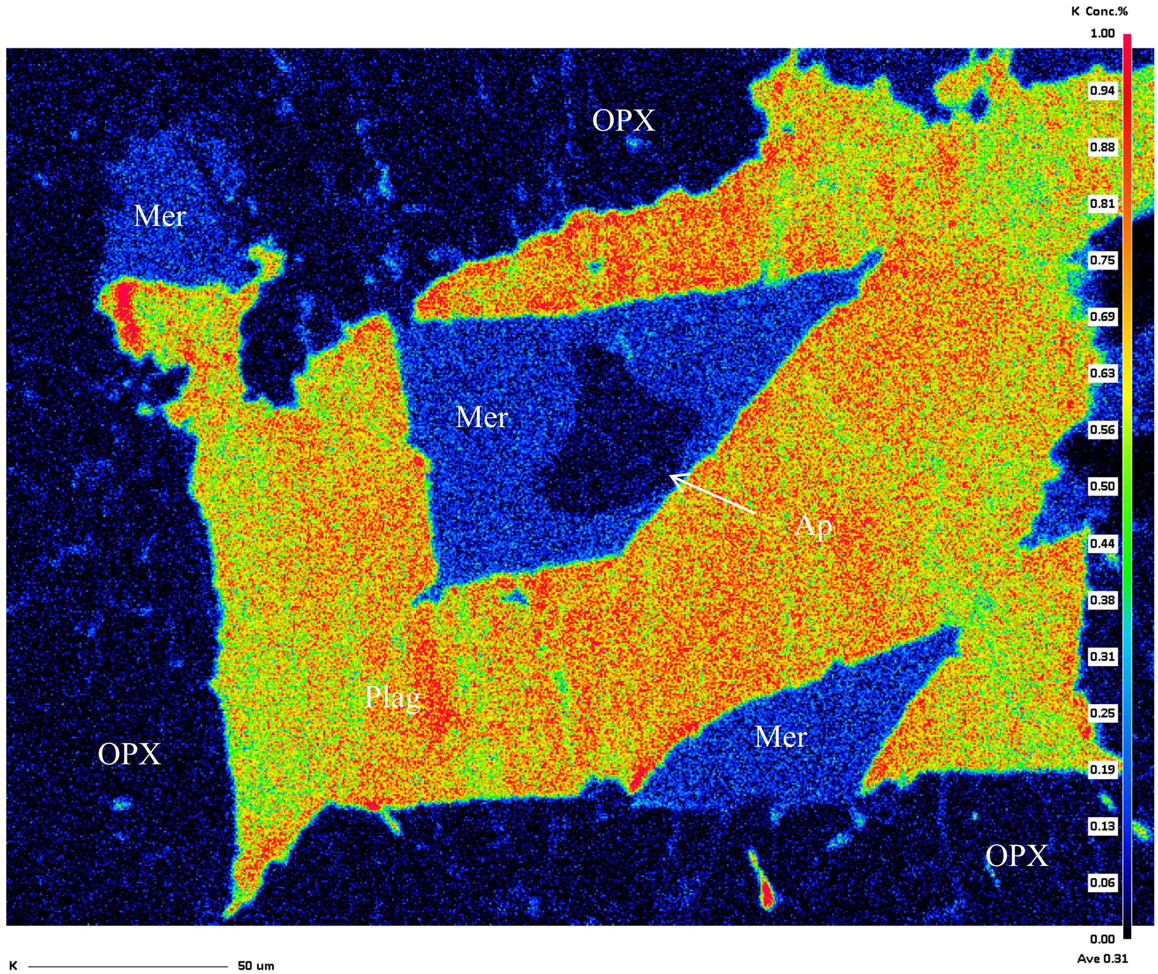

Supplementary Figure 43. Quantitative WDS (Wavelength Dispersive Spectrometry) elemental map distribution of potassium (K) in apatite-merrillite intergrown grains #1-3 in ALH 84001. WDS element maps are given in weight percent (wt%). WDS element maps correspond to BSE image from Figure 53. Plag = plagioclase; Mer = merrillite; Ap = apatite; OPX = orthopyroxene. Scale bar is 50 μm in length.

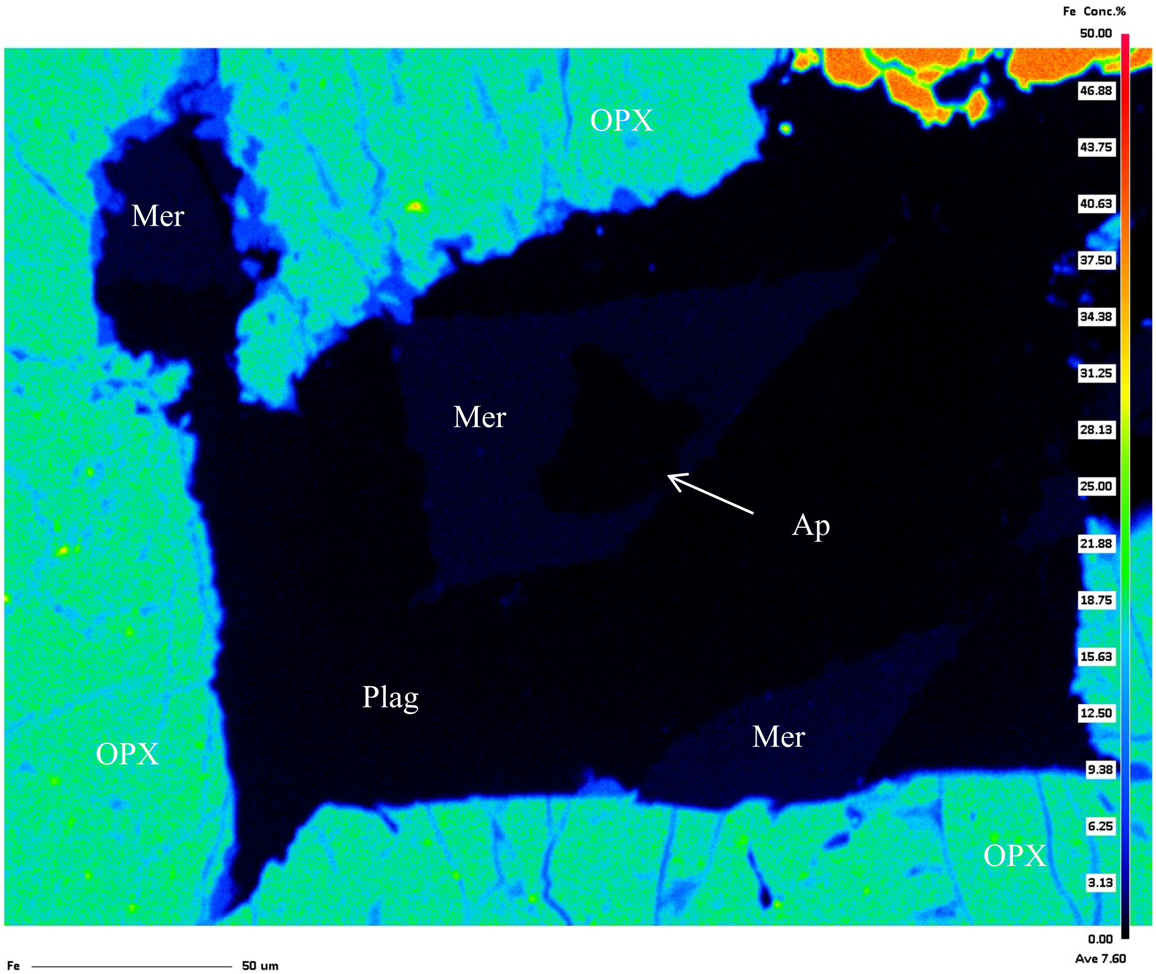

Supplementary Figure 44. Quantitative WDS (Wavelength Dispersive Spectrometry) elemental map distribution of iron (Fe) in apatite-merrillite intergrown grains #1-3 in ALH 84001. WDS element maps are given in weight percent (wt%). WDS element maps correspond to BSE image from Figure 53. Plag = plagioclase; Mer = merrillite; Ap = apatite; OPX = orthopyroxene. Scale bar is 50 μm in length.

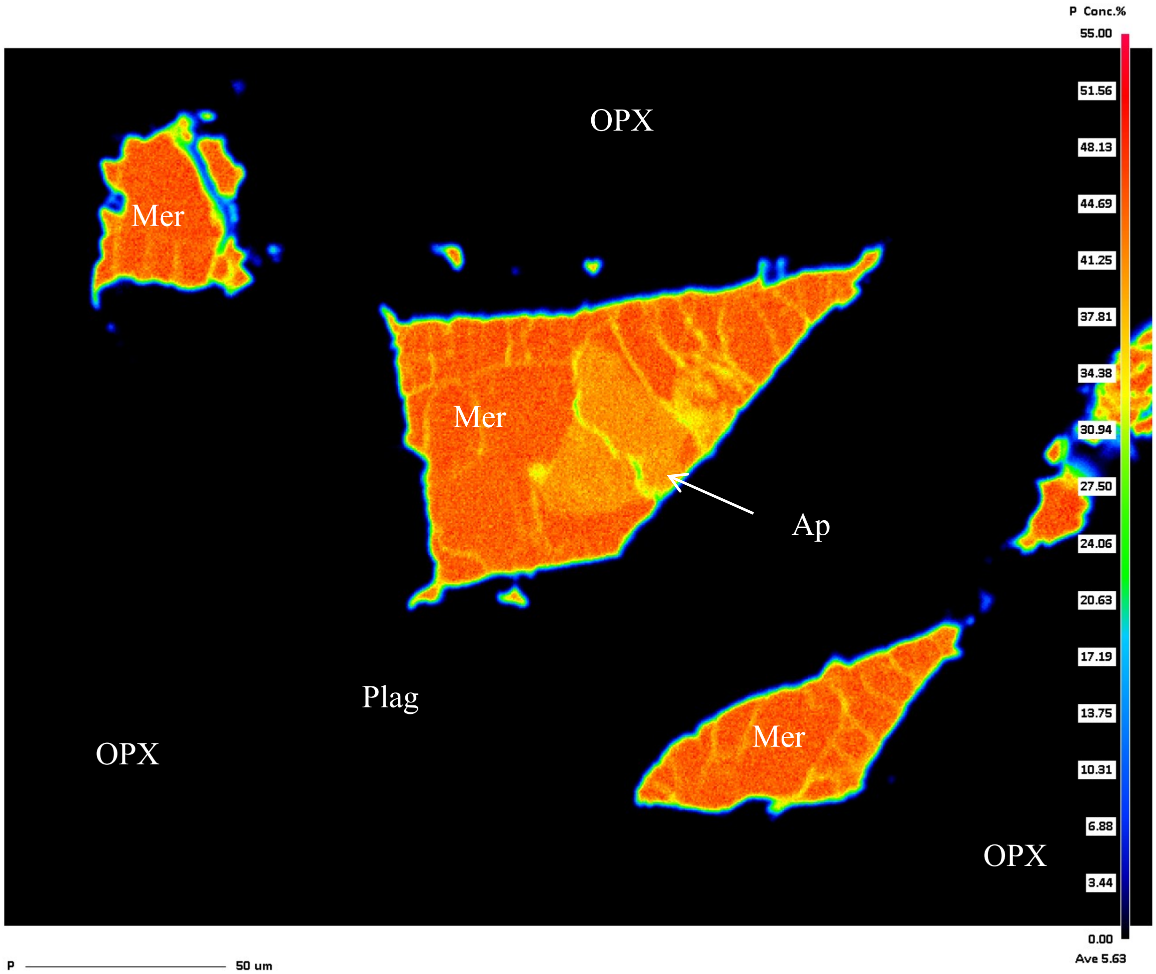

Supplementary Figure 45. Quantitative WDS (Wavelength Dispersive Spectrometry) elemental map distribution of phosphorus (P) in apatite-merrillite intergrown grains #1-3 in ALH 84001. WDS element maps are given in weight percent (wt%). WDS element maps correspond to BSE image from Figure 53. Plag = plagioclase; Mer = merrillite; Ap = apatite; OPX = orthopyroxene. Scale bar is 50 μm in length.

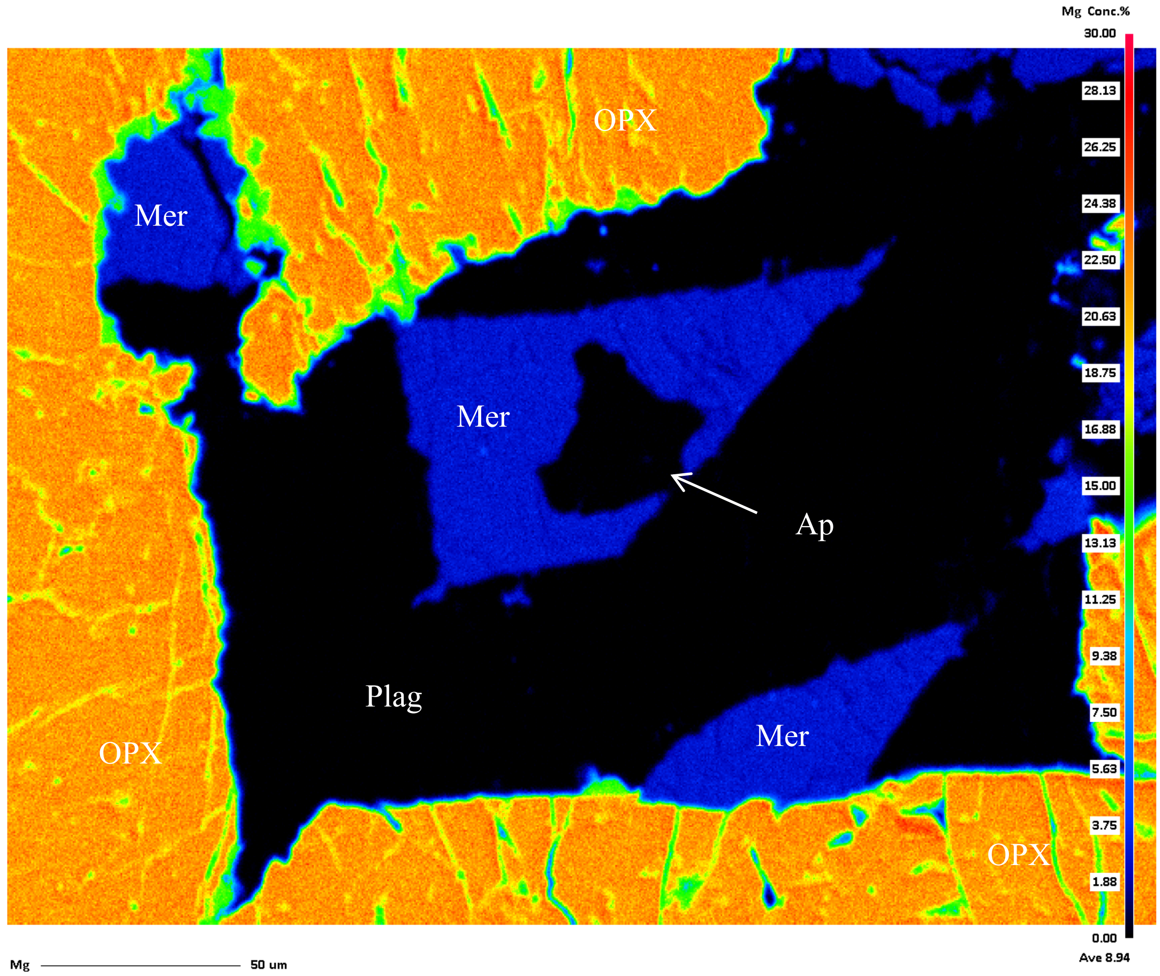

Supplementary Figure 46. Quantitative WDS (Wavelength Dispersive Spectrometry) elemental map distribution of magnesium (Mg) in apatite-merrillite intergrown grains #1-3 in ALH 84001. WDS element maps are given in weight percent (wt%). WDS element maps correspond to BSE image from Figure 53. Plag = plagioclase; Mer = merrillite; Ap = apatite; OPX = orthopyroxene. Scale bar is 50 μm in length.

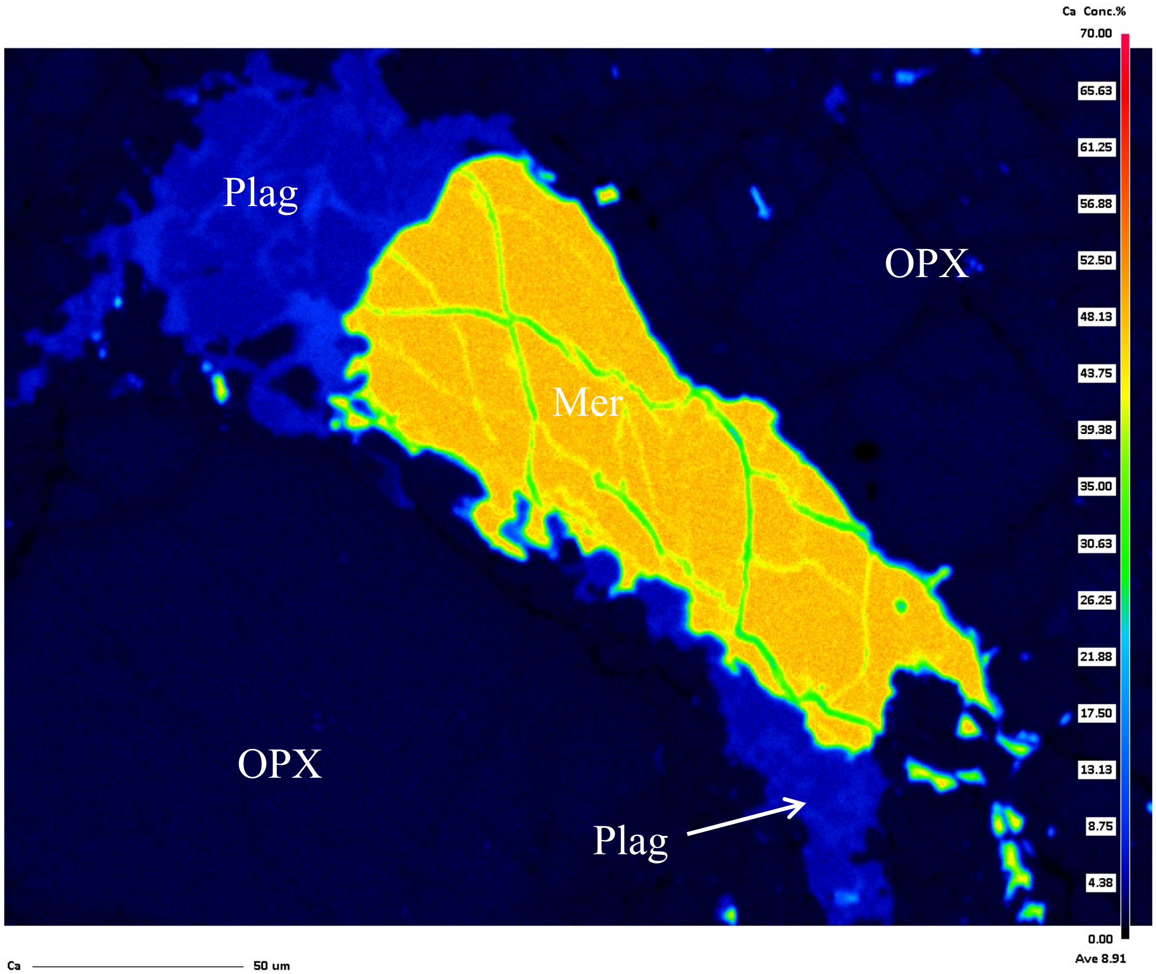

Supplementary Figure 47. Quantitative WDS (Wavelength Dispersive Spectrometry) elemental map distribution of calcium (Ca) in apatite-merrillite intergrown grain #8 in ALH 84001. WDS element maps are given in weight percent (wt%). WDS element maps correspond to BSE image from Figure 57. Plag = plagioclase; Mer = merrillite; Ap = apatite; OPX = orthopyroxene. Scale bar is 50 µm in length.

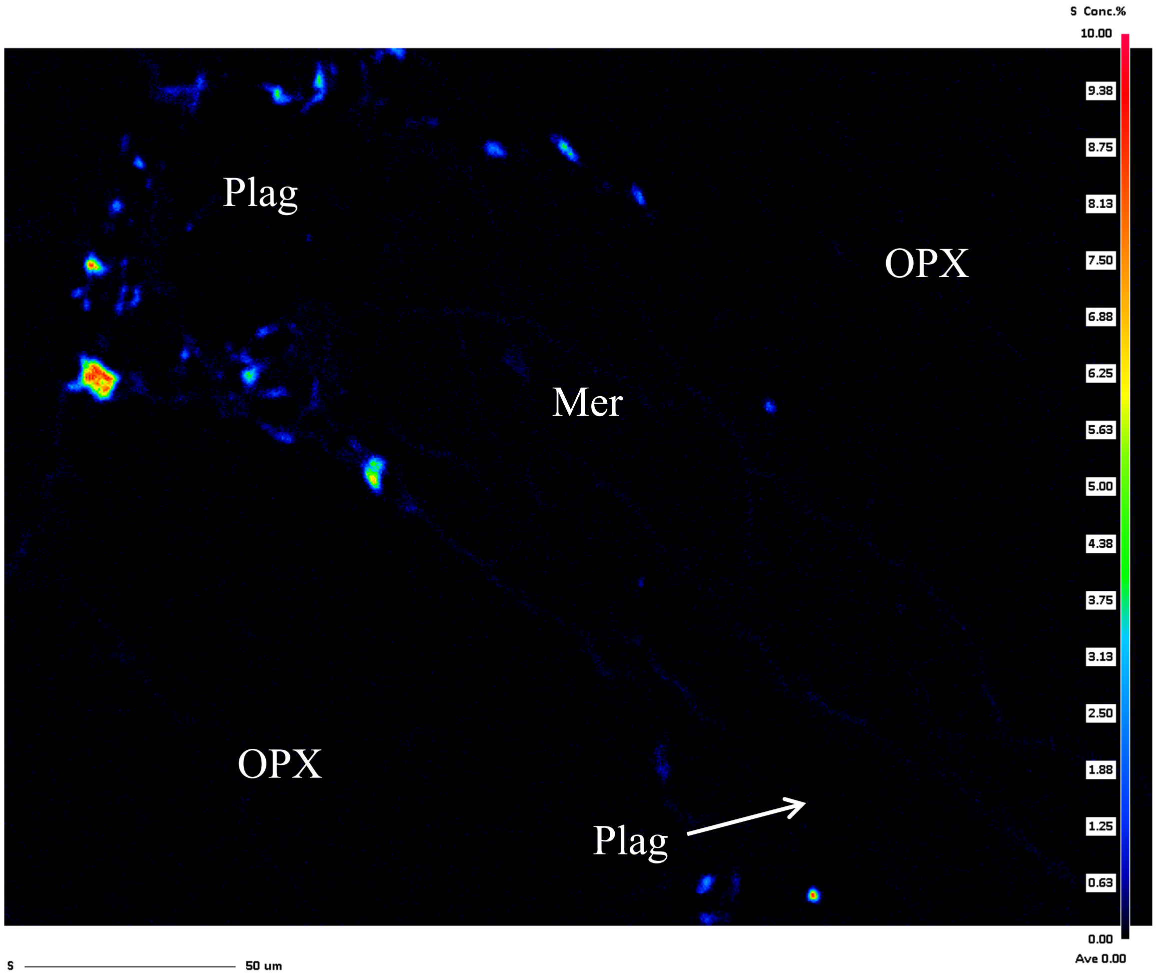

Supplementary Figure 48. Quantitative WDS (Wavelength Dispersive Spectrometry) elemental map distribution of sulfur (S) in apatite-merrillite intergrown grain #8 in ALH 84001. WDS element maps are given in weight percent (wt%). WDS element maps correspond to BSE image from Figure 57. Plag = plagioclase; Mer = merrillite; Ap = apatite; OPX = orthopyroxene. Scale bar is 50 µm in length.

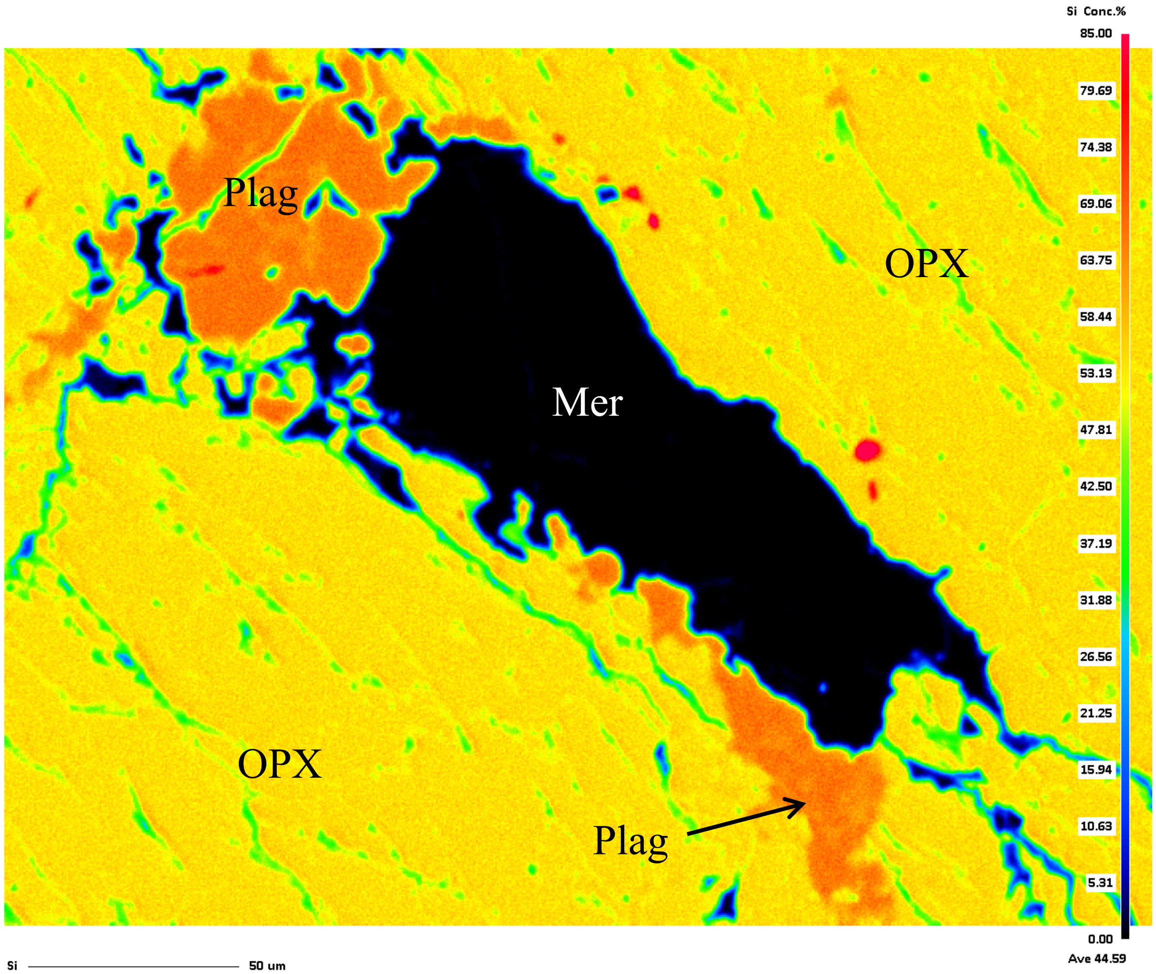

Supplementary Figure 49. Quantitative WDS (Wavelength Dispersive Spectrometry) elemental map distribution of silicon (Si) in apatite-merrillite intergrown grain #8 in ALH 84001. WDS element maps are given in weight percent (wt%). WDS element maps correspond to BSE image from Figure 57. Plag = plagioclase; Mer = merrillite; Ap = apatite; OPX = orthopyroxene. Scale bar is 50 µm in length.

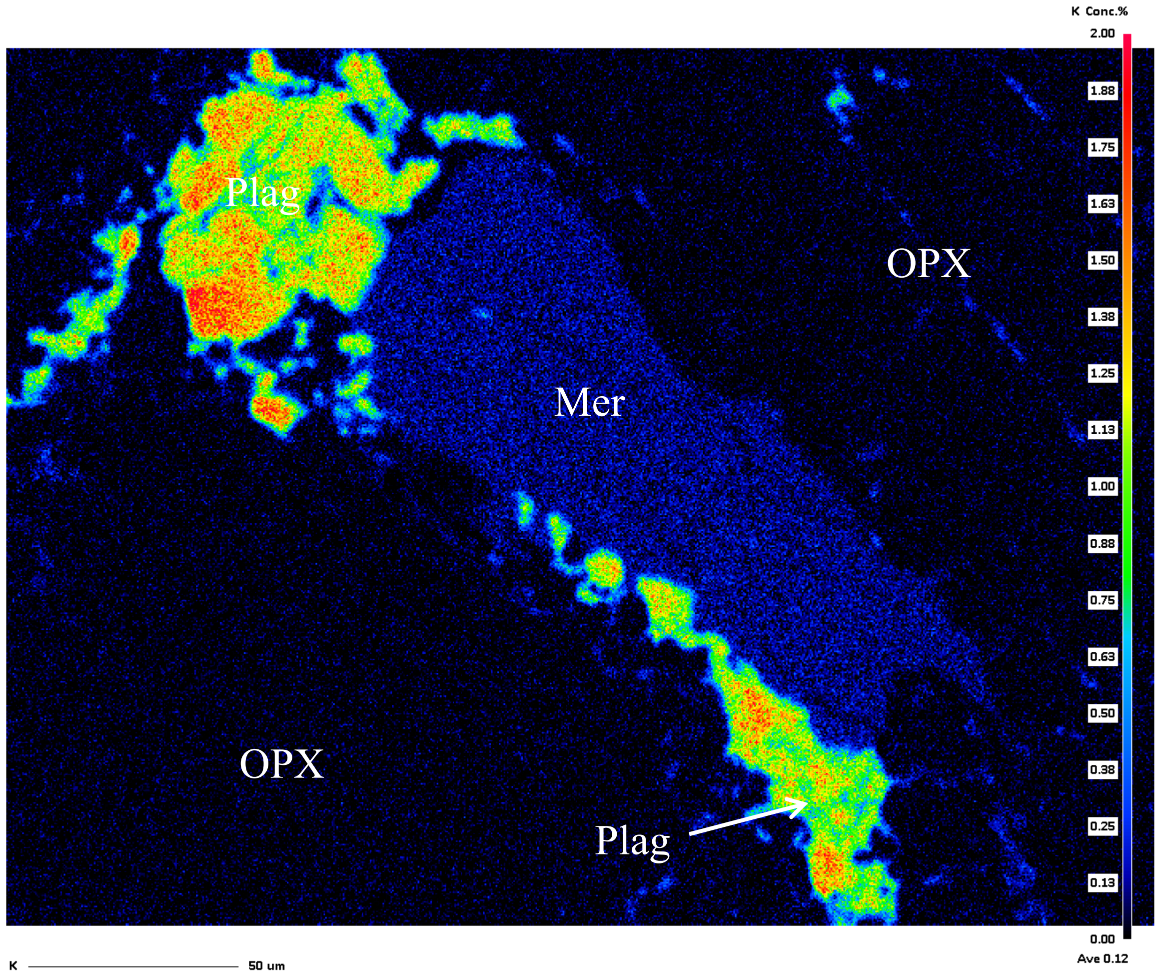

Supplementary Figure 50. Quantitative WDS (Wavelength Dispersive Spectrometry) elemental map distribution of potassium (K) in apatite-merrillite intergrown grain #8 in ALH 84001. WDS element maps are given in weight percent (wt%). WDS element maps correspond to BSE image from Figure 57. Plag = plagioclase; Mer = merrillite; Ap = apatite; OPX = orthopyroxene. Scale bar is 50 µm in length.

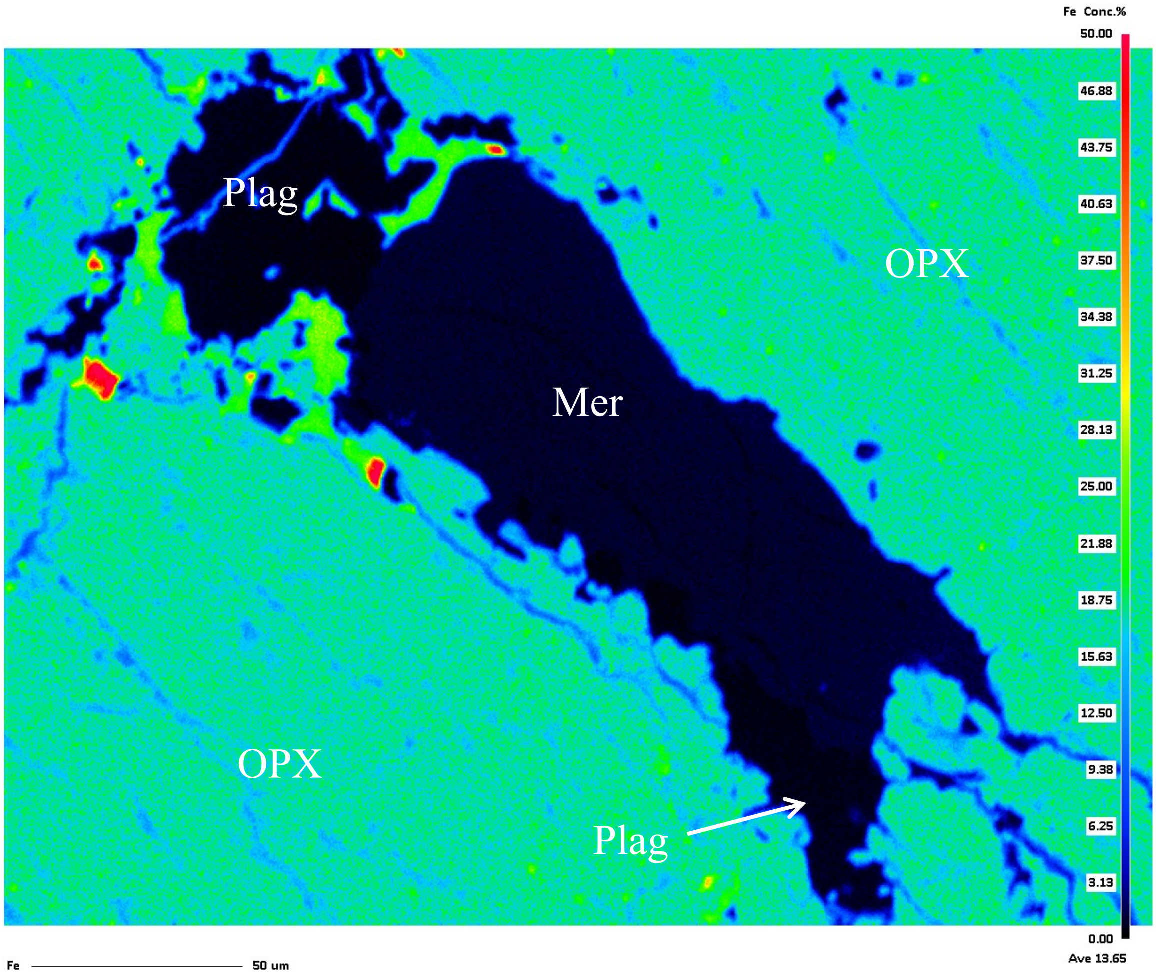

Supplementary Figure 51. Quantitative WDS (Wavelength Dispersive Spectrometry) elemental map distribution of iron (Fe) in apatite-merrillite intergrown grain #8 in ALH 84001. WDS element maps are given in weight percent (wt%). WDS element maps correspond to BSE image from Figure 57. Plag = plagioclase; Mer = merrillite; Ap = apatite; OPX = orthopyroxene. Scale bar is 50 µm in length.

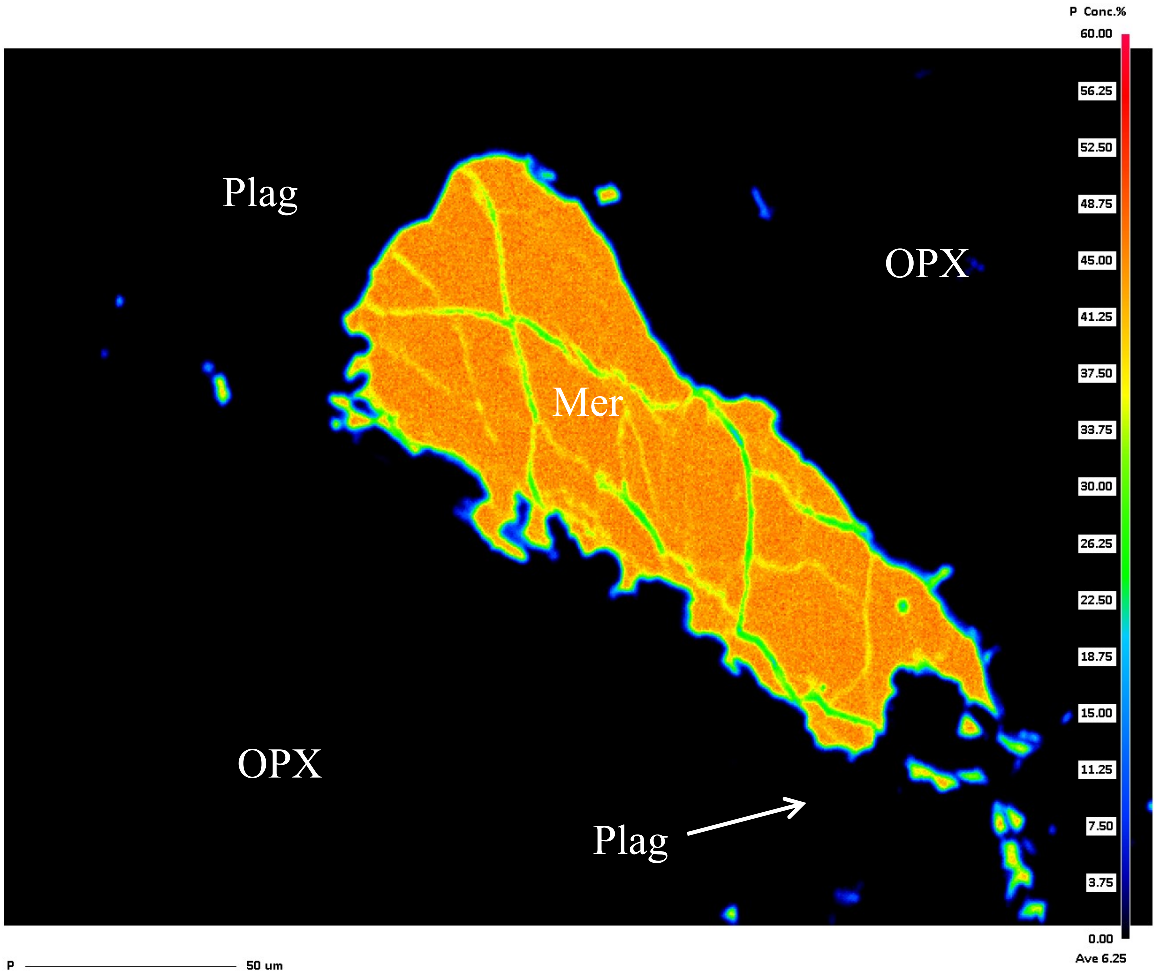

Supplementary Figure 52. Quantitative WDS (Wavelength Dispersive Spectrometry) elemental map distribution of phosphorous (P) in apatite-merrillite intergrown grain #8 in ALH 84001. WDS element maps are given in weight percent (wt%). WDS element maps correspond to BSE image from Figure 57. Plag = plagioclase; Mer = merrillite; Ap = apatite; OPX = orthopyroxene. Scale bar is 50 µm in length.

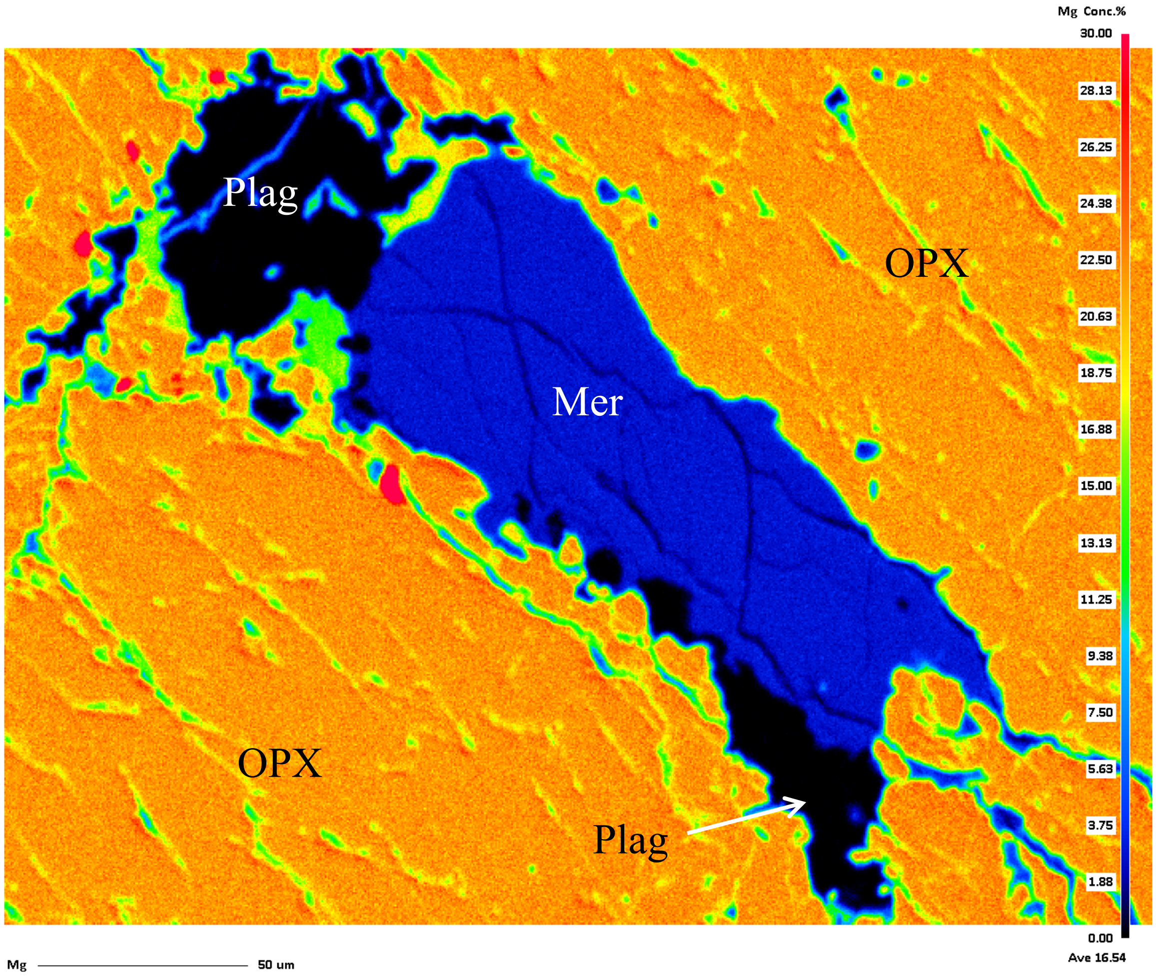

Supplementary Figure 53. Quantitative WDS (Wavelength Dispersive Spectrometry) elemental map distribution of magnesium (Mg) in apatite-merrillite intergrown grain #8 in ALH 84001. WDS element maps are given in weight percent (wt%). WDS element maps correspond to BSE image from Figure 57. Plag = plagioclase; Mer = merrillite; Ap = apatite; OPX = orthopyroxene. Scale bar is 50 μm in length.

NWA 998

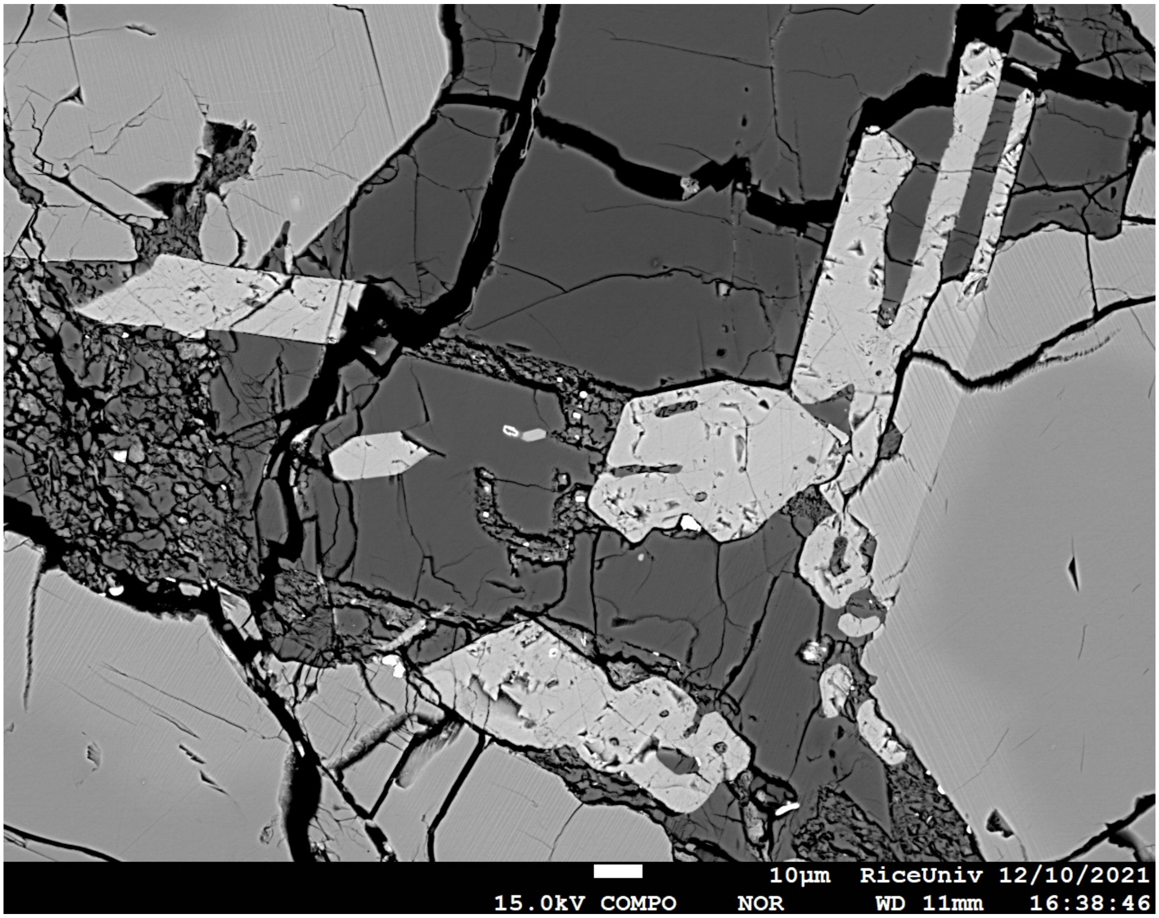

Supplementary Figure 54. BSE (BackScattered Electron) image of apatite-bearing assemblage #1 in NWA-998.

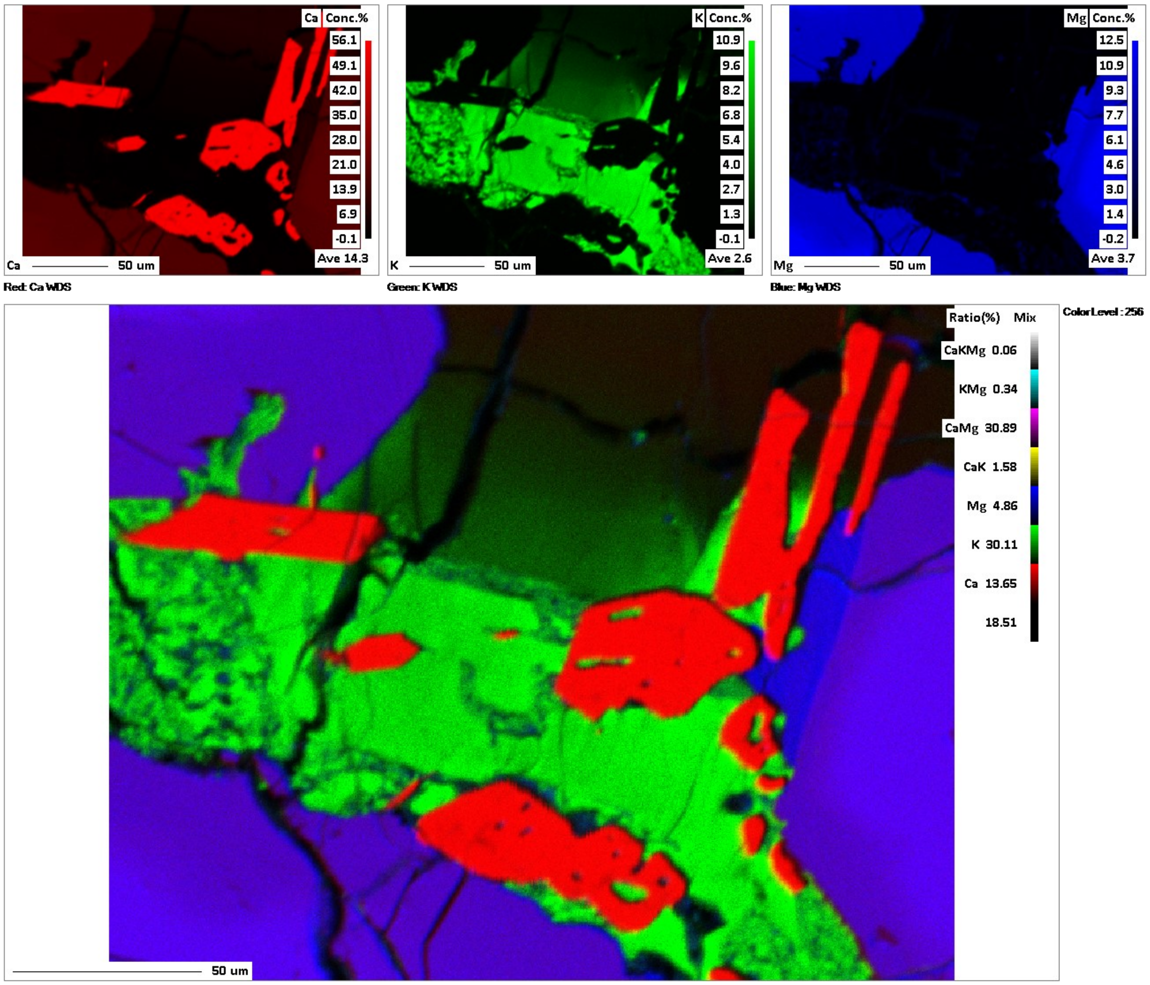

Supplementary Figure 55. False color composite map of Ca-K-Mg in apatite-assemblage #1 in NWA 998.

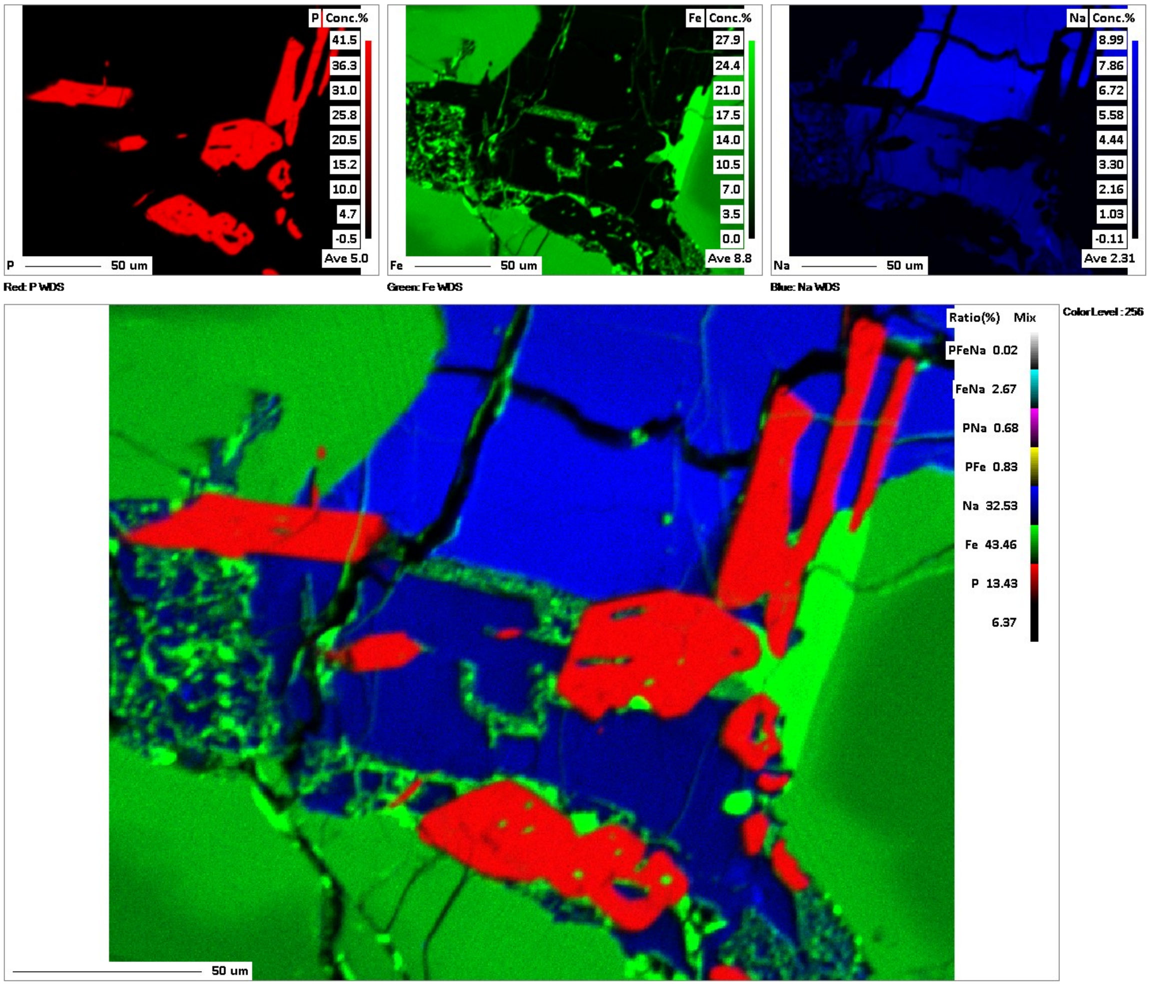

Supplementary Figure 56. False color composite map of P-Fe-Na in apatite-assemblage #1 in NWA 998.

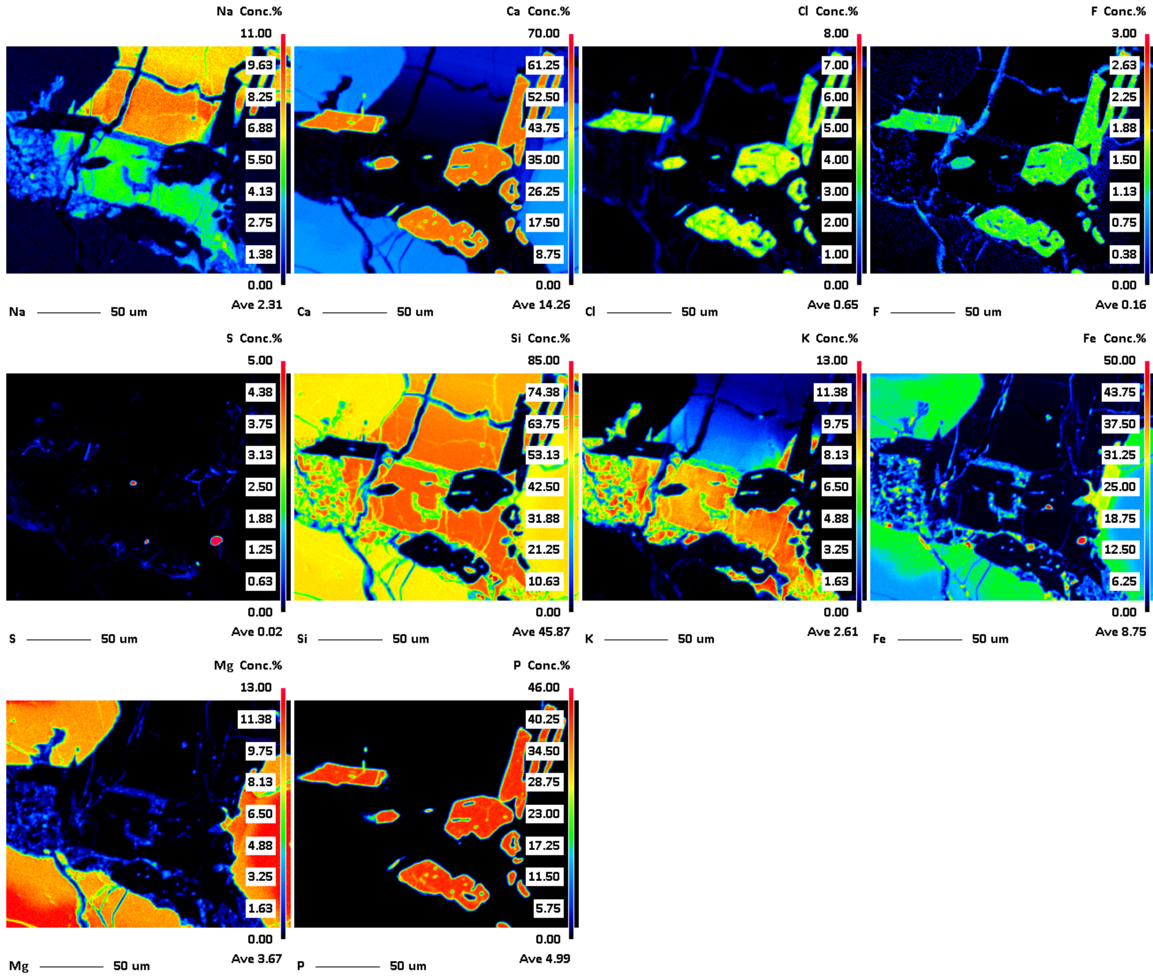

Supplementary Figure 57. Quantitative WDS (Wavelength Dispersive Spectrometry) element map distribution of apatite-assemblage #1 in NWA 998.

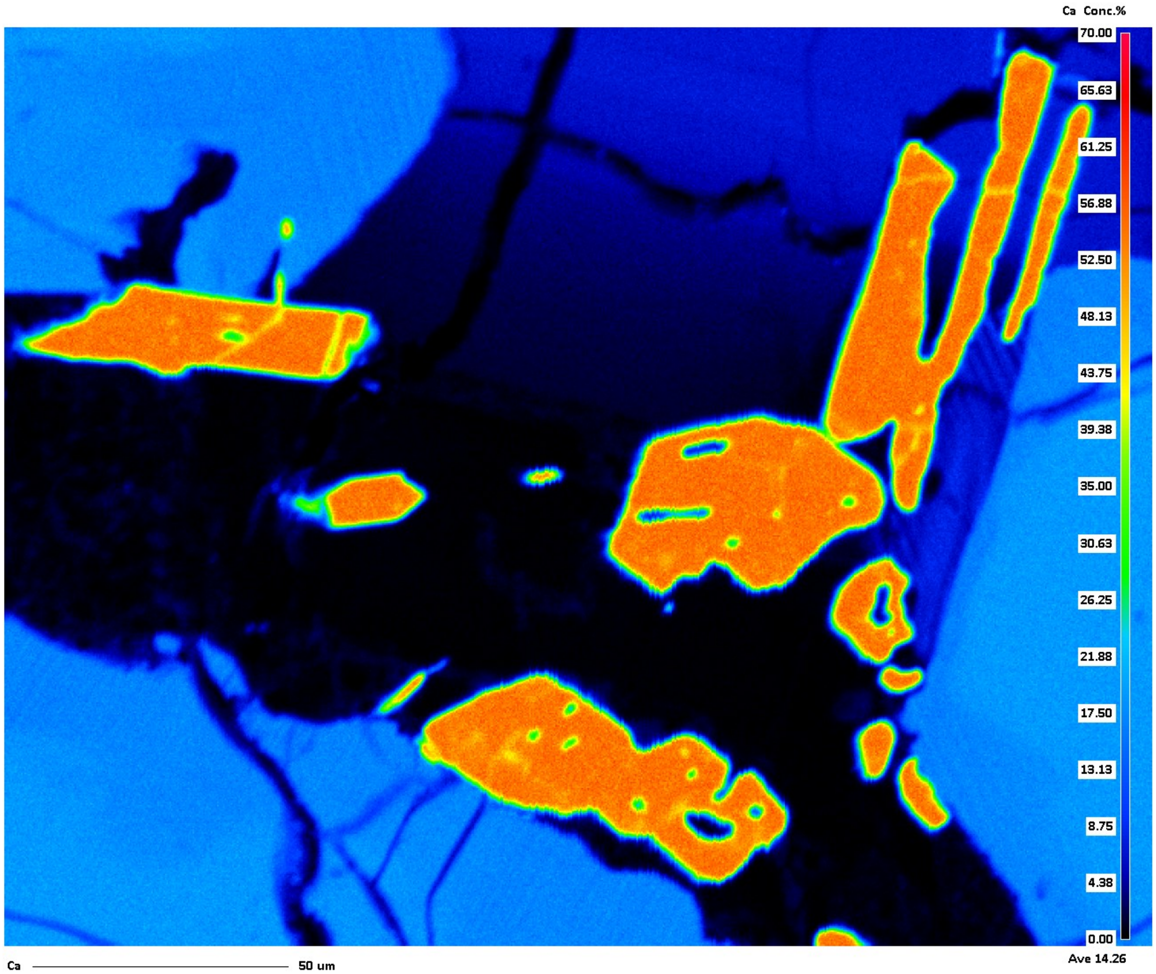

Supplementary Figure 58. Quantitative WDS (Wavelength Dispersive Spectrometry) elemental map distribution of calcium (Ca) in apatite-assemblage #1 in NWA 998.

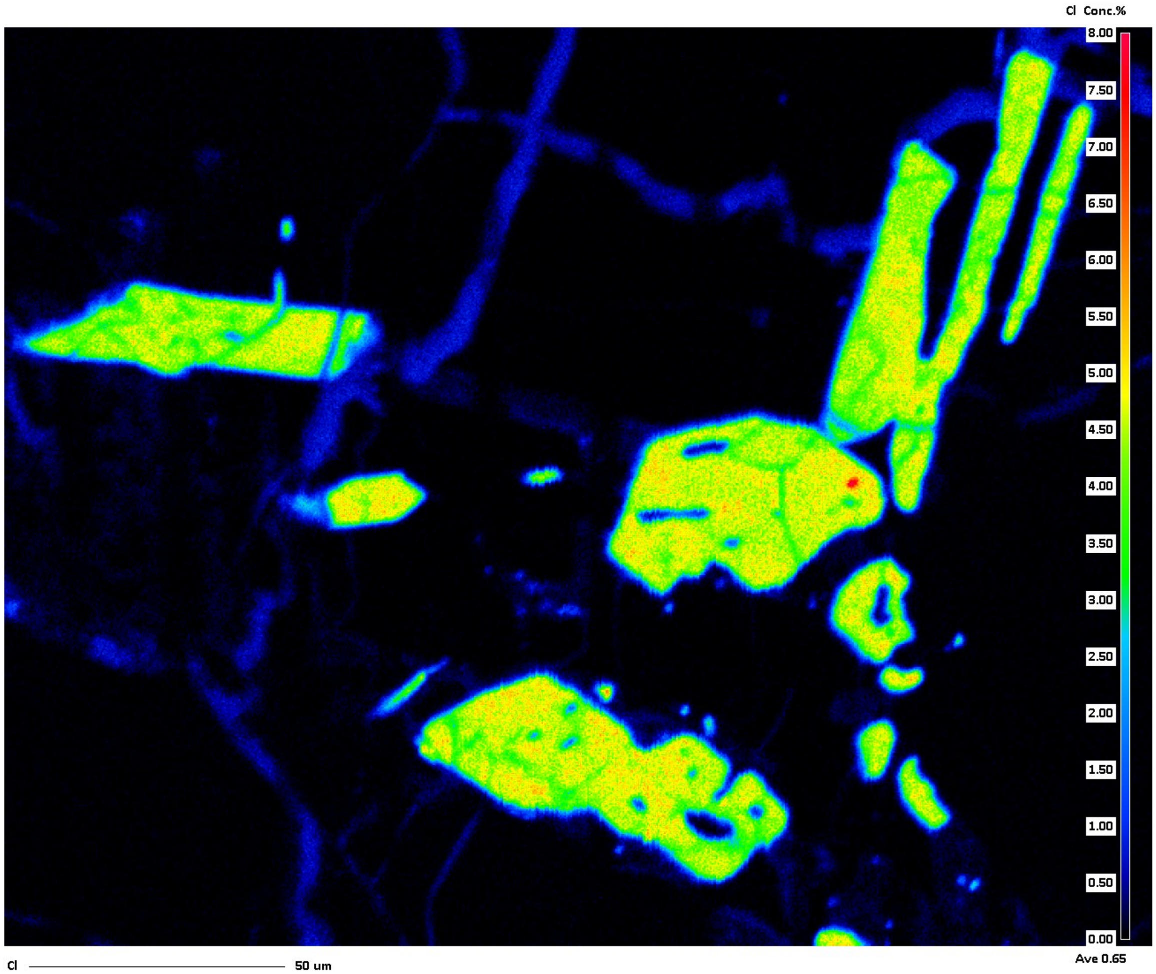

Supplementary Figure 59. Quantitative WDS (Wavelength Dispersive Spectrometry) elemental map distribution of chlorine (Cl) in apatite-assemblage #1 in NWA 998.

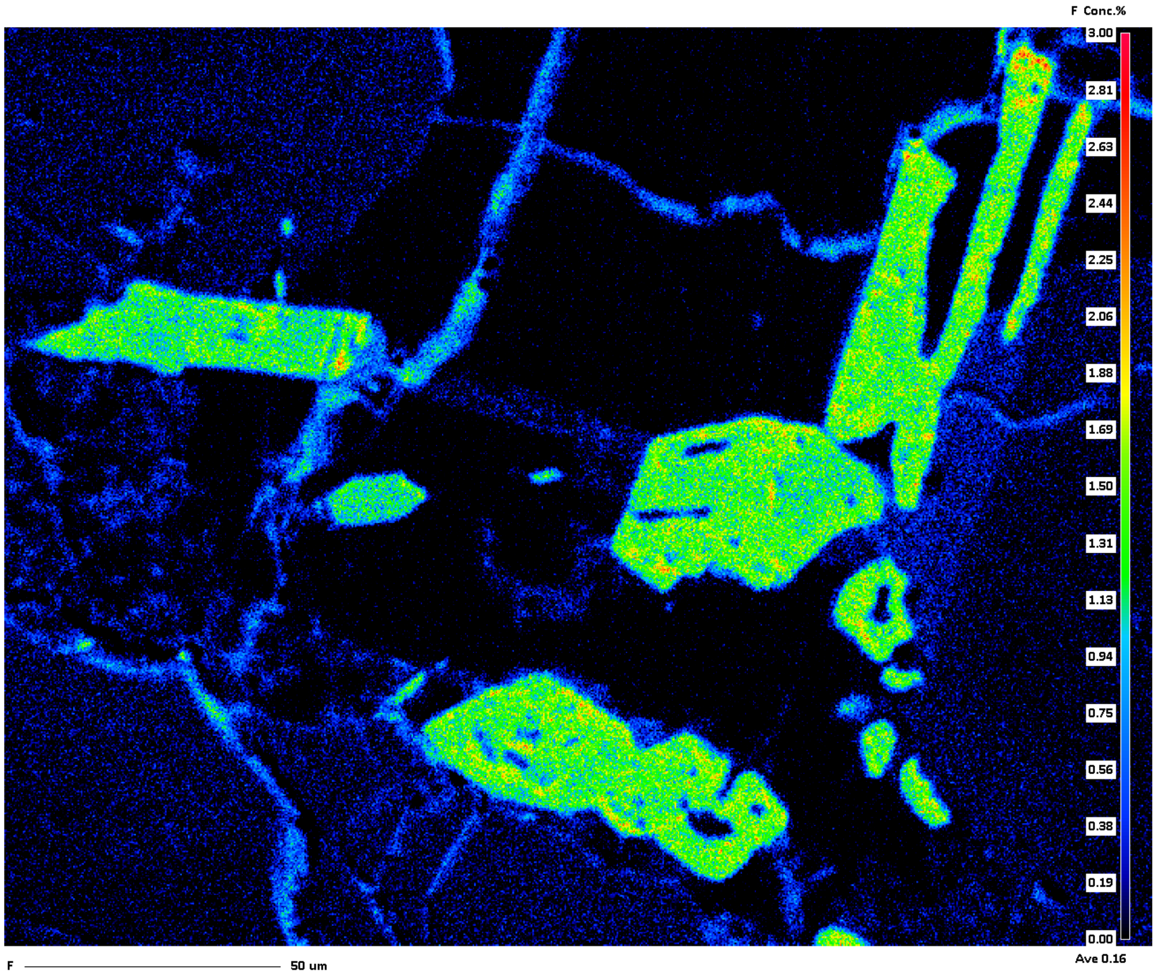

Supplementary Figure 60. Quantitative WDS (Wavelength Dispersive Spectrometry) elemental map distribution of fluorine (F) in apatite-assemblage #1 in NWA 998.

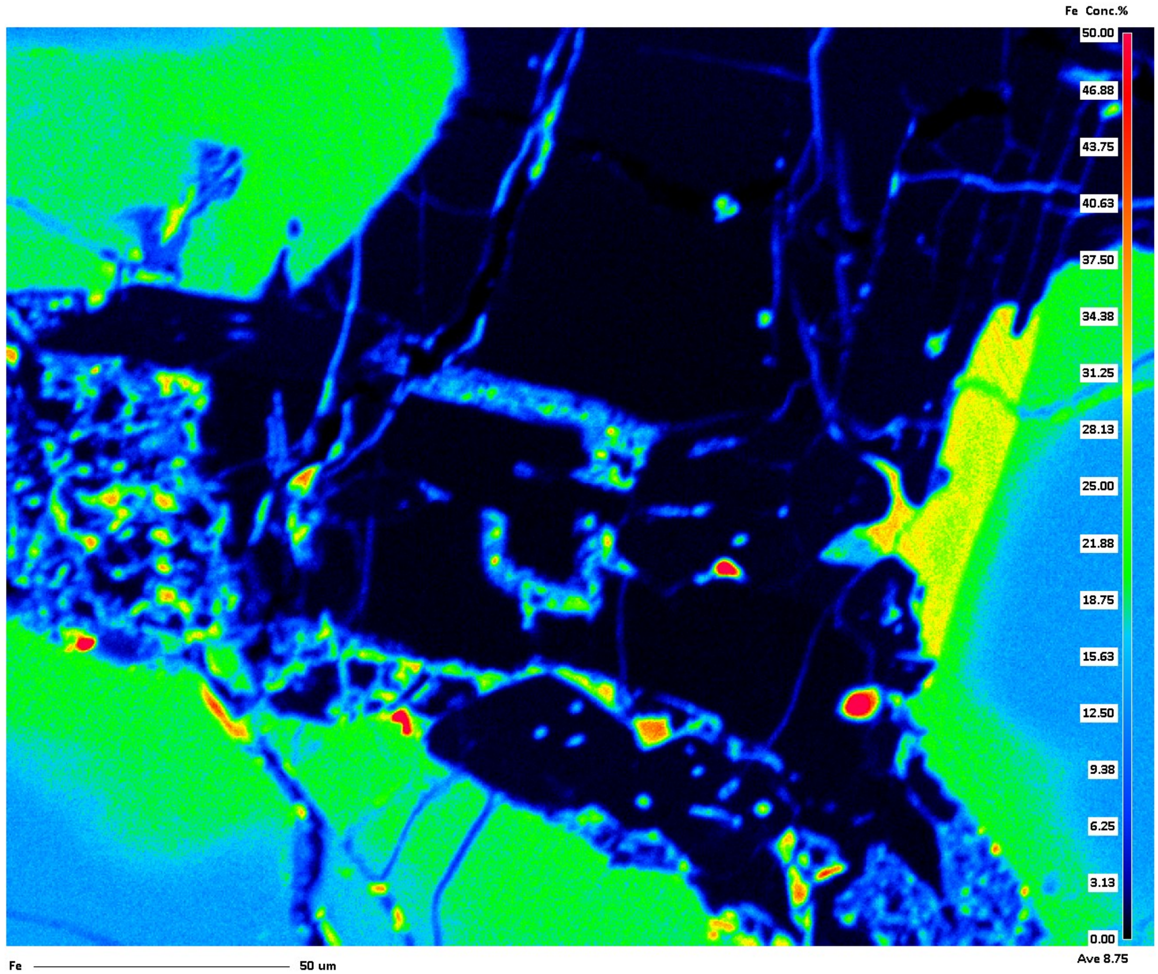

Supplementary Figure 61. Quantitative WDS (Wavelength Dispersive Spectrometry) elemental map distribution of iron (Fe) in apatite-assemblage #1 in NWA 998.

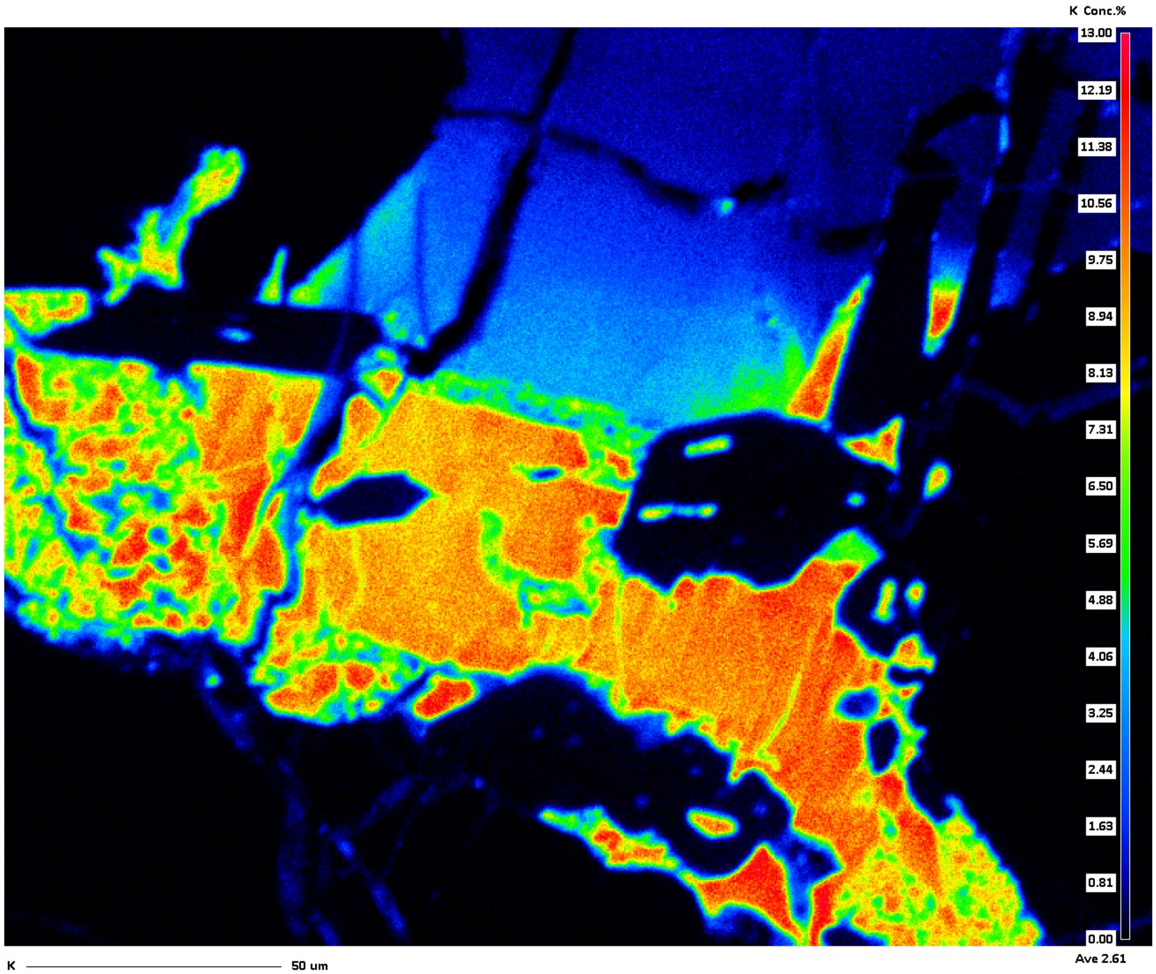

Supplementary Figure 62. Quantitative WDS (Wavelength Dispersive Spectrometry) elemental map distribution of potassium (K) in apatite-assemblage #1 in NWA 998.

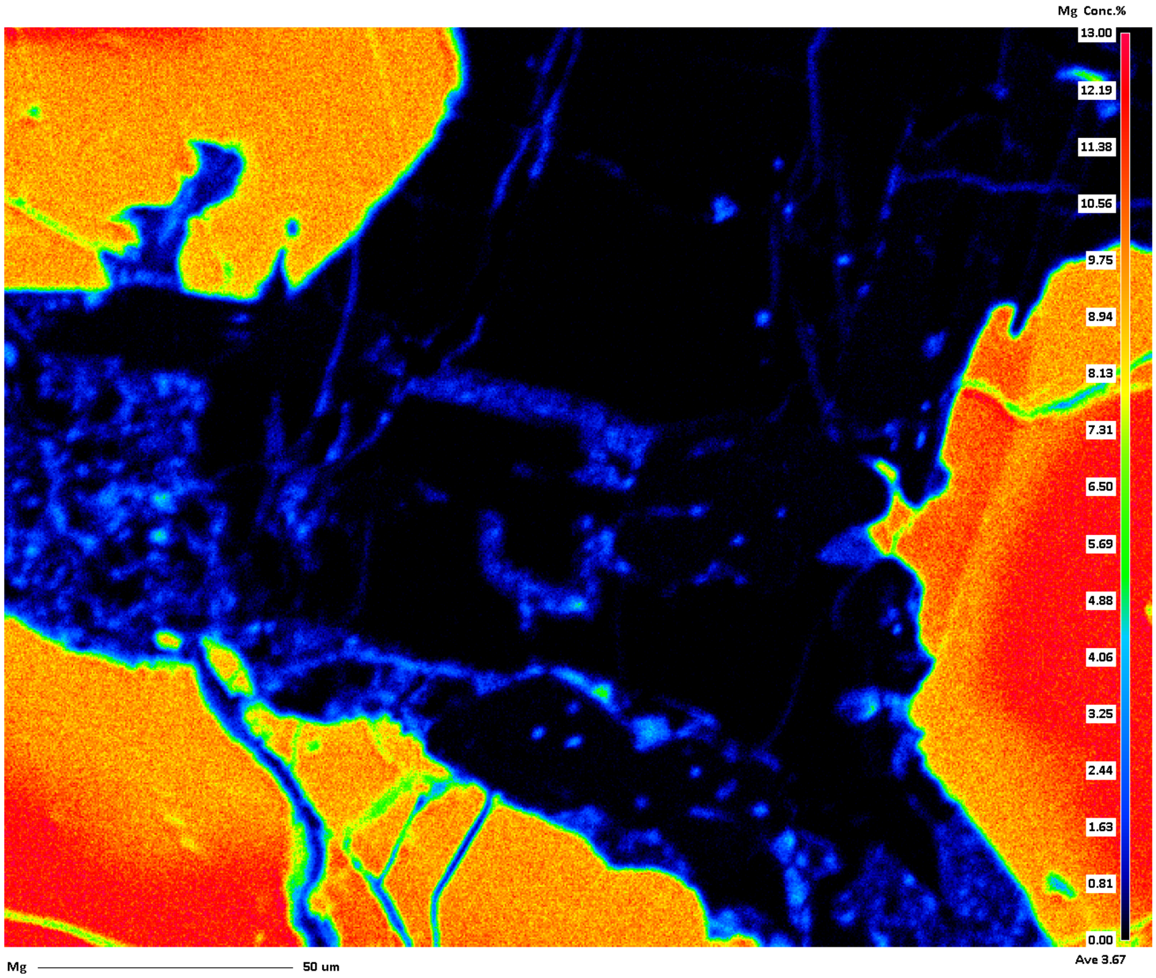

Supplementary Figure 63. Quantitative WDS (Wavelength Dispersive Spectrometry) elemental map distribution of magnesium (Mg) in apatite-assemblage #1 in NWA 998.

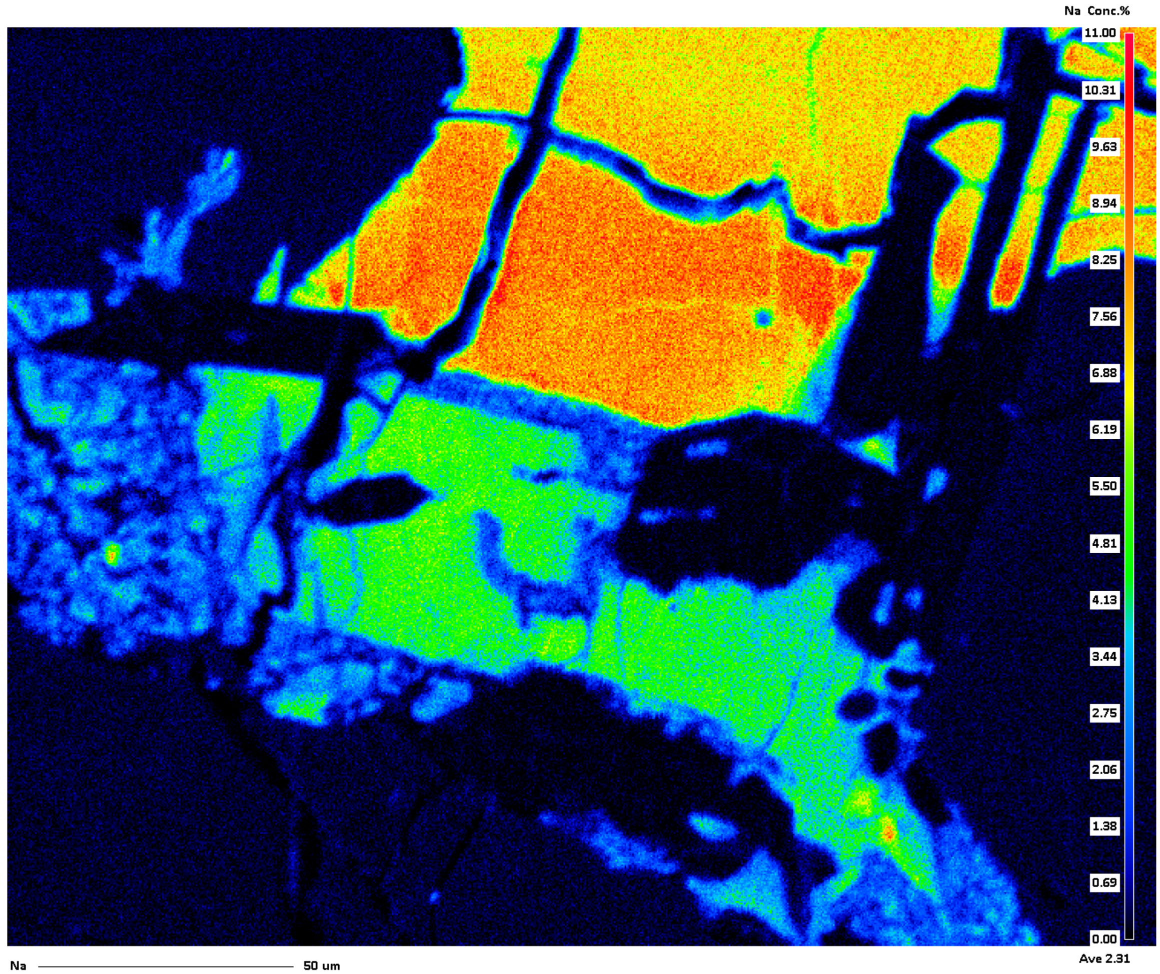

Supplementary Figure 64. Quantitative WDS (Wavelength Dispersive Spectrometry) elemental map distribution of sodium (Na) in apatite-assemblage #1 in NWA 998.

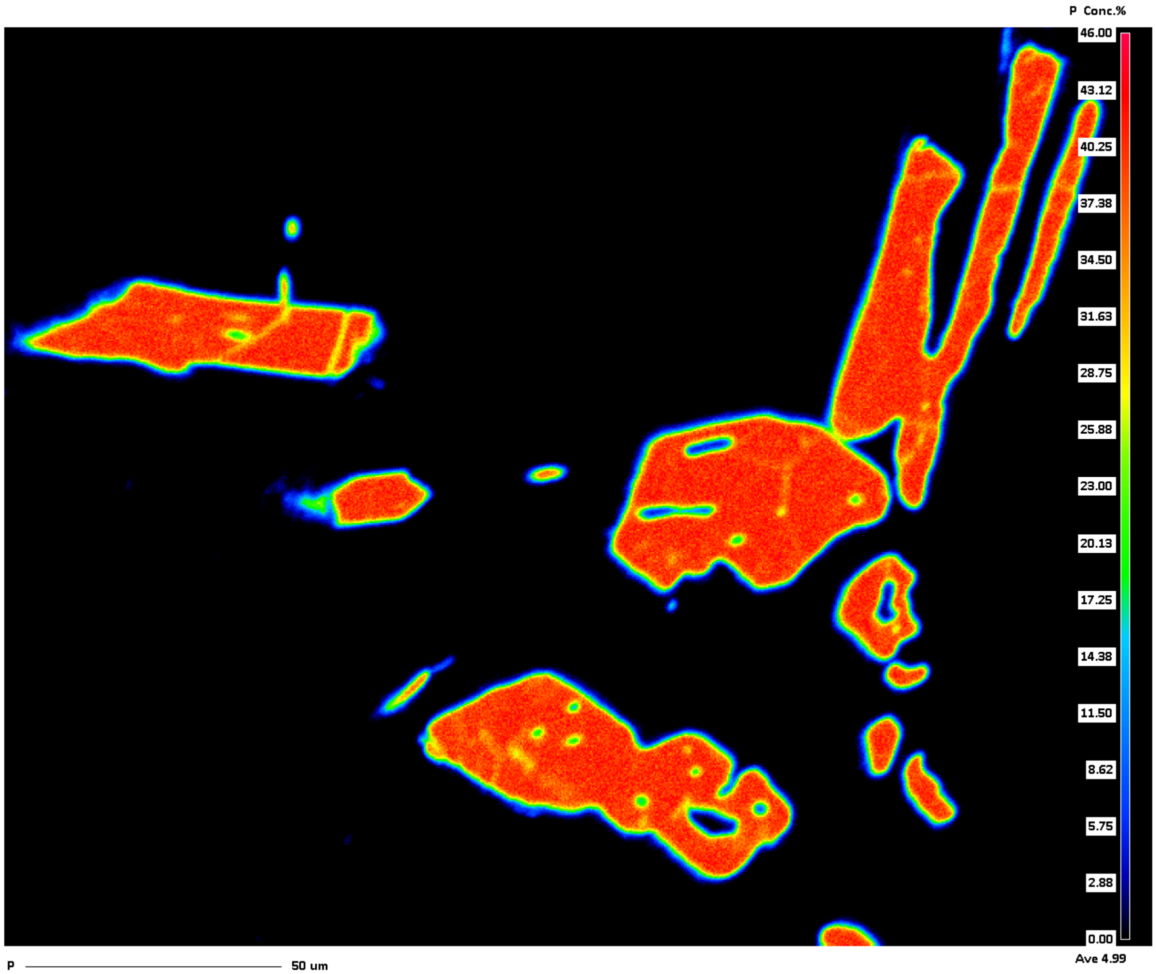

Supplementary Figure 65. Quantitative WDS (Wavelength Dispersive Spectrometry) elemental map distribution of phosphorous (P) in apatite-assemblage #1 in NWA 998.

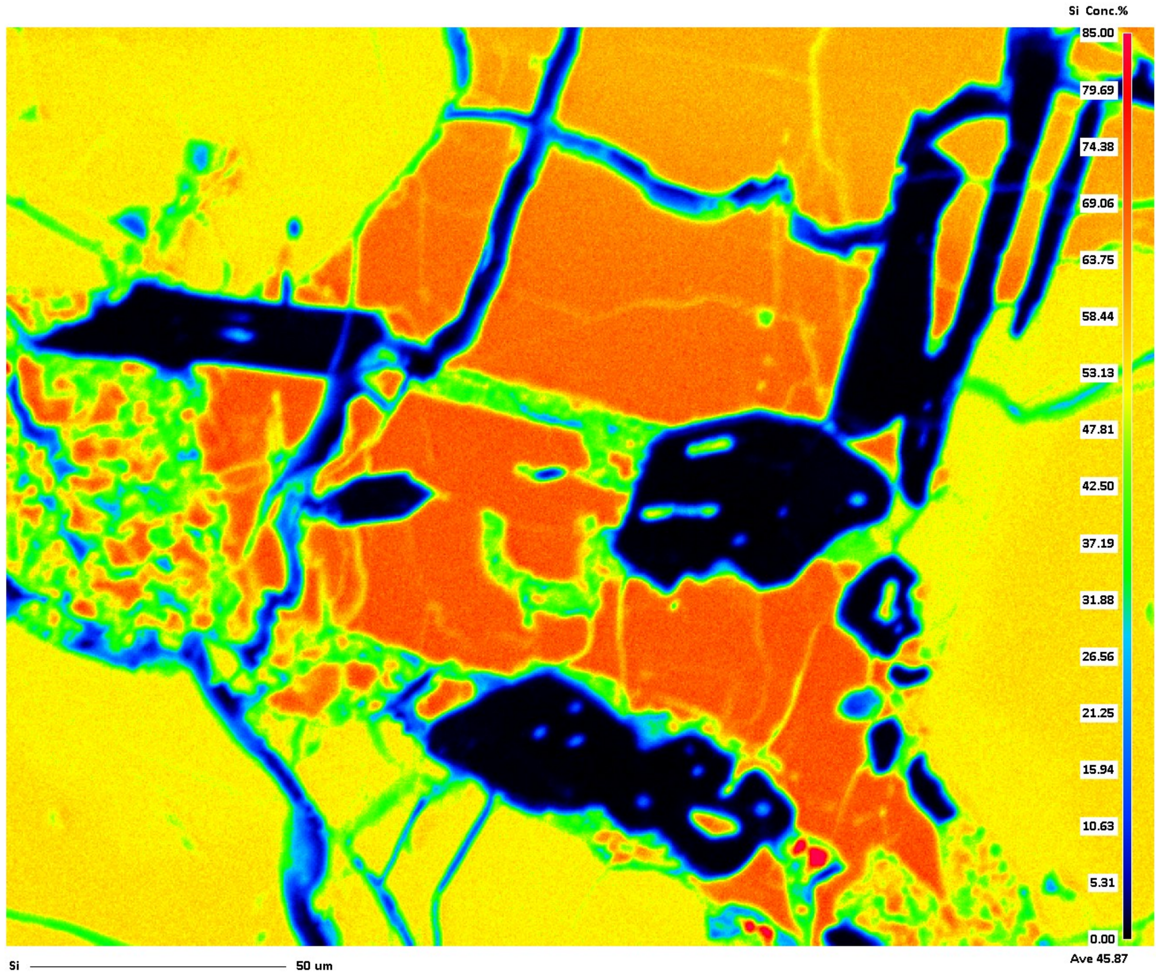

Supplementary Figure 66. Quantitative WDS (Wavelength Dispersive Spectrometry) elemental map distribution of silicon (Si) in apatite-assemblage #1 in NWA 998.

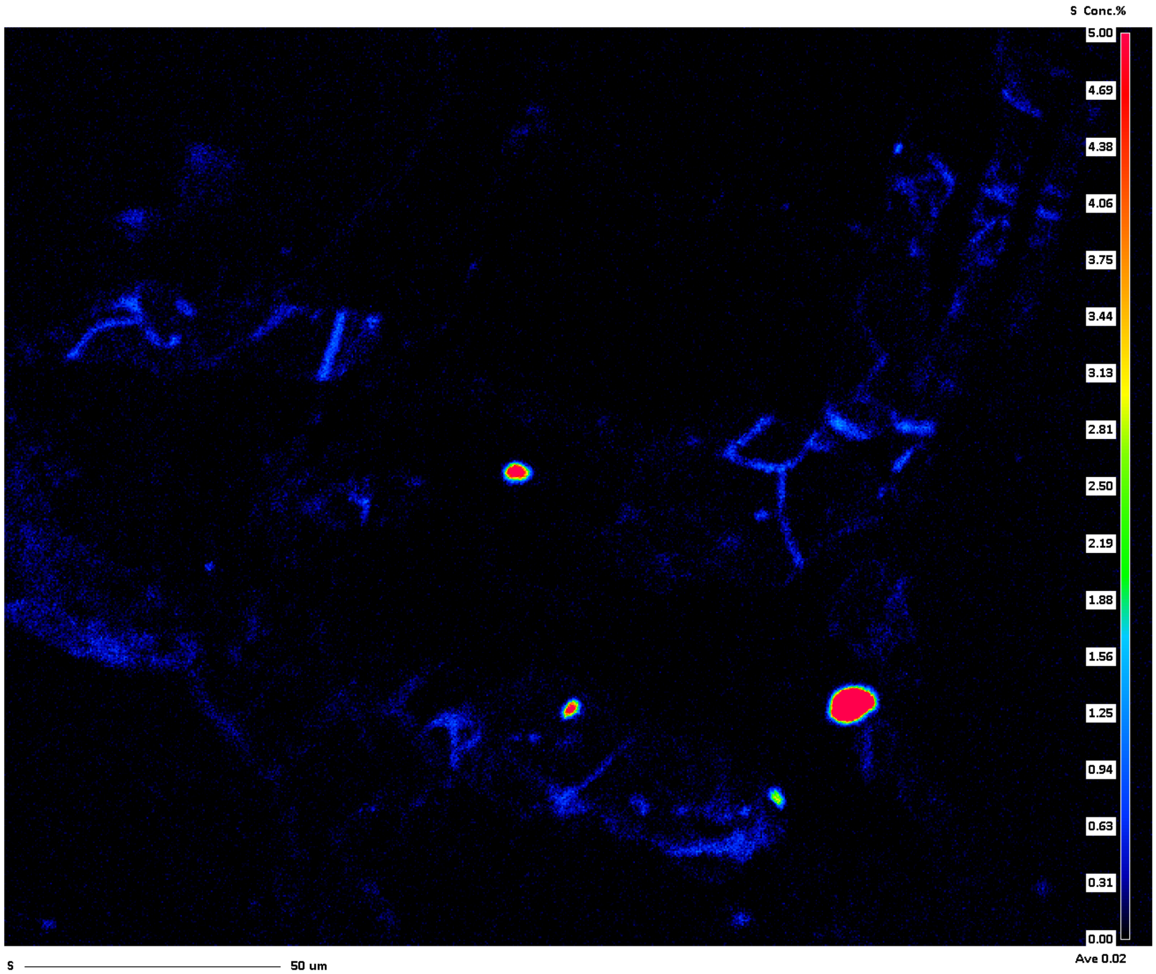

Supplementary Figure 67. Quantitative WDS (Wavelength Dispersive Spectrometry) elemental map distribution of sulfur (S) in apatite-assemblage #1 in NWA 998.

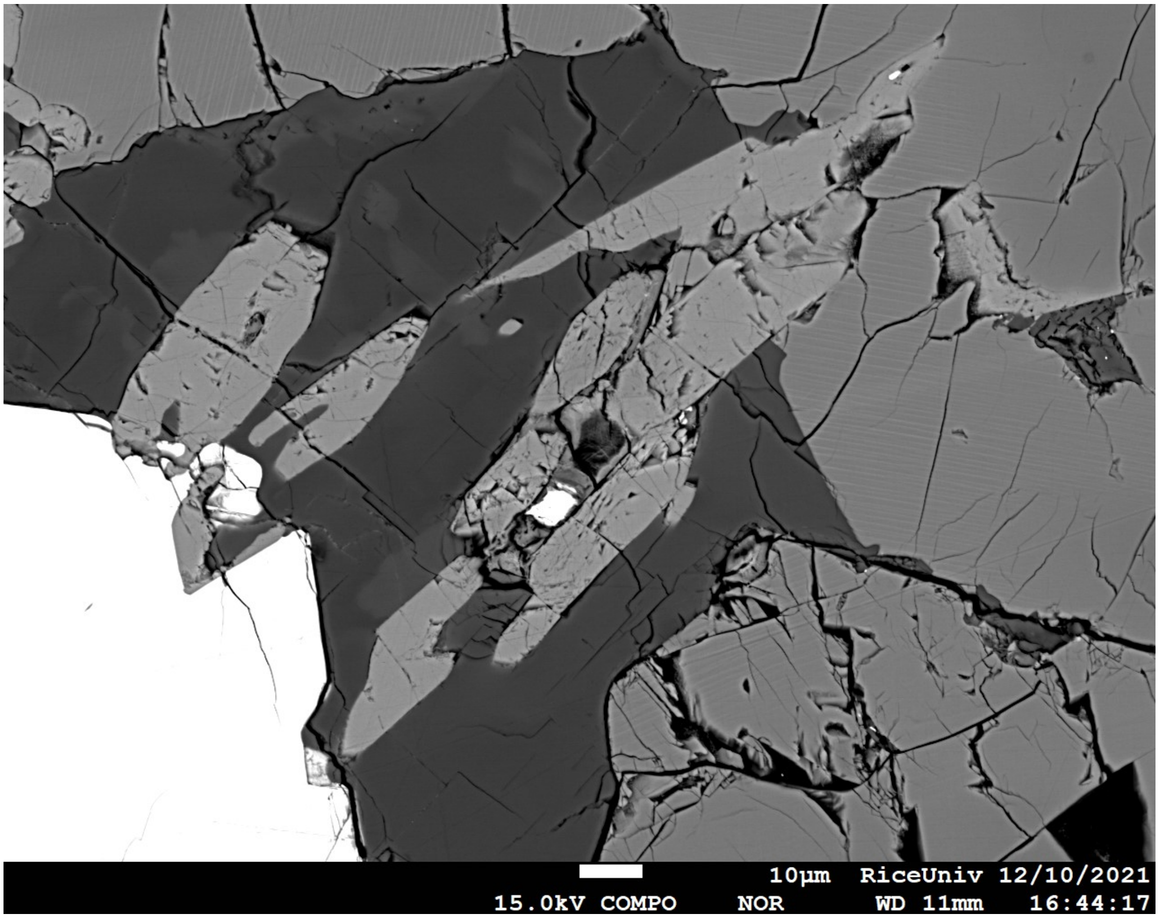

Supplementary Figure 68. BSE (BackScattered Electron) image of apatite-bearing assemblage #2 in NWA-998.

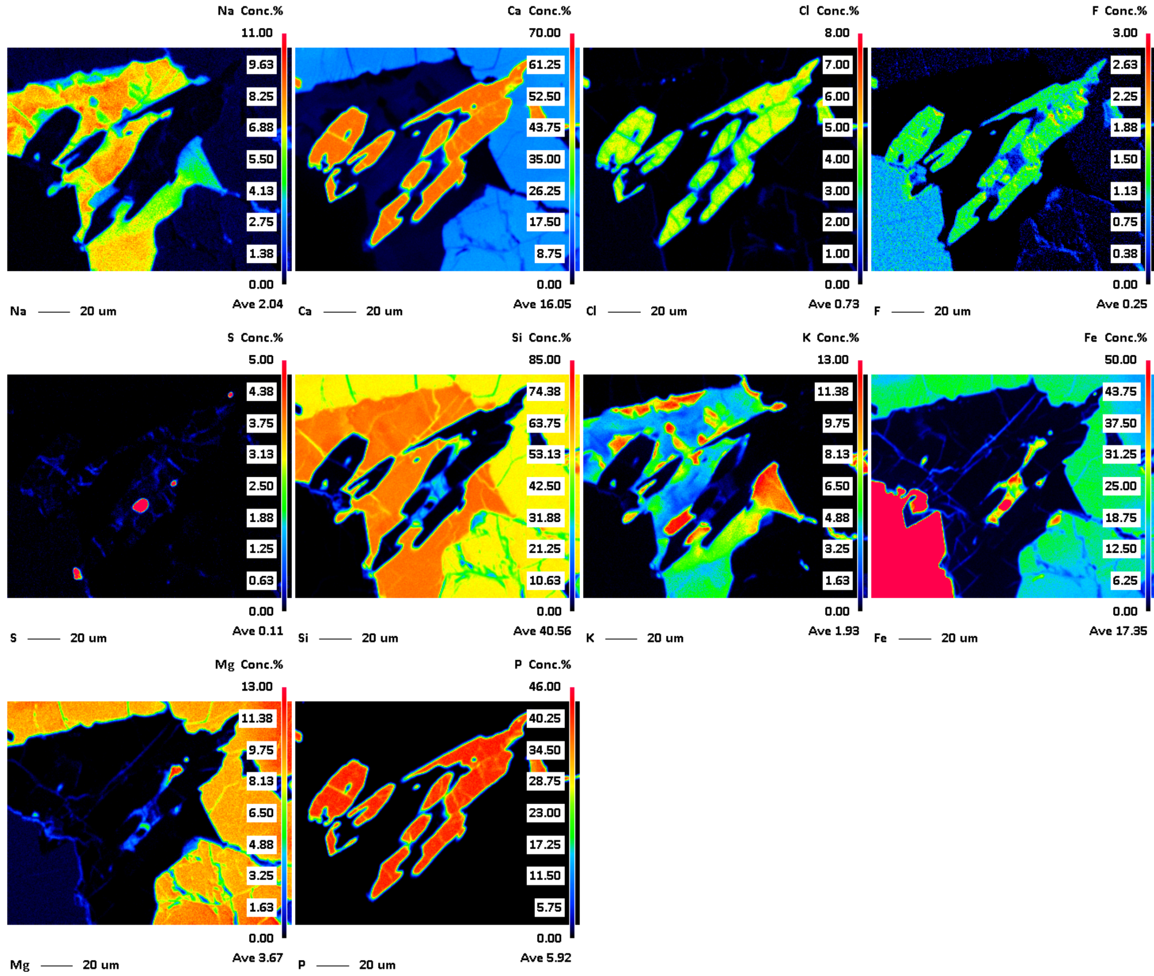

Supplementary Figure 69. Quantitative WDS (Wavelength Dispersive Spectrometry) element map distribution of apatite-assemblage #2 in NWA 998.

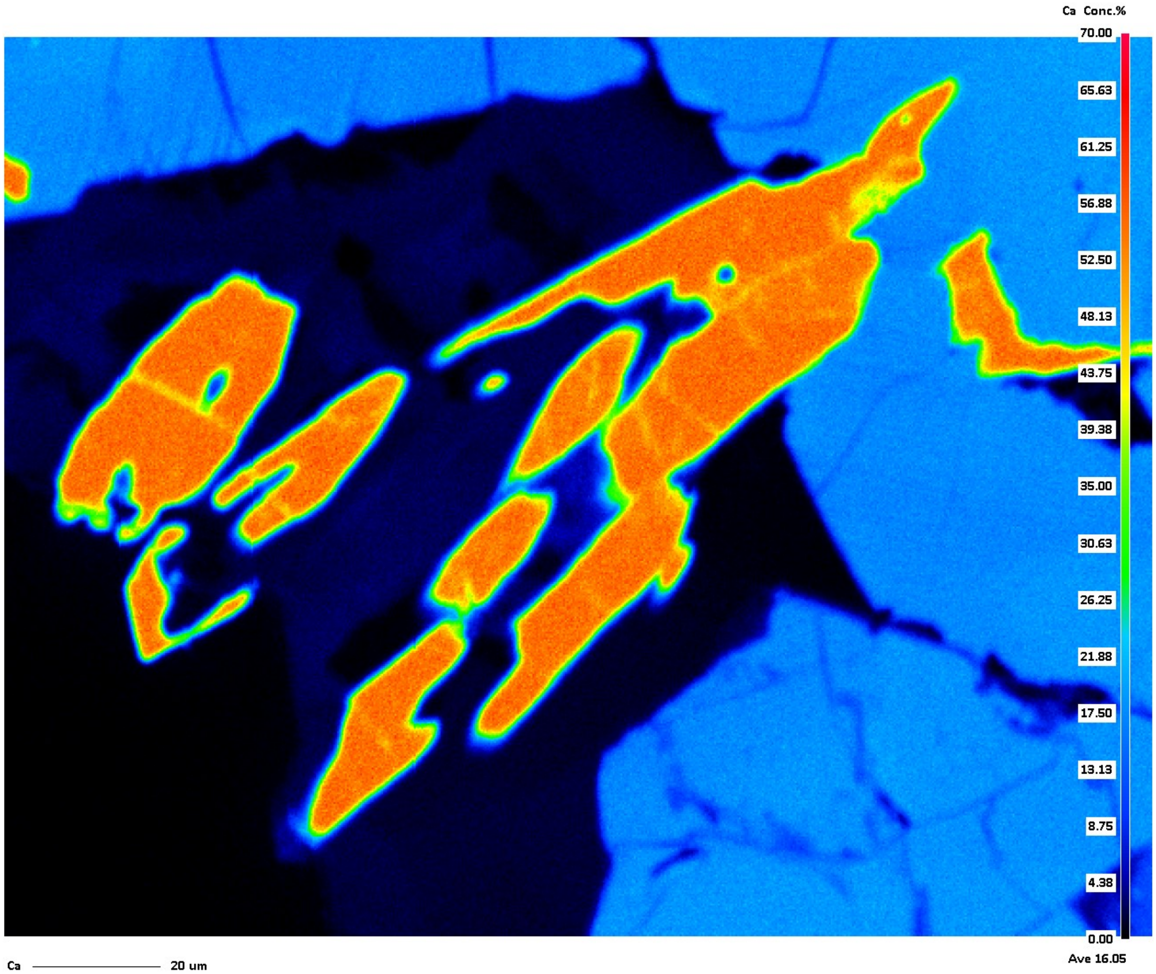

Supplementary Figure 70. Quantitative WDS (Wavelength Dispersive Spectrometry) elemental map distribution of calcium (Ca) in apatite-assemblage #2 in NWA 998.

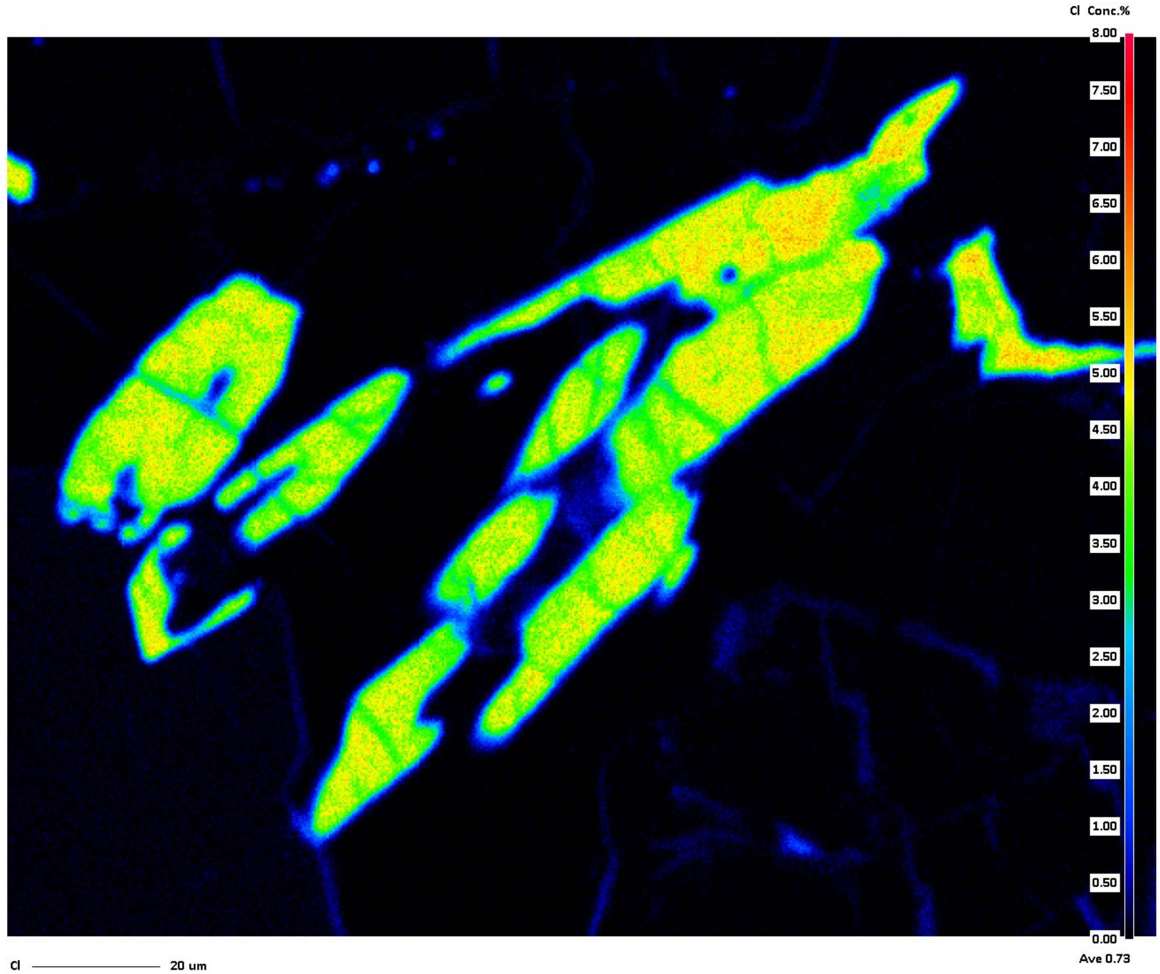

Supplementary Figure 71. Quantitative WDS (Wavelength Dispersive Spectrometry) elemental map distribution of chlorine (Cl) in apatite-assemblage #2 in NWA 998.

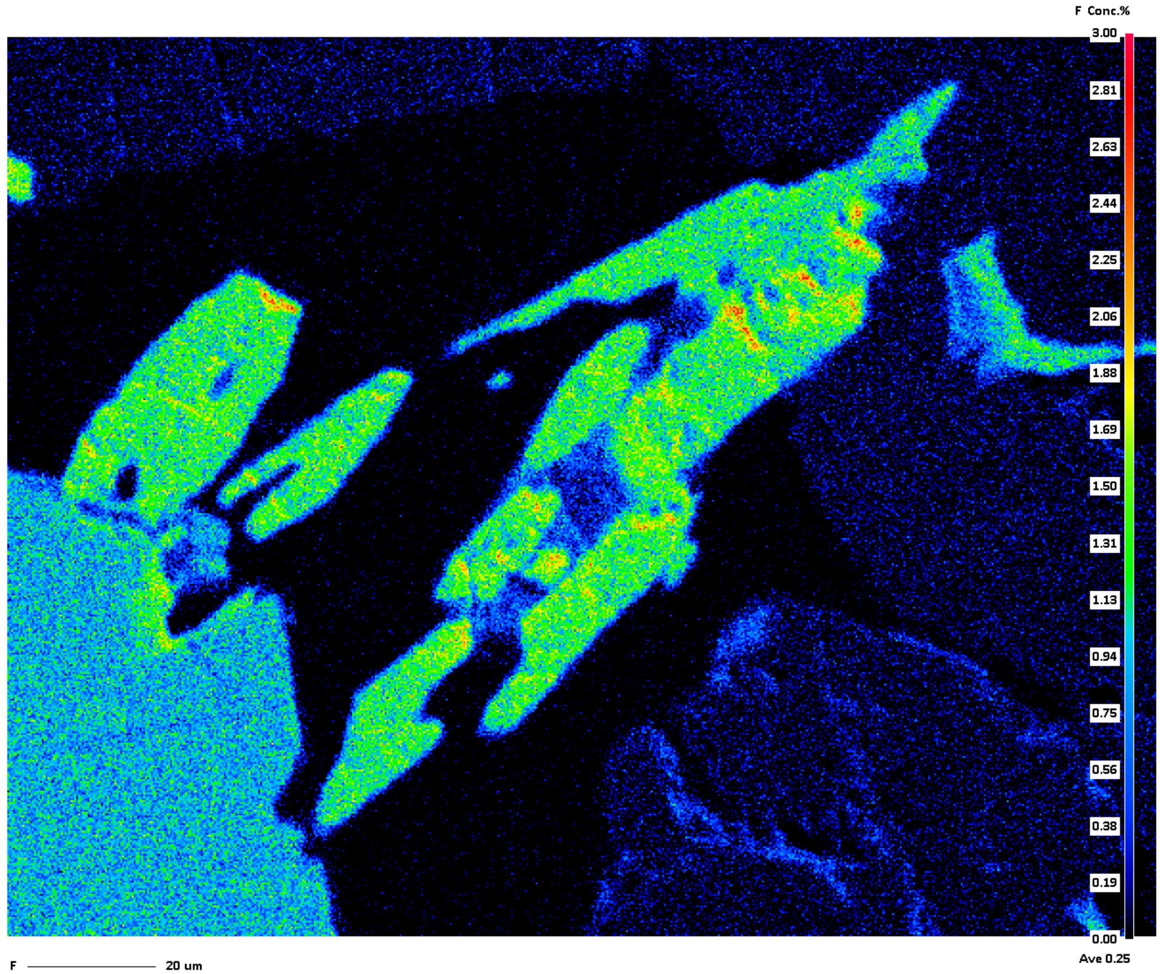

Supplementary Figure 72. Quantitative WDS (Wavelength Dispersive Spectrometry) elemental map distribution of fluorine (F) in apatite-assemblage #2 in NWA 998.

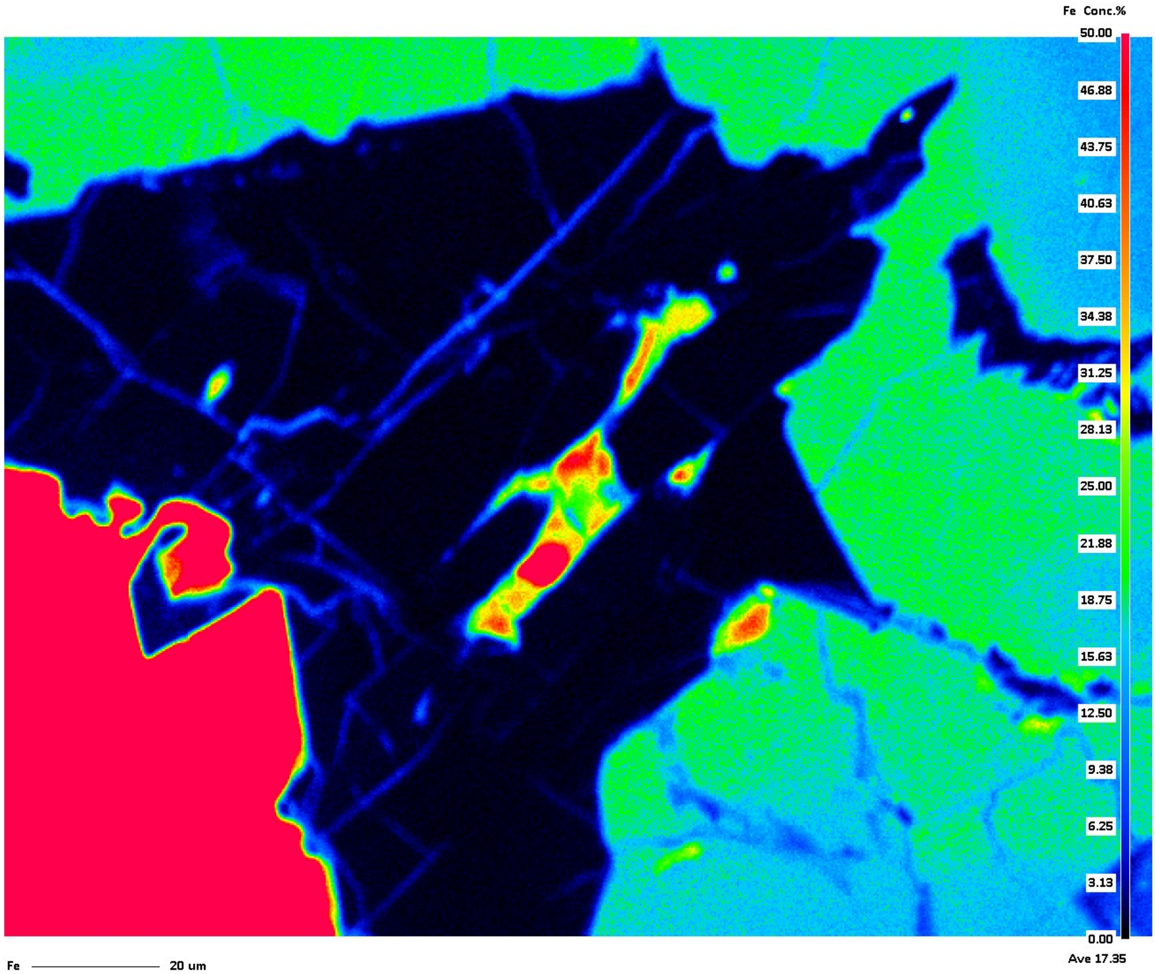

Supplementary Figure 73. Quantitative WDS (Wavelength Dispersive Spectrometry) elemental map distribution of iron (Fe) in apatite-assemblage #2 in NWA 998.

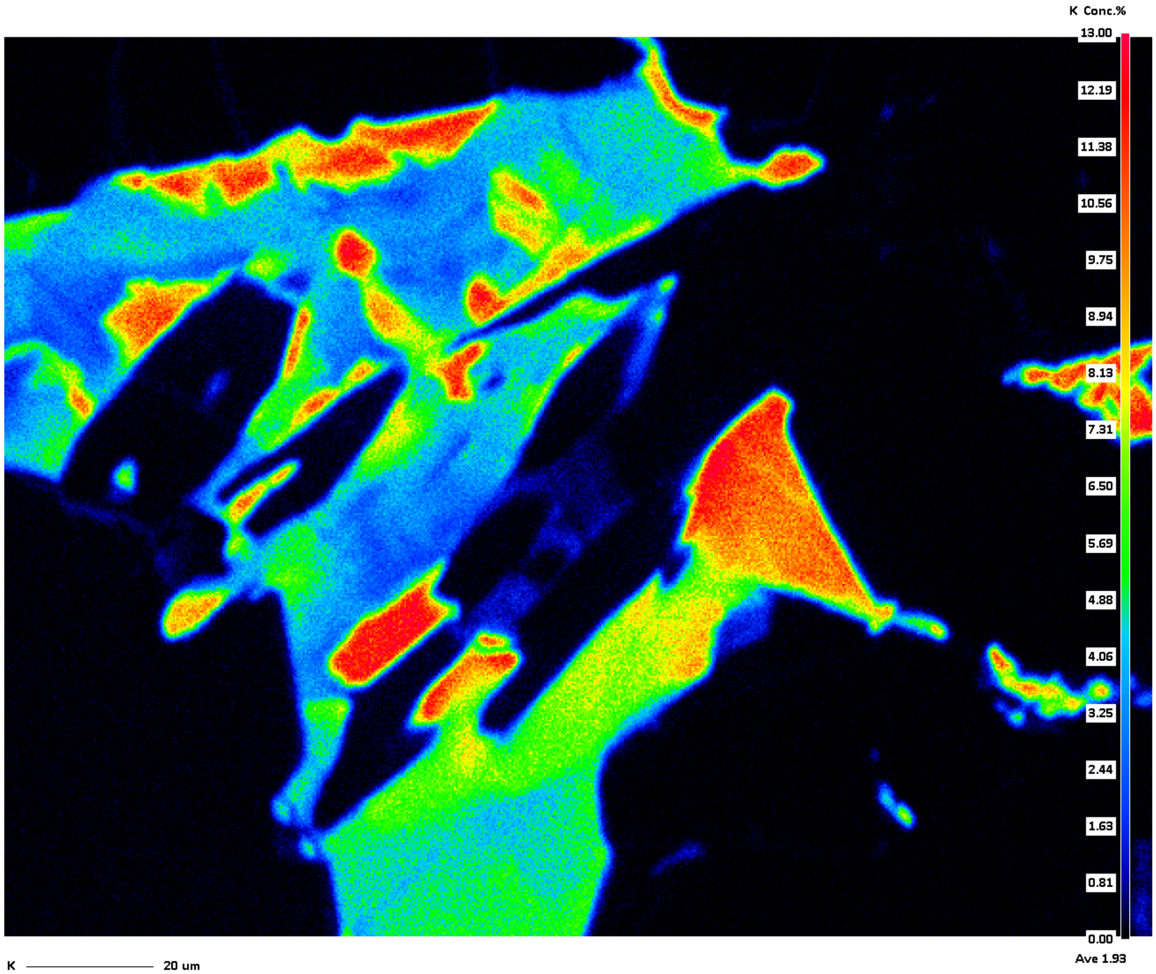

Supplementary Figure 74. Quantitative WDS (Wavelength Dispersive Spectrometry) elemental map distribution of potassium (K) in apatite-assemblage #2 in NWA 998.

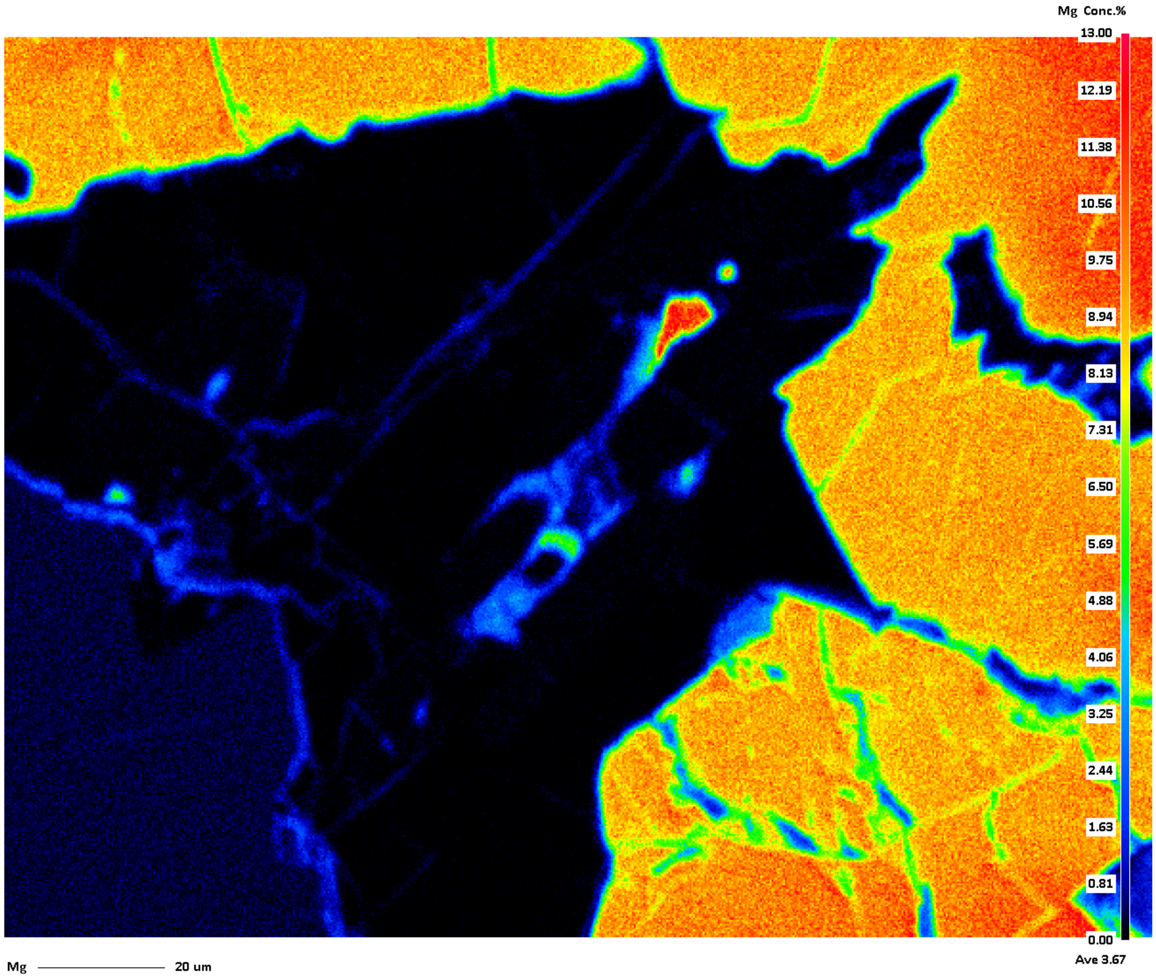

Supplementary Figure 75. Quantitative WDS (Wavelength Dispersive Spectrometry) elemental map distribution of magnesium (Mg) in apatite-assemblage #2 in NWA 998.

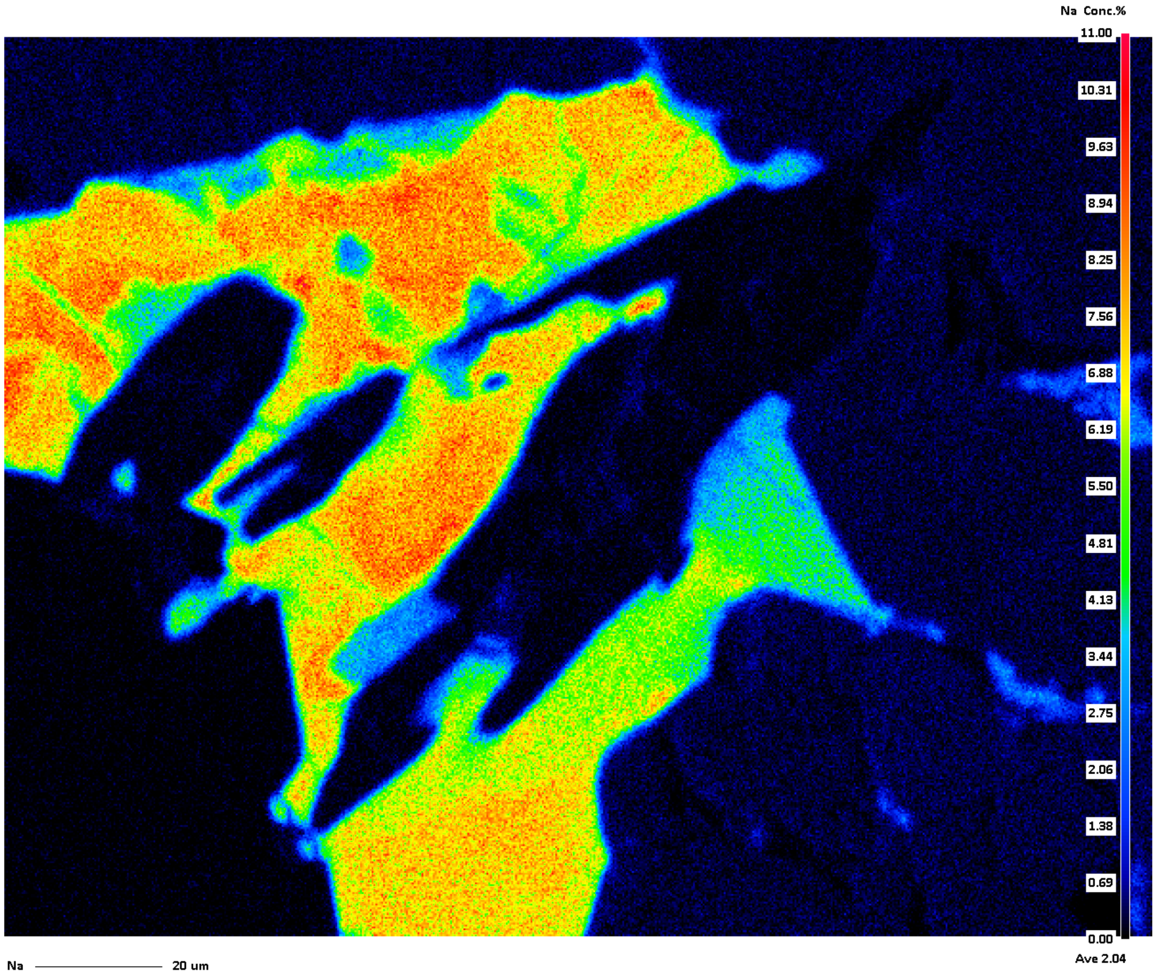

Supplementary Figure 76. Quantitative WDS (Wavelength Dispersive Spectrometry) elemental map distribution of sodium (Na) in apatite-assemblage #2 in NWA 998.

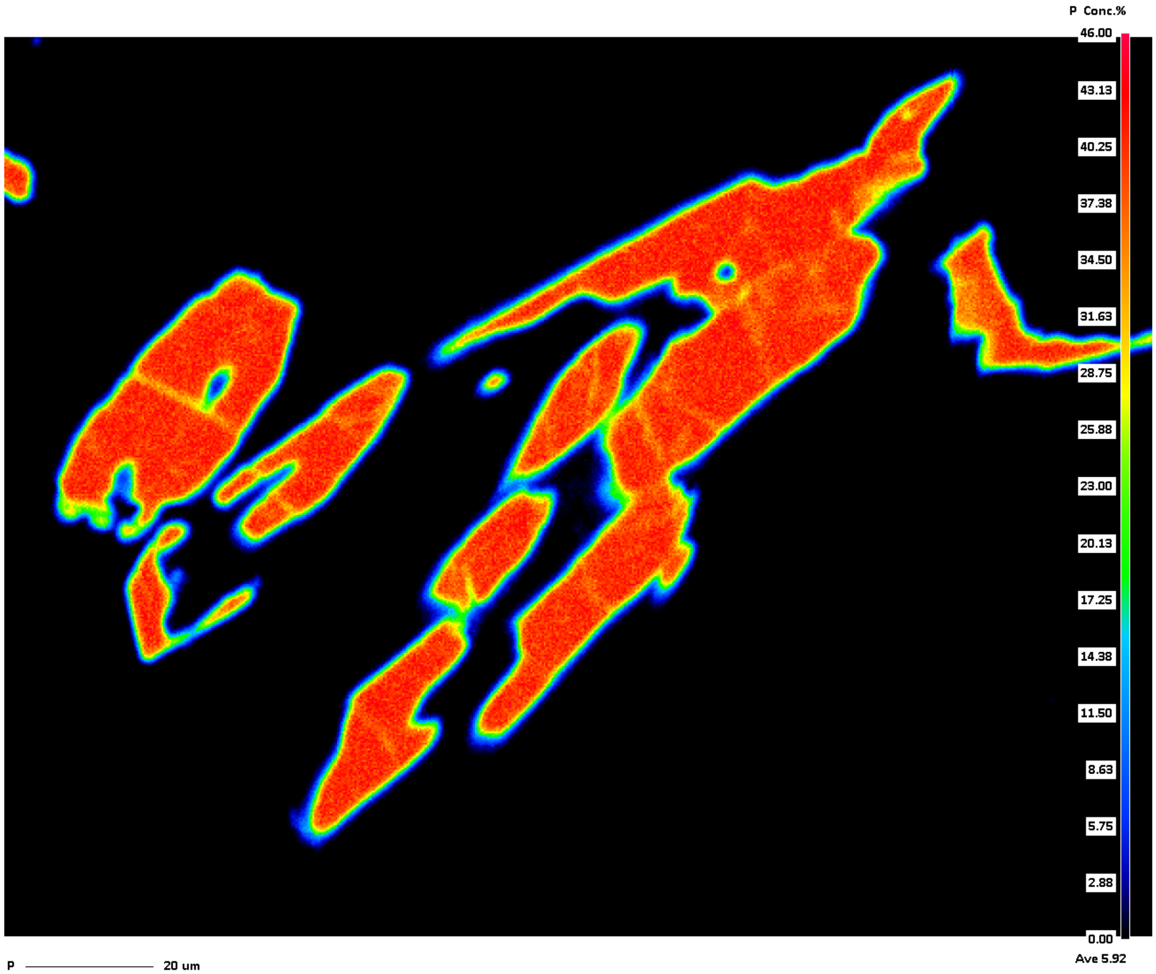

Supplementary Figure 77. Quantitative WDS (Wavelength Dispersive Spectrometry) elemental map distribution of phosphorous (P) in apatite-assemblage #2 in NWA 998.

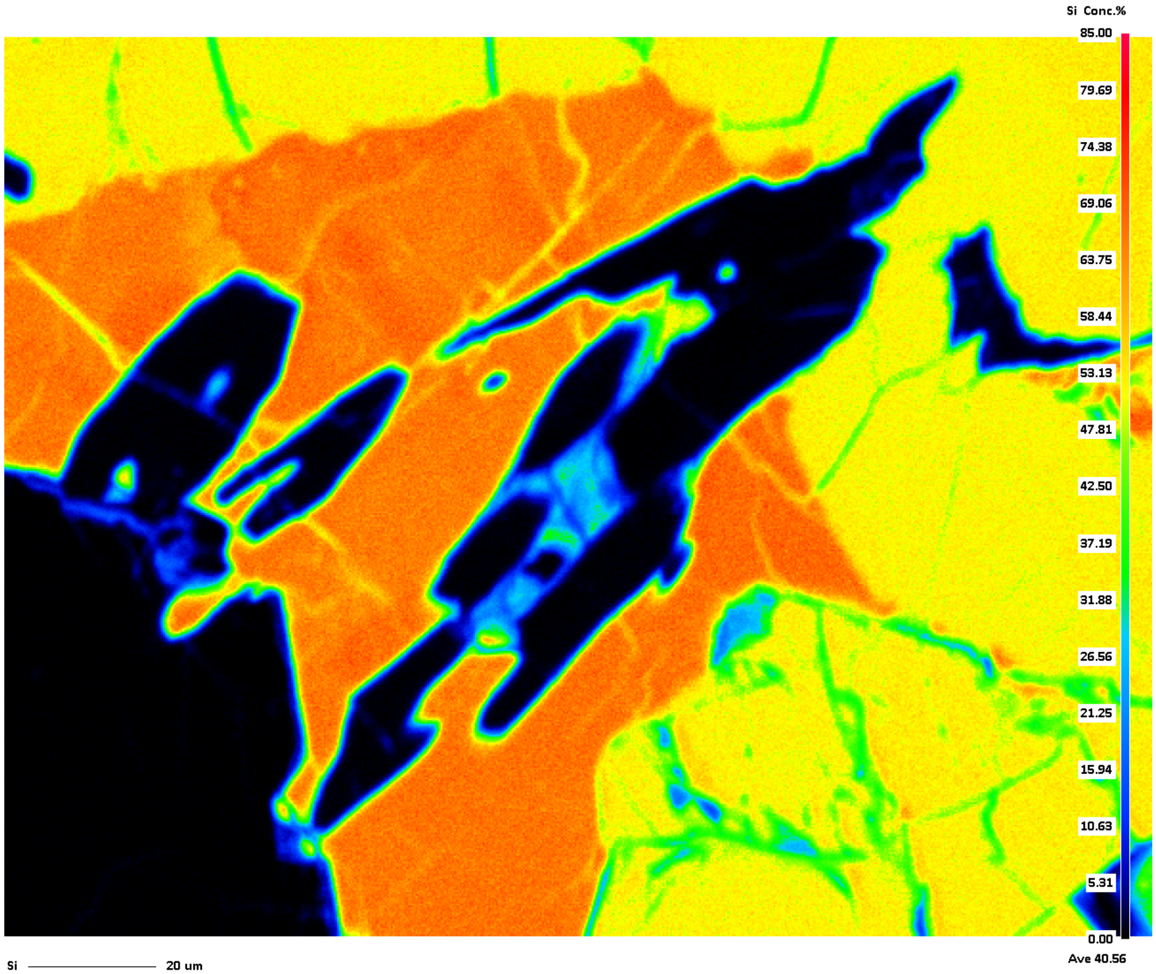

Supplementary Figure 78. Quantitative WDS (Wavelength Dispersive Spectrometry) elemental map distribution of silicon (Si) in apatite-assemblage #2 in NWA 998.

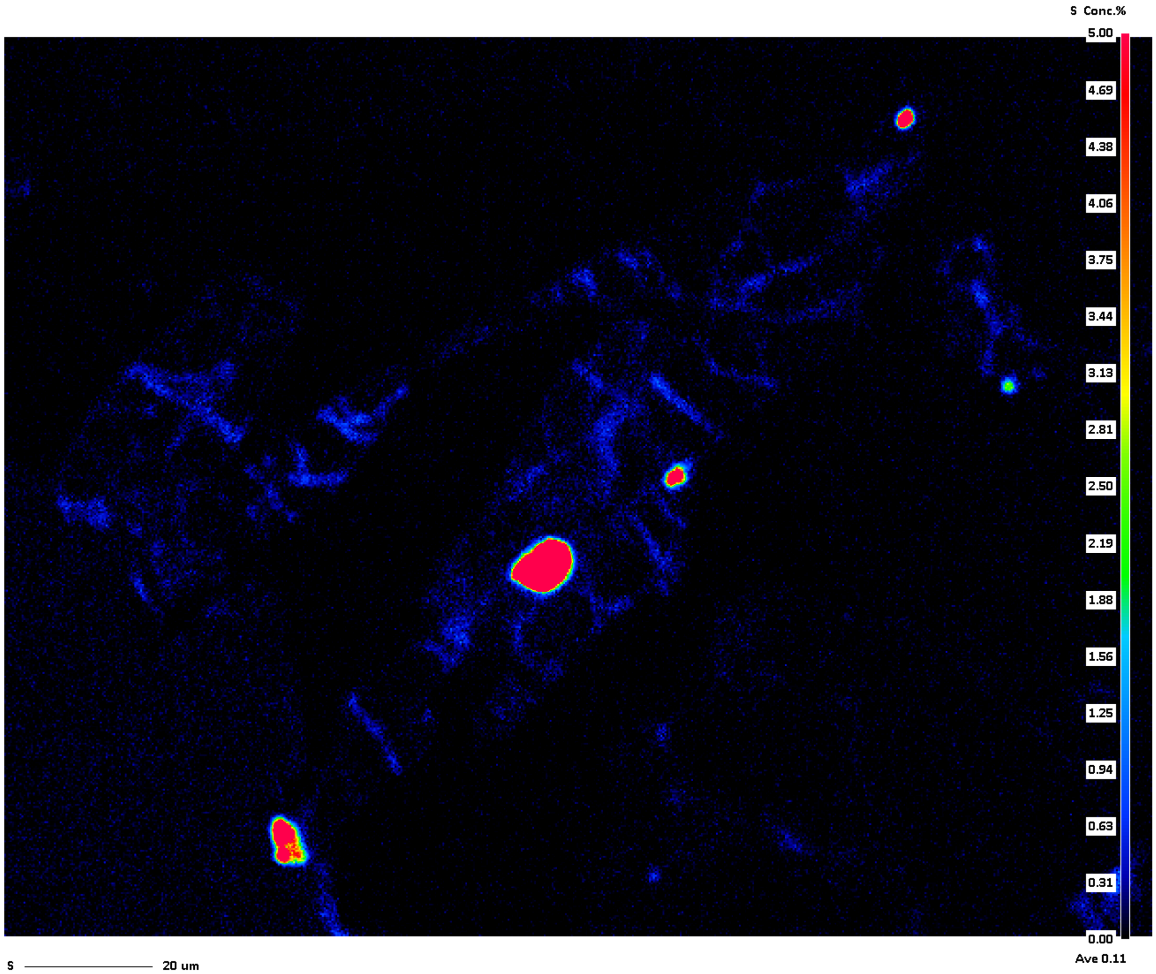

Supplementary Figure 79. Quantitative WDS (Wavelength Dispersive Spectrometry) elemental map distribution of sulfur (S) in apatite-assemblage #2 in NWA 998.

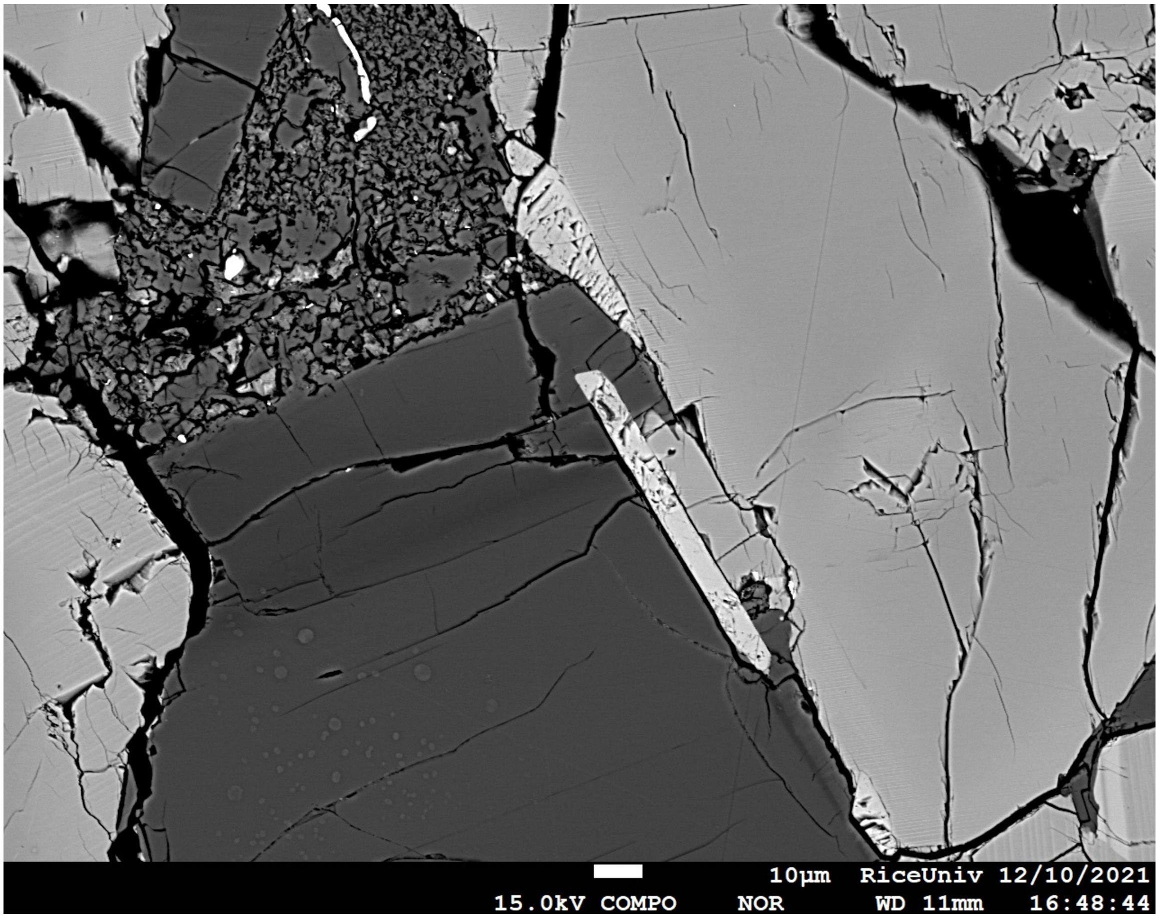

Supplementary Figure 80. BSE (BackScattered Electron) image of apatite-bearing assemblage #3 in NWA-998.

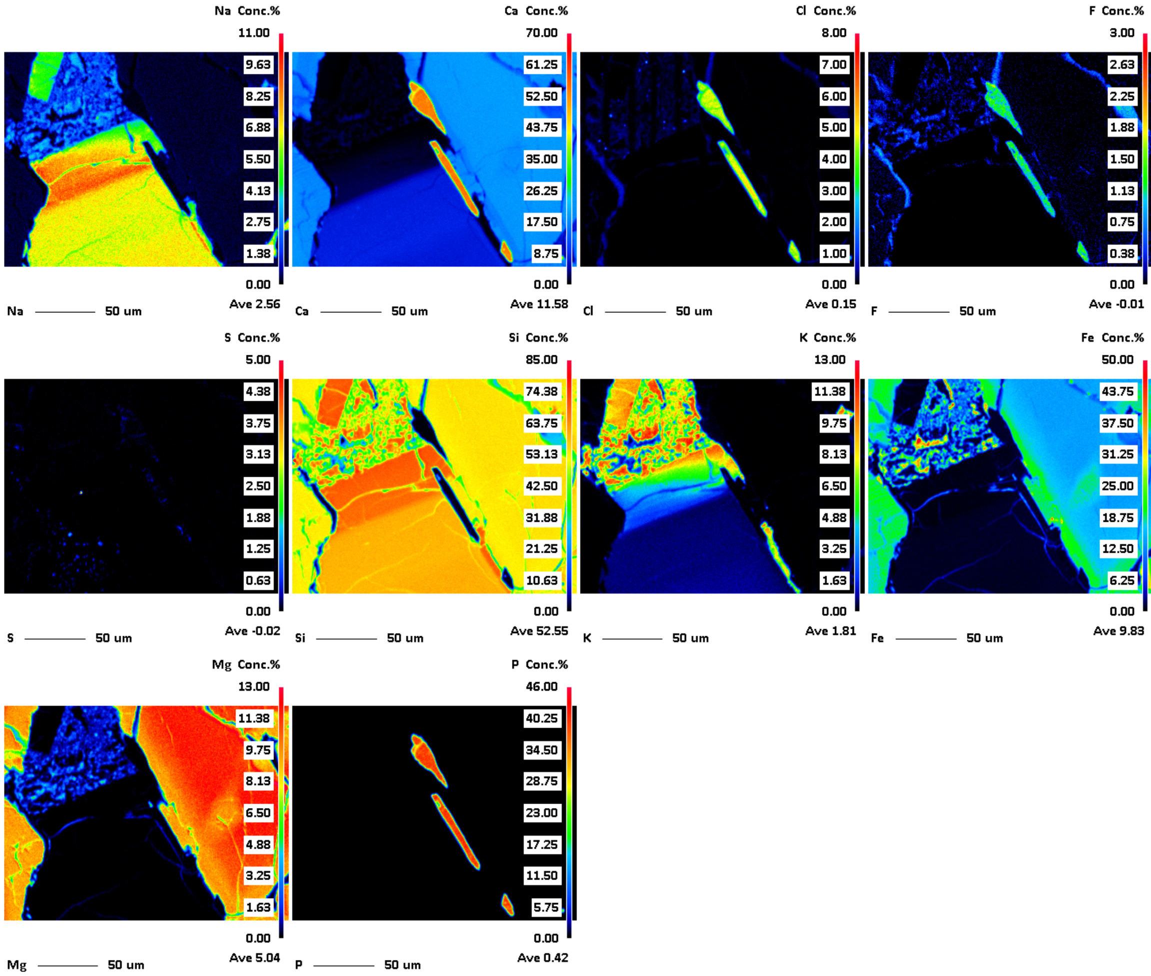

Supplementary Figure 81. Quantitative WDS (Wavelength Dispersive Spectrometry) element map distribution of apatite-assemblage #3 in NWA 998.

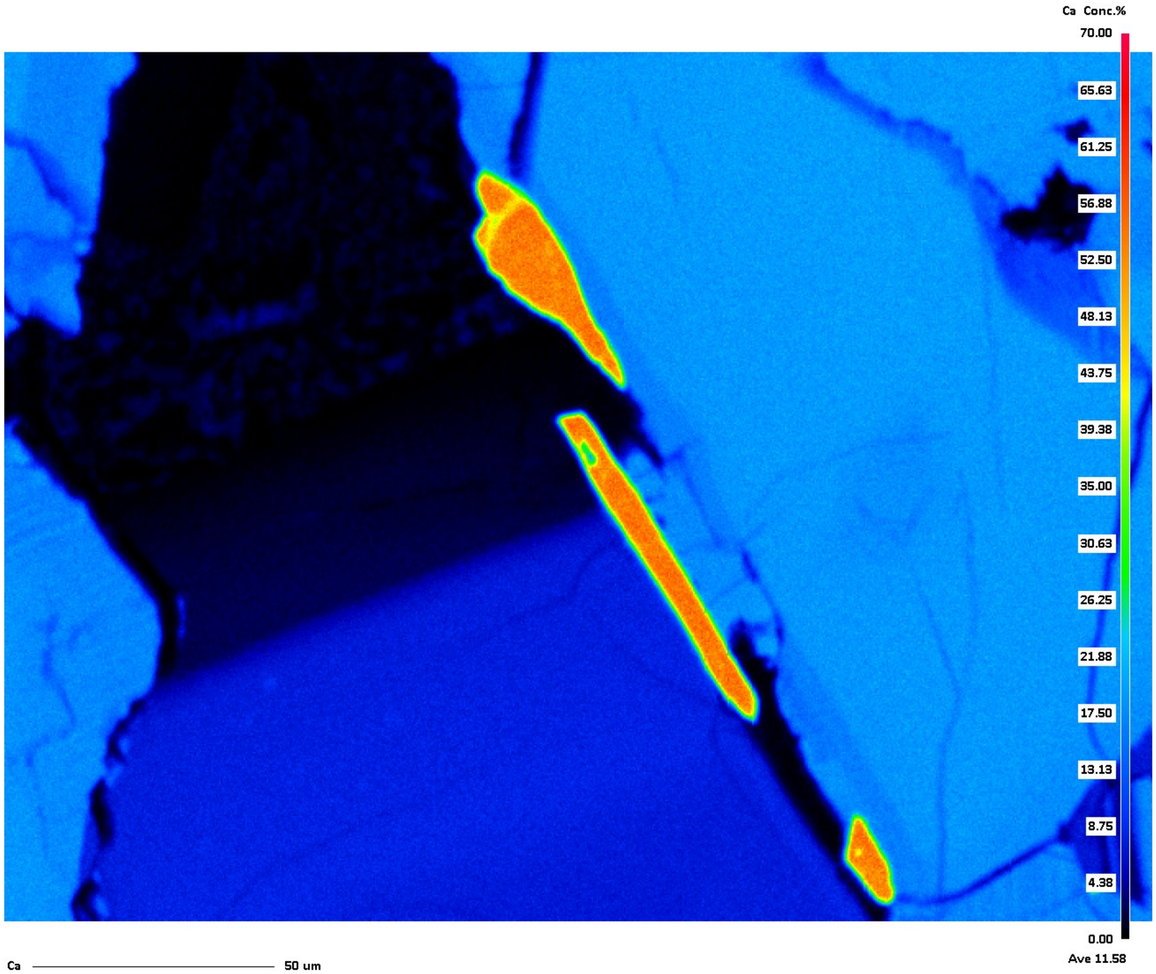

Supplementary Figure 82. Quantitative WDS (Wavelength Dispersive Spectrometry) elemental map distribution of calcium (Ca) in apatite-assemblage #3 in NWA 998.

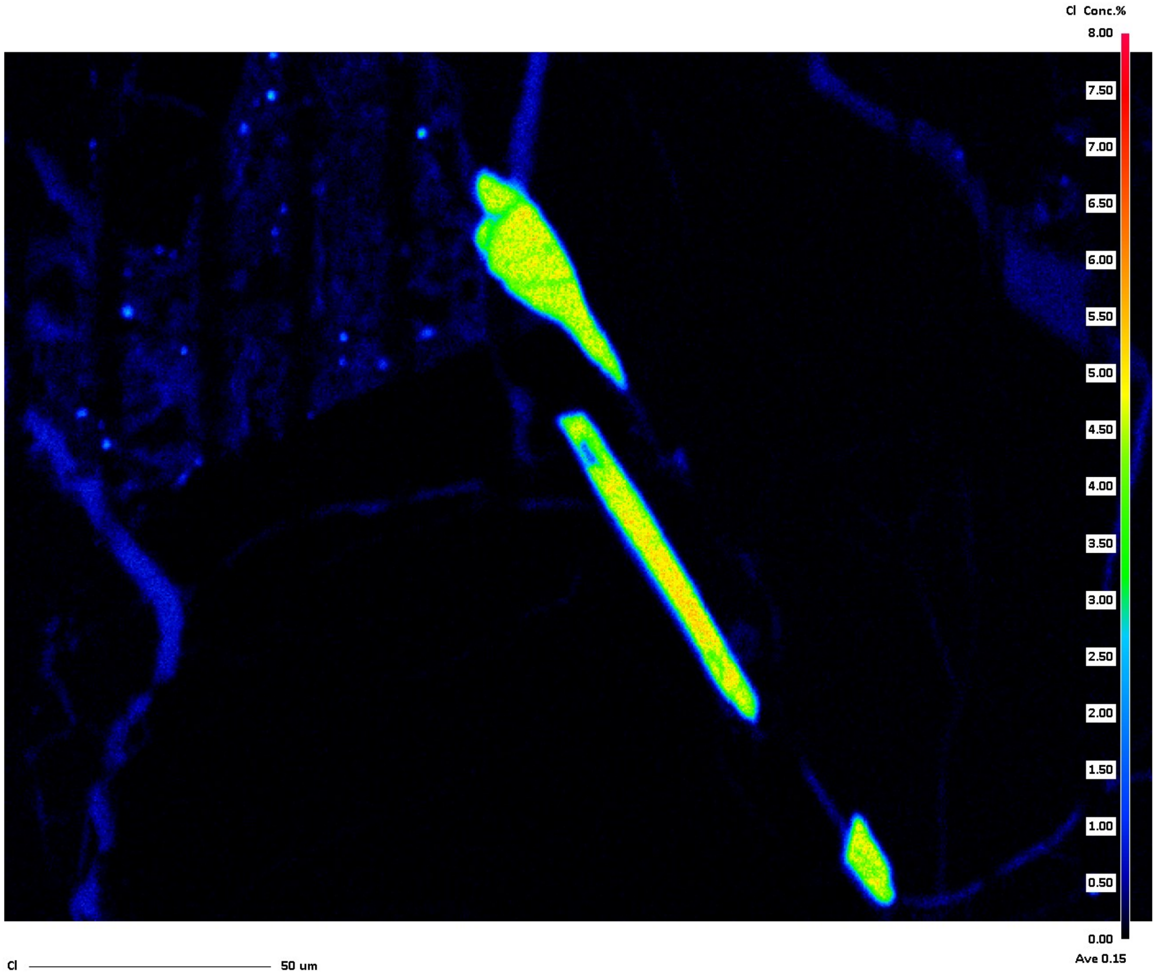

Supplementary Figure 83. Quantitative WDS (Wavelength Dispersive Spectrometry) elemental map distribution of chlorine (Cl) in apatite-assemblage #3 in NWA 998.

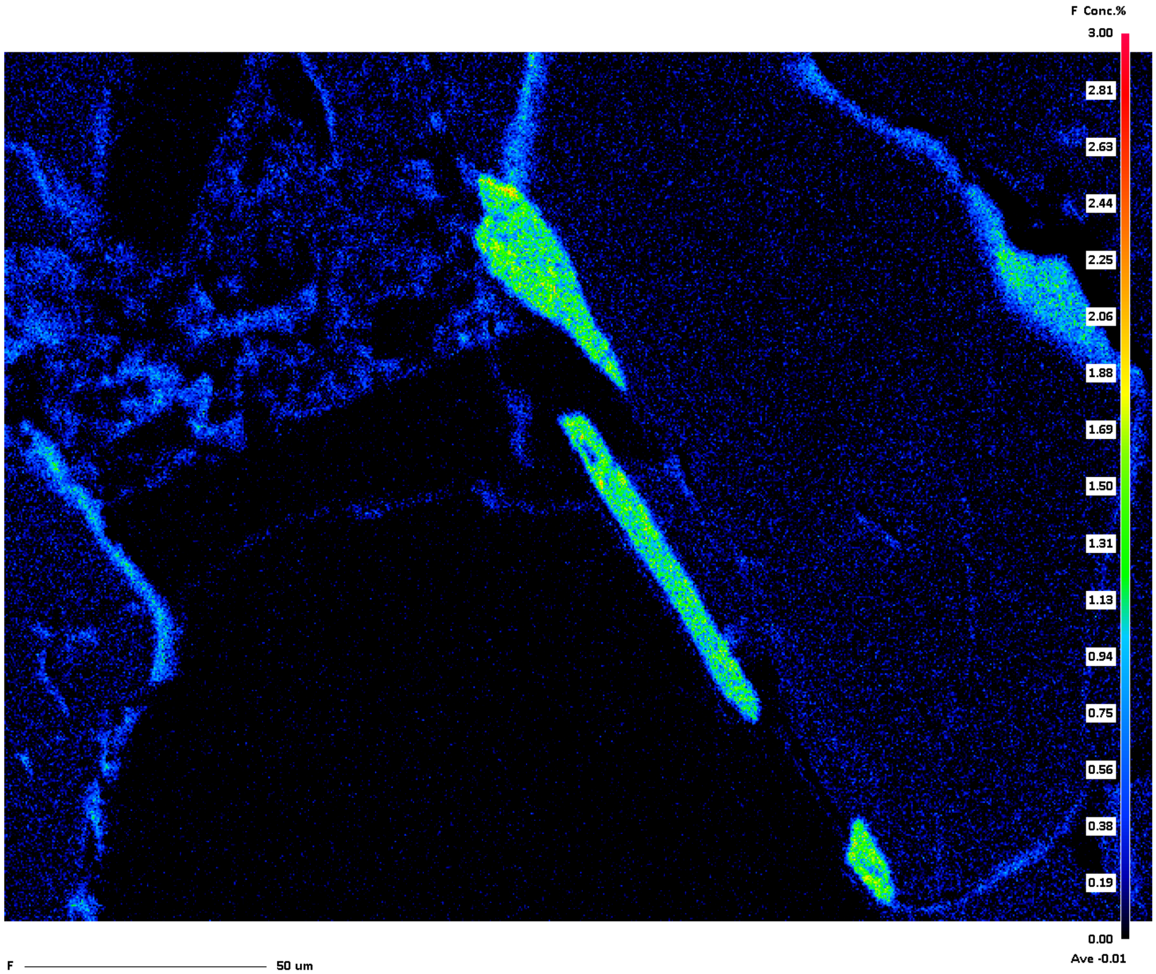

Supplementary Figure 84. Quantitative WDS (Wavelength Dispersive Spectrometry) elemental map distribution of fluorine (F) in apatite-assemblage #3 in NWA 998.

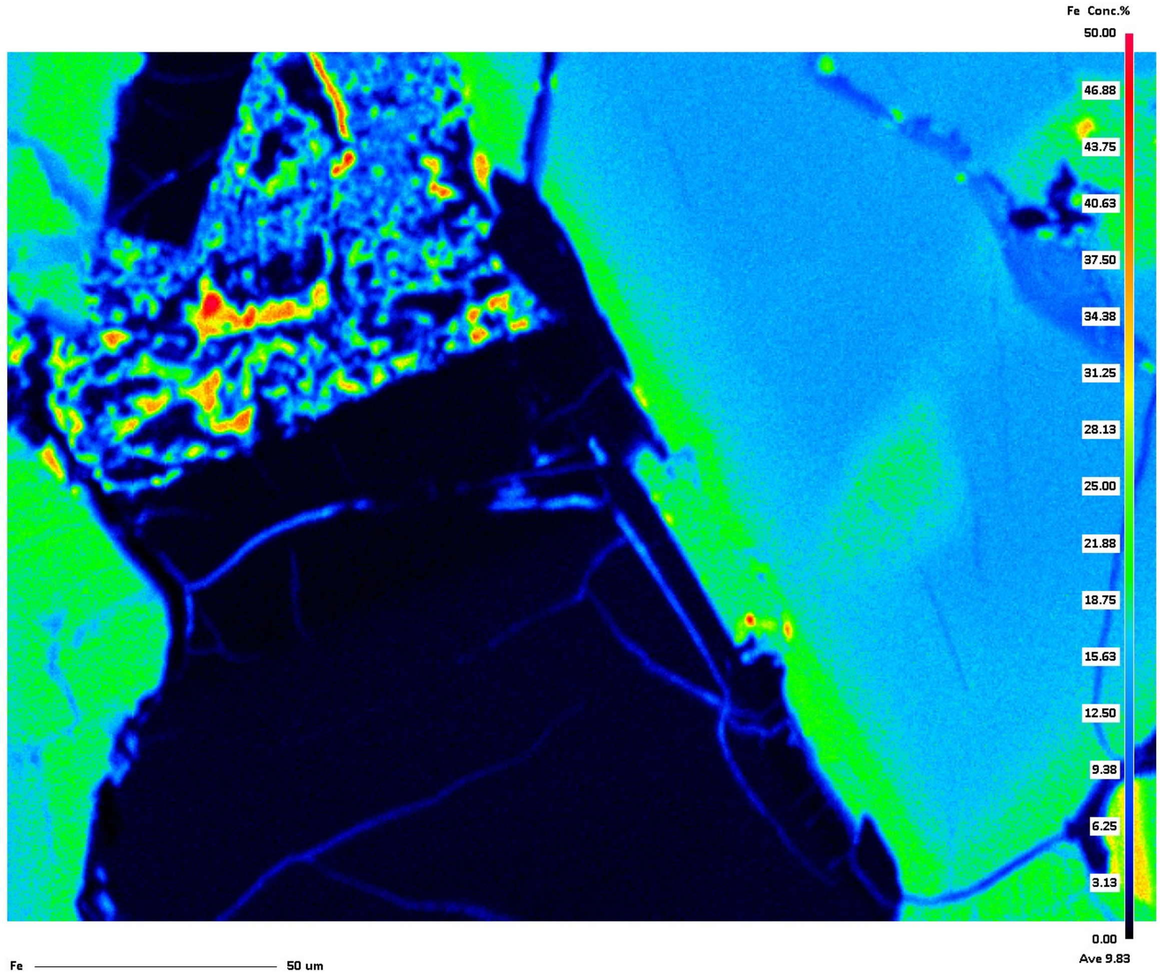

Supplementary Figure 85. Quantitative WDS (Wavelength Dispersive Spectrometry) elemental map distribution of iron (Fe) in apatite-assemblage #3 in NWA 998.

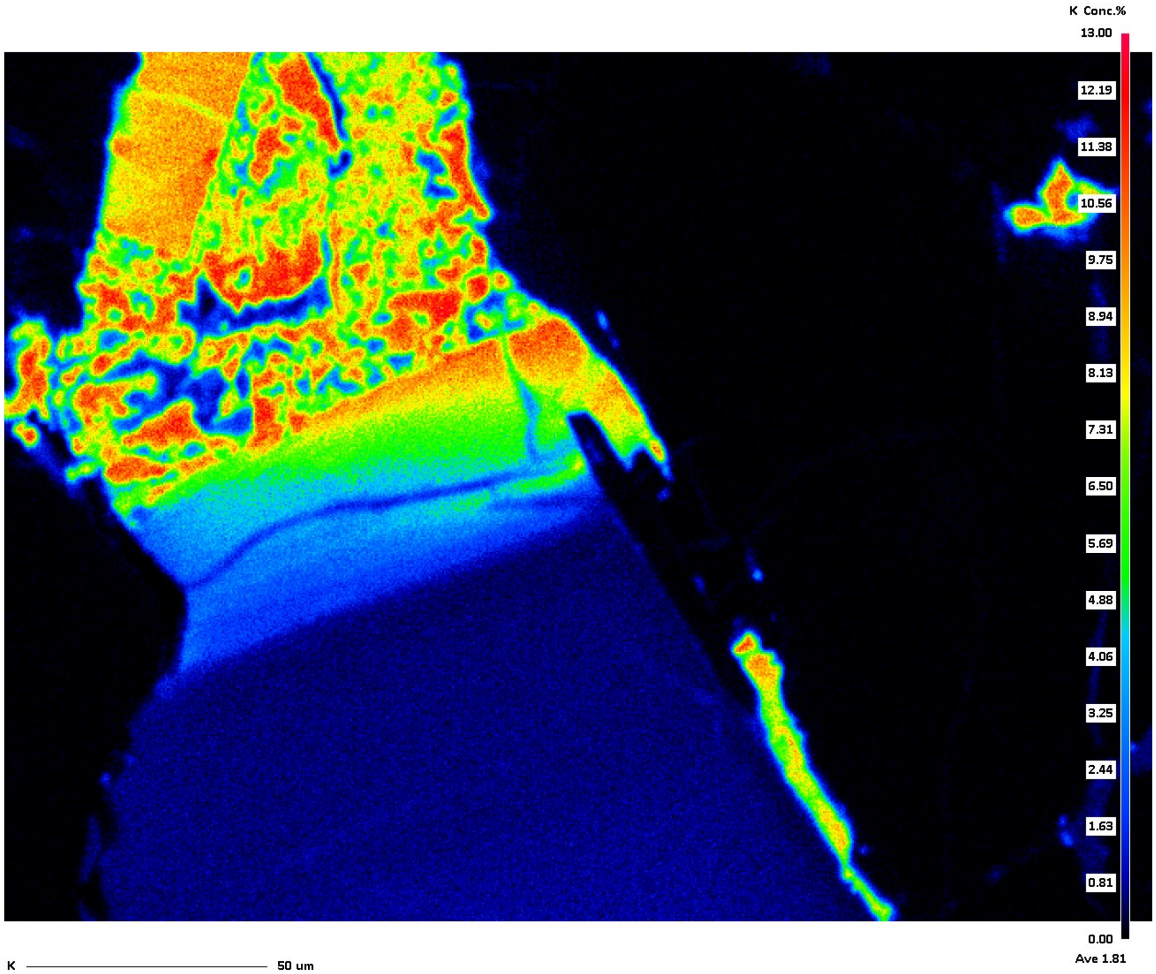

Supplementary Figure 86. Quantitative WDS (Wavelength Dispersive Spectrometry) elemental map distribution of potassium (K) in apatite-assemblage #3 in NWA 998.

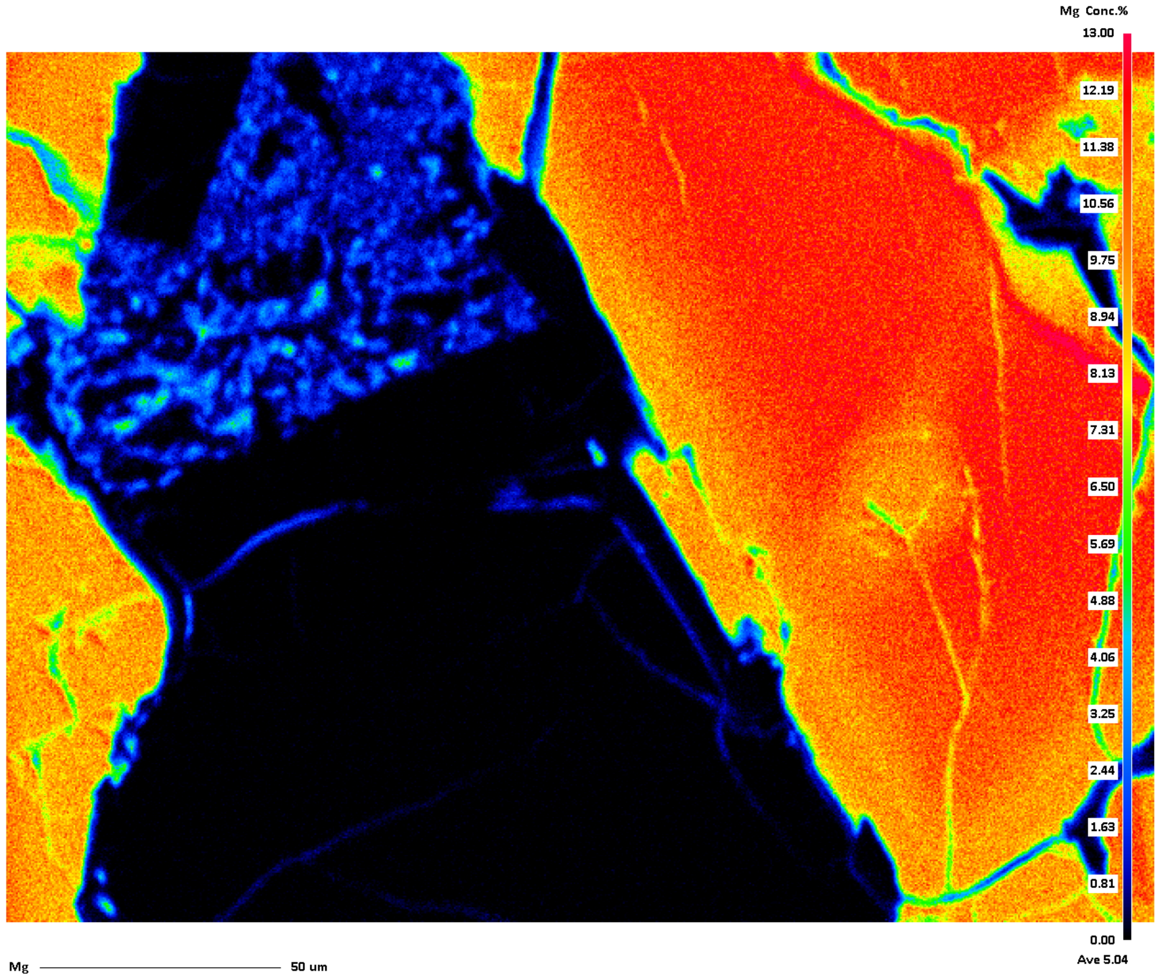

Supplementary Figure 87. Quantitative WDS (Wavelength Dispersive Spectrometry) elemental map distribution of magnesium (Mg) in apatite-assemblage #3 in NWA 998.

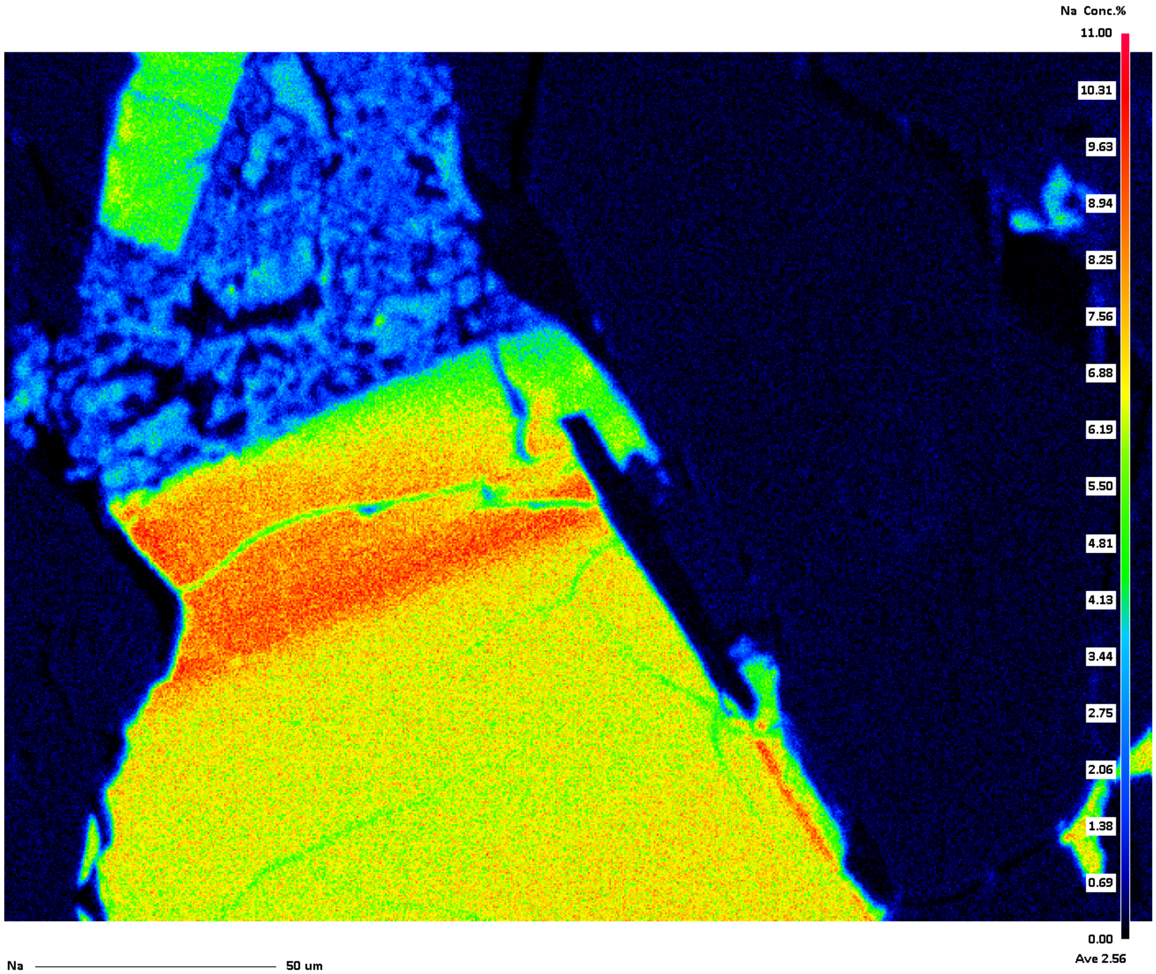

Supplementary Figure 88. Quantitative WDS (Wavelength Dispersive Spectrometry) elemental map distribution of sodium (Na) in apatite-assemblage #3 in NWA 998.

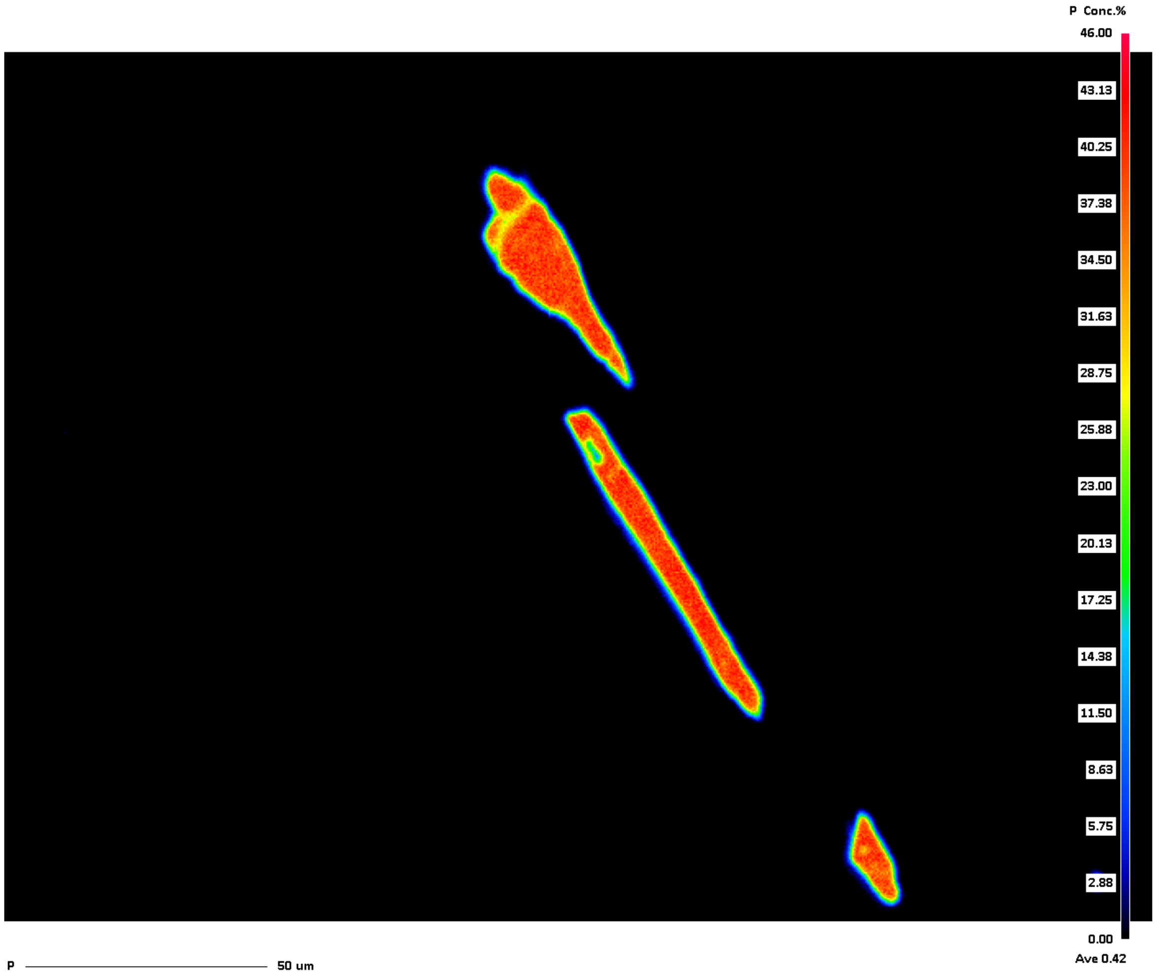

Supplementary Figure 89. Quantitative WDS (Wavelength Dispersive Spectrometry) elemental map distribution of phosphorus (P) in apatite-assemblage #3 in NWA 998.

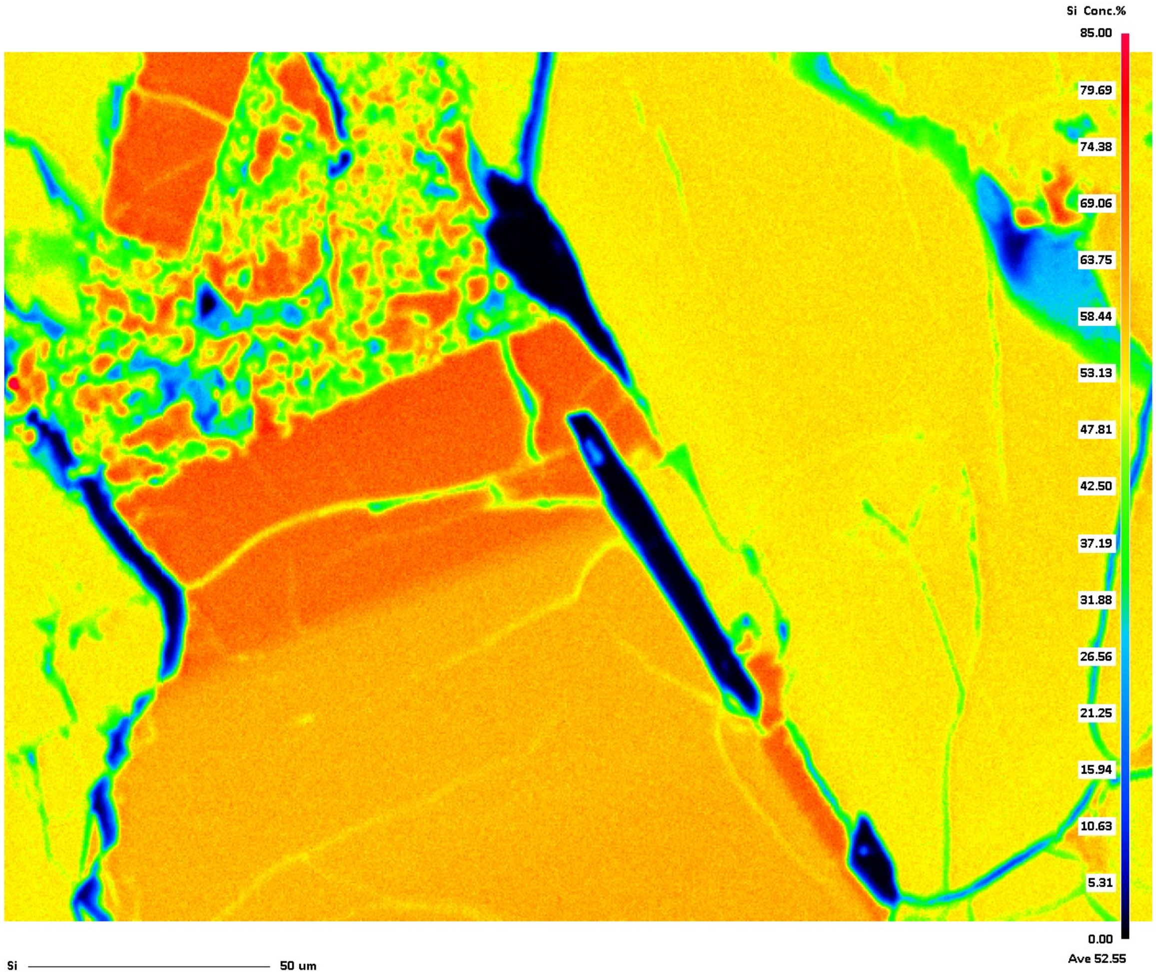

Supplementary Figure 90. Quantitative WDS (Wavelength Dispersive Spectrometry) elemental map distribution of silicon (Si) in apatite-assemblage #3 in NWA 998.

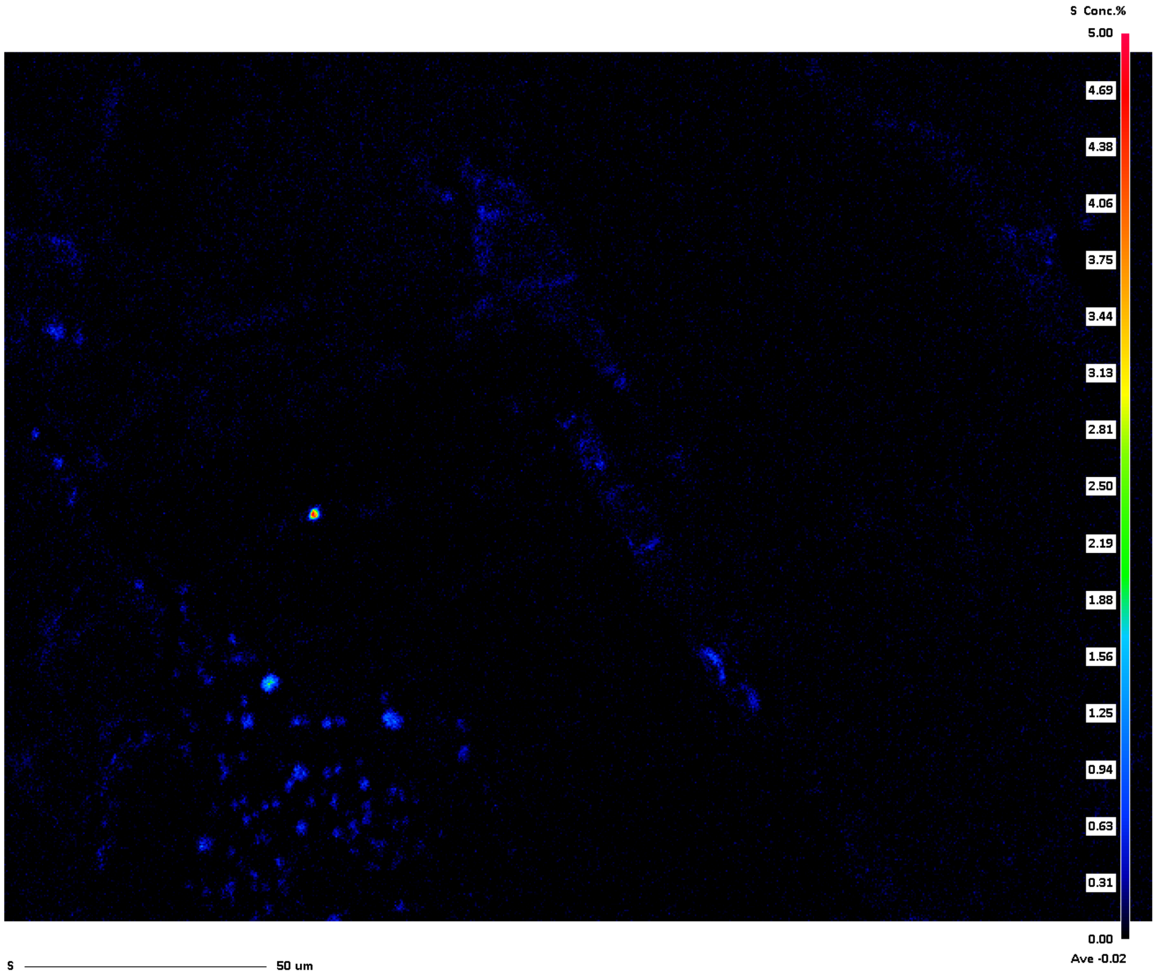

Supplementary Figure 91. Quantitative WDS (Wavelength Dispersive Spectrometry) elemental map distribution of sulfur (S) in apatite-assemblage #3 in NWA 998.

APPENDIX D:

RAMAN SPECTROSCOPY

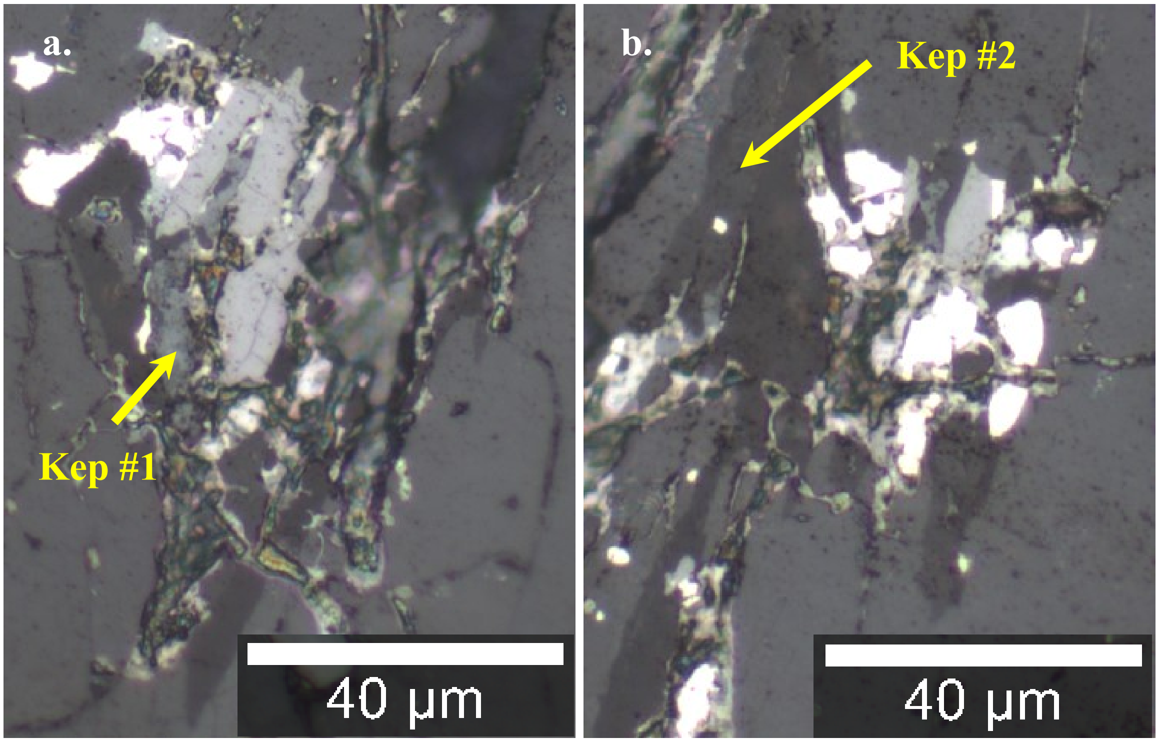

Supplementary Figure 92. Backscattered electron (BSE) image of keplerite grains targeted for Raman analysis. BSE image (a) is of keplerite grain #1. BSE image (b) is of keplerite grain #2. Highly birefringent "phases" noted in BSE images are carbon coating.

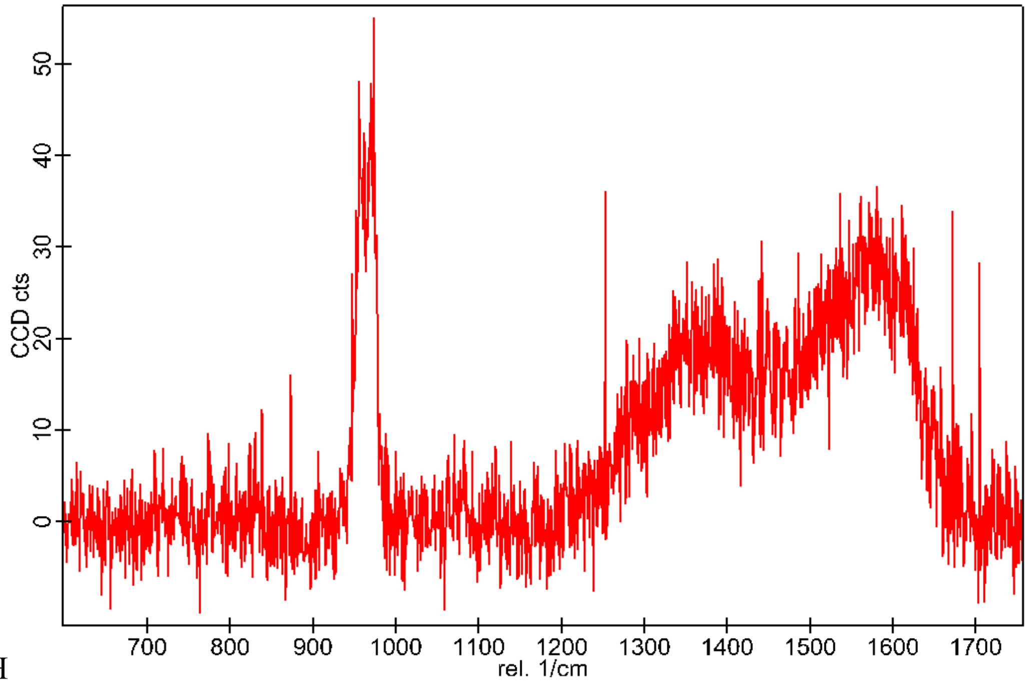

H

Supplementary Figure 93. Representative analysis of measured Raman spectra for keplerite (grain #1) in Tissint over the 700 to 1700 cm^{-1} range. Spectrum 212.

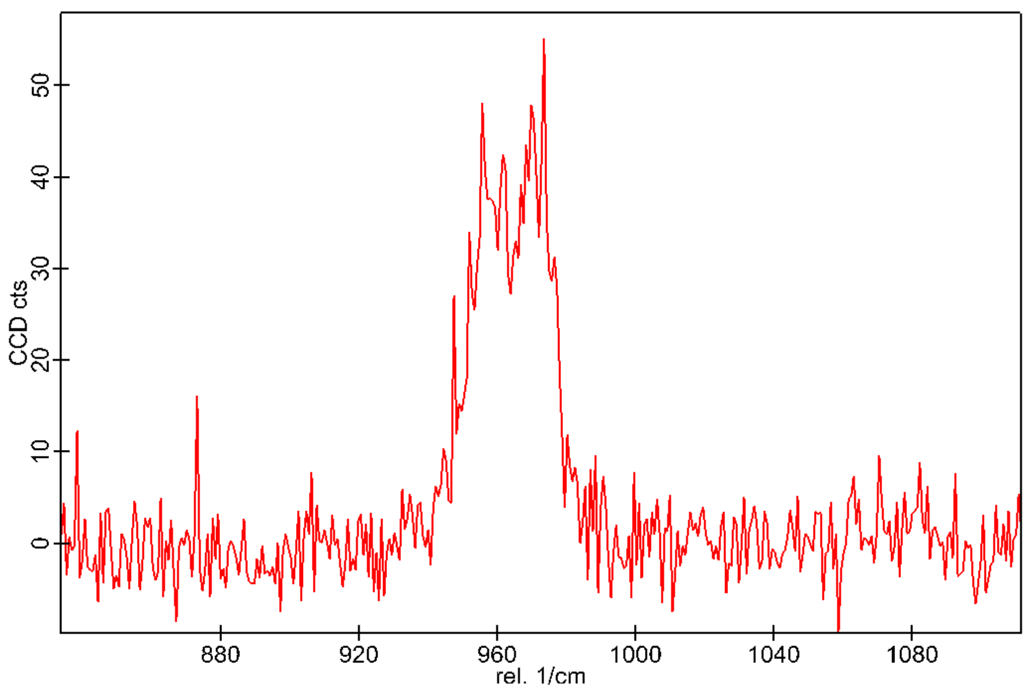

Supplementary Figure 94. Representative analysis of measured Raman spectra for keplerite (grain #1) in Tissint over the 880 to 1080 cm^{-1} range. Spectrum 212.

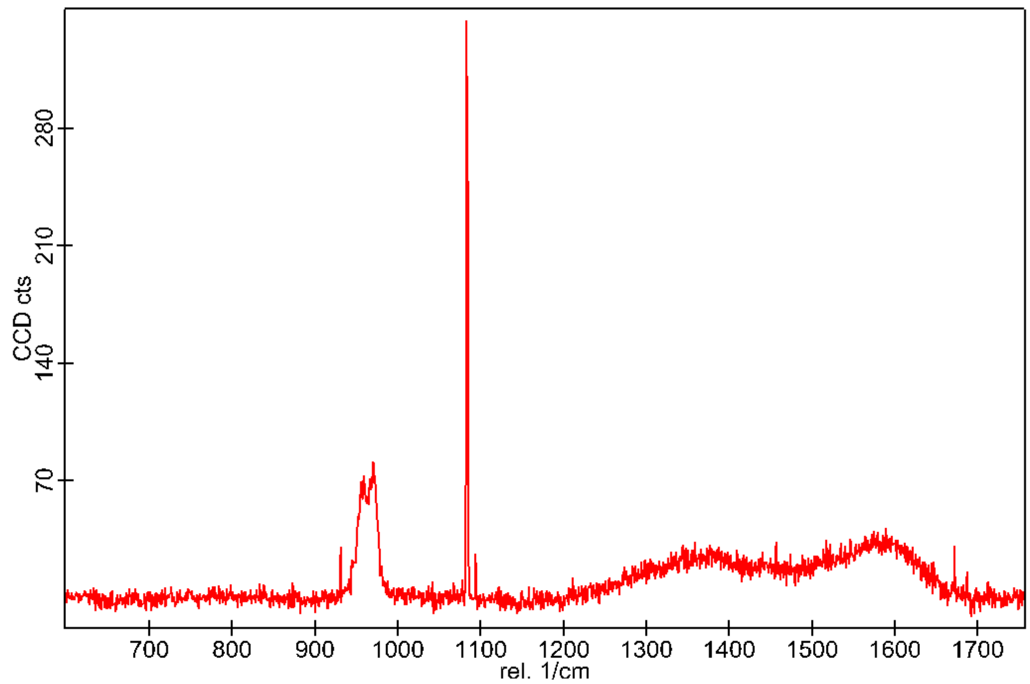

Supplementary Figure 95. Representative analysis of measured Raman spectra for keplerite (grain #1) in Tissint over the 850 to 1100 cm^{-1} range. Spectrum 213.

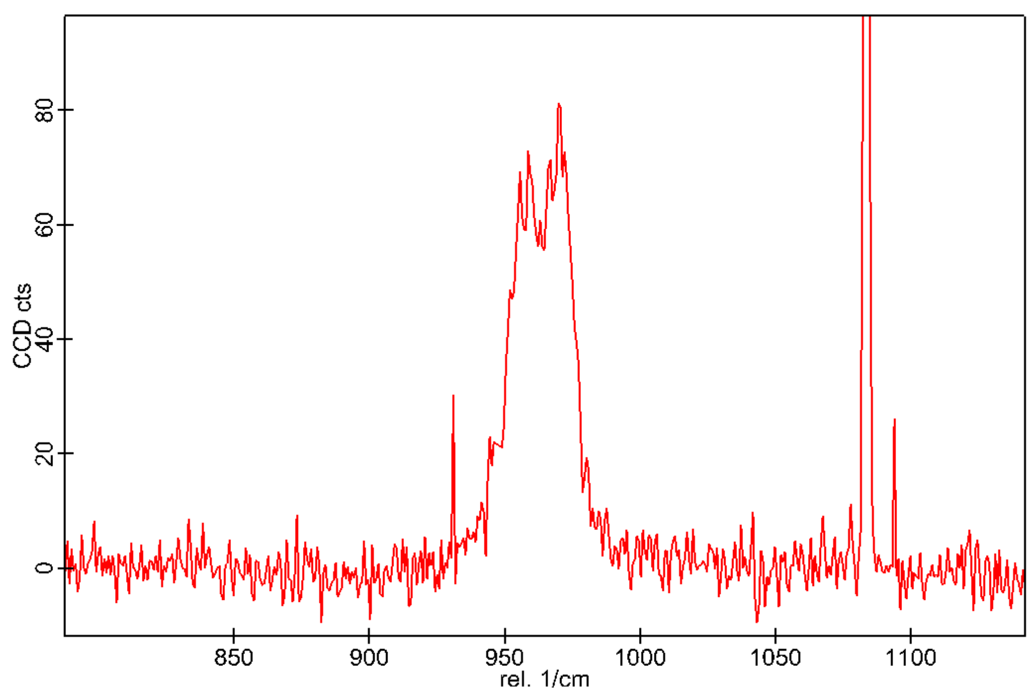

Supplementary Figure 96. Representative analysis of measured Raman spectra for keplerite (grain #1) in Tissint over the 850 to 1100 cm^{-1} range. Spectrum 213.

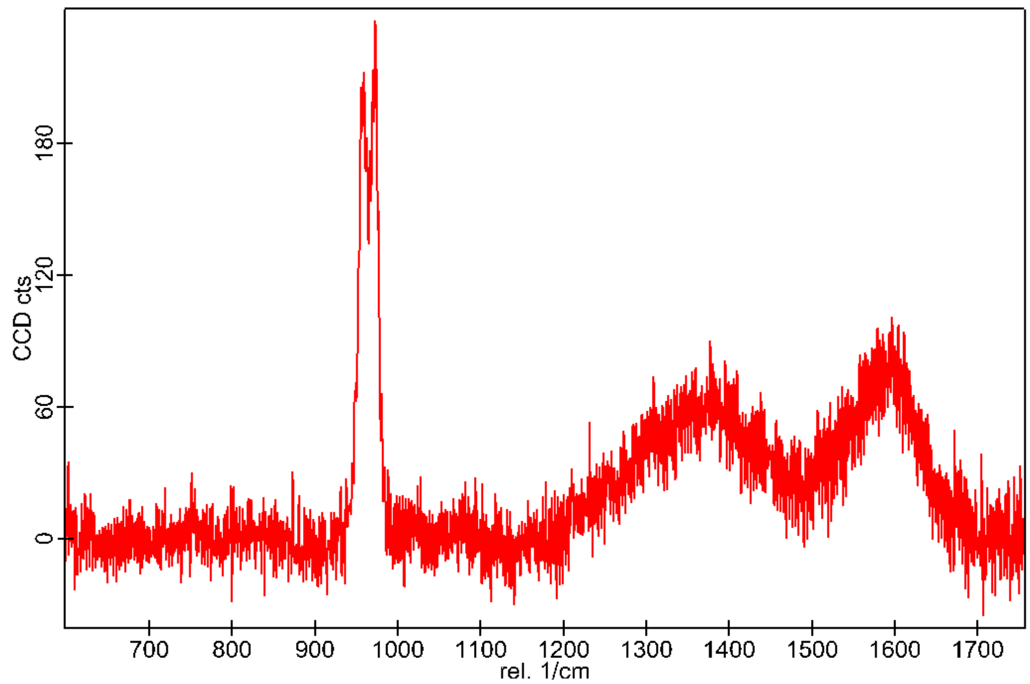

Supplementary Figure 97. Representative analysis of measured Raman spectra for keplerite (grain #2) in Tissint over the 700 to 1700 cm^{-1} range. Spectrum 215.

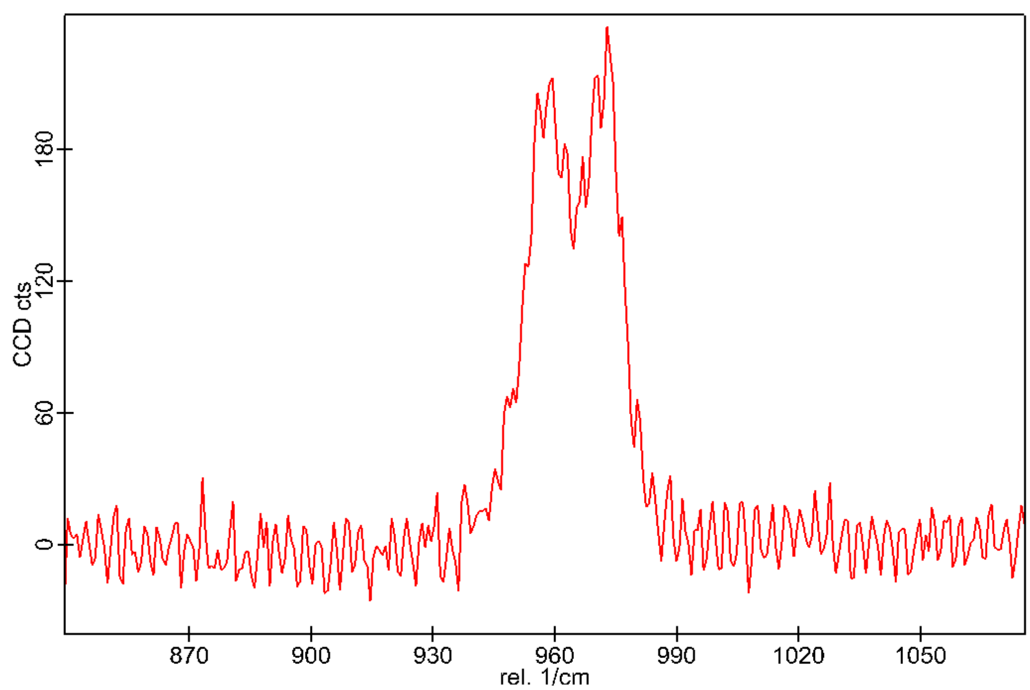

Supplementary Figure 98. Representative analysis of measured Raman spectra for keplerite (grain #2) in Tissint over the 870 to 1050 cm^{-1} range. Spectrum 215.

Supplementary Table 13. Analytical conditions for Raman spectrum 212 (keplerite grain #1).

Spectrum--212: Keplerite Grain #1	
General:	
System ID:	100-1200-1546
Start Time:	10:51:37 AM
Start Date:	Tuesday, October 4, 2022
Duration:	0h 5m 7s
User Name:	Witec
Sample Name:	
Configuration:	Raman 532
UHTS600S_VIS:	
Excitation Wavelength [nm]:	487.954
Laser Power [mW]:	3.175
Grating:	G2: 1200 g/mm BLZ=500nm
Center Wavelength [nm]:	518.303
Spectral Center [rel. 1/cm]:	1200
DU970P_BVF:	
Serial Number:	21926
Readout Mode:	Single Track (1-20)
Output Amplifier:	Conventional
Vertical Shift Speed [µs]:	9.68
Horizontal Shift Speed [MHz]:	0.05
Preamplifier Gain:	4
Cycle Time [sec]:	30.13534
Sensor Temperature [°C]:	-59
Number Of Accumulations:	10
Integration Time [s]:	30
Objective:	
Objective Name:	Zeiss EC Epiplan 50x / 0.75
Objective Magnification:	50
Sample Location (global position):	
Position X [µm]:	-2917.5
Position Y [µm]:	-319.5
Position Z [µm]:	2001.12

Supplementary Table 14. Lorentz conditions for Raman spectrum 213 (keplerite grain #1).

Spectrum--213: Keplerite Grain #1				
General:				
Fit Function Name:	Lorentz			
Fit Function Description:	y = y0 + 2 * Sum(i=0->N-1) (A(i) / PI * w(i) / (4*(x-x0(i))^2 + w(i)^2)			
GOOD KEP1 Big grain Spectrum--213--Spec.Data 1 (CRR) (Repaired) (Sub BG)				
Fit Description:				
Number of Sampling Points:	170			
Degree of Freedom (DoF):	161			
ChiSqr / DoF:	19.2832			
Coefficient of Determination				
CoD (R^2):	0.968732			
Correlation (R):	0.984242			
Average Error:	4.27345			
Parameters:				
Name	Value	Error	Vary	Unit
y0	0	0	no	CCD cts
x0(0)	971.889	0.498979	yes	rel. 1/cm
w(0)	8.16653	0.92389	yes	rel. 1/cm
A(0)	731.481	182.359	yes	(rel. 1/cm)*(CCD cts)
x0(1)	966.559	0.854878	yes	rel. 1/cm
w(1)	7.25837	3.55889	yes	rel. 1/cm
A(1)	301.287	240.876	yes	(rel. 1/cm)*(CCD cts)
x0(2)	957.14	0.405754	yes	rel. 1/cm
w(2)	13.0625	0.872712	yes	rel. 1/cm
A(2)	1240.1	116.976	yes	(rel. 1/cm)*(CCD cts)

Supplementary Table 15. Analytical conditions for Raman spectrum 213 (keplerite grain #1).

Spectrum--213: Keplerite Grain #1	
General:	
System ID:	100-1200-1546
Start Time:	10:57:29 AM
Start Date:	Tuesday, October 4, 2022
Duration:	0h 10m 9s
User Name:	Witec
Sample Name:	
Configuration:	Raman 532
UHTS600S_VIS:	
Excitation Wavelength [nm]:	487.954
Laser Power [mW]:	4.997
Grating:	G2: 1200 g/mm BLZ=500nm
Center Wavelength [nm]:	518.303
Spectral Center [rel. 1/cm]:	1200
DU970P_BVF:	
Serial Number:	21926
Readout Mode:	Single Track (1-20)
Output Amplifier:	Conventional
Vertical Shift Speed [µs]:	9.68
Horizontal Shift Speed [MHz]:	0.05
Preamplifier Gain:	4
Cycle Time [sec]:	30.13534
Sensor Temperature [°C]:	-59
Number Of Accumulations:	20
Integration Time [s]:	30
Objective:	
Objective Name:	Zeiss EC Epiplan 50x / 0.75
Objective Magnification:	50
Sample Location (global position):	
Position X [µm]:	-2917.5
Position Y [µm]:	-319.5
Position Z [µm]:	2001.12

Supplementary Table 16. Lorentz conditions for Raman spectrum 214 (keplerite grain #2).

Spectrum--214: Keplerite Grain #2				
General:				
Fit Function Name:	Lorentz			
Fit Function Description:	y = y0 + 2 * Sum(i=0->N-1) (A(i) / PI * w(i) / (4*(x-x0(i))^2 + w(i)^2)			
GOOD Kep2 Left Grain Spectrum--214--Spec.Data 1 (CRR) (Sub BG)				
Fit Description:				
Number of Sampling Points:	173			
Degree of Freedom (DoF):	164			
ChiSqr / DoF:	91.1895			
Coefficient of Determination				
CoD (R^2):	0.979214			
Correlation (R):	0.989552			
Average Error:	9.29761			
Parameters:				
Name	Value	Error	Vary	Unit
y0	0	0	no	CCD cts
x0(0)	958.037	0.235535	yes	rel. 1/cm
w(0)	10.9012	0.661396	yes	rel. 1/cm
A(0)	2852.16	239.381	yes	(rel. 1/cm)*(CCD cts)
x0(1)	968.764	0.715944	yes	rel. 1/cm
w(1)	8.76938	2.1779	yes	rel. 1/cm
A(1)	1576.22	676.434	yes	(rel. 1/cm)*(CCD cts)
x0(2)	973.699	0.320652	yes	rel. 1/cm
w(2)	5.96298	1.05165	yes	rel. 1/cm
A(2)	1271.45	468.628	yes	(rel. 1/cm)*(CCD cts)

Supplementary Table 17. Analytical conditions for Raman spectrum 214 (keplerite grain #2).

Spectrum--214: Keplerite Grain #2	
General:	
System ID:	100-1200-1546
Start Time:	11:08:33 AM
Start Date:	Tuesday, October 4, 2022
Duration:	0h 10m 11s
User Name:	Witec
Sample Name:	
Configuration:	Raman 532
UHTS600S_VIS:	
Excitation Wavelength [nm]:	487.954
Laser Power [mW]:	5.01
Grating:	G2: 1200 g/mm BLZ=500nm
Center Wavelength [nm]:	518.303
Spectral Center [rel. 1/cm]:	1200
DU970P_BVF:	
Serial Number:	21926
Readout Mode:	Single Track (1-20)
Output Amplifier:	Conventional
Vertical Shift Speed [µs]:	9.68
Horizontal Shift Speed [MHz]:	0.05
Preamplifier Gain:	4
Cycle Time [sec]:	30.13534
Sensor Temperature [°C]:	-59
Number Of Accumulations:	20
Integration Time [s]:	30
Objective:	
Objective Name:	Zeiss EC Epiplan 50x / 0.75
Objective Magnification:	50
Sample Location (global position):	
Position X [µm]:	-2754.7
Position Y [µm]:	56.3
Position Z [µm]:	2001.12

Supplementary Table 18. Lorentz conditions for Raman spectrum 215 (keplerite grain #2).

Spectrum--215: Keplerite Grain #2				
General:				
Fit Function Name:	Lorentz			
Fit Function Description:	y = y0 + 2 * Sum(i=0->N-1) (A(i) / PI * w(i) / (4*(x-x0(i))^2 + w(i)^2)			
GOOD Kep Right bottom grain Spectrum--215--Spec.Data 1 (CRR) (Sub BG)				
Fit Description:				
Number of Sampling Points:	207			
Degree of Freedom (DoF):	198			
ChiSqr / DoF:	176.213			
Coefficient of Determination				
CoD (R^2):	0.962298			
Correlation (R):	0.980968			
Average Error:	12.9827			
Parameters:				
Name	Value	Error	Vary	Unit
y0	0	0	no	CCD cts
x0(0)	973.807	0.390616	yes	rel. 1/cm
w(0)	5.79932	1.24623	yes	rel. 1/cm
A(0)	1388.38	622.436	yes	(rel. 1/cm)*(CCD cts)
x0(1)	969.054	0.984628	yes	rel. 1/cm
w(1)	8.46137	2.76667	yes	rel. 1/cm
A(1)	1509.46	862.201	yes	(rel. 1/cm)*(CCD cts)
x0(2)	957.891	0.24783	yes	rel. 1/cm
w(2)	10.6055	0.727197	yes	rel. 1/cm
A(2)	3270.86	285.248	yes	(rel. 1/cm)*(CCD cts)

Supplementary Table 19. Analytical conditions for Raman spectrum 215 (keplerite grain #2).

Spectrum--215: Keplerite Grain #2	
General:	
System ID:	100-1200-1546
Start Time:	11:20:57 AM
Start Date:	Tuesday, October 4, 2022
Duration:	0h 10m 10s
User Name:	Witec
Sample Name:	
Configuration:	Raman 532
UHTS600S_VIS:	
Excitation Wavelength [nm]:	487.954
Laser Power [mW]:	5.017
Grating:	G2: 1200 g/mm BLZ=500nm
Center Wavelength [nm]:	518.303
Spectral Center [rel. 1/cm]:	1200
DU970P_BVF:	
Serial Number:	21926
Readout Mode:	Single Track (1-20)
Output Amplifier:	Conventional
Vertical Shift Speed [µs]:	9.68
Horizontal Shift Speed [MHz]:	0.05
Preamplifier Gain:	4
Cycle Time [sec]:	30.13534
Sensor Temperature [°C]:	-59
Number Of Accumulations:	20
Integration Time [s]:	30
Objective:	
Objective Name:	Zeiss EC Epiplan 50x / 0.75
Objective Magnification:	50
Sample Location (global position):	
Position X [µm]:	-2722.1
Position Y [µm]:	28.3
Position Z [µm]:	2001.12

APPENDIX E:

ELECTRON BACKSCATTERED DIFFRACTION (EBSD)

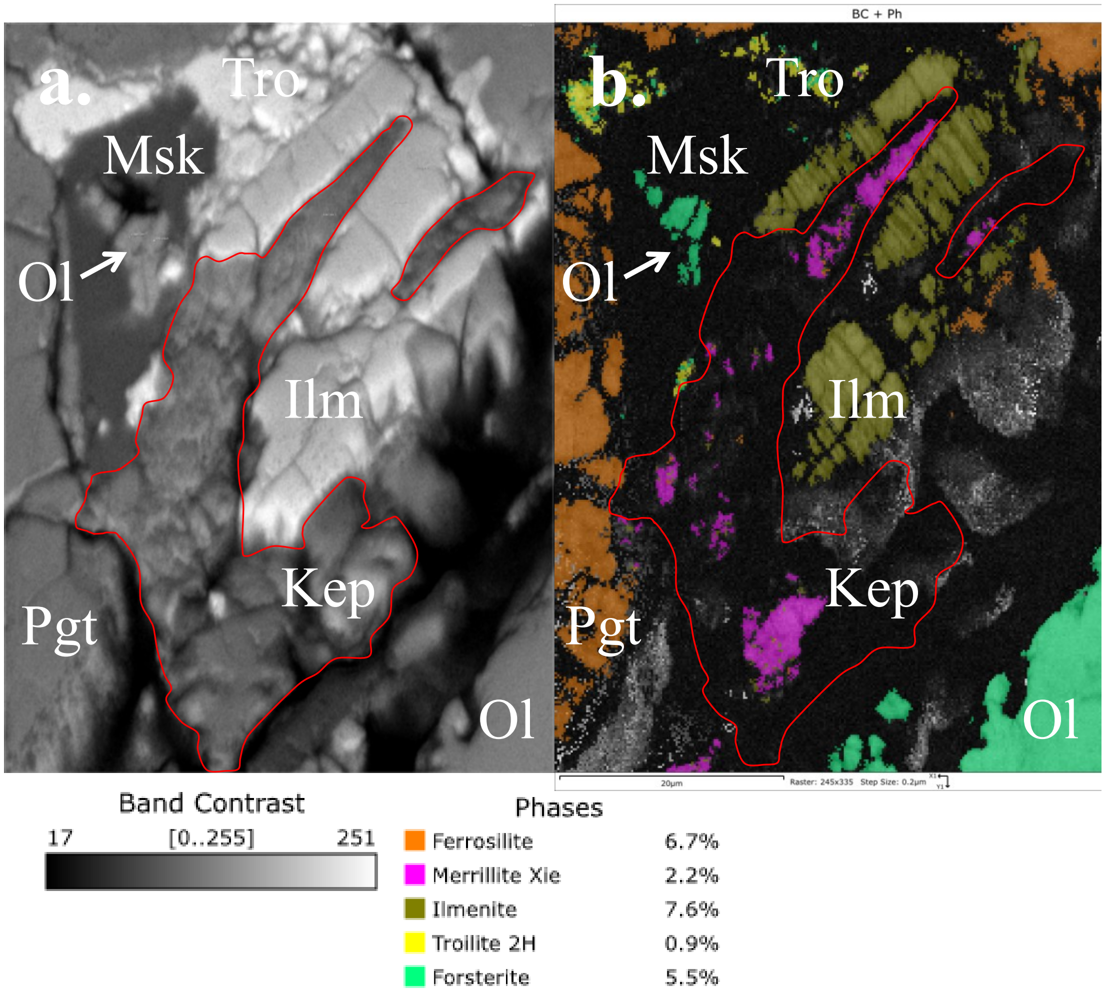

Supplementary Figure 99. Backscattered electron (BSE) image and phase map (Ph) of keplerite grain #1 (and associated) phases in Tissint. Keplerite grains outlined in red.

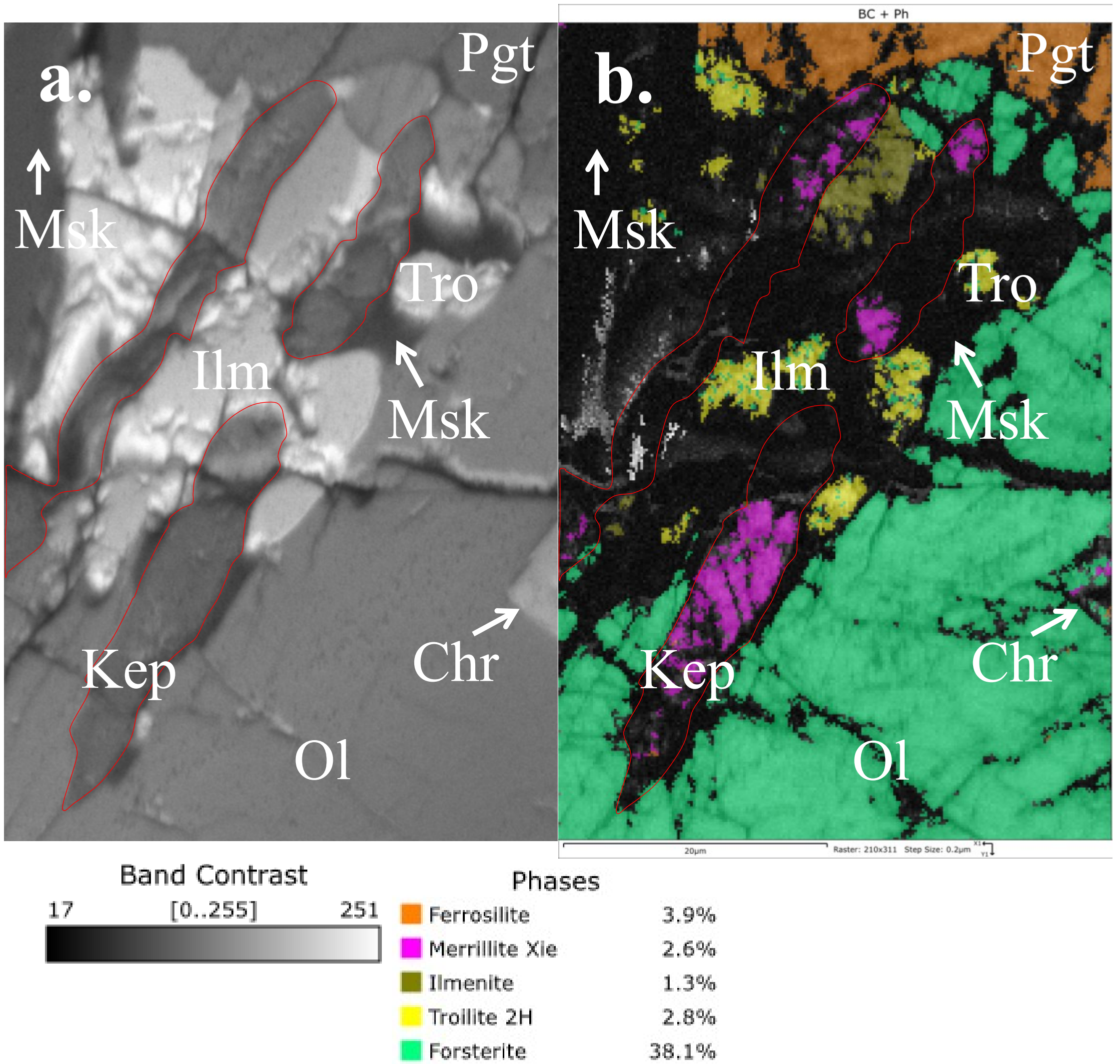

Supplementary Figure 100. Backscattered electron (BSE) image and phase map (Ph) of keplerite grain #2 (and associated) phases in Tissint. Keplerite grains outlined in red.